

**A MECHANICAL FLUID ASSESSMENT OF ANATOMICAL MODELS OF THE
TOTAL CAVOPULMONARY CONNECTION (TCPC)**

A Thesis

Presented to

The Academic Faculty

By

Diane de Julien de Zélicourt

In Partial Fulfillment

Of the Requirements for the Degree

Master of Science in Bioengineering

Georgia Institute of Technology

December, 2004

**A MECHANICAL FLUID ASSESSMENT OF ANATOMICAL MODELS OF THE
TOTAL CAVOPULMONARY CONNECTION (TCPC)**

Approved by:

Ajit P. Yoganathan, PhD (Advisor)

Department of Biomedical Engineering
Georgia Institute of Technology and Emory
University

Don P. Giddens, PhD

College of Engineering
Georgia Institute of Technology

Shiva Sharma, MD

Pediatric Cardiology
Emory University

Date Approved: 11/10/2004

ACKNOWLEDGEMENTS

To all of you who were by my side through these two and half years:

THANK YOU!!!

I would have liked to list here all the little insignificant details that are all that really matters in the end, but if I had done so, this chapter would have unfolded from Atlanta to Paris. Thus I will be brief and rely on you to read in between the lines.

I would first like to thank my advisor, Dr. Ajit P. Yoganathan, for his guidance and insight as I worked through the research for this Master Thesis. Without his support and advice, this thesis could not have been completed.

Special thanks go to Dr. Kerem Pekkan who has provided me with guidance for the development and improvement of my thesis research, but also with his moral support, his priceless smile and his always renewed excitement, whether it be for Turkey, round the world trips or, more simply, new scientific advances.

I would also like to thank all the members of our research laboratory group. Each of them supported me in a different way, helping me in all aspects of my research and the writing of this thesis. Thank you to all of you: H el ene, Jenni, Jorge, Dave, Dennis, Yun, Suchitra, Kartik, Ashley, Dr. Zhoaming He, Dr. Chang Wang, and Steffan. Special thanks go to

Leo, Hiroumi, Anna, Dr. Josie Carberry, Dr. Lakshmi Prasad and Dr. Kerem Pekkan for their review of this thesis, as well as to Lisa, Glenn, Tom and Garrett who worked with me as undergraduates with an always refreshing enthusiasm for the experiments, the power losses, model polishing and DAQAnnal processing.

I would like to express gratitude to Rachel Arnold, Pat Fowler, Chris Ruffin, Rudy Paratchek, Michelle Mayberry, and Tracy Dinkins for their administrative assistance. They have done a great job of making my life a lot easier.

I would like to especially thank Dr Don Giddens and Dr Shiva Sharma for their support throughout my thesis research, for their critical inputs and finally for being on my thesis committee.

This thesis is also addressed to all the surgeons and physicians who worked with us on the Fontan grant and whom I admire for their dedication to their patients and their availability and patience when it comes to answering our questions. Dr. Kanter, Dr. Forbess, Dr. Fogel, Dr. Sharma, Dr. Parks, you were all a great help in bringing together engineering and medicine in this project.

Finally, I would like to thank all my friends and family for their faith in my successful completion of this thesis, and sharing the difficulties that I had. I dedicate this thesis to my parents, Anne and Marc, brother and sister, Olivier and Claire, to my grandfather,

Gaston de Zélicourt, and all my family and apologize for not being more present when hard times were around.

I wrote this thesis as a long smile, to Grégoire with whom I shared hard but also many good years, to my two roommates Franklin and Léon, “c’est les meilleurs y’a pas mieux”, and the long nights spent on the porch discussing the shape of the trees and other deeply philosophic matters, to the silent phone calls and long emails, to Rémi, Leo, Hiroumi, Srin and all the runners, to the frequent flyer numbers, Montreal, Boston, Bologna and Paris, to Héléne and radio-gossip, to Fred, Olive, Juju, Phiphi, Cédric, Tof, Yann, Matthieu, Kheldar, Nath, Rémi, Igor, Gilles, Chris, and all of you who were there:

THIS THESIS IS FOR YOU!!!

And I will never thank you enough for standing by my side.

TABLE OF CONTENTS

ACKNOWLEDGMENTS	iii
LIST OF TABLES	xvi
LIST OF FIGURES	xx
LIST OF ANIMATIONS	xxxii
LIST OF ABBREVIATIONS	xxxiv
SUMMARY	xxxv
CHAPTER I INTRODUCTION	1
CHAPTER II BACKGROUND	4
2.1 Normal Cardiovascular System.....	4
2.2 Congenital Heart Defects.....	8
2.3 Single Ventricle (SV) Heart	9
2.4 Single Ventricle Heart Repairs	12
2.4.1 Historical Perspective on SV Heart Repairs	12
2.4.1.1 The Fontan procedure	13
2.4.1.2 The atrio-pulmonary (AP) connection.....	15
2.4.1.3 The total cavopulmonary connection (TCPC).....	17
2.4.2 Staging the TCPC Procedure	17
2.4.2.1 Stage I: Norwood procedure	18
2.4.2.2 Stage II: Hemi-Fontan or bi-directional Glenn	19
2.4.2.3 Stage III: TCPC	20

2.4.3	Optimal TCPC Procedure	21
2.4.3.1	Connection type	21
2.4.3.2	Fenestration	22
2.4.3.3	Material choice	22
2.4.3.4	Surgical planning.....	23
2.5	Improving the Functional Outcome of Fontan Patients	23
2.5.1	Outcome of Fontan Patients.....	23
2.5.2	Possible Risk Factors and Opportunities for Surgical Outcome Improvement	24
2.5.3	Previous Investigation of the TCPC Hemodynamics	25
2.5.3.1	In vivo studies.....	25
2.5.3.2	In vitro studies	27
2.5.3.3	Numerical simulations	29
2.5.4	Summary and Future Directions	31
2.6	Anatomical Models	32
2.6.1	Magnetic Resonance Imaging (MRI) Techniques	32
2.6.2	Available Fluid Mechanic Assessment Methods.....	35
2.6.3	Manufacturing Methods.....	36
CHAPTER III HYPOTHESIS AND SPECIFIC AIMS.....		38
3.1	Hypothesis I.....	40
3.1.1	Specific Aim 1:.....	40
3.1.2	Specific Aim 2:.....	41
3.2	Hypothesis II.....	42
3.2.1	Specific Aim 3	42
3.2.2	Specific Aim 4	42

CHAPTER IV EQUIPMENT AND MATERIAL	44
4.1 In Vitro Models	44
4.1.1 In Vitro Glass Models.....	44
4.1.1.1 Model 1.....	45
4.1.1.2 Model 2.....	45
4.1.1.3 Model 3.....	46
4.1.1.4 Model 4.....	46
4.1.1.5 Model 5.....	47
4.1.1.6 Model 6.....	47
4.1.2 Stereolithographic Models	49
4.1.2.1 RP replica of the control glass model.....	49
4.1.2.2 Anatomical intra-atrial model.....	49
4.1.2.3 Anatomical bilateral SVC.....	51
4.2 Steady Flow Loop.....	53
4.2.1 Set-Up for Two Inlets/ Two Outlets	53
4.2.2 Set-Up for Three Inlets/ Two Outlets	55
4.2.3 Working Fluid.....	55
4.3 Experimental Measurements Material	58
4.3.1 Flow Rate Measurements	58
4.3.2 Pressure Measurements	58
4.3.2.1 Pressure transducers	58
a. Reluctance pressure transducer technology	58
b. Catheters and liquid filling.....	60
c. Sensing membrane	61
4.3.2.2 Carrier demodulator.....	62
4.3.2.3 A/D board	62
4.3.2.4 Data acquisition software	63
4.3.2.5 Data processing software.....	63

4.3.3	Flow Visualization.....	64
4.3.3.1	Particle flow visualization.....	64
4.3.3.2	Dye flow visualization.....	64
4.3.4	2D Digital Particle Image Velocimetry (DPIV)	66
4.3.4.1	Theory of operation.....	66
a.	Single-frame autocorrelation.....	67
b.	Double-frame cross-correlation	68
4.3.4.2	DPIV hardware	70
a.	Lasers	71
b.	TSI Incorporated (Shoreview, MN).....	72
c.	LaVision (LaVision GmbH, Goettingen, Germany).....	74
d.	Flow seeding	74
4.3.5	Laser Doppler Velocimetry (LDV)	75
4.3.5.1	Laser	76
4.3.5.2	Flow seeding.....	77
4.3.5.3	LDV measurement principle	77
4.3.5.4	Signal acquisition	79
4.4	Computational Fluid Dynamics (CFD).....	80
4.4.1	CFD-Ace (Version 5, CFD Research Corporation, Huntsville, AL).....	81
4.4.2	FIDAP (Fluent Inc., NH)	81
4.4.2.1	Numerical scheme	81
4.4.2.2	Convergence	82
4.4.2.3	Grid generation.....	82
4.4.2.4	Boundary conditions	83
4.4.3	In-House Flow Solver	84
4.4.3.1	Numerical scheme	85
4.4.3.2	Convergence	85
4.4.3.3	Grid generation.....	86
4.4.3.4	Boundary conditions	87

CHAPTER V METHODS AND PROTOCOLS	88
5.1 Anatomical Model Manufacturing Methodology	88
5.1.1 Model Construction Overview	88
5.1.2 Patient Data Acquisition.....	89
5.1.3 Anatomical Geometry Reconstruction	91
5.1.4 Design Inversion.....	92
5.1.4.1 Exporting the reconstructed blood volume.....	92
a. Using IGES polylines: the intra-atrial TCPC.....	92
b. Using STL surfaces: the bilateral SVC	93
c. Methods comparison.....	95
5.1.4.2 Design of the experimental box.....	97
5.1.5 Model Manufacturing	99
5.2 Experimental Methods	101
5.2.1 Power Losses Calculation.....	101
5.2.1.1 Pressure drop measurements	101
5.2.1.2 Statistical treatment	101
a. Regional median filtering.....	102
b. Data replacement and interpolation	102
c. Impact on the computed power losses	103
5.2.1.3 Power loss calculation.....	104
5.2.1.4 Friction loss correction.....	105
5.2.1.5 Equal pulmonary vascular resistance (EPVR)	108
5.2.2 Digital Particle Image Velocimetry (DPIV)	110
5.2.2.1 Interrogation sites	110
5.2.2.2 Validation of the DPIV measurements in transparent RP models	115
5.2.2.3 Parameters for data acquisition	115
a. Image calibration.....	115
b. Illumination of the test section.....	116
c. Optimal δt and number of frames	118

5.2.2.4	Vector calculation.....	119
a.	Processing algorithm.....	119
b.	Interrogation window size.....	120
c.	Mask.....	121
d.	Vector post-processing.....	121
5.2.2.5	Summary of the acquisition and processing parameters used for this study	123
5.2.3	Laser Doppler Velocimetry	124
5.2.3.1	Interrogation sites	124
5.2.3.2	Data acquisition.....	124
5.2.3.3	Data processing	126
5.3	CFD Validation Methodology	128
5.3.1	Control Volume Power Losses	128
5.3.2	Average Flow Field	129
5.4	Experimental Flow Conditions	130
5.4.1	Experimental Flow Measurements	130
5.4.2	Motivation for the Tested Flow Conditions.....	130
5.4.2.1	Total flow rate	130
5.4.2.2	Caval flow ratio	132
5.4.2.3	Pulmonary flow ratio.....	132
5.4.3	Experimental and Numerical Flow Settings	132
5.4.3.1	Pressure drop measurements	133
5.4.3.2	Flow visualization	134
5.4.3.3	PIV.....	134
5.4.3.4	LDV.....	135
5.4.3.5	CFD	135
5.4.3.6	Summary.....	136

CHAPTER VI RESULTS	137
6.1 Validation of the Methods	138
6.1.1 Static Pressure Measurements	138
6.1.2 Impact of the Surface Roughness	139
6.1.3 Suitability of the RP Models for Quantitative Optical Flow Measurements	141
6.2 Simplified Models.....	144
6.2.1 Flow Visualization.....	145
6.2.1.1 Models 1 and 2 [Ensley, 2000; Ryu, 2000].....	145
6.2.1.2 Models 3 and 4	147
6.2.1.3 Model 5.....	150
6.2.1.4 Model 6.....	151
6.2.2 Experimental Pressure Drops and Power Losses.....	154
6.2.2.1 General comments	154
6.2.2.2 Model 1.....	157
6.2.2.3 Model 2.....	159
6.2.2.4 Model 3.....	160
6.2.2.5 Model 4.....	161
6.2.2.6 Model 5.....	162
6.2.2.7 Model 6.....	163
6.3 Anatomical Intra-Atrial Model	167
6.3.1 Power Losses	167
6.3.2 Qualitative Flow Field Assessment	169
6.3.3 Quantitative Flow Field Assessment	174
6.3.4 Flow Structure Summary.....	180
6.4 Anatomical Bilateral SVC Model.....	181
6.4.1 Pressure Drops and Power Loss	181
6.4.2 Qualitative Flow Structure.....	185
6.4.3 Quantitative Flow Structure.....	189
6.4.4 Flow Structure Summary.....	196

CHAPTER VII DISCUSSION.....	198
7.1 Manufacturing Methodology	199
7.1.1 Geometric Accuracy.....	199
7.1.2 Material Properties.....	201
7.1.2.1 Surface roughness.....	201
7.1.2.2 Optical measurement accuracy.....	201
7.1.3 Suitability for CFD Validation and Cardiovascular Studies.....	202
7.2 TCPC Hemodynamics	204
7.2.1 Relative Impact of Vessel Diameters and Connection Design on the Power Loss.....	204
7.2.2 Correlation Between Geometric Features and Flow Structures	211
7.2.2.1 Vessel flaring and caval offset	211
7.2.2.2 Pouch.....	211
7.2.2.3 Curvature	212
7.2.2.4 Vessel diameters.....	212
a. Caval diameters.....	213
b. Pulmonary diameters.....	213
7.2.3 Fluid Mechanics in Anatomic TCPC's.....	214
7.2.3.1 Intra-atrial connection	214
7.2.3.2 Bilateral SVC connection.....	218
7.3 CFD Validation	221
7.3.1 Motivation.....	221
7.3.2 Power Losses	222
7.3.2.1 Simplified glass models 1 to 4.....	222
7.3.2.2 Anatomic intra-atrial model	226
7.3.3 Mean Velocity Field	229
7.3.4 Detailed Physics of the Flow Field.....	234
7.3.5 Modeling Issues and Comparison Criteria	237
7.4 Clinical Significance.....	241

CHAPTER VIII LIMITATIONS OF THE STUDY	245
8.1 CFD and In Vitro Modeling	245
8.2 Geometric Accuracy	246
8.3 CFD Validation	246
8.4 3D Velocity Measurements.....	247
8.5 Characterization of the TCPC Efficiency	248
CHAPTER IX CONCLUSIONS	249
9.1 Anatomical In Vitro Models (Specific Aims 1 and 3)	249
9.2 TCPC Hemodynamics (Specific Aim 2).....	250
9.2.1 Summary of the Anatomical Flows	250
9.2.2 Major Hemodynamic Parameters	251
9.2.3 Equal Lung Perfusion	252
9.3 CFD Validation Methodology (Specific Aim 4).....	253
CHAPTER X RECOMMENDATIONS FOR FUTURE WORK	255
10.1 Characterization of the Different TCPC Templates.....	255
10.2 Flare and Secondary Flow Structures.....	256
10.3 Characterization of the Energy Dissipation	256
10.4 Accuracy of the Anatomical Reconstruction.....	257
10.5 Compliant TCPC Models.....	257
10.6 Physiologic Flow Conditions	258
10.7 Comparison of 3D DPIV Measurements with MR Flow Measurements and CFD Results	259
10.8 Temporal Resolution	260
10.9 Development of the CAD Interface for Surgical Planning	261
APPENDIX A LAVISION INC. DPIV EQUIPMENT	262
A.1 Hardware	262
A.2 Software	264

APPENDIX B	MICROSOFT® EXCEL 2000 SPREADSHEET USED FOR POWER LOSS COMPUTATION	265
B.1. Going from the Raw Data to Microsoft® Excel 2000		265
B.1.1 Raw Data Nomenclature		265
B.1.2 Import Macro.....		266
B.2. Power Loss Computation.....		267
B.2.1 Summary		267
B.2.2 No Flow Measurements		268
B.2.3 Raw Data		268
B.2.4 Processed Data		269
APPENDIX C	POWER LOSS AND PRESSURE DATA	272
C.1	Model 1.....	272
C.2	Model 2.....	273
C.3	Model 3.....	274
C.4	Model 4.....	275
C.5	Model 5.....	276
C.6	Model 6.....	277
C.7	RP Model 1	278
C.8	Anatomic Intra -Atrial Model.....	279
C.9	Anatomic Bilateral SVC Model.....	280
APPENDIX D	POWER LOSS VS. FLOW RATE.....	281
D.1	30/70 RPA/LPA	281
D.2	40/60 RPA/LPA	282
D.3	50/50 RPA/LPA	283
D.4	60/40 RPA/LPA	284
D.5	70/30 RPA/LPA	285
REFERENCES	286

LIST OF TABLES

Table 2.2.1: Frequencies of congenital heart defects [Moller, 1992]	8
Table 4.1.1: Overview of the geometrical characteristics of the simplified glass models	45
Table 4.3.1: Sensitivity of the membranes used in the differential pressure transducers in each in vitro model.	62
Table 5.2.1: Filtering and interpolation process illustrated for a given data set (example given: Transducer 1 at 1L/min, 60/40 IVC/SVC, 30/70 RPA/LPA, Repetition 1). Original pressure measurements (P), removed data (-) and average of the pressure measurements remaining after filtering (Ave).....	103
Table 5.2.3: Summary of the acquisition and processing parameters used for this study.....	123
Table 5.3.1: Height of DPIV acquisition planes and coordinates of the corresponding CFD planes.....	129
Table 5.4.1: Flow rates at which the pressure drops measurements and the subsequent power loss calculations were conducted. For each total flow rate, the pulmonary and caval flow ratios were varied according to Table 5.4.2.	133
Table 5.4.2: Pulmonary and caval flow ratios at which the pressure drops measurements and power loss calculations were conducted for each total flow rate (Table 5.4.1)	133
Table 5.4.3: Flow rates at which flow visualization was performed. Caval flow ratio was fixed at 60/40 IVC/SVC and pulmonary flow ratio varied between 70/30, 50/50 and 30/70 LPA/RPA.	134
Table 5.4.4: Flow rates at which PIV measurements were taken with the corresponding caval and pulmonary flow ratios.	134
Table 5.4.5: Flow rates at which LDV measurements were taken with the corresponding caval and pulmonary flow ratios.	135

Table 5.4.6: Flow solvers and flow conditions that were used for the CFD simulations	135
Table 5.4.7: Summary of all the experiments and numerical simulations that were conducted in our laboratory. v refers to the experimental work that was conducted for this study.	136
Table 6.2.1: Pressure drops and power losses corresponding to equal pulmonary vascular resistance conditions (R Lung = 1.79 Wood units) for Model 1 at 2, 4 and 6L/min	158
Table 6.2.2: Pressure drops and power losses corresponding to equal pulmonary vascular resistance conditions (R Lung = 1.79 Wood units) for Model 2 with flow rates ranging from 2 to 6 L/min.....	159
Table 6.2.3: Pressure drops and power losses corresponding to equal pulmonary vascular resistance conditions (R Lung = 1.79 Wood units) for Model 3 with flow rates ranging from 2 to 6 L/min.....	160
Table 6.2.4: Pressure drops and power losses corresponding to equal pulmonary vascular resistance conditions (R Lung = 1.79 Wood units) for Model 4 with flow rates ranging from 2 to 6 L/min.....	161
Table 6.2.5: Pressure drops and power losses corresponding to equal pulmonary vascular resistance conditions (R Lung = 1.79 Wood units) for Model 5 with flow rates ranging from 1 to 6 L/min.....	162
Table 6.2.6: Pressure drops and power losses corresponding to equal pulmonary vascular resistance conditions (R Lung = 1.79 Wood units) for Model 6 at 1, 2 and 3 L/min ...	165
Table 6.3.1: Pressure drops and power losses corresponding to equal pulmonary vascular resistance conditions (R Lung = 1.79 Wood units) for the anatomical intra-atrial model at 1, 2 and 3 L/min.	169
Table 6.4.1: Pressure drops and power losses corresponding to equal pulmonary vascular resistance conditions (R Lung = 1.79 Wood units) for the anatomical bilateral SVC model at 2, 3 and 4 L/min.	183
Table 7.2.1: Comparison of Transparent Model Alternatives	203
Table A.1: List of the DPIV hardware (LaVision GmbH, Goettingen, Germany).....	262

Table A.2: List of the DPIV software (LaVision GmbH, Goettingen, Germany)	264
Table C.1: Summary of all power losses and pressure drop measurements for Model 1	272
Table C.2: Equal pulmonary vascular resistance points for Model 1	272
Table C.3: Summary of all power losses and pressure drop measurements for Model 2	273
Table C.4: Equal pulmonary vascular resistance points for Model 2	273
Table C.5: Summary of all power losses and pressure drop measurements for Model 3	274
Table C.6: Equal pulmonary vascular resistance points for Model 3	274
Table C.7: Summary of all power losses and pressure drop measurements for Model 4.....	275
Table C.8: Equal pulmonary vascular resistance points for Model 4	275
Table C.9: Summary of all power losses and pressure drop measurements for Model 5	276
Table C.10: Equal pulmonary vascular resistance points for Model 5	276
Table C.11: Summary of all power losses and pressure drop measurements for Model 6	277
Table C.12: Equal pulmonary vascular resistance points for Model 6	277
Table C.13: Summary of all power losses and pressure drop measurements for the RP Model 1	278
Table C.14: Equal pulmonary vascular resistance points for the RP Model 1	278
Table C.15: Summary of all power losses and pressure drop measurements for the anatomic intra-atrial model.....	279
Table C.16: Equal pulmonary vascular resistance points for the anatomic intra-atrial model.....	279

Table C.17: Summary of all power losses and pressure drop measurements for the anatomic bilateral SVC model.....280

Table C.18: Equal pulmonary vascular resistance points for the anatomic bilateral SVC model.....280

LIST OF FIGURES

Figure 2.1.1: Schematic of the two primary circuits of the human blood circulation. The pulmonary circuit drives the blood from the heart to the lungs and back to the heart while the systemic circulation transports the blood to and from the rest of the body.....5

Figure 2.1.2: Schematic of a normal heart. [Schneider Children’s Hospital]7

Figure 2.3.1: Schematic showing the human blood circulation in a single ventricle physiology as opposed to the normal physiology. There is only one effective ventricle where the oxygenated pulmonary blood mixes with the deoxygenated systemic blood.....9

Figure 2.3.2: Ventricular Septal Defect (VSD, Left) and Atrial Septal Defect (ASD, Right). One or multiple holes in the ventricular or atrial septum that allow blood to mix. If the hole is small enough a patch may be used to prevent mixing. In more complex cases, delicate surgical procedures may be required. [Schneider Children’s Hospital].....10

Figure 2.3.3:Tricuspid Atresia (TA). Absence or closure of the tricuspid valve resulting in a lack of communication between the right atrium and the right ventricle. Survival depends on the presence of other defects, such as an ASD, for the blood returning from the systemic circulation to be redistributed and for the lungs to be perfused. [Schneider Children’s Hospital].....11

Figure 2.3.4: Hypoplastic Left Heart Syndrome (HLHS) associated with an ASD and a patent ductus arteriosus. A hypoplastic organ is an organ whose development was not fully completed. In acute cases of HLHS the left ventricle cannot pump the blood through the systemic circulation. In these cases, an ASD combined with a patent ductus arteriosus may allow the blood returning from the lungs to be pumped back to the body. [Schneider Children’s Hospital]11

Figure 2.3.5: Transposition of the Great Arteries associated with a VSD. [Schneider Children’s Hospital]12

Figure 2.4.1: Schematic of the five major steps of the Fontan procedure applied on a patient with a Tricuspid Atresia (TA) combined with an Atrial Septal Defect (ASD) [Fontan, 1971]14

Figure 2.4.2: Schematic of an atrio-pulmonary connection in the context of a double-inlet single left ventricle with a transposition of the great arteries, a ventricular septal defect and a rudimentary right ventricle. The right atrial appendage is sewn directly onto the pulmonary arteries. The tricuspid valve is sutured to separate systemic and pulmonary circulations.[Gersony, 2003]16

Figure 2.4.3: Norwood procedure18

Figure 2.4.4: Schematic showing a bi-directional cavopulmonary anastomosis [Bridges, 1990]19

Figure 2.4.5: Schematic showing an intra-atrial TCPC [Pearl, 1991]20

Figure 2.4.6: Schematics showing a completed extra-cardiac conduit [Tam, 1999].....21

Figure 2.5.1: Pressure relations in normal and Fontan circulations. Ao, Aorta; LV left ventricle; RV, right ventricle; VCs, venae cavae; PAs, pulmonary arteries; RA, right atrium; LA, left atrium; PVR pulmonary vascular resistance; SVR, systemic vascular resistance. [Bull, 1998].....24

Figure 2.6.1: Schematic showing that in the presence of a magnetic field B_0 , net magnetization M_0 is produced as a result of the protons aligning with the external magnetic field.....34

Figure 2.6.2: Schematic showing that in absence of an external magnetic, a proton spinning around its own axis generates a magnetic field M_0 . In presence of an external magnetic field B_0 , not only does the proton precess around its own axis but also around the B_0 axis.34

Figure 4.1.1: Simplified Glass models 1 to 4, varying VC diameters and PA curvature. .48

Figure 4.1.2: Simplified glass models 5 and 6, incorporating the impact of a pouch-like connection and PA diameters variation.48

Figure 4.1.3: Intra-atrial anatomical model when looking from the posterior side (Left) and from the right hand side (Right)51

Figure 4.1.4: Anatomical bilateral SVC when looking from the anterior side (Left) and from the right hand side (Right).....52

Figure 4.2.1: Steady flow loop used for all experimental studies performed in TCPC models with a single SVC. The flow rates in the different branches are controlled

with ball-valves and 4 rotameters (RTOT, RIVC, RLPA, RRPA). A constant pressure head maintains steady flow conditions.	56
Figure 4.2.2: Steady flow loop used for all experimental studies in the anatomical bilateral SVC model. The set-up is identical to the previous loop, except for the rotameters. Two more accurate rotameters were acquired to measure the flow in the SVCs.	57
Figure 4.3.1: Functioning of a differential pressure transducer. The fluid contained in the pressure cavity pushes the membrane towards one coil or the other. The unbalanced half bridge outputs an electrical signal proportional to the pressure difference.	59
Figure 4.3.2: Transducer permutations in the case of a TCPC model with a single SVC. For each set of flow conditions (total flow rate, pulmonary and caval flow splits) all pressures are acquired at the same time, and after 3 permutations all pressures have been acquired by all three transducers.	61
Figure 4.3.3: Experimental set-up for the pressure drop measurements.....	63
Figure 4.3.4: Set-up used for the flow visualization using dye injection.	65
Figure 4.3.5: PIV vectors calculation using Single-frame autocorrelation [DaVis FlowMaster Software, LaVision GmbH, Goettingen, Germany]	67
Figure 4.3.6: PIV vectors calculation using double-frame cross-correlation [DaVis FlowMaster Software, LaVision GmbH, Goettingen, Germany]	69
Figure 4.3.7: frame straddling: the laser beam is pulsed at the end of the first exposure and then at the beginning of the second exposure.	70
Figure 4.3.8: DPIV Laser light-sheet optics	72
Figure 4.3.9: General DPIV set-up. In our set-up the CCD camera was located underneath the model, which required extreme caution in order to avoid any spill. Using a set of mirrors may be more appropriate as it would allow the experimenter to image from the same location without endangering the hardware.	73
Figure 4.3.10: Schematic of the 2D LDV system.....	76
Figure 4.3.11: Doppler pulse obtained from light scattered by particle [Simon, 2004] ...	78

Figure 4.4.1: Typical view of the FIDAP computational mesh, generated with Gridgen on the intra-atrial TCPC geometry.....83

Figure 4.4.2: Correlation between the pressures imposed at the boundaries and the PA flow split for correct PA flow split specification.84

Figure 4.4.3: Typical view of the overset mesh used with the in-house code. A cut-out is provided on the SVC-IVC block surface to show the intersecting LPA and RPA blocks.86

Figure 4.4.4: Outlet flow conditions for the in-house flow solver. Q_n is the outlet flow rate at time step n and Q^* the correction factor computed according to Equation 4.4.1 and applied so as to obtained the desired flow split.....87

Figure 5.1.1: Work flow of the methodology for anatomical model manufacture.90

Figure 5.1.2: Orientation of the MRI planes and two series of illustrating MR images. Spin echo images (A to C) offer a high spatial resolution and decreased artifact from biomedical implants. Their clinical use includes cardiac tumors, vessel wall abnormalities. Gradient echo sequences are faster and provide a better contrast between vascular and non-vascular structures (A' to C'). They are typically used to delineate cardiovascular anatomies.....91

Figure 5.1.3: Anatomical bilateral SVC at different stages of the reconstruction: (a) As was reconstructed in Mimics (Materialise Inc. Ann Arbor, MI); (b) After automatic NURBS surfaces fitting in GeomagicStudio 6.0 (Raindrop Geomagic, Research Triangle Park, NC); (c) After vessel extension in Pro/ENGINEER Wildfire (PTC, Needham, MA).....94

Figure 5.1.4: Comparison of the intra-atrial TCPC at the beginning and at the end of the reverse engineering process. (a) The TCPC as it was reconstructed in Mimics (Materialise Inc. Ann Arbor, MI); (b) the same with vessel extension imported into I-DEAS 9.0 (EDS, Plano TX); (c) Color maps of the deviation between the final and original geometries.96

Figure 5.1.5: Quantitative comparison of the final blood flow versus the original reconstruction of the anatomical bilateral SVC. Green regions correspond to the areas were both models overlapped exactly while red and blue regions show higher divergence.97

Figure 5.1.6: Model in the SLA machine as the anterior half is being manufactured. Terminology used to describe the orientation of the model (**bold**). Recommendations for the design and orientation of the model in correlation with the experimental use.....98

Figure 5.1.6: Rapid prototypes, from left to right: simplified Model 1 (control), anatomical intra-atrial, anatomical bilateral SVC.....	99
Figure 5.2.1: L1 and LHS as a function of the pulmonary flow split, in the anatomical intra-atrial model at 1L/min. Visual determination of the EPVR point: L1 and LHS intersect at the pulmonary flow split corresponding to equal pulmonary vascular resistance $R = 1.8$ Wood unit.	110
Figure 5.2.2: DPIV set-up for the intra-atrial TCPC. The DPIV images were acquired from the anterior side while the laser was located on the right side.	112
Figure 5.2.3: DPIV interrogation planes viewed from the top (Right). The domain that was imaged is highlighted on the posterior view (Left).	112
Figure 5.2.4: General DPIV set-up for the bilateral SVC. The DPIV images were acquired from the anterior side while the laser shot from the left or the right side of the model.....	113
Figure 5.2.5: DPIV interrogation sites for the anatomical bilateral SVC. The whole domain was imaged at once for one single plane.....	114
Figure 5.2.6: DPIV interrogation sites for the anatomical bilateral SVC, focusing on the IVC flow. 5 planes separated by 2.5mm were imaged throughout the IVC.....	114
Figure 5.2.7: DPIV interrogation sites for the anatomical bilateral SVC, focusing on the RSVC and LSVC flow. Solely the median plane was imaged in the SVCs.....	114
Figure 5.2.8: Typical DPIV images and intensity profiles obtained in the anatomical intra-atrial model (a) and in the bilateral SVC (b). As a ground of comparison Figure (c) shows the optimal seeding and contrast recommended in the DPIV manual (LaVision GmbH, Goettingen, Germany). Such a quality could not be achieved in the RP models.....	117
Figure 5.2.9: Convergence of the DPIV measurements	118
Figure 5.2.10: LDV interrogation sites for the anatomical intra-atrial model. The arrows show the direction from which the PA and VC cross-sections were viewed. \circ : data acquired in 1D, \bullet : data acquired in 2D, x: rejected data (data acquisition rate under 0.5Hz). All the distances are given in mm.	125
Figure 5.2.11: [Simon, 2004] Velocity bias in LDV measurements. Arrows indicate velocity magnitude. The particles at the bottom of the probe volume flow slower than those at the top, there will thus be fewer of them flowing across the probe	

volume in a given acquisition time, and more of the faster ones. On the other hand the slower particles will take longer to flow across the probe volume (longer gate-time). Weighing the measured velocities by the gate-time is thus a way to remove the velocity bias.	127
Figure 6.1.1: Experimental friction factors obtained for three different pressure transducers, T1, T2 and T3. The dashed line displays the theoretical values for the friction factor in the laminar regime.	139
Figure 6.1.2: Comparative power losses in Model 1, depending on the manufacturing method. Power losses in the unpolished rapid prototype were systematically higher than in the handcrafted glass model.	140
Figure 6.1.3: Fully developed velocity profile in a one-inch pipe	142
Figure 6.1.4: Comparison of the velocity along the centerline of the RP pipe measured using DPIV and LDV and computed after the total flow rates measured with the ultrasonic flow probe. The DPIV and LDV results are plotted as a function of V_{Theor} , while dotted line represents the theoretical values V_{Theor}	143
Figure 6.1.5: Comparison of velocity bias of the LDV and DPIV techniques along with the mean and 95% confidence intervals of the respective bias. The velocities computed with the ultrasonic flow measurements are taken as reference. The continuous lines provide the mean bias while the dashed lines picture the 95% confidence interval (2 standard deviations away from the corresponding mean).....	143
Figure 6.2.1: Model 1. Qualitative flow visualization at 4L/min and with a pulmonary flow split of 70/30 RPA/LPA [Ensley, 2000].....	146
Figure 6.2.2: Model 1. Qualitative flow visualization at 4L/min and with a pulmonary flow split of 50/50 RPA/LPA [Ensley, 2000].....	146
Figure 6.2.3: Model 1. Qualitative flow visualization at 4L/min and with a pulmonary flow split of 30/70 RPA/LPA [Ensley, 2000].....	147
Figure 6.2.4: Model 3. Qualitative flow visualization at 4L/min and with a pulmonary flow split of 70/30 RPA/LPA [Ryu, 2000]	148
Figure 6.2.5: Model 3. Qualitative flow visualization at 4L/min and with a pulmonary flow split of 30/70 RPA/LPA [Ryu, 2000]	148

Figure 6.2.6: Model 4. Qualitative flow visualization at 4L/min and with a pulmonary flow split of 70/30 RPA/LPA. Unlike all the others, these images were acquired from the posterior side, with the LPA on the left (a) and the RPA on the right (b).	149
Figure 6.2.7: Model 4. Qualitative flow visualization at 4L/min and with a pulmonary flow split of 30/70 RPA/LPA. Unlike all the others, these images were acquired from the posterior side, with the LPA on the left (a) and the RPA on the right (b).	149
Figure 6.2.8: Model 5. Qualitative flow visualization 4L/min and with a pulmonary flow split of 50/50 RPA/LPA. Dye injected (a) from the SVC and (b) from the IVC....	150
Figure 6.2.9: Model 5. Qualitative flow visualization at 4L/min and with a pulmonary flow split of 70/30 RPA/LPA. Dye injected (a) from the SVC and (b) from the IVC.....	151
Figure 6.2.10: Model 6. Qualitative flow visualization at 1L/min and with a pulmonary flow split of 30/70 RPA/LPA.	152
Figure 6.2.11: Model 6. Qualitative flow visualization at 1L/min and with a pulmonary flow split of 50/50 RPA/LPA.	153
Figure 6.2.12: Model 6. Qualitative flow visualization at 1L/min and with a pulmonary flow split of 70/30 RPA/LPA	153
Figure 6.2.13: Model 6. Qualitative flow visualization at 1L/min and with a pulmonary flow split of 70/30 RPA/LPA seen from the side. The recirculation region occupied the entire connection region, leading to important 3D mixing of the caval flows.....	154
Figure 6.2.14: Pressure in SVC, RPA and LPA with respect to that in the IVC measured in Model 1 at 2 L/min.	155
Figure 6.2.15: Power losses measured in Model 1 at 2, 4 and 6L/min. The power loss points were fitted with a second-degree polynomial curve. The EPVR points, described by the red line, corresponded to a 50/50 LPA/RPA flow split irrespective of the total flow rate.	156
Figure 6.2.16: Comparison of the control volume hydrodynamic power losses obtained at 4L/min in this study in the simplified glass Model 1 with previous results by Ensley et al. [Ensley, 2001]	157

Figure 6.2.17: Pressure drops measured in Model 5 at 2L/min.	163
Figure 6.2.18: Pressure drops measured in Model 6 at 2 L/min.	164
Figure 6.2.19: Power losses observed in Model 6 at 1, 2 and 3L/min. The dashed lines denote the regions where the flow became turbulent in the LPA, while the red line describes the power losses at EPVR. Power losses and EPVR points were fitted with a second order polynomial curve.	166
Figure 6.3.1: Power losses observed in the anatomical intra-atrial model at 1, 2 and 3L/min. The dashed lines denote the regions where the flow became turbulent either in the LPA (3L/min, %RPA < 50%) or in the RPA (3L/min, %RPA >60%), while the red line describes the power losses at EPVR. Power losses and EPVR points were fitted with a second order polynomial curve.	168
Figure 6.3.2: Qualitative flow visualization of the anatomical intra-atrial model at 1L/min and with a pulmonary flow split of 70/30 RPA/LPA. (1) to (5): dye injected in the SVC; (6) to (10): dye injected in the IVC.....	170
Figure 6.3.3: Qualitative flow visualization of the anatomical intra-atrial model at 1L/min and with a pulmonary flow split of 30/70 RPA/LPA. (1) to (5): dye injected in the SVC; (6) to (10): dye injected in the IVC.....	170
Figure 6.3.4: Quantitative assessment of the flow field using DPIV at 3L/min with varying pulmonary flow splits. The data acquisition planes are indexed from the most anterior (a) to the most posterior (d), and correspond to the laser heights 8 mm, 11 mm, 12 mm and 18 mm (Table 5.3.1).	177
Figure 6.3.5: Quantitative assessment of the IVC and SVC flow profiles using LDV at 3L/min. The arrow shows the angle under which the two cross-sections are viewed. (a) Out-of-plane IVC velocity component. (b) 2D sagittal SVC velocities.....	178
Figure 6.3.7: Assessment of the total velocity using CFD (1st order-accurate, Fidap) at 3L/min; pulmonary flow split: 50/50 LPA/RPA. The location of the imaged planes is shown in Schematics 1 and 2. The sagittal planes are indexed from the most anterior (a) to the most posterior (d). They correspond to the CFD plane heights of 6.5 mm, 9.5 mm, 10.5 mm and 16.5 mm (Table 5.3.1) and are the numerical counterpart of the experimental flow fields shown in Figure 6.3.4.	179
Figure 6.3.7: Schematic of the flow structure observed in the anatomical intra-atrial model at 1L/min. The SVC flow was 5 to 6 times faster than the IVC stream and recirculated deep down into the IVC. Flow separation was observed in the SVC. A stagnation point appeared at the end of the full turn of the recirculating SVC flow	

and was located at the RPA inlet proximal to the SVC. Pulmonary flow followed a helical pattern.	180
Figure 6.4.1: Pressure measurements for the anatomical bilateral SVC at 2L/min, the measurements were taken in the RSVC, LSVC, RPA and LPA with respect to the IVC.....	183
Figure 6.4.2: Hydrodynamic power losses measured in the anatomical bilateral SVC model at 2, 3 and 4 L/min. The power losses at equal pulmonary resistance, which are described by the red line, corresponded to a pulmonary flow split of about 60/40 RPA/LPA irrespective of the total flow rate.	184
Figure 6.4.3: Qualitative flow visualization of the anatomical bilateral SVC model at 2L/min and with a pulmonary flow split of 70/30 RPA/LPA. The dye was injected in turns from the IVC (a), from the LSVC (b) and finally from the RSVC (c).	186
Figure 6.4.4: At a pulmonary flow split of 70/30 RPA/LPA, flow recirculation and slight disturbances were observed in the RSVC stream along the posterior aspect of the RPA-IVC-RSVC anastomosis.	186
Figure 6.4.5: The LSVC flow was steady for all pulmonary flow splits. It followed the same flow path irrespective of whether most of the flow went into the RPA (a), or into the LPA (b).	187
Figure 6.4.6: Qualitative flow visualization of the anatomical bilateral SVC model at 2L/min and with a pulmonary flow split of 50/50 RPA/LPA. The dye was injected in turns from the IVC (a) and from the RSVC (b).	187
Figure 6.4.7: Qualitative flow visualization of the anatomical bilateral SVC model at 2L/min and with a pulmonary flow split of 30/70 RPA/LPA. The dye was injected in turns from the IVC (a) and from the RSVC (b).	187
Figure 6.4.9: Quantitative assessment of the flow field through the entire bilateral SVC model using DPIV at 2L/min with a 70/30 RPA/LPA flow split.	190
Figure 6.4.10: Quantitative assessment of the flow field through the entire bilateral SVC model using DPIV at 2L/min with a 50/50 RPA/LPA flow split.	191
Figure 6.4.11: Quantitative assessment of the flow field through the entire bilateral SVC model using DPIV at 2L/min with a 30/70 RPA/LPA flow split.	191
Figure 6.4.12: Quantitative assessment of the flow field using DPIV at 2L/min with a 70/30 RPA/LPA flow split and focusing on the IVC anastomosis site. The data	

acquisition planes were 2.5 mm apart (Figure 5.2.6) and are labeled from the most anterior (a) to the most posterior (d).	193
Figure 6.4.13: Quantitative assessment of the flow field using DPIV at 2L/min with a 50/50 RPA/LPA flow split and focusing on the IVC anastomosis site. The data acquisition planes were 2.5 mm apart (Figure 5.2.6) and are labeled from the most anterior (a) to the most posterior (e).	194
Figure 6.4.14: Quantitative assessment of the flow field using DPIV at 2L/min with a 30/70 RPA/LPA flow split and focusing on the IVC anastomosis site. The data acquisition planes were 2.5 mm apart (Figure 5.2.6) and are labeled from the most anterior (a) to the most posterior (e).	194
Figure 6.4.15: Quantitative assessment of the flow field using DPIV at 2L/min with a 70/30 RPA/LPA flow split and focusing on the LSVC anastomosis site (a) and on the LSVC vessel (b).	195
Figure 6.4.16: Quantitative assessment of the flow field using DPIV at 2L/min with a 50/50 RPA/LPA flow split and focusing on the LSVC anastomosis site (a) and on the LSVC vessel (b).	195
Figure 6.4.17: Quantitative assessment of the flow field using DPIV at 2L/min with a 30/70 RPA/LPA flow split and focusing on the LSVC anastomosis site (a) and on the LSVC vessel (b).	196
Figure 6.4.18: Schematic of the flow structure observed in the anatomical bilateral SVC model at 2L/min with a 70/30 RPA/LPA flow split. LSVC flow went exclusively to the LPA, while the vast majority of the RSVC and IVC flows went to the RPA. Only a little amount of fluid slowly came from the IVC and RSVC, along the anterior wall, across the intermediate PA section. Two recirculation regions were identified, facing the opening of each one of the PA's.	197
Figure 6.4.19: Schematic of the flow structure observed in the anatomical bilateral SVC model at 2L/min with a 30/70 RPA/LPA flow split. LSVC flow went exclusively to the LPA, together with the vast majority of the RSVC and IVC flows. IVC and RSVC flows collided before splitting into both PA's, yielding a stagnation region. Both RSVC and IVC contributed to RPA flow. The flow across the intermediate PA section was twice as fast as in the IVC.	197
Figure 7.2.1: Power losses in the simplified glass models and in the anatomic intra-atrial model at 2L/min, with a fixed 60/40 IVC/SVC flow split and varying RPA/LPA flow splits.	205

Figure 7.2.2: Power losses in the simplified models at 60/40 IVC/SVC and 50/50 RPA/LPA as a function of the total flow rate.	206
Figure 7.4.1: Pressure distribution in the anatomic intra-atrial model at 1L/min; inlet flow split: 60/40 IVC/SVC; outlet flow split: 70/30 RPA/LPA. Pressures are given in mmHg. IVC pressure was chosen as the reference. [de Zélicourt, 2004].....	216
Figure 7.3.1: Experimental (Exp) and numerical power loss results for Models 1 to 3 [Ryu, 2001] and 4 [Liu, 2004] at 4L/min, with a fixed caval flow split of 60/40 IVC/SVC. The computational power losses were obtained using structured meshes and either the simplified control volume (SCV), the full control volume (FCV) or the viscous dissipation (VD) approach.	224
Figure 7.3.2: Numerical power loss results for Model 4 [Liu, 2004] using (a) structured and (b) unstructured meshes. The computational power losses were obtained at 4L/min, with a 60/40 IVC/SVC flow split using either the simplified control volume (SCV), the full control volume (FCV) or the viscous dissipation (VD) approach. The experimental data (Exp) are provided as a ground for comparison.	226
Figure 7.3.3: Grid size verification and experimental comparison of the steady-laminar CFD model. Dashed lines denote conditions where Re_{LPA} or $Re_{RPA} > 2300$ i.e. flow should be fully developed turbulent at one of the pulmonary arteries. [Pekkan, 2004]	228
Figure 7.3.4: Axial velocity component contours (m/s) in the mid coronal plane, showing the influence of two SVC inflow boundary condition profiles on the calculated flow field.	230
Figure 7.3.5: Quantitative assessment of the flow field using PIV, CFD 1st and 2nd order accurate at 1L/min; inflow split: 60/40 IVC/SVC; outflow split: 50/50 LPA/RPA. The data acquisition planes are indexed from the most anterior (a) to the most posterior (d), and correspond to the laser heights 8 mm, 11 mm, 12 mm and 18 mm (Table 5.3.1). [Pekkan, 2004]	232
Figure 7.3.6: Quantitative assessment of the flow field using PIV and CFD. Flow conditions: 3L/min, 60/40 IVC/SVC, 50/50 LPA/RPA. The data acquisition planes are indexed from the most anterior (a) to the most posterior (d), and correspond to the laser heights 8 mm, 11 mm, 12 mm and 18 mm (Table 5.3.1). [Pekkan, 2004]	233
Figure 7.3.7: At 1 L/min, flow visualization (left) showed that the TCPC flow was dominated by complex, unsteady, and highly 3D flow structures. Using 2nd order accurate transient simulations those were also captured in CFD (right).	236

Figure B.1: Typical Summary page of the Microsoft® Excel files that were used in this study to compute the power losses.....270

Figure D.1: Power losses in the six simplified glass models at 60/40 IVC/SVC and 30/70 RPA/LPA as a function of the total flow rate.281

Figure D.2: Power losses in the six simplified glass models at 60/40 IVC/SVC and 40/60 RPA/LPA as a function of the total flow rate.282

Figure D.3: Power losses in the six simplified glass models at 60/40 IVC/SVC and 50/50 RPA/LPA as a function of the total flow rate.283

Figure D.4: Power losses in the six simplified glass models at 60/40 IVC/SVC and 60/40 RPA/LPA as a function of the total flow rate.284

Figure D.5: Power losses in the six simplified glass models at 60/40 IVC/SVC and 70/30 RPA/LPA as a function of the total flow rate.285

LIST OF ANIMATIONS

Animation 6.3.1: Flow visualization of the anatomic intra-atrial model at 1 L/min, with a 60/40 IVC/SVC and 70/30 RPA/LPA flow split. Dye injected within the IVC stream. (MOV, 82K, de_zelicourt_diane_a_200412_mast_anim631_intraatrial_fv.mov).....171

Animation 6.3.2: Flow visualization of the anatomic intra-atrial model at at 1 L/min, with a 60/40 IVC/SVC and 70/30 RPA/LPA flow split. Dye injected within the SVC stream. (MOV, 43K, de_zelicourt_diane_a_200412_mast_anim632_intraatrial_fv.mov).....171

Animation 6.3.3: Instantaneous DPIV velocity fields of the anatomic intra-atrial model at 3 L/min and for the following flow splits: 60/40 IVC/SVC and 70/30 RPA/LPA. The plane being imaged corresponds to the laser height of 12 mm. (MOV, 1,635K, de_zelicourt_diane_a_200412_mast_anim633_intraatrial_piv.mov).....174

Animation 6.4.1: Flow visualization of the anatomic bilateral SVC model at 2 L/min. The dye is injected at the center of the RSVC stream. There was no noticeable difference between the flow behavior at 30/70 RPA/LPA and at 70/30 RPA/LPA. (MOV, 158K, de_zelicourt_diane_a_200412_mast_anim641_bilateral_fv.mov) .188

Animation 6.4.2: Flow visualization of the anatomic bilateral SVC model at 2 L/min. The dye is injected at the center of the LSVC stream. There was no noticeable difference between the flow behavior at 30/70 RPA/LPA and at 70/30 RPA/LPA. (MOV, 149K, de_zelicourt_diane_a_200412_mast_anim642_bilateral_fv.mov)188

Animation 6.4.3: Flow visualization of the anatomic bilateral SVC model at 2 L/min. The streaklines observed when injecting the dye at the center of the IVC (Left) were the same irrespective of the flow rate. The streaklines (Right) obtained when injecting the dye along the left side of the IVC demonstrated higher flow disturbances than the central flow. (MOV, 184K, de_zelicourt_diane_a_200412_mast_anim643_bilateral_fv.mov).....188

Animation 7.3.1: Animated streamlines of the numerical solution obtained for the anatomical intra-atrial model with the commercial flow solver FIDAP (Fluent Inc., NH). This solution converged towards a steady state and thus failed to capture the complexity of the flow within the connection area. (MOV, 11K, de_zelicourt_diane_a_200412_mast_anim731_cfd_fidap.mov)235

Animation 7.3.2: Animated streamlines of the numerical solution obtained for the anatomical intra-atrial model with the in house flow solver. Flow conditions: 1L/min, 60/40 IVC/SVC and 50/50 RPA/LPA flow splits. The in-house code captured the complex flow features observed in the experiments with reasonable accuracy. (MOV, 114K, de_zelicourt_diane_a_200412_mast_anim732_cfd_inhouse.mov).....235

LIST OF ABBREVIATIONS

TCPC	Total cavopulmonary connection
IVC	Inferior vena cava
SVC	Superior vena cava
LPA	Left pulmonary artery
RPA	Right pulmonary artery
LSVC	Left superior vena cava
RSVC	Right superior vena cava
DPIV	Digital particle image velocimetry
LDV	Laser Doppler velocimetry
CFD	Computational fluid dynamics
MRI	Magnetic resonance imaging
RP	Rapid prototyping
EPVR	Equal pulmonary vascular resistance
PA	pulmonary artery
VC	Vena cava
MR	Magnetic resonance
CAD	Computer aided design

SUMMARY

The concept of total right ventricular bypass, first introduced by Fontan and Baudet in 1971[Fontan, 1971], is a palliative procedure for the surgical repairs of single ventricle heart defects. Since its inception, modifications of the Fontan procedure brought the post-operative mortality down to the level of the repair of simpler types of congenital heart disease. However, the marked improvement in surgical outcome is balanced by the numerous and serious long-term complications encountered by the Fontan patients. Understanding the hemodynamics/fluid dynamics of the total cavopulmonary connection (TCPC) may lead to further optimization of the connection design and surgical planning, which in turn may lead to improved surgical outcome. While most experimental and numerical investigations have mainly focused on somewhat simplified geometries, we believe that the investigation of the flow field of true TCPC configurations is necessary for a thorough understanding. Although computational fluid dynamics (CFD) has been used to try and accomplish this task, very few studies report appropriately validated computational results.

This study details a manufacturing methodology yielding more accurate *in vitro* models that would provide a better understanding of the TCPC hemodynamics and adequate data for the validation of anatomical CFD simulations. This approach is illustrated on two different TCPC templates: an intra-atrial TCPC with a single superior vena cava (SVC) and a bilateral SVC with an extra-cardiac conduit. Power loss, flow

visualization, digital particle image velocimetry (DPIV) flow measurements as well as computational fluid dynamics simulations are performed to characterize the anatomic flow structure. Additional parametric glass models of the TCPC were manufactured to help understand the fluid dynamics of the anatomical models and support the computational model validation effort.

Anatomic TCPC configurations were reconstructed from digital medical images and then directly converted to a solid experimental model and a CFD grid. Transparent stereolithography was used to produce experimental models that reproduced any computer-designed geometry within a small tolerance and also meet all optical requirements for flow visualization, DPIV and/or laser Doppler velocimetry.

Prototype TCPC connection geometries were investigated in an effort to better understand the underlying hemodynamics and find more efficient alternative for the current surgical palliation. It was shown

Both anatomic configurations revealed very different fluid dynamics underlining once again the need for at least one comprehensive experimental campaign per TCPC template for a good understanding of the flow phenomena. The absence of caval offset in the anatomical intra-atrial model resulted in important flow turbulence, which was enhanced by the large connection area and yielded high pressure drops and power losses. On the other hand, the bilateral SVC, which featured a smooth extra-cardiac conduit and wider vessels, led to power losses that were one order of magnitude

lower than those of the anatomic intra-atrial model and a smooth flow field with lower levels of instability.

Numerical simulations of the intra-atrial flow demonstrated that most of the dissipation occurred in the pulmonary arteries due to the helical flow patterns and the small dimensions of the arteries. Concordantly the simplified glass models demonstrated that the diameter of the connecting vessels and of the pulmonary arteries in particular, was a parameter of prime importance.

In addition to the characteristic power loss curves traditionally used to describe the efficiency of a given TCPC design, this study tried to quantify the quality of the lung perfusion assuming that both lungs had an equal pulmonary vascular resistance. For the templates with a single SVC, lung perfusion was dictated by the PA diameters and by the amount of flare at the anastomosis site. The position of the IVC with respect to the two SVC's was an additional parameter to take into account when considering TCPC connection with bilateral SVC's.

Finally, this study also reports on a combined experimental and numerical validation methodology, suggesting a cautious approach for the straightforward use of available CFD tools and pointing out the need for developing high resolution CFD techniques specifically tailored to tackle the complexities of cardiovascular flows.

CHAPTER I

INTRODUCTION

The incidence of children born with a single congenital heart defect, in which there is one effective pumping chamber, is about 2 per 1000 births. In patients with such an anatomy, oxygenated and deoxygenated blood mix in the single ventricle. The concept of a total right ventricular bypass, first introduced by Fontan and Baudet in 1971 [Fontan, 1971], is a palliative procedure aimed at separating the systemic and pulmonary circulations thus eliminating venous blood mixing. The remaining left ventricle drives the blood flow throughout the entire body. Since its inception, modifications of the Fontan procedure have steadily improved surgical outcomes, reducing the post-operative mortality to the level of more simple types of congenital heart disease repairs. However, the marked improvement in surgical outcome is balanced by the numerous and serious long-term complications encountered by the Fontan patients such as ventricular dysfunction, thromboembolism, arrhythmias and protein loss [Gersony, 2003].

Amongst the multiple variables that determine the outcome and the quality of life of these patients, one that allows for some degree of control is the surgically created design of the bypass connection. Since the first *in vitro* experiment done by de Leval et al. [de Leval, 1988] understanding the hemodynamics/fluid dynamics at the connection site in order to optimize the connection design has been a major concern. In the current Fontan procedure, the total cavopulmonary connection (TCPC), the inferior (IVC) and

superior (SVC) venae cavae are anastomosed directly onto the pulmonary arteries (PAs) forming a “+” shaped connection.

In vivo, *in vitro* and numerical studies have all underscored the great sensitivity of the TCPC efficiency to its design. Parametric *in vitro* and CFD studies have attempted to identify the contribution of different geometric parameters to the overall flow fields, leading to suggestions for improvements, such as including a caval offset or enlarging the IVC anastomosis. To our knowledge, however, *in vitro* studies have all been performed on simplified glass models. While breaking down this complex problem into its simpler components does provide insight into the hemodynamics of this structure, the complete picture still requires the study of the true anatomical TCPC flow, including more accurate TCPC geometries, wall material properties, respiration, lung resistance, etc. Although CFD has been used to try and accomplish this task, very few studies report appropriately validated results. As was demonstrated by Khunatorn et al. [Khunatorn, 2003], accurately mimicking the primary flow structures does not imply that the whole flow field has been captured.

In this work we propose a methodology to manufacture more accurate *in vitro* models to provide both a better understanding of the TCPC hemodynamics and adequate data for the validation of anatomical CFD simulations. This approach is illustrated on two completely different TCPC templates: an intra-atrial TCPC with a single SVC and a bilateral SVC with an extra-cardiac conduit. Both revealed very different fluid dynamics underlining once again the need for at least one comprehensive experimental campaign

per TCPC template for a good understanding of the flow phenomena. Additional simplified models were built in an effort to understand the complex fluid structures observed in the anatomical models and support the CFD validation effort. This study also reports on a combined experimental and numerical validation methodology, suggesting a cautious approach for the straightforward use of available CFD tools and pointing out the need for developing high resolution CFD techniques specifically tailored to tackle the complexities of cardiovascular flows.

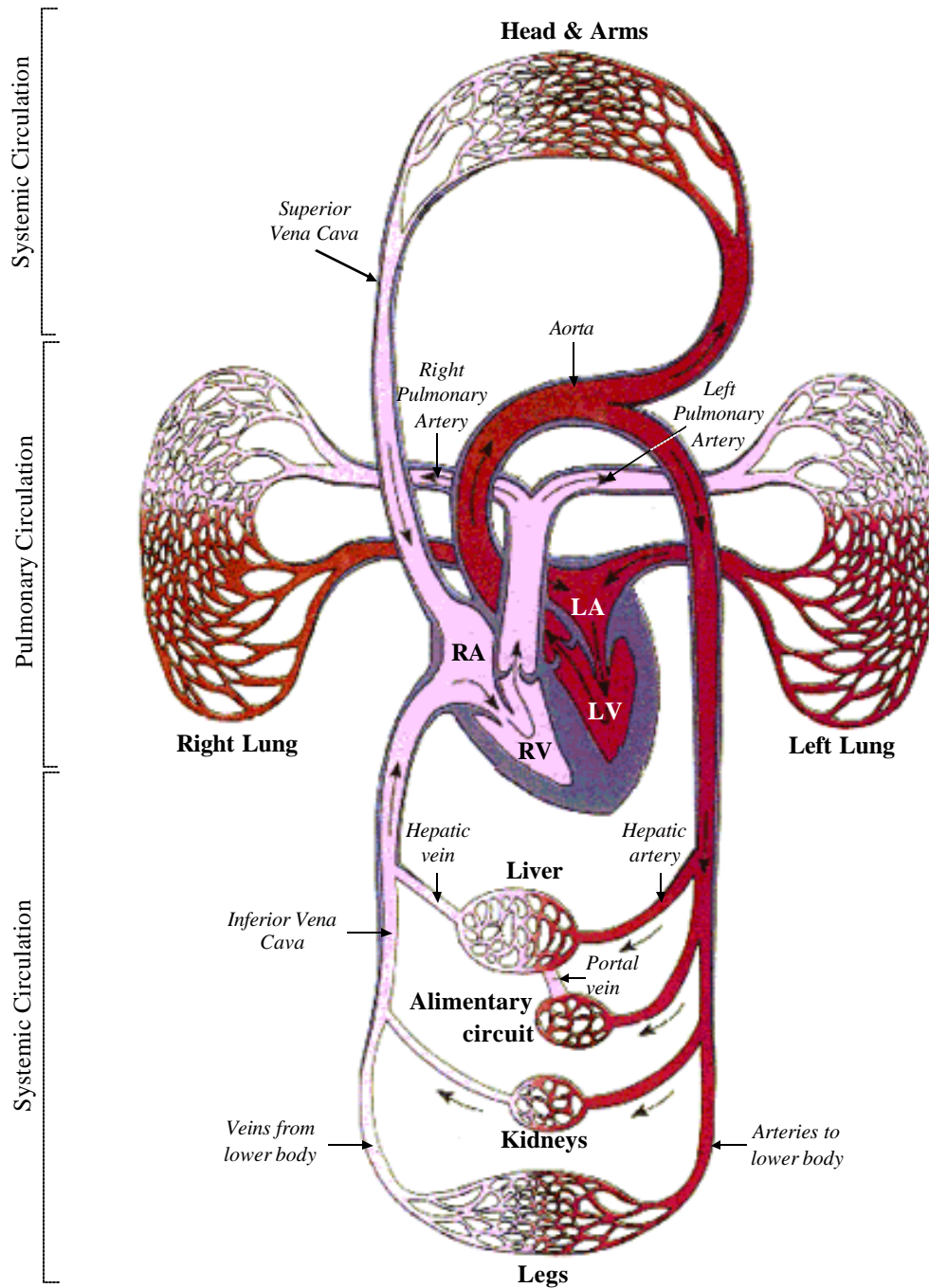
CHAPTER II

BACKGROUND

This chapter will provide a brief background on the physiology of the heart to better introduce single ventricle heart diseases. It will then discuss the efforts to improve the outcomes of these patients that motivated our study.

2.1 Normal Cardiovascular System

Blood is a major means of transportation for the nutrients and wastes that travel to and from our tissues. It is pumped through our entire body by the heart, and then perfuses each single tissue through a complex network of arteries, capillaries and veins. The cardiovascular circulation can be subdivided into two primary circuits: the pulmonary and systemic circulations (Figure 2.1.1). The pulmonary circuit describes the path going from the heart to the lungs and back, and the systemic circulation transports the blood between the heart and the remainder of the body.



© Polar Electro 2004
<http://www.pursuit-performance.com.au>

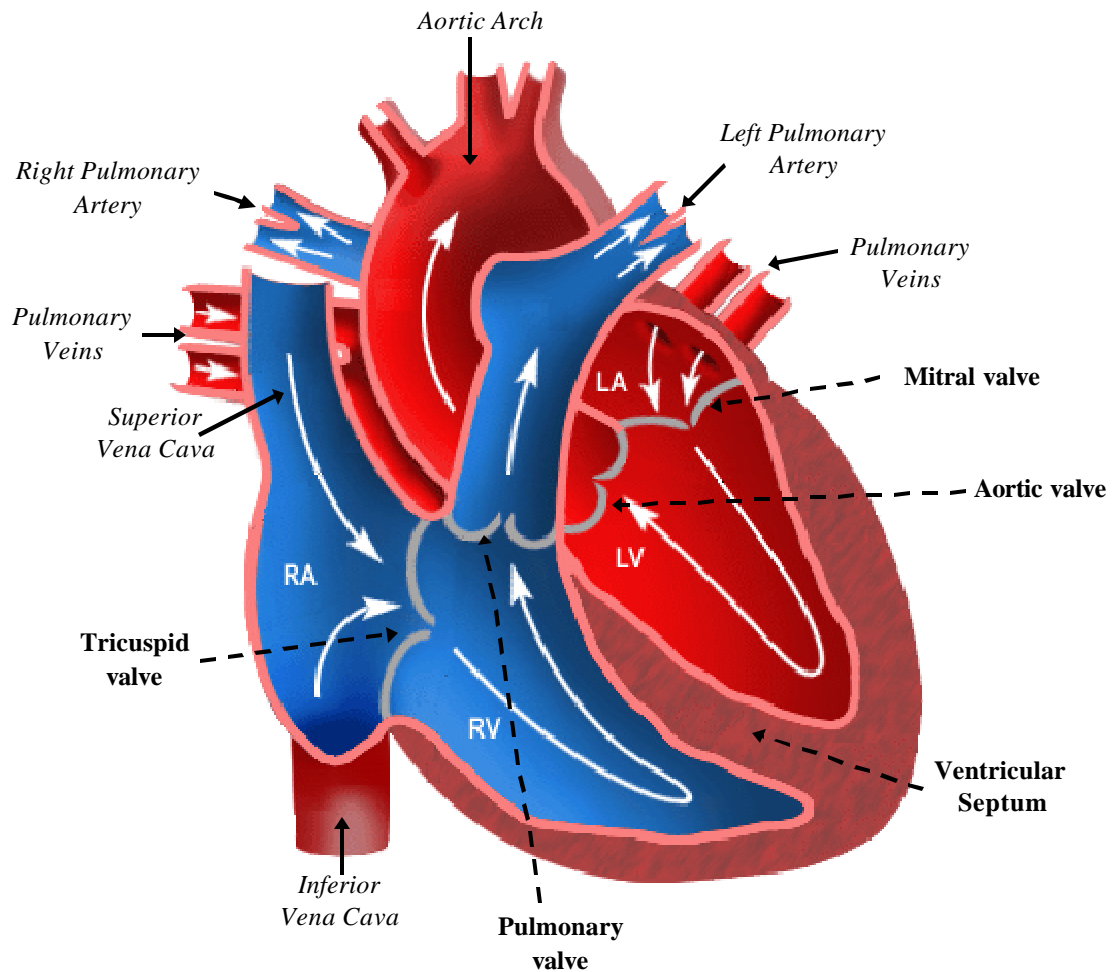
Figure 2.1.1: Schematic of the two primary circuits of the human blood circulation. The pulmonary circuit drives the blood from the heart to the lungs and back to the heart while the systemic circulation transports the blood to and from the rest of the body.



The heart consists of four chambers: the left and right atria and the left and right ventricles. In a normal physiology the septum separates the right and left sides of the heart creating two distinct pumps that function in parallel. The left side of the heart drives the blood through the systemic circuit while the right side drives the blood through the pulmonary circuit.

This four-chambered structure of the heart (Figure 2.1.2) is essential to its function. The ventricles provide the pumping force while the atria provide the buffer volume needed to receive the continuous blood flow returning from the body or the lungs. In addition to these four chambers, four valves control the inlet and outlet of both ventricles to prevent blood-flow reversal and ensure the efficiency of the ventricular contraction. When the left ventricle contracts during systole, the increase in ventricular pressure closes the bileaflet mitral valve and forces the trileaflet aortic valve open. Consequently, the blood that was present in the left ventricle before systolic contraction must flow from the left ventricle through the open aortic valve into the aorta then to the rest of the body. Meanwhile, the blood returning from the lungs through the pulmonary veins is stored in the left atrium. As pressure builds up in the left atrium and in the aorta and decreases in the left ventricle during diastole, the mitral valve reopens and the aortic valve closes. Blood then flows from the left atrium through the mitral valve into the left ventricle.

Similarly, the systemic blood coming back from the body flows through the inferior vena cava (IVC) and superior vena cava (SVC) into the right atrium. It then

passes through the tricuspid valve into the right ventricle from where it is discharged through the trileaflet pulmonary valve into the pulmonary circulation for gas exchange.



 Oxygenated blood
 Deoxygenated blood

LA = Left Atrium
RA = Right Atrium
LV = Left Ventricle
RV = Right Ventricle

Figure 2.1.2: Schematic of a normal heart. [Schneider Children's Hospital]

2.2 Congenital Heart Defects

Congenital heart defects (CHDs) describe all abnormalities of the heart or of the great arteries (pulmonary arteries and aorta) that are present at birth. Birth defects in general affect one of every 33 babies. They are the leading cause of infant mortality in the western world accounting for about 20% of all infant death [Anderson, 2003; Rosano, 2000]. CHDs alone account for one third of all birth defects affecting one in every 100 infants in the United States [Birth defects, Center for Disease Control, 2004]. They are the number one cause of birth defect related deaths during the first year of life and the mortality of these children may be as high as 50% depending on the condition [CHD Statistics, The Children's Heart Foundation, 2004].

Table 2.2.1: Frequencies of congenital heart defects [Moller, 1992]

CHD	% of all CHD
Ventricular Septal Defects (VSD)	33
Patent Ductus Arteriosus (PDA)	10
Pulmonary Stenosis (VS)	10
Tetralogy of Fallot	9
Aortic Stenosis (AS)	8
Coarctation of the Aorta	5
Atrial Septal Defect (ASD)	5
Transposition of the Great Arteries	5
Atrioventricular Septal Defect	4
Truncus Arteriosus	1
Tricuspid Atresia	1
Total Pulmonary Venous Connection (TPVC)	1
Others	8

CHDs arise from faulty embryogenesis between the third and eighth week of gestation, when major cardiovascular structures develop going from a simple straight tube to a complex four-chambered heart with separate pulmonary and systemic circuits. Over 35 different forms of CHDs have been reported, the most prevalent of which are listed in Table 2.2.1. The exact cause of CHDs is unknown in most cases, but multifactorial genetic and environmental parameters, including chromosomal defects, viruses, chemicals and radiation are suspected [Cotran, 1994].

2.3 Single Ventricle (SV) Heart

Amongst all CHDs, particularly challenging are the defects (or combination of defects) observed in about 20% of the CHD cases that effectively lead to a single-ventricle (SV) anatomy. This physiology results in communication between the systemic and pulmonary circulation, thereby eliminating the two-pump system and allowing for the mixing of oxygenated and deoxygenated blood (Figure 2.3.1).

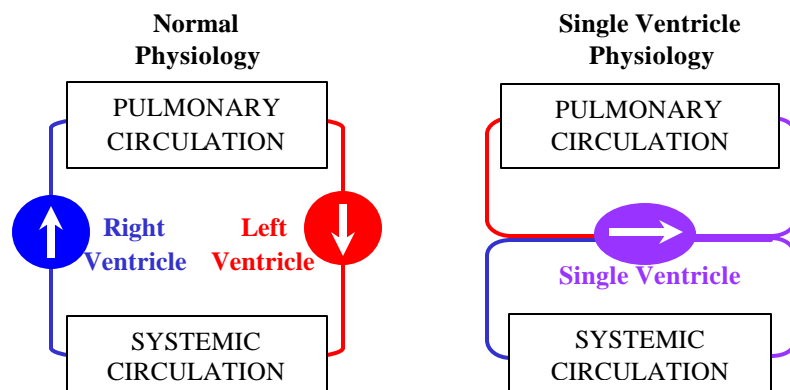


Figure 2.3.1: Schematic showing the human blood circulation in a single ventricle physiology as opposed to the normal physiology. There is only one effective ventricle where the oxygenated pulmonary blood mixes with the deoxygenated systemic blood.

The most prevalent CHDs leading to a SV anatomy include multiple ventricular and/or atrial septal defects, tricuspid atresia, hypoplastic left or right heart syndrome, transposition of the great arteries, and a double inlet ventricle, which are all illustrated and briefly explained in Figures 2.3.2 to 2.3.5.

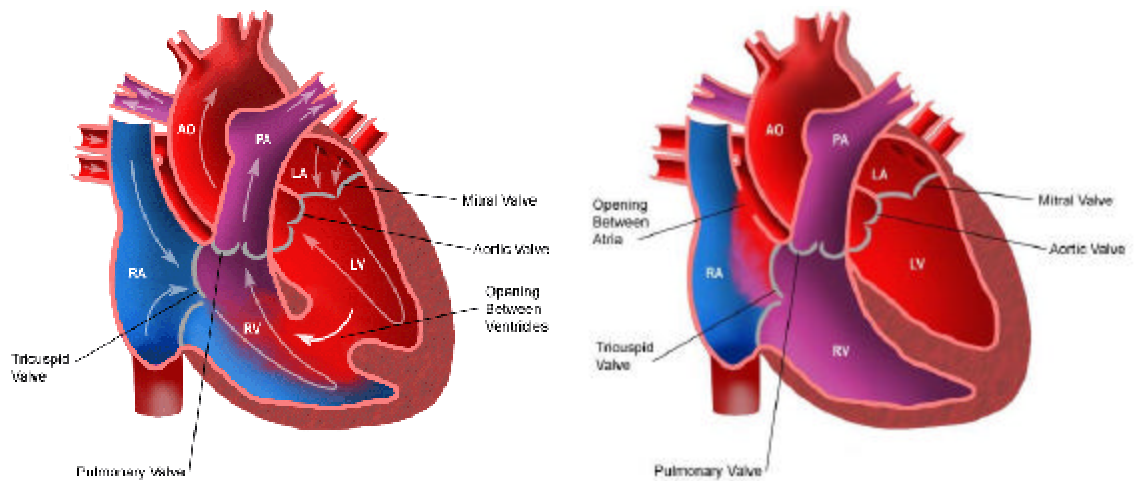


Figure 2.3.2: Ventricular Septal Defect (VSD, Left) and Atrial Septal Defect (ASD, Right). One or multiple holes in the ventricular or atrial septum that allow blood to mix. If the hole is small enough a patch may be used to prevent mixing. In more complex cases, delicate surgical procedures may be required. [Schneider Children's Hospital]

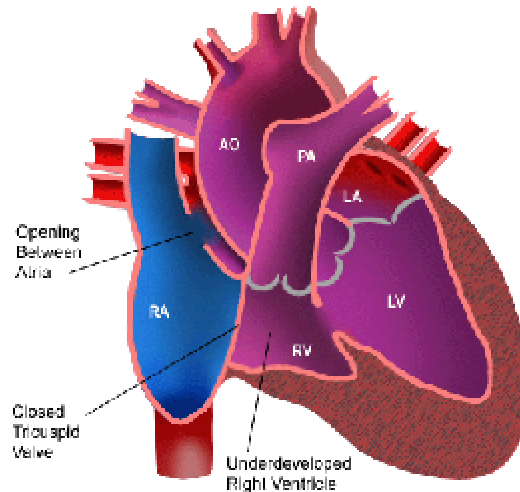


Figure 2.3.3: **Tricuspid Atresia (TA)**. Absence or closure of the tricuspid valve resulting in a lack of communication between the right atrium and the right ventricle. Survival depends on the presence of other defects, such as an ASD, for the blood returning from the systemic circulation to be redistributed and for the lungs to be perfused. [Schneider Children’s Hospital]

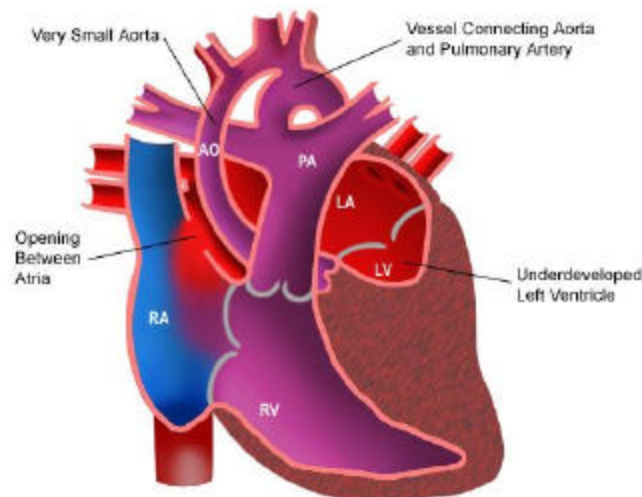


Figure 2.3.4: **Hypoplastic Left Heart Syndrome (HLHS)** associated with an ASD and a patent ductus arteriosus. A hypoplastic organ is an organ whose development was not fully completed. In acute cases of HLHS the left ventricle cannot pump the blood through the systemic circulation. In these cases, an ASD combined with a patent ductus arteriosus may allow the blood returning from the lungs to be pumped back to the body. [Schneider Children’s Hospital]

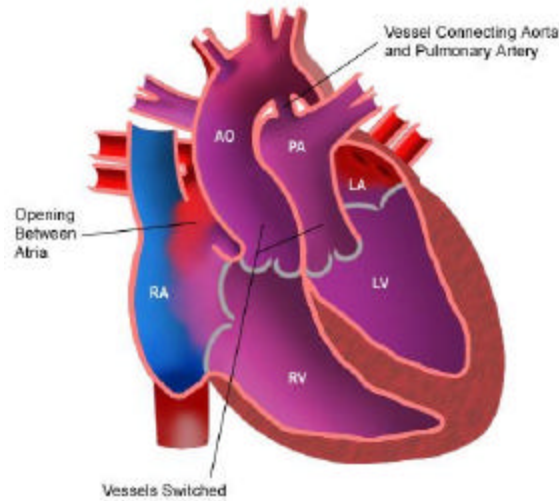


Figure 2.3.5: **Transposition of the Great Arteries** associated with a VSD. [Schneider Children's Hospital]

2.4 Single Ventricle Heart Repairs

2.4.1 Historical Perspective on SV Heart Repairs

Without surgical intervention, survival of patients with blocked right or left heart pathways as a result of a transposition of the great arteries, a tricuspid atresia or an acute hypoplastic heart syndrome once depended on the presence of coexisting defects such as a septal defect or a patent ductus arteriosus (Figures 2.3.3 to 2.3.5). In the middle of the 20th century, surgical shunt procedures were developed as a palliative procedure for cyanotic CHD. The purpose was to connect the pulmonary arteries (PAs) with the systemic arteries [Blalock, 1945; Potts, 1946] or with the SVC [Glenn, 1958] so as to try and augment the pulmonary blood flow.

These shunts enabled short-term survival. However ventricular dysfunction, pulmonary vascular disease, and chronic cyanosis prohibited a normal existence and

drastically shortened patient life expectancies with only few patients surviving beyond adolescence.

2.4.1.1 The Fontan procedure

The advent of the Fontan operation in 1971 [Fontan, 1971] brought about a revolution in the management of SVHD. The principle of a complete right heart bypass, where the systemic veins were directly connected to the pulmonary arteries without going through the single ventricle, achieved a number of salutary transformations to the SV anatomy. It re-separated the systemic and pulmonary circuits and abolished blood mixing, which in turn ostensibly improved arterial oxygen saturation and patient color.

The original Fontan procedure (Figure 2.4.1) included the construction of two independent VC-to-PA tracks, the IVC-to-LPA and SVC-to-RPA, with the anastomosis of the right atrium directly onto the PAs and a valve placed in the IVC.

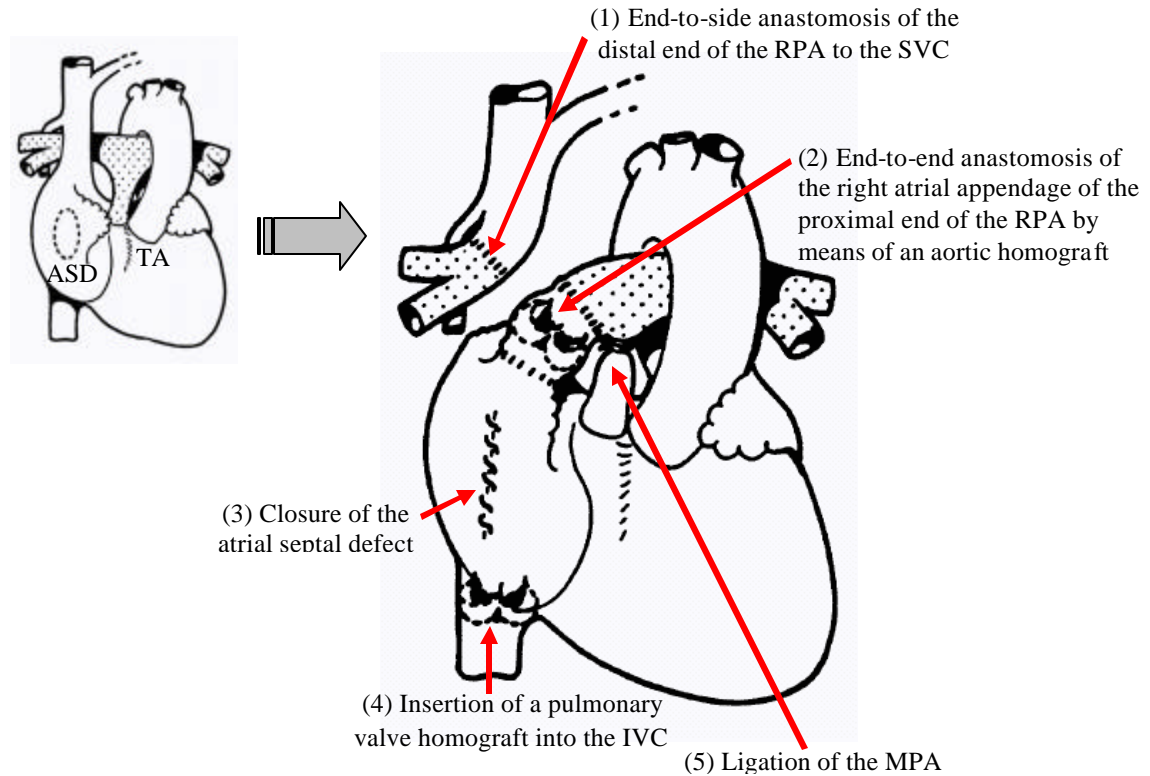


Figure 2.4.1: Schematic of the five major steps of the Fontan procedure applied on a patient with a Tricuspid Atresia (TA) combined with an Atrial Septal Defect (ASD) [Fontan, 1971]

However, it soon became clear that placing a valve in the caval conduits, rather than being advantageous, resulted in obstruction of the low-pressure VC-to-PA circulation [Shemin, 1979]. Furthermore, the separation of the IVC-to-LPA and SVC-to-RPA tracks, that had been designed to ensure an even perfusion of the right and left lungs, did not allow for any adaptation of the LPA/RPA blood flow ratio, leading to serious complications when one of the pulmonary tracks became obstructed. Additionally, such a cardiovascular configuration excluded all hepatic blood flow from the RPA, which was demonstrated to be strongly correlated with pulmonary venous malformation [Justino, 2001; Pike, 2004; Srivastava, 1995].

2.4.1.2 The atrio-pulmonary (AP) connection

Shortly after the first successful right ventricular heart bypass operation for tricuspid atresia [Fontan, 1971], Kreutzer et al. [Kreutzer, 1973] described a modified Fontan procedure and demonstrated that the entire venous return could be diverted to the pulmonary circulation through a single valveless atrio-pulmonary (AP) connection (Figure 2.4.2). This procedure had the combined advantages of providing the pulsatile action of the atrium, redistributing the hepatic fluid to both lungs and splitting the pulmonary blood flow depending upon the needs and resistance of either lung.

The description of the valveless AP-connection by Kreutzer et al [Kreutzer, 1973] was the first in a series of modifications of the original Fontan procedure. Although this procedure was quickly endorsed and has had widespread use in many centers, the long-term follow-up of patients with an AP-connection indicated that they were prone to late complications. Patients developed supraventricular arrhythmias, right atrial thrombus, exercise intolerance and other symptoms of low cardiac output [Dobell, 1986; Driscoll, 1992; Fontan, 1990; Mair, 1992]. These complications were usually related to a markedly dilated right atrium appendage, which was suspected to be due to the increased pressure load imposed on the atrium [Lardo, 1997]. This atrial dilatation was in turn associated with stagnant flows along the dilated right side of the atrium and turbulent flows elsewhere in the connection, resulting in significant fluid energy dissipation [Lardo, 1997].

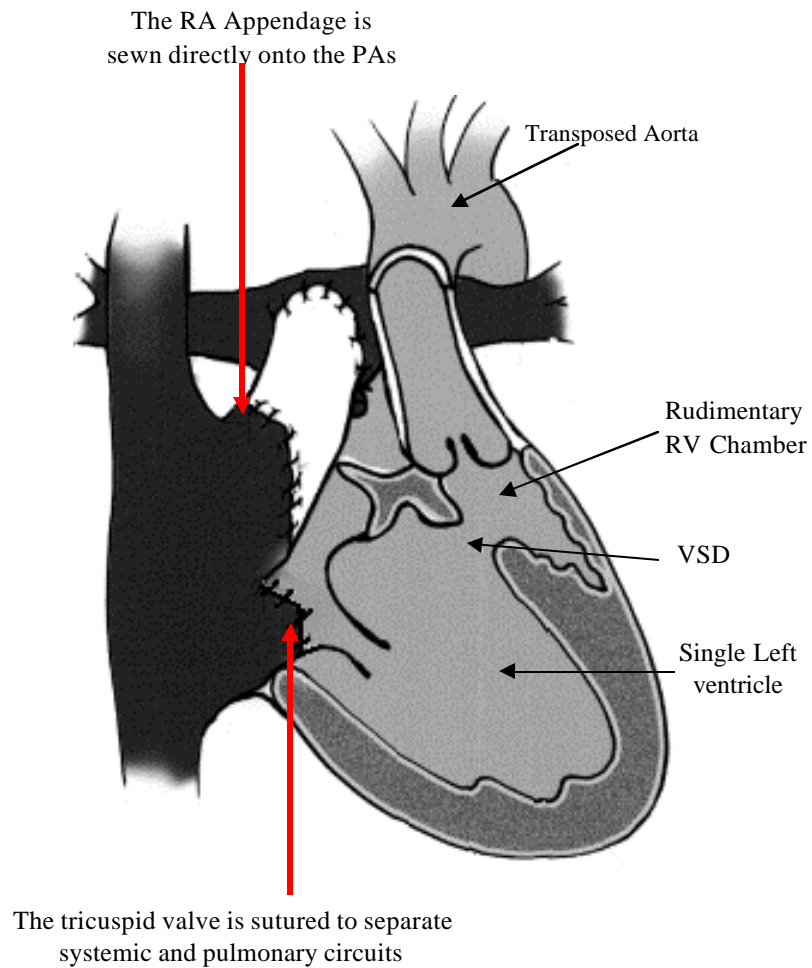


Figure 2.4.2: Schematic of an atrio-pulmonary connection in the context of a double-inlet single left ventricle with a transposition of the great arteries, a ventricular septal defect and a rudimentary right ventricle. The right atrial appendage is sewn directly onto the pulmonary arteries. The tricuspid valve is sutured to separate systemic and pulmonary circulations.[Gersony, 2003]

2.4.1.3 The total cavopulmonary connection (TCPC)

The high incidence of right-atrium related complications led many to question the role of the pulsating right atrium and its actual contribution to the Fontan circulation. De Leval et al. provided *in vitro* and *in vivo* evidence that the interposition of a passive chamber with impaired systolic function between the VCs and PAs was a major cause of flow inefficiency and proposed the total cavopulmonary connection (TCPC) as a logical alternative to the Fontan procedure [de Leval, 1988]. De Leval and colleagues described the TCPC as the anastomosis of the SVC directly onto the RPA followed by the creation of a tunnel through the right atrium connecting the IVC to the inferior aspect of the RPA (Figure 2.4.5). They demonstrated that such geometry leads to more streamlined flow patterns with less turbulence and fluid energy loss when compared to the AP-connection. These findings were confirmed by *in vitro* [Kim, 1995; Low, 1993] and computational [Van Haesdonck, 1995] fluid dynamic studies. Retrospective clinical studies also investigated early and late mortality rates. Findings show that the TCPC is accompanied by a lower mortality rate, improved outcomes and a more favorable course during the postoperative period [Marcelletti, 2000; Pearl, 1991; Podzolkov, 1997].

2.4.2 Staging the TCPC Procedure

Staging the operations has markedly improved surgical outcomes and allowed the Fontan surgery to be applied to a larger range of SV-patients [McGuirk, 2003]. It is now an integral part of the methodology for SV heart repairs.

2.4.2.1 Stage I: Norwood procedure

During the neonatal period, in babies who would otherwise not survive, a viable circulation is obtained through the Norwood procedure [Norwood, 1993]. A shunt is placed between the systemic (the distal innominate and proximal sub-clavian) and pulmonary arteries to control the pulmonary blood flow. Additionally, in children with a stenosed aortic arch, the aortic arch is reconstructed so as to increase the systemic blood flow to the body.

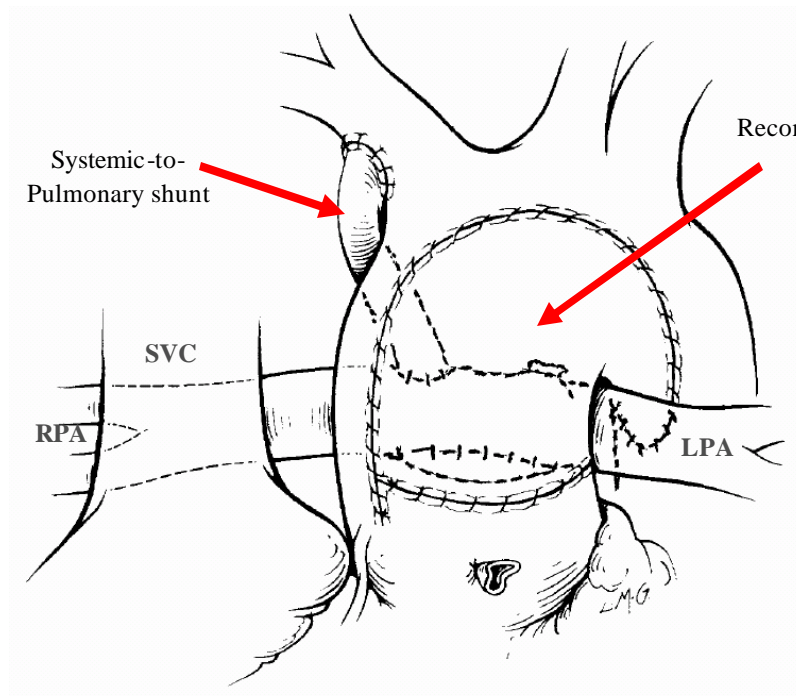


Figure 2.4.3: Norwood procedure

2.4.2.2 Stage II: Hemi-Fontan or bi-directional Glenn

The TCPC procedure itself is then be performed in two steps. The first step is the removal of the existing or surgically created systemic-to-pulmonary shunt and the second the creation of the SVC-to-RPA anastomosis (Figure 2.4.4) via a hemi-Fontan [Norwood, 1993] or bi-directional Glenn procedure [Tanoue, 2001]. The IVC and hepatic flow path are left in their original configuration. This stage is a first step toward the complete separation of the systemic and pulmonary circulations. It alleviates the ventricular overload imposed by the shunt, visibly reduces cyanosis via a more efficient lung perfusion [Bridges, 1990], and gives the heart some time to adapt to the increase in systemic resistance [Tanoue, 2003]. Presently this stage is usually performed in the first years of life with an average age of 1.2 years for the patients operated on at our affiliated institution, Emory University, Atlanta, GA [Kanter, 1999].

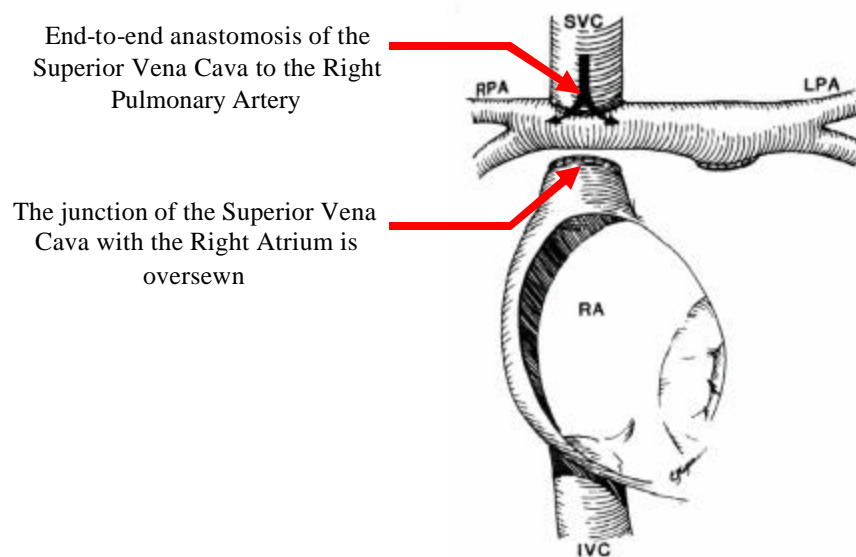


Figure 2.4.4: Schematic showing a bi-directional cavopulmonary anastomosis [Bridges, 1990]

2.4.2.3 Stage III: TCPC

During this stage the IVC-to-PA anastomosis is completed, thereby completely separating the systemic and pulmonary circuits. De Leval et al. [de Leval, 1988] had originally suggested the use of a lateral intra-atrial tunnel (Figure 2.4.5). However, several different practices have emerged since then including extra-cardiac IVC conduits [Petrossian, 1999] (Figure 2.4.6) and direct IVC-to-MPA connections. Other modifications focus on giving the patient time to adapt to the Fontan post-operative flow conditions by creating a temporary fenestration [Lemler, 2002], which is a communication between the IVC and the right atrium.

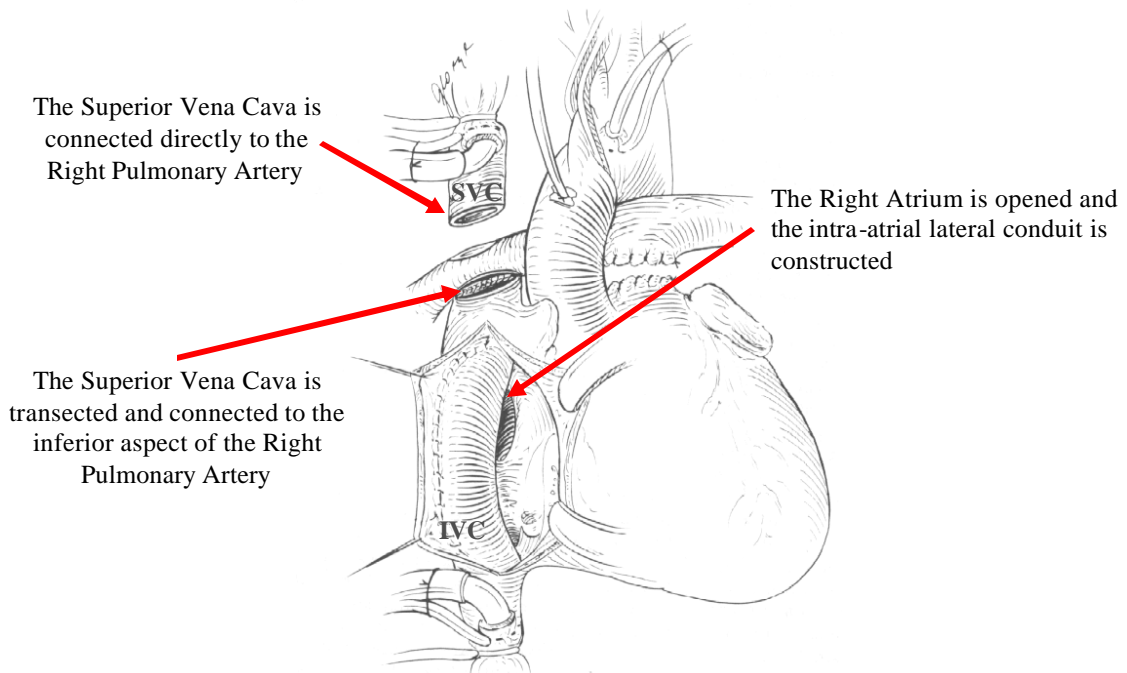


Figure 2.4.5: Schematic showing an intra-atrial TCPC [Pearl, 1991]

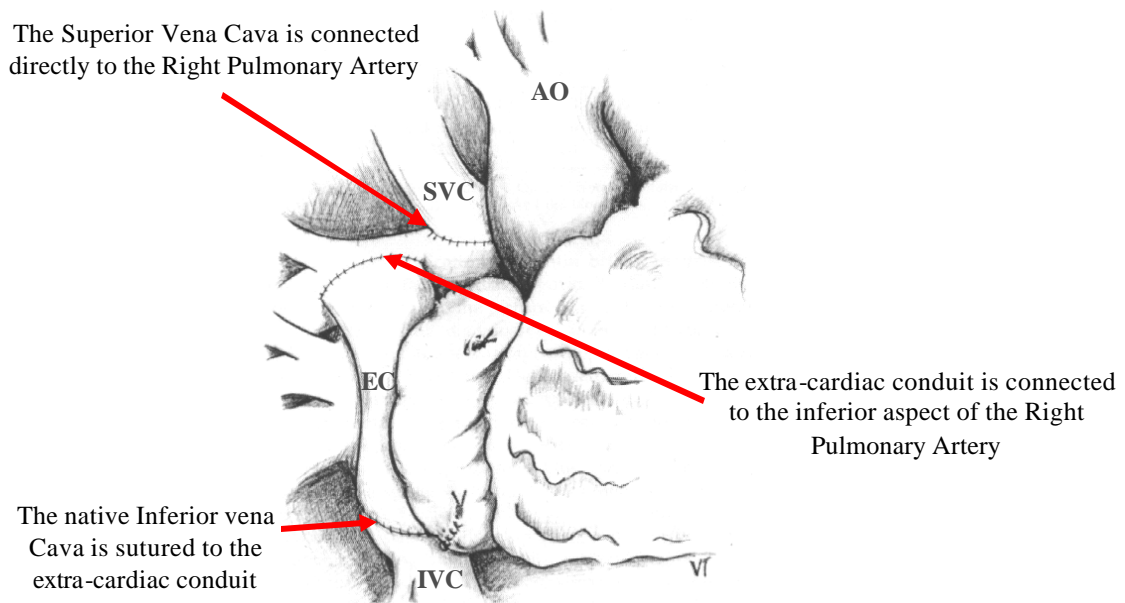


Figure 2.4.6: Schematics showing a completed extra-cardiac conduit [Tam, 1999]

2.4.3 Optimal TCPC Procedure

Although most surgeons agree on the staged TCPC as being the current procedure of choice for Fontan repairs, controversies exist about the selection of the connection type, the type of material to use, the need for fenestration, and the timing of the operations.

2.4.3.1 Connection type

The choice of connection type seems to be dictated by surgeon preference, each type with pros and cons. When compared to intra-atrial tunnels, extra-cardiac conduits provide numerous advantages including smoother geometries (Figure 2.4.6), fewer atrial suture lines thus minimizing sinus-node damage, and less or no time on the

heart-lung machine. On the other hand they provide no growth potential and may lead to conduit stenosis and thromboembolism [Haas, 2000; Petrossian, 1999; Tam, 1999]. Although long-term follow-ups are not yet available, early- and mid-term results for extra-cardiac conduits are favorable [Amodeo, 1997], especially combined with a fenestration in the inferior conduit [Mavroudis, 1992; Quinones, 1997].

2.4.3.2 Fenestration

Including a fenestration was demonstrated to lower the systemic venous pressures as well as to improve ventricular filling, consequently leading to improved cardiac output and overall oxygen delivery [Mavroudis, 1992; Thompson, 1999]. While some institutions advocate systematic fenestration, others argue that it should be used more selectively, balancing the potential benefits against the risks and costs of the additional intervention needed to close the fenestration [Thompson, 1999].

2.4.3.3 Material choice

Similarly, the material of choice varies from institution to institution and patient to patient. Intra-atrial tunnels have been built out of polytetrafluoroethylene (PTFE) patches, pericardial patches and autologous pericardial patches. Extra-cardiac conduits have been constructed using PTFE, Dacron, GoreTex and autologous pericardium flaps [Chowdhury, 2004; Yalcinbas, 2004]. Mid-term results have been favorable for all synthetic materials and only short-term follow-up data (30 months) is available for autologous conduits.

2.4.3.4 Surgical planning

Finally, the mean age at TCPC completion and mean interval since previous palliation have significantly decreased over the past decade. While some see this as a beneficial trend [Francois, 2004] that has reduced most of the major complications, others recommend caution pointing out that suture lines significantly limit vessel growth and that vessel size is a major factor for hemodynamic efficiency [DeGroff, 2002].

2.5 Improving the Functional Outcome of Fontan Patients

2.5.1 Outcome of Fontan Patients

As previously discussed, over the past three decades, cardiologists and cardiac surgeons have successfully improved the outcome of the Fontan operation. In many centers mortality after the Fontan operation is as low as that of simpler types of CHD repairs [Mott, 2001]. In a review of 137 consecutive patients with a tricuspid atresia, Sittiwangkul and colleagues [Sittiwangkul, 2004] report a total survival of 95% at 1-month, 93% at 1 year and 82% at 10 years.

However, concurrent with the marked improvement in surgical outcomes is the sobering realization that many patients suffer from a number of serious long-term complications including: diminished exercise tolerance [Gewillig, 1990; Shachar, 1982], fatigue, palpitations, obstruction of the systemic pathway, competitive pulmonary collateral blood flow, significant atrio-ventricular valve insufficiency, ventricular dysfunction, arrhythmias, protein losing enteropathy (PLE) and thromboembolism [Gersony, 2003]. In their autopsy review, Kiaffas and colleagues [Kiaffas, 1999] identified congestive heart failure (82% of all deaths), arrhythmias (12%) and central venous system dysfunction (6%) as the leading causes for mortality. PLE is reported with

a low incidence ranging from 1.5 to 11%, but a 50% mortality rate was reported 5-years from the time of diagnosis [Mertens, 1998]. A review of 592 patients showed evidence of thrombus formation in 9% of patients at a mean follow-up time of 22 months [Coon, 2001].

2.5.2 Possible Risk Factors and Opportunities for Surgical Outcome Improvement

The Fontan surgery produces a non-physiologic geometry with many variables and the exact causes and mechanisms of the aforementioned complications are still unclear. Rychichk and colleagues [Rychik, 2002] underscored the importance of two major consequences of the Fontan procedure:

- (1) Higher than normal overall resistance imposed upon the remaining ventricle, as the total resistance is the sum of both the systemic and pulmonary resistance.
- (2) Higher than normal systemic venous pressures, typically a mean of 1-15mmHg when it should be <10mmHg (Figure 2.5.1)

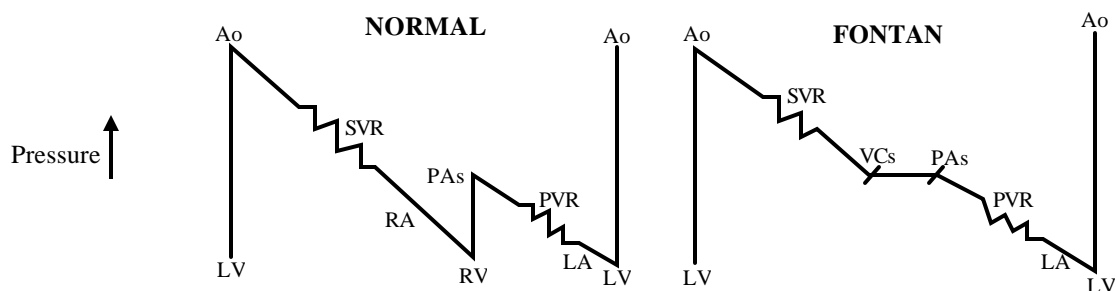


Figure 2.5.1: Pressure relations in normal and Fontan circulations. Ao, Aorta; LV left ventricle; RV, right ventricle; VCs, venae cavae; PAs, pulmonary arteries; RA, right atrium; LA, left atrium; PVR pulmonary vascular resistance; SVR, systemic vascular resistance. [Bull, 1998]

Accordingly, low pulmonary pressure and resistance [Choussat, 1978] and unimpaired single ventricle function with low end-diastolic pressure [Seliem, 1989] were shown to be critical parameters for a successful Fontan surgery. Along the same lines, minimum pressure drops and energy dissipation across the connection are the main criteria that have been used to evaluate the performance of a specific TCPC design. Based on the observed long-term complications, other possible criteria include the repartition of hepatic and caval flows between the lungs, the amount of recirculation, and the presence of stagnant regions or flow instabilities, since all these may impact lung perfusion, energy dissipation, platelet activation and thrombus formation.

In this study we focused our attention on the TCPC geometry, as it is one of the variables that allows for some degree of control and for possible improvements. The goal of this study was to improve surgical planning and design by providing a better understanding of how the geometry of the TCPC impacts its hemodynamics and efficiency.

2.5.3 Previous Investigation of the TCPC Hemodynamics

2.5.3.1 In vivo studies

Major improvements in medical imaging technologies have enabled in vivo assessments of the TCPC hemodynamics and geometry. Salim et al. used Doppler echocardiography to follow-up on the SVC contribution to the total cardiac output in children that went from 49% in infants, down to 35% after 6.6 years of age, with a maximum contribution of 55% at the age of 2.5 years [Salim, 1995]. Improvements of echocardiographic techniques, development of new technologies combined with the use

of transoesophageal echocardiography enable high resolution imaging of intra-cardiac structures in CHD patients [Shiota, 1999].

Thanks to the recent development in acquisition methods and hardware, magnetic resonance imaging (MRI) has emerged as a convenient alternative noninvasive imaging methodology [Geva, 2003]. In 1996, Fogel et al. [Fogel, 1996] used MRI to characterize the evolution of the ventricular geometry. They demonstrated that there were no changes in ventricular geometry or performance before and after the hemi-Fontan procedure, while drastic changes in mass, volume and vigor were observed 2 years after the completion of the TCPC. They inferred that the intra-atrial baffle and suture lines might have played a role in the restriction of the ventricular motion.

Using MRI and tagging each one of the caval flows individually, Fogel et al. [Fogel, 1999] were able to characterize the contribution of each vena cava to each one of the pulmonary arteries in 10 Fontan patients with intra-atrial tunnels. In agreement with previous findings [Salim, 1995], they found that at an average age of 1.8 ± 0.3 year-old most of the caval flow emanated from the SVC, $60 \pm 6\%$ of the SVC blood went to the RPA, and $67 \pm 12\%$ of the IVC blood went to the LPA. Overall both lungs received an equal amount of blood, even though the right lung was bigger than the left.

Hjortdal et al. [Hjortdal, 2003] demonstrated that inspiration facilitated IVC flow under resting conditions, increasing it to 2.99 ± 1.25 L/min/m² during inspiration versus 0.83 ± 0.44 L/min/m² during expiration. SVC flow was not significantly affected by the respiratory cycle, and under exercise conditions, the peripheral pump seemed to have more influence than respiration on the Fontan circulation.

Finally MRI has been used to provide a full characterization of the flow field through a slice. Sharma et al reported on the flow structures within twelve different patients, 7 with an intra-atrial lateral tunnel and 5 five with an extra-cardiac conduit [Sharma, 2001]. MRI velocity mapping combined with the use of adequate interpolation methods is capable of producing three-dimensional in vivo velocity data [Frakes, 2004], which can in turn be used to compute energy dissipation [Healy, 2001] or other parameters to characterize the efficiency of a given TCPC geometry.

2.5.3.2 *In vitro* studies

Since the first *in vitro* experiment done by de Leval et al. that demonstrated the superiority of the TCPC over atrio-pulmonary connection [de Leval, 1988], parametric *in vitro* studies aimed at better understanding the TCPC hemodynamics and optimizing its design have flourished. Sharma et al. [Sharma, 1996] studied the effects of varying caval offsets at various RPA/LPA flow ratios to determine the optimal combination for minimizing energy losses across the TCPC. The energy loss was measured in a custom crafted Pyrex glass model that featured four straight vessels of equal diameter (13.3mm) using a control volume analysis at 2, 4 and 6 L/min total flow rate under steady flow conditions. This study revealed that the power dissipated across the connection could be significantly reduced by offsetting the IVC and SVC by 1.0 or 1.5 caval diameters.

These findings were balanced by DeGroff et al. [DeGroff, 2002]. Comparing the results obtained using two different sets of models with the typical vessel dimensions of 3-year old and 15-year-old patients, respectively, they demonstrated that the increase in efficiency produced by a caval offset decreased with larger vessels. More importantly

they pointed out that the improvement brought in by a caval offset was not comparable to that of bigger vessels and thus questioned the trend of performing the Fontan on increasingly younger patients.

Caval offset decreases the fluid energy dissipation by avoiding direct collision of the caval flows. Another option is to curve the venae cavae and direct the caval flows so that they do not collide. Gerdes et al. [Gerdes, 1999] demonstrated that this option leads to improved hemodynamics as well, but may impair caval blood mixing.

Ensley et al. [Ensley, 1999] further demonstrated that curving the venae cavae was only optimal under specific flow conditions and instead recommended flaring the vessels towards the connection site. This method was shown to lower the power loss as well as allow for caval blood mixing. Using digital particle image velocimetry (DPIV) in custom-crafted glass models, Giorgini et al. [Giorgini, 2000] confirmed the flow visualization observations of Ensley et al. [Ensley, 1999] as they identified a vortex at the confluence of the venae cavae and demonstrated its role in the regulation of pulmonary blood flow.

Also using DPIV technique, Khunatorn et al. [Khunatorn, 2003] demonstrated the significant contribution of the secondary pulmonary flow structures to the power loss and their high sensitivity to small differences in vessel geometry. Additionally, despite the steady inflow conditions, flow instabilities were identified in the cavae, which were presumed to arise from the amplification of small-scale perturbations.

2.5.3.3 Numerical simulations

Computational fluid dynamics (CFD) were used by de Leval et al. to investigate their intuition about the impact of caval diameter and IVC anastomosis size on the competition of IVC and SVC flows [de Leval, 1996]. This numerical study was the first of a series. The major advantages of CFD simulations include a full 3D representation of the flow field and a high degree of freedom regarding the geometry to be simulated. Knowledge of the whole flow field allows for the assessment of parameters such as mechanical stresses, flow distribution, pressure gradients and vorticity that are otherwise more complex to quantify. Developments in medical image acquisition and processing have enabled hemodynamic analysis of patient-specific anatomic geometries. CFD is a useful tool that enables fast explorative and morphological studies. It has been widely used and applied to numerous research areas including flow through large airways and lungs [Nowak, 2003], blood flow through the carotid artery [Cebal, 2002], coronary arteries [Johnston, 2004], detailed aortic arch models [Shahcheraghi, 2002], aneurysms [Iordanis, 2003], anastomosis and graft designs [Ku, 2002], heart development [DeGroff, 2003] and heart motion [Saber, 2001].

In the Fontan area, CFD studies have explored the flow structure of intra-atrial tunnels [de Leval, 1996] and extra-cardiac conduits [Migliavacca, 1999]. The latter design was shown to have superior hemodynamics [Hsia, 2004], which was in agreement with previous in vivo observations [Lardo, 1999]. Parametric studies have focused on the design of the IVC anastomosis site [Migliavacca, 2003]; the influence of varying caval flow ratios on dissipation, flow structures, and shear stress [Khunatorn, 2003], and the effect of pulmonary after-load [Guadagni, 2001]. The geometry of the TCPC has been

modeled with increasing accuracy, from angular parametric models based on average anatomical measurements [de Leval, 1996] to realistic models directly reconstructed from patient MRI data [Guadagni, 2001; Migliavacca, 2003]. Lumped-parameter models of the Fontan circulation [de Leval, 1996; Rydberg, 1997], pulsatile inlet flows [de Leval, 1996; DeGroff, 2002], and vessel wall compliance [Orlando, 2002] have also been implemented in an effort to model the interaction between the Fontan connection and the rest of the cardiovascular system.

However only a few of these studies yield an adequate CFD validation. De Leval et al. [de Leval, 1996] mention that the power loss across the zero-offset model did not match previous experimental findings but report no other validation of their results. Comparing their results with DPIV measurements, Khunatorn et al. show that even though their code performed well on primary flow structures, it failed to capture secondary flows and flow instabilities [Khunatorn, 2003]. The limitations of CFD tools have been documented on many occasions [Freitas, 1995; Laccarino, 2001], and the need for high-resolution numerical schemes, comprehensive experimental validation, and careful application have been reinforced [Freitas, 1993]. This is of particular importance when dealing with biomedical engineering flows since they exhibit a host of unique modeling challenges and difficulties. Such flows take place in complex, multi-connected domains with compliant walls and flexible immersed boundaries and are dominated, among others, by pulsatile effects, three-dimensional separation and vortex formation, regions of flow reversal, periodic transition to turbulence and laminarization, and non-Newtonian effects. In spite of these enormous complexities, which pose a formidable challenge to even the most advanced CFD tools available today, the notion that CFD is a

mature technology that can be applied indiscriminately to model any flow physics is becoming *de facto* in the biomedical field. In reality, CFD for complex, cardiovascular flows is an intricate and continuously evolving science that necessitates a close synergy and integration between modeling efforts and *in vitro* experimentation to guide model development and validation.

2.5.4 Summary and Future Directions

In vivo, *in vitro* and numerical studies have all underscored the great sensitivity of the TCPC efficiency to its design. Parametric *in vitro* and CFD studies have attempted to identify the contribution of different geometric parameters to the overall flow fields, leading to suggestions for improvement, such as including a caval offset or enlarging the IVC anastomosis. To our knowledge, however, *in vitro* studies have all been performed on simplified glass models. While breaking down this complex problem into its simpler components does provide insight into the hemodynamics of this structure, the complete picture still requires the study of the true anatomical TCPC flow, including more accurate TCPC geometries, wall material properties, respiration, lung resistance, etc.

CFD has been used to try and accomplish this task. However, very few studies report appropriately validated results. As was demonstrated by Khunatorn et al. [Khunatorn, 2003] accurately mimicking the primary flow structures does not imply that the whole flow field has been captured.

Thus, there is a need for more accurate *in vitro* modeling to provide both a better understanding of the TCPC hemodynamics and adequate data for the validation of anatomical CFD simulations.

2.6 Anatomical Models

As a first step towards more physiological modeling of the TCPC hemodynamics, we chose to focus our study on the geometrical aspects of the connection. Improved medical imaging quality and reconstruction methods [Frakes, 2003] enable accurate digital regeneration of the three-dimensional lumen of any cardiovascular structure based on two-dimensional medical images. The regenerated digital volume can then conveniently be used for CFD mesh generation. The transition to a solid model for *in vitro* experiments has presented greater challenges. Not only must the model be geometrically accurate but it should also be usable with any experimental flow analysis method.

2.6.1 Magnetic Resonance Imaging (MRI) Techniques

As is discussed by Geva et al., the major advances in MRI technology as well as growing evidence from clinical applications indicate that MRI is ideally suited for noninvasive assessment of the cardiovascular system in Fontan patients [Geva, 2003].

MRI technology is based on the principle that an unpaired spinning proton (such as in a hydrogen nucleus) creates a magnetic field due to its rotation and its electric charge. Hydrogen based MRI is the most common MRI technique used clinically because it is very abundant in the human body. In the presence of a large external magnetic field (B_0), such as that of the MR scanner, the protons align either parallel (low energy state) or anti-parallel (high energy state) with the external magnetic field, with the parallel orientation slightly prevailing (Figure 2.6.1). Therefore, there is net magnetization M_0 pointing in the direction of B_0 .

The combination of B_0 and of the spinning motion of the proton causes a complex motion called precession (Figure 2.6.2). The frequency at which the proton precesses is the Larmor frequency given by the Larmor equation

$$\omega = gB_0 \quad (\text{Equation 2.6.1})$$

where ω is the angular precessional frequency of the proton, g is the gyromagnetic ratio (42.6 MHz/Tesla for hydrogen), and B_0 is the strength of the external magnetic field. In order to image a particular region of the body, the protons in that region are excited with an electromagnetic pulse (called RF pulse) at the Larmor frequency. This excitation brings them from the low energy state (parallel) to the high-energy state (anti-parallel). The relaxation of the protons from this excitation releases energy, which is proportional to the amount of protons present. In order to select a specific slice in space for imaging, magnetic field gradients are used. Varying the magnetic field spatially varies the corresponding Larmor frequency according to Equation 2.6.1, so that by applying an RF pulse at a specific Larmor frequency, only protons in the slice with the equivalent Larmor frequency will be excited and contribute to the image.

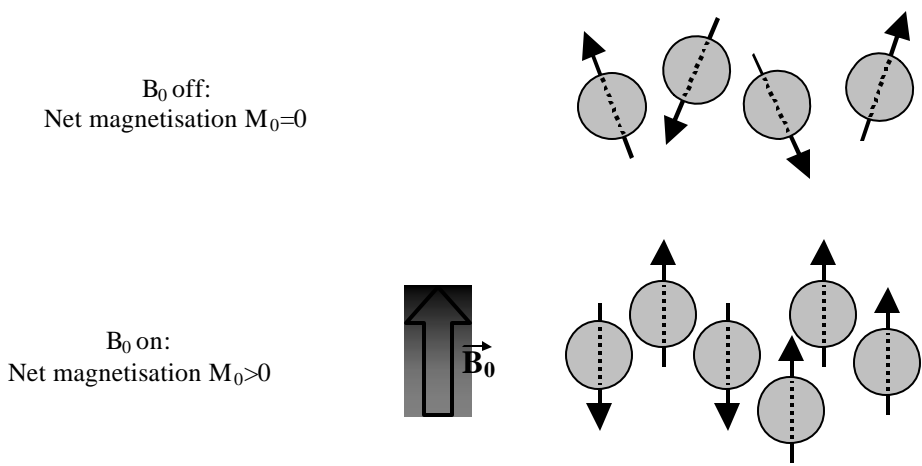


Figure 2.6.1: Schematic showing that in the presence of a magnetic field B_0 , net magnetization M_0 is produced as a result of the protons aligning with the external magnetic field.

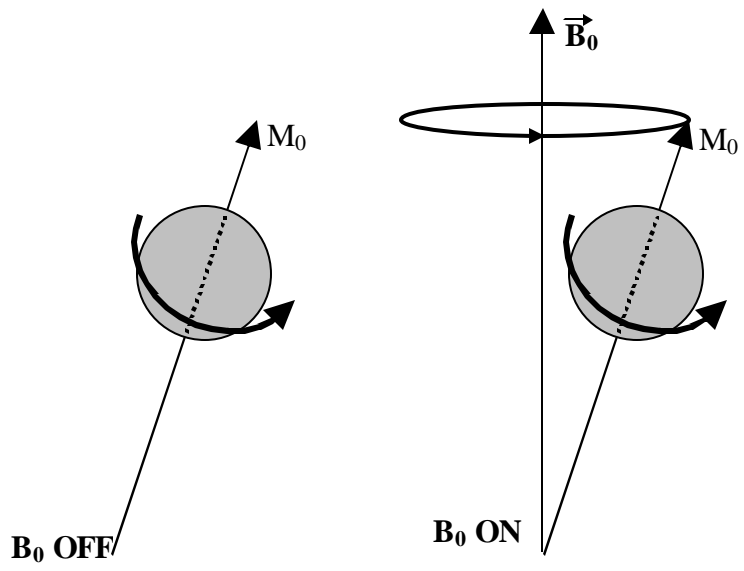


Figure 2.6.2: Schematic showing that in absence of an external magnetic, a proton spinning around its own axis generates a magnetic field M_0 . In presence of an external magnetic field B_0 , not only does the proton precess around its own axis but also around the B_0 axis.

A pulse sequence describes how the magnetic field gradients and RF pulses are applied and read during image acquisition. There are two major types of pulse sequences: spin echo and gradient echo. Spin echo sequences are characterized by a first RF pulse that tips the hydrogen protons by 90° followed by a second 180° pulse. Spin echo sequences generate images in which blood appears black while the other tissues appear as varying shades of gray. Spin echo sequences provide high spatial resolution and decreased artifacts from metallic implants (e.g. sternal wires, stents, etc) but require relatively long scan times (several minutes, depending on heart rate and number of signal averages). Gradient echo sequences on the other hand are much faster. They are characterized by less than 90° RF pulses (typically $15-60^\circ$) and generate images in which flowing blood appears white, which provides increased contrast between vascular and non-vascular structures. Another technique to improve the contrast between blood and tissues is to administer an exogenous contrast agent that dramatically shortens the relaxation time of the protons in blood, resulting in spin echo-sequences with a bright blood signal.

The accuracy and quality of the reconstructed digital geometry will highly depend upon the quality of the original patient images. MR settings should thus be chosen to optimize the image quality without keeping the patient in the MR scanner for too long. In this study, both spin echo and gradient echo sequences have been used.

2.6.2 Available Fluid Mechanic Assessment Methods

Information on the flow structure and efficiency of the TCPC has mainly been obtained through flow visualization, pressure drop measurements, and power loss calculations. However flow visualization is only qualitative, and quantitative control

volume power losses are both time averaged and integrated over the whole TCPC volume.

Khunatorn et al [Khunatorn, 2003] performed a more detailed quantitative flow analysis using digital particle image velocimetry (DPIV), which acquires the velocity field over an entire plane at once. Another quantitative flow analysis technique extensively used for *in vitro* studies of cardiovascular flows [Ku, 1987; Leo, 2002] is laser Doppler velocimetry (LDV), which provides velocity profiles and wall shear stresses with much higher temporal and spatial resolution than DPIV but at the cost of the researcher's time since the velocity can only be measured a single point at a time.

2.6.3 Manufacturing Methods

High accuracy optical flow measurement techniques, such as LDV and PIV, require the use of transparent *in vitro* models. Complex patient-specific anatomical models have traditionally been reproduced with glass blowing techniques, which are accompanied by high operator dependency and poor accuracy. Rapid-prototyping (RP) and computer-aided design (CAD) technologies have eliminated operator dependence, enabling exact geometry replication. In literature, this approach has been applied skillfully to specific research areas of biomedical fluid mechanics [Bale-Glickman, 2003; Chong, 1999; Friedman, 1993; Hopkins, 2000]. In these studies the general methodology is to use RP with *opaque* resins to obtain an accurate water-soluble negative of the flow passage that is then encased in transparent Sylgard© (Dow Corning Inc.). This multi-step process involves time-consuming chemical casting procedures and carefully controlled vacuum curing conditions.

RP has been extensively used in wind tunnels to fabricate opaque components for external flow measurements as an alternative to numerically controlled machining, [Springer, 1998]. Chuk and Thomson [Chuk, 1998] detail the component requirements for surface finish, dimensional accuracy and material strength as well as production costs, time and availability. For most biomedical studies experimental models do not undergo important load or extreme thermal conditions, and accordingly mechanical properties are not as crucial as manufacturing accuracy, production time, and transparency.

The production time and accuracy of the RP technology are already satisfactory. With the development of *transparent* RP resins, such as Vantico Water clear resins, arises the possibility of eliminating all the laborious casting processes to provide a faster and more direct transition from computer files to transparent anatomic *in vitro* model. Thus geometrical similarity between the experimental and numerical model, which is critical for accurate CFD validation, is increased.

CHAPTER III

HYPOTHESIS AND SPECIFIC AIMS

Although the current procedure of choice for single ventricle heart repairs, the total cavopulmonary connection (TCPC), has reduced the post-operative mortality to the level of simpler types of congenital heart disease repairs, Fontan patients are still subjected to serious long-term complications. The TCPC procedure, which restores the vital separation between oxygenated and deoxygenated blood, also leads to an increased workload for the remaining single ventricle, as it is now responsible for pumping the blood through both the systemic and pulmonary circulation. Previous work has shown that this workload may be reduced by altering the surgically created design of the TCPC in order to optimize its hemodynamics. Improved fluid mechanics and reduced energy dissipation at the connection site translates into less work for the single ventricle and improved transport of deoxygenated blood to the lungs, which may in turn contribute to improved post-operative results and quality of life.

The long-term goal of this research effort is to combine the knowledge gained from *in vivo*, *in vitro* and computational fluid dynamics (CFD) studies to gain a better understanding of the TCPC hemodynamics and yield improved TCPC designs and surgical planning. *In vitro* and computational studies have investigated the impact of caval offset [Ensley, 1999], pulmonary artery curvature, and vessel diameter [Liu, 2004; Ryu, 2001] in idealized and simplified models. Developments in numerical capabilities

have lead to more realistic modeling of the TCPC connection [Hsia, 2004; Migliavacca, 2003], but in spite of the complexity of the geometries involved, only a few of them report adequate CFD validation [Khunatorn, 2003]. CFD for complex, cardiovascular flows is an intricate and continuously evolving science that necessitates a close synergy and integration between modeling efforts and *in vitro* experimentation to guide model development and validation. To our knowledge, however, there have been no studies performed on an accurate replica of a TCPC involving both experimental and numerical studies. The present study used the recent progress in medical imaging, image post-processing and manufacturing techniques, to generate *in vitro* models that accurately replicate patients' TCPC anatomies and are well suited for comprehensive *in vitro* studies and CFD validation.

3.1 Hypothesis I

The first hypothesis of this study is that a complete understanding of the TCPC hemodynamics/fluid dynamics requires an accurate of the physiological TCPC geometry.

The specific aims originating from this hypothesis are:

3.1.1 Specific Aim 1:

To develop a manufacturing methodology for *in vitro* models that would:

- accurately replicate patients' TCPC anatomies
- allow for quantitative flow characterization

This aim will be achieved by reconstructing the true patient anatomy based on chest MRI data and then using the recently available transparent rapid prototyping resins to build the *in vitro* models. Material properties, geometric accuracy, suitability for qualitative flow visualization and quantitative velocity measurements using digital particle image velocimetry (DPIV) and laser Doppler velocimetry (LDV), as well as manufacturing time and difficulty, are the many parameters that will be taken into account to evaluate the suitability of this manufacturing methodology for our purposes.

3.1.2 Specific Aim 2:

To assess the fluid dynamics of two different anatomical TCPC templates:

- a TCPC with an intra-atrial tunnel and a single SVC
- a TCPC with an extra-cardiac conduit and a bilateral SVC

This aim will be achieved through *in vitro* experiments. Two completely different anatomical TCPC templates will be manufactured. A physiologic flow loop with varying pulmonary resistances will be used to investigate selected pulmonary artery flows and total cardiac outputs. Flow visualization, pressure drop measurements, power loss calculations, and DPIV measurements will be used in combination to assess the fluid dynamics of the connection. Simplified *in vitro* glass models will also be manufactured in an effort to better understand the complex anatomical flows.

3.2 Hypothesis II

The second hypothesis of this study is that a physicsdriven numerical modeling and comprehensive numerical model validation are the two sine qua non conditions for developing a reliable CFD tool.

3.2.1 Specific Aim 3

To develop an experimental *in vitro* approach allowing for appropriate CFD validation.

This aim will be achieved through the use of the transparent RP technologies. Stereolithography produces solid *in vitro* models that are within 0.1 mm of their digital counterpart, the latter serving as the geometry that will be numerically studied. Transparent RP resins will enable the gathering of both quantitative and qualitative information on the flow field.

3.2.2 Specific Aim 4

To provide all the experimental data needed to investigate the ability of different CFD models to characterize the flow patterns of the TCPC.

This aim will be achieved by providing quantitative and qualitative experimental results and comparing them to the numerical solutions obtained concurrently in our laboratory. These comparisons will be done on models of increasing

complexity, starting with simplified glass models and ending with the anatomical intra-atrial TCPC. Different degrees of accuracy will be considered in this validation effort, namely:

- the simplified control volume power losses, which are time-averaged and integrated over the whole control volume.
- the time-averaged velocity field
- the detailed physics of the flow

They will be addressed in the aforementioned order so as to avoid the tendency of jumping into the most complex computational model before sorting out the fundamental concerns.

CHAPTER IV

EQUIPMENT AND MATERIAL

In this Chapter, the experimental models, the *in vitro* flow loop and the experimental equipment are described. As numerical simulations were also performed on each one of the models concurrently to the experiments, this chapter also provides a brief description of the CFD tools that were studied in collaboration with Ryu et al. [Ryu, 2001], Liu et al. [Liu, 2004], Pekkan et al. [Pekkan, 2004].

4.1 In Vitro Models

4.1.1 In Vitro Glass Models

Six idealized glass models were custom crafted. These simplified models provided further understanding of the individual contribution of different geometrical features to the global flow field that was observed in the anatomical intra-atrial model and supported the numerical validation effort. Table 4.1.1 provides a brief overview of the geometrical characteristics of the six different models that are described in detail in the subsequent paragraphs. All models are shown in Figures 4.1.1 and 4.1.2.

Table 4.1.1: Overview of the geometrical characteristics of the simplified glass models

Model	Vessel Diameter (mm)				Connection design		
	IVC	SVC	LPA	RPA	PA Curvature	Offset (mm)	Pouch
Model 1	13.34	13.34	13.34	13.34	0°	13.34	No
Model 2	13.34	13.34	13.34	13.34	120°	13.34	No
Model 3	15.00	8.00	13.34	13.34	0°	13.34	No
Model 4	15.00	8.00	13.34	13.34	120°	13.34	No
Model 5	15.00	8.00	13.34	13.34	0°	0	Yes
Model 6	13.34	5.00	5.00	8.00	0°	0	Yes

4.1.1.1 Model 1

Model 1 was built after the one-diameter offset model that had been extensively studied by Ensley et al. [Ensley, 1999]. It served as a reference in order to validate our experimental set-up. The model was planar. All four vessels, venae cavae and pulmonary arteries, were of equal diameter, 13.3mm; dimension that had been retained by Ensley et al. based on the chest MRI of an eight-year-old Fontan patient. The radius of curvature at the corners of the connection was half a diameter, 6.65mm. The IVC and SVC were offset by one pulmonary diameter, 13.3mm.

Model 1 was manufactured using rapid prototyping as well as in glass so as to compare material properties.

4.1.1.2 Model 2

Model 2 reproduced the non-planar model numerically studied in our lab by Keesuk Ryu [Ryu, 2001]. This model was studied experimentally to support the CFD

validation on simple geometries. Qualitative validation had been done through flow visualization, however quantitative power loss measurements were missing.

Model 2 was non-planar; the pulmonary arteries formed a 120° angle. Similarly to Model 1, vessel diameters were set to 13.3mm and the radius of curvature at the corners of the connection to 6.65mm. The IVC and SVC were offset by one pulmonary diameter, 13.3mm.

4.1.1.3 Model 3

The motivation behind the design and quantitative study of Model 3 was identical to that of Model 2. Model 3 reproduced the model with more physiological diameters numerically studied by Keesuk Ryu [Ryu, 2001]. It was planar. The inner diameter of the pulmonary arteries was 13.3mm, while the caval diameters were of 8mm and 15mm for the SVC and IVC respectively. The radius of curvature at the connection was set to half the diameter of the corresponding vessel. The venae cavae were offset by one pulmonary diameter, 13.3mm.

4.1.1.4 Model 4

Model 4 was a combination of Model 2 and 3: vessel dimensions were identical to those in Model 2 (8mm, 13.3mm and 15mm for the SVC, the PAs and the IVC respectively) and the pulmonary arteries formed an angle of 120° degrees. The radius of curvature at the connection was set to half the diameter of the corresponding vessel. The venae cavae were offset by one pulmonary diameter, 13.3mm.

4.1.1.5 Model 5

Model 5 reproduced the vessel diameters taken for Model 3 and 4, with another design for the connection area. The vessel dimensions were 8mm, 13.3mm and 15mm for the SVC, the PAs and the IVC respectively. A pouch-like connection area with no caval offset was designed after the configuration of the anatomical intra-atrial TCPC. The radius of curvature at the connection was set to half the diameter of the corresponding vessel: respectively 4mm, 6.65mm and 7.5mm for the SVC-pouch, PA-pouch and IVC-pouch anastomosis.

4.1.1.6 Model 6

Model 6 was the closest to the anatomical configuration. It was designed on the exact same principle as Model 5 except for the vessel diameters. Those were chosen to reproduce the hydraulic diameters of the anatomical intra-atrial model. The inner SVC and LPA diameters were thus 5mm, while the inner diameter of the IVC was of 13.3mm and that of the RPA was of 8mm.

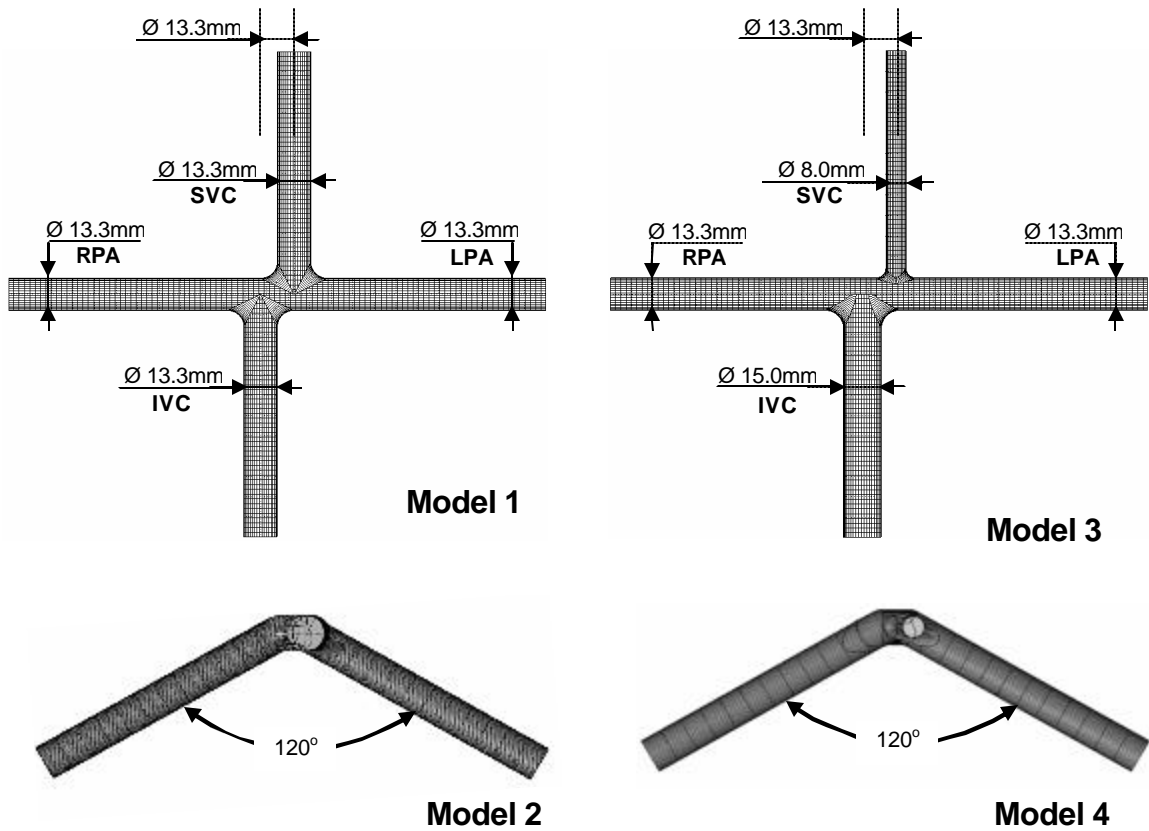


Figure 4.1.1: Simplified Glass models 1 to 4, varying VC diameters and PA curvature.

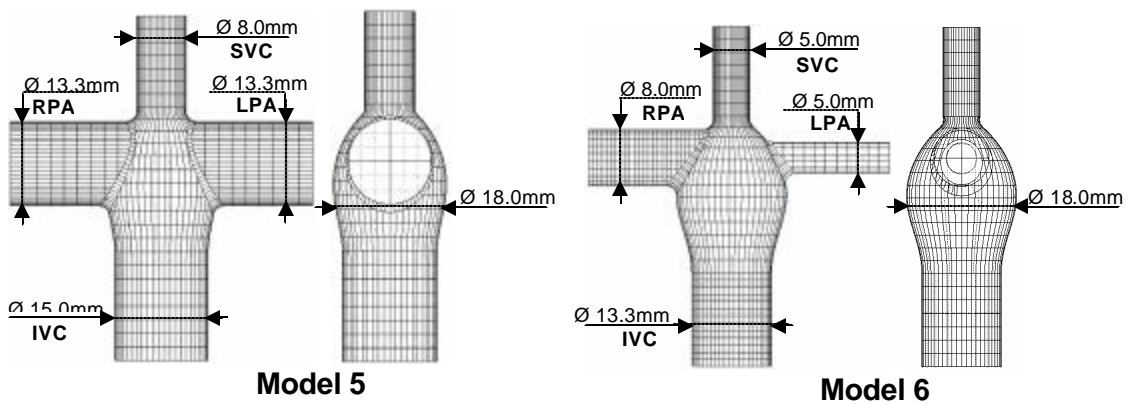


Figure 4.1.2: Simplified glass models 5 and 6, incorporating the impact of a pouch-like connection and PA diameters variation.

4.1.2 Stereolithographic Models

Stereolithographic techniques were used to fulfill specific aim 1 and manufacture experimental models that would accurately reproduce the anatomical TCPC configuration of a patient. Using rapid prototyping techniques we were able replicate CAD files of the anatomical reconstructions in a fast and accurate fashion (see Section 5.1); two major advantages that facilitate further engineering analysis and surgical design. In this study, rapid prototyping was used to manufacture two anatomical models reconstructed from MRI, as well as a copy of the control model, for validation purposes.

4.1.2.1 RP replica of the control glass model

Our CFD simulations did not model any surface roughness. If this matched the experimental set-up for the simplified glass models whose surface roughness could be approximated to zero ($R_a = 0.014 \mu\text{m}$), it no longer did with the RP models. As will be detailed in Section 5.1, the surface roughness of the RP models when coming out of the SLA® machine is about $R_a = 10.0 \mu\text{m}$ and may be brought down to $R_a = 0.3 \mu\text{m}$ through a careful polishing of the inner surfaces. Such process however may not always be desirable as it may alter the geometry. RP Model 1 was thus built to assess the sensitivity of the power losses to the manufacturing material. It was designed so as to be the RP copy of the control glass model, Model 1, and was left unpolished.

4.1.2.2 Anatomical intra-atrial model

The first patient specific anatomy that was studied was that of 13 years-old white female with a hypoplastic left heart. She had undergone a hemi-Fontan followed by

an intra-atrial TCPC surgery. The MRI scan that was used for the anatomical reconstruction was performed at the Children Hospital of Philadelphia in 2001. Eighteen slices with a 256*256 pixels field of view were acquired to cover the entire connection area. The pixel size was of 0.78mm*0.78mm for a slice thickness of 5mm. As is explained in section 5.1, interpolated images were fit between two raw images [Frakes, 2003], in order to improve the out-of-plane MRI resolution and obtain isotropic voxels. For this specific scan, five interpolated images were created for each raw MRI slice, which brought the total number of slices up to 102 and the slice thickness down to 0.83mm.

The characteristic dimensions of the intra-atrial TCPC obtained were considerably smaller than what had previously been studied in the TCPC literature. Liu et al.[Liu, 2004] and Ryu et al.[Ryu, 2001] had already studied idealized models mimicking the anatomical diameters. Both proposed a SVC and IVC of 8mm and 15mm, respectively, and PA diameters of 13.335mm. However, in our reconstructed geometry, the hydraulic diameters 2cm away from the connection area were only 5.1mm, 4.2mm, 4.2mm and 12.4mm, for the RPA, LPA, SVC and IVC respectively. The connection site had a pouch shape with a hydraulic diameter of 18mm and all vessels were enlarged towards the anastomosis site. Typically the LPA diameter ranged from 10.8mm at the anastomosis site down to 4.2mm at 2cm downstream of the connection. In the same manner, the SVC and RPA connected to the pouch with a hydraulic diameter of 8.5 and 8.2mm, respectively, but quickly tapered down to the dimensions mentioned previously. As had been addressed by Ryu et al. [Ryu, 2001], all four vessels were not co-planar. While both the IVC and RPA stood in the coronal plane, the SVC and LPA bent towards

the posterior side, respectively forming an angle of 48° and 37° with the IVC_RPA plane. The complexity of its geometry, as well as its small dimensions, conditioned the complex flow behavior that took place in this specific TCPC.

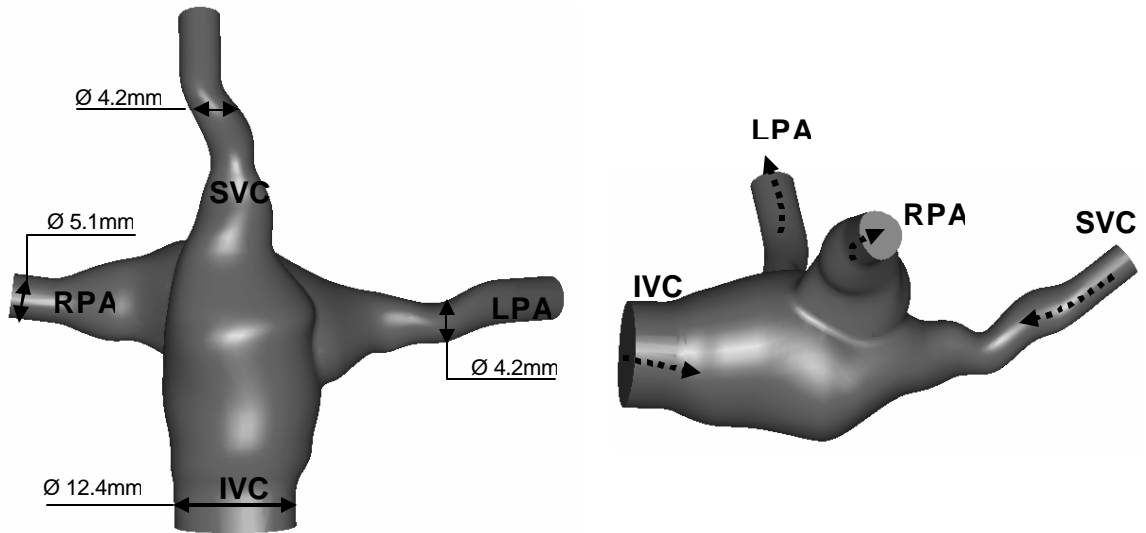


Figure 4.1.3: Intra-atrial anatomical model when looking from the posterior side (Left) and from the right hand side (Right)

4.1.2.3 Anatomical bilateral SVC

The second patient whose Fontan connection was modeled, was 7 years-old male with hypoplastic left heart too who had undergone an extra-cardiac TCPC connection and had bilateral superior venae cavae. The MRI scan was performed at the Children Hospital of Philadelphia in 2003. 45 slices were acquired over the entire span of the connection with a 256×192 pixels field of view. The pixel size was of $0.879\text{mm} \times 0.880\text{mm}$ for a slice thickness of 4mm. Four interpolated images were fit

between two raw MRI images, bringing the total number of slices up to 220 with a slice thickness of 0.8mm.

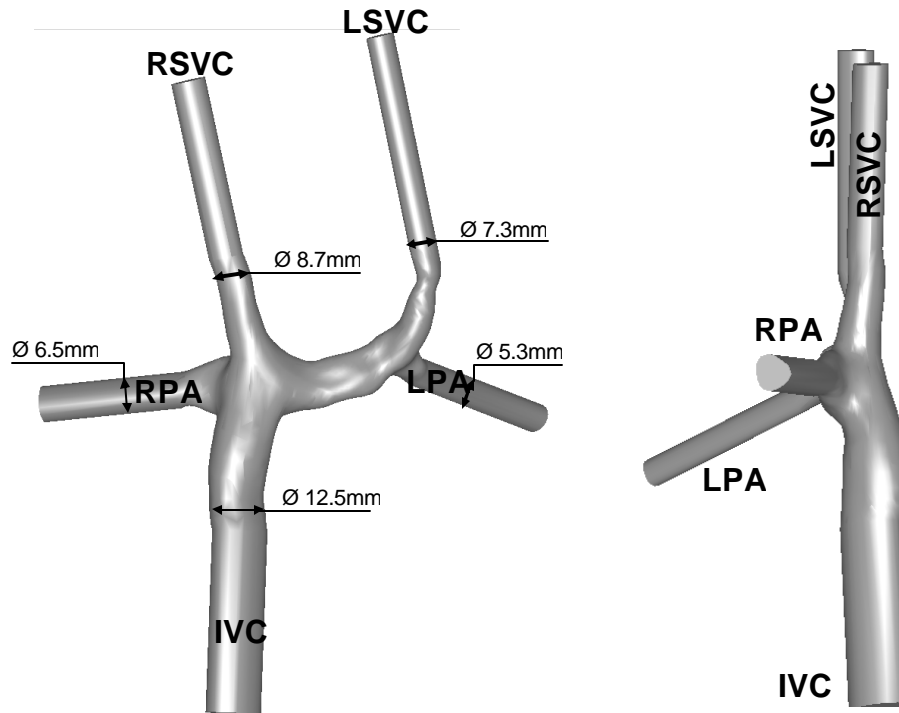


Figure 4.1.4: Anatomical bilateral SVC when looking from the anterior side (Left) and from the right hand side (Right)

Figure 4.1.4 shows the reconstructed geometry from both the anterior and the left hand side perspective. The geometry of this TCPC connection was smoother than the intra-atrial model described previously. All three venae cavae were pretty much coplanar. The caval diameters 3cm away from the connection were of 12.5mm, 7.3mm and 8.7mm for the IVC, the left SVC and the right SVC respectively. At the anastomosis location

those same vessels had a diameter of 16.1mm, 7.7mm and 9mm. The two SVC had a nearly constant diameter and the IVC was smoothly flared from 12.5mm to 16.1mm. While the SVC could be described as straight pipes, the IVC described a curve as it went around the heart. The pulmonary artery trunk between the two SVC had a diameter of 12.7mm, which was comparable to the IVC diameter. The two pulmonary arteries had similar shape and diameter: the RPA diameter went from 10.3 at the anastomosis location down to 6.5mm 2cm downstream while the LPA diameter went from 10.5mm at the anastomosis down to 5.3mm 2cm downstream.

4.2 Steady Flow Loop

All in vitro experiments were conducted under carefully maintained steady flow conditions. A schematic of the first loop that was constructed is shown in Figure 4.2.1, while Figure 4.2.2 shows the set-up after it had modified for the bilateral SVC, with three inlets and two outlets.

4.2.1 Set-Up for Two Inlets/ Two Outlets

The first loop, Figure 4.2.1, was used for the intra-atrial model as well as for all the simplified models. All experiments were run under steady inflow conditions maintained by a constant pressure head. Three rotameters calibrated for 0.75 to 7.5 L/min (acrylic flowmeters ½” FNTF model 6B0206, Dakota Instruments, Orangeburg, NY) were used to measure the total flow rate as well as the IVC and the RPA flow rates. To improve the accuracy of the flow rate readings at low total cardiac outputs, a more sensitive rotameter, calibrated for 0.35 to 3.5 L/min (acrylic flowmeters ½” FNTF model

6B0204, Dakota Instruments, Orangeburg, NY), was inserted in the LPA. Total flow rate, caval and pulmonary flow splits were controlled using ball valves. Additional ball valves were added where the tubing was the less elevated to empty the loop. A fully developed inflow profile was achieved by connecting extension pipes of matching hydraulic diameter to both the IVC and SVC. The length L_e required to achieve fully developed flow was computed using the following formula [Langhaar, 1942]:

$$\frac{L_e}{D} = 0.0575 \text{Re}_D = 0.0575 \frac{\bar{V}_{\max} \cdot D}{\boldsymbol{n}} = 0.0575 \frac{4000 \cdot Q_{\max}}{60pD\boldsymbol{n}} \quad (\text{Equation 4.2.1})$$

where D is the vessel diameter, \boldsymbol{n} the viscosity of the working fluid, \bar{V}_{\max} the maximum expected mean velocity and Q_{\max} the maximum expected flow rate through that vessel in L/min.

Most tubing consisted of PVC pipes. Some sections of transparent Plexiglas pipes or transparent soft tubing were inserted, which allowed the experimenter to check if there was any air or impurity getting into the loop. Different pieces of tubing were connected using PVC connectors. The connections were made leak-free with rubber joints maintained with metal rings. Other options include fixing the parts together using glue or silicone. The major advantage of rubber joints over the two latter techniques is that the loop may be mounted and dismantled easily, which is essential when the loop has to be cleaned or modified to adapt for a new model.

4.2.2 Set-Up for Three Inlets/ Two Outlets

The overall set-up that was used for this second loop, Figure 4.2.2, was very similar to the first one. Changes included two additional rotameters (FL46300 Series, OMEGA Engineering Inc, Stamford, CT) with a smaller range (0.1 to 1L/min) for the LSVC and RSVC and the substitution of a steady pump to the constant pressure head. The motivation behind this last change was the increased resistance in the model, which would have required the pressure head to be too high.

4.2.3 Working Fluid

For pressure drop measurements as well as for flow visualization, a solution of 40% glycerin and 60% de-ionized water reproduced the kinematic viscosity of blood in large vessels ($\nu = 3.5\text{cSt} \pm 0.1\text{cSt}$). Viscosity was checked using a Cannon-Fenske viscometer (Model CFRC-75, Fisher Scientific, Pittsburg, PA).

In order to avoid laser beam distortion in DPIV and flow visualization, an aqueous solution of sodium iodide that matched both the kinematic viscosity of blood ($\nu = 3.5\text{cSt} \pm 0.1\text{cSt}$) and the refractive index of the RP resin ($n = 1.51$) was used in LDV and PIV experiments

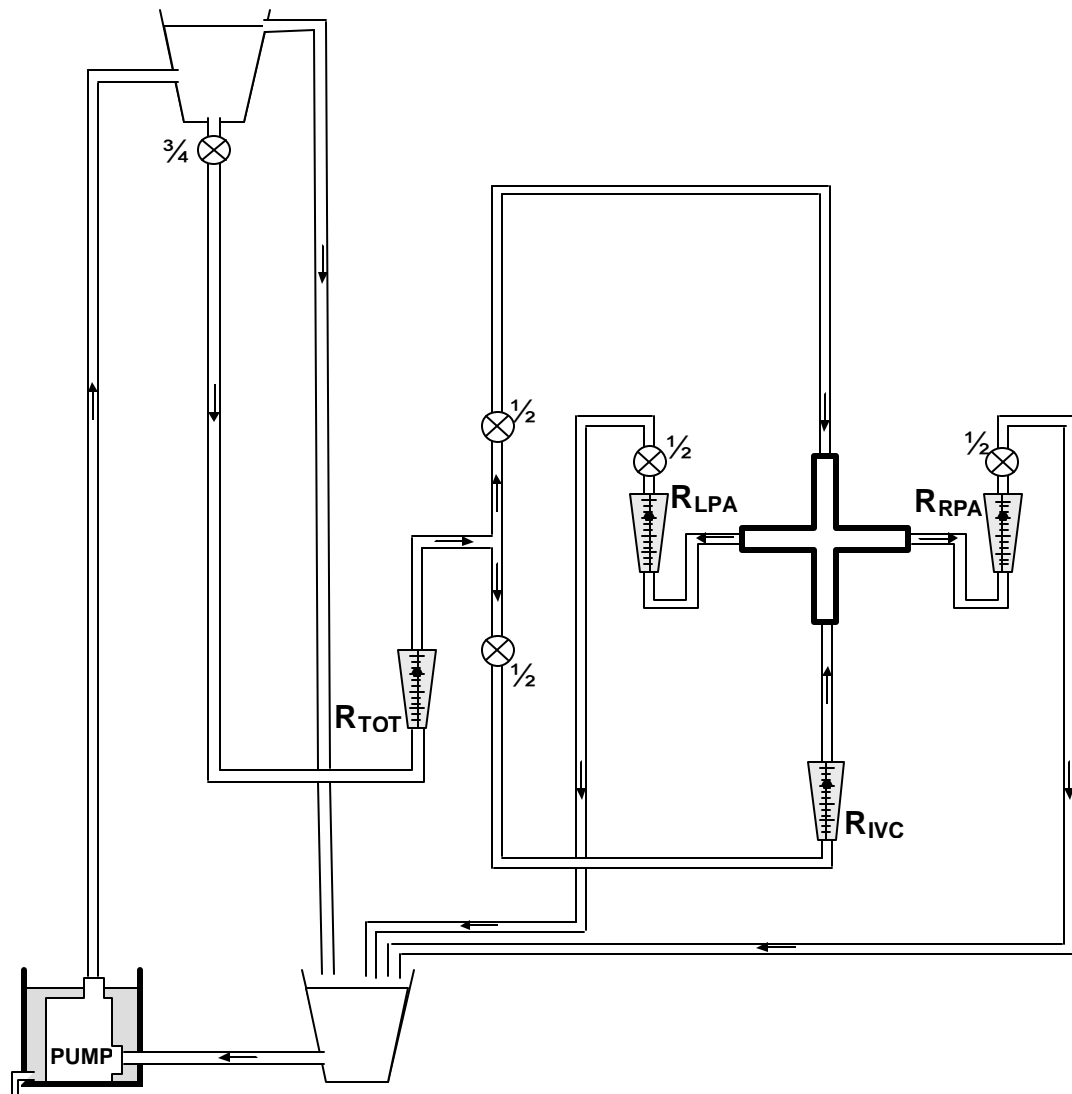


Figure 4.2.1: Steady flow loop used for all experimental studies performed in TCPC models with a single SVC. The flow rates in the different branches are controlled with ball-valves and 4 rotameters (R_{TOT} , R_{IVC} , R_{LPA} , R_{RPA}). A constant pressure head maintains steady flow conditions.

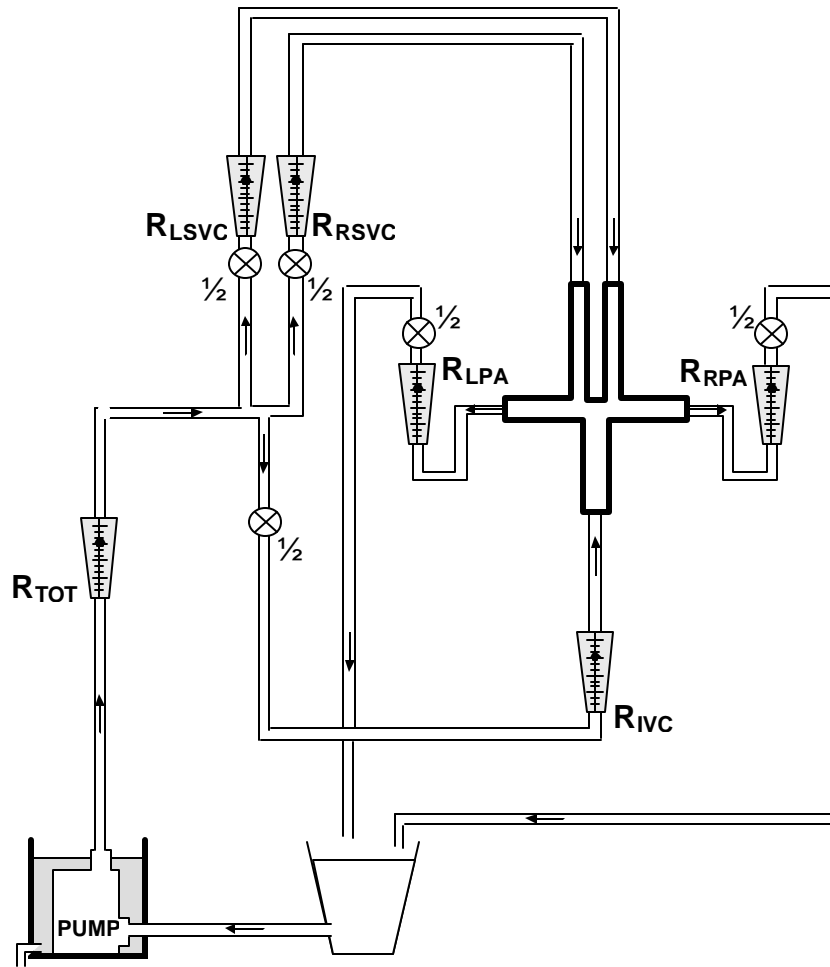


Figure 4.2.2: Steady flow loop used for all experimental studies in the anatomical bilateral SVC model. The set-up is identical to the previous loop, except for the rotameters. Two more accurate rotameters were acquired to measure the flow in the SVCs.

4.3 Experimental Measurements Material

4.3.1 Flow Rate Measurements

The flow rates were controlled with ball valves and measured using rotameters according to the set-up previously described. Rotameter measurement depends on the density of the working fluid. All the rotameters were thus recalibrated for the water/glycerin solution and for the aqueous solution of sodium iodide and glycerin.

4.3.2 Pressure Measurements

4.3.2.1 Pressure transducers

As is detailed in Chapter V, power losses were computed for every in vitro model using the pressure and flow rate in each one of its branches. However power losses do not depend on absolute pressure but rather on the pressure variation through the model. For a better accuracy, we measured the static differential pressures with respect to the IVC using multiple range differential pressure transducers (Validyne Engineering Corp. Northridge, model DP15), instead of measuring the absolute pressures at each point (Table 4.3.7).

a. Reluctance pressure transducer technology

Reluctance pressure transducers convert pressures into electrical signals. The transducer may be described as an inductive half-bridge, consisting of a pressure sensing diaphragm tightly clamped between the coil housings and two coils of equal impedance. The coils are placed in series and mounted so that their axis is orthogonal to the plane of the diaphragm. A schematic of the electrical circuit is shown Figure 4.3.1. When a differential pressure is applied on the diaphragm it deflects away from one coil and

towards the other one. The diaphragm material is magnetically permeable, and its presence nearer to one coil increases the magnetic flux density around the coil, thus increasing its impedance. Based upon the same principle, the impedance of the other coil decreases. The change in coil impedance brings the bridge out of balance and a small AC signal appears on the signal line. Within a given range the diaphragm displacement is linear with pressure so that the bridge output is again linear with pressure. The phase relationship between the output and excitation signals provides the direction of the pressure gradient. Whether the diaphragm is displaced in one direction or in the opposite one, the phase will be reversed 180°.

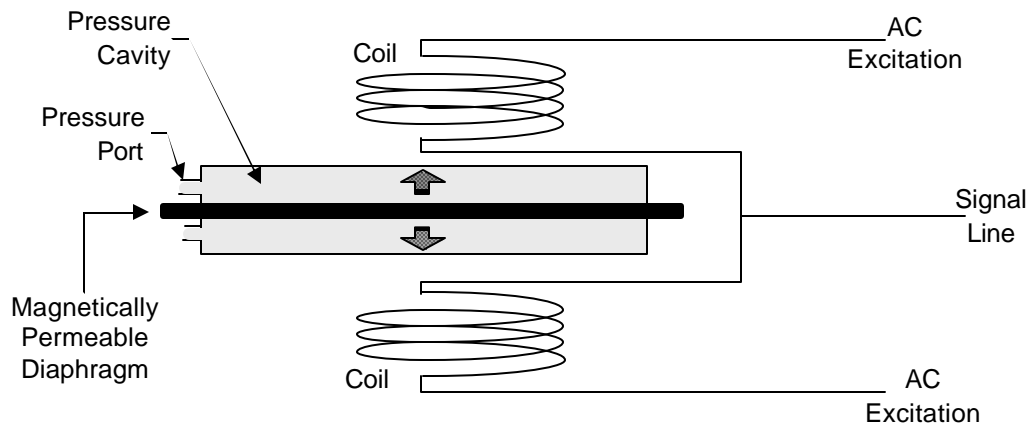


Figure 4.3.1: Functioning of a differential pressure transducer. The fluid contained in the pressure cavity pushes the membrane towards one coil or the other. The unbalanced half bridge outputs an electrical signal proportional to the pressure difference.

b. Catheters and liquid filling

Pressure is applied onto the diaphragm by the gas or fluid that lies in the two pressure cavities. Each cavity has a pressure port, which was connected to the pressure measurement location by non-compliant catheters, and a bleed port, which facilitates cleaning or liquid filling of the cavities. For static pressure measurements filling the sensor cavity with the liquid media is not necessary as any entrapped air will transmit the pressure to the sensing diaphragm of the transducer. For dynamic pressure measurements, however, the presence of entrapped gas will severely limit the frequency response of the transducer. Prior to any experiment, the chambers and catheters were filled up with the working fluid and all air bubbles were carefully removed.

In order to remove transducer bias, the catheters were rotated so that all 3 (or 4) differential pressures were acquired at each data acquisition, and so that after 3 (or 4) permutations, each transducer had acquired all of the differential pressure. This was achieved using 3-position valves and a complex catheter wiring. The whole process is summarized in Figure 4.3.2.

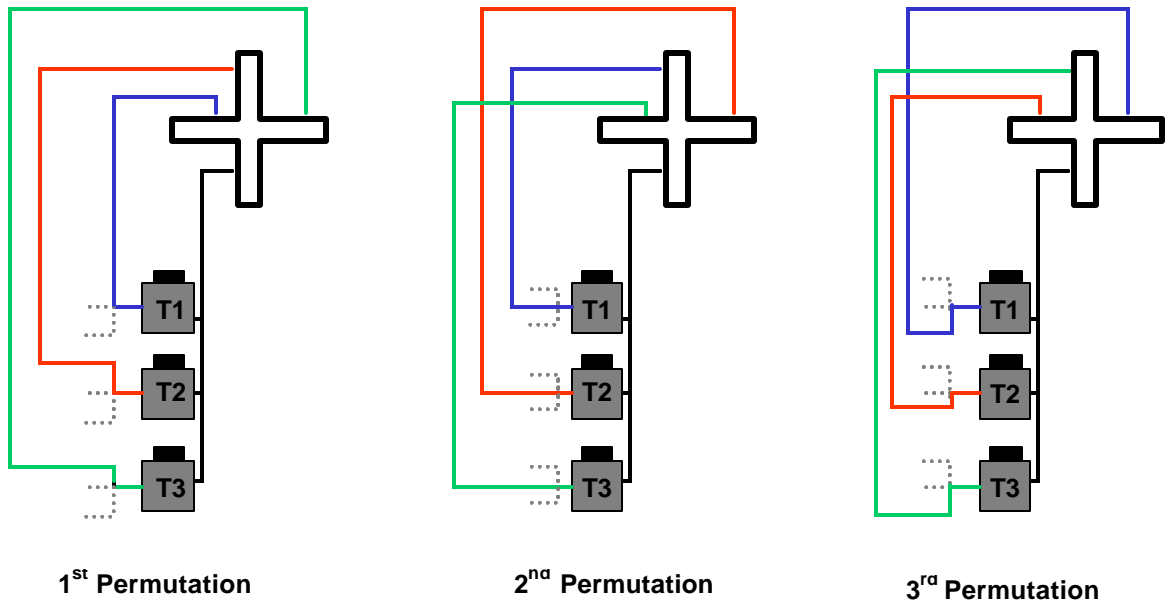


Figure 4.3.2: Transducer permutations in the case of a TCPC model with a single SVC. For each set of flow conditions (total flow rate, pulmonary and caval flow splits) all pressures are acquired at the same time, and after 3 permutations all pressures have been acquired by all three transducers.

c. Sensing membrane

Test runs were performed for each new model in order to determine the range of the pressure drops and choose the best-suited membrane. Table 4.3.1 displays the membranes that were used in the different models. The pressures in the anatomical models went over the recommended range for the membranes that were used. A calibration performed prior to the experiment demonstrated that the membrane response was still linear even for pressures on the order of +/- 40mmHg. An additional calibration was performed after the experiments, which demonstrated that the mechanical properties of the membrane had not been altered.

Table 4.3.1: Sensitivity of the membranes used in the differential pressure transducers in each in vitro model.

		Membrane	
		Reference #	Differential pressure range
Simplified Models	1, 2, 3 & 4	20	+/- 6.35 mmHg
	Design 5	22	+/- 10.4 mmHg
	Design 6	24	+/- 16.5 mmHg
Intra-atrial TCPC		24	+/- 16.5 mmHg
Bilateral SVC		24	+/- 16.5 mmHg

4.3.2.2 Carrier demodulator

The global set-up for the pressure measurements is displayed Figure 4.3.3. The small AC signal coming out of the transducers is amplified, demodulated and finally filtered by a carrier demodulator (Validyne Engineering Corp. Northridge, model CD19), which provides a +/- DC voltage that represents the magnitude and sign of the measured pressure.

4.3.2.3 A/D board

A data acquisition box was manufactured to take up the electrical signals coming out of the carrier demodulators and interface them with the acquisition computer. It was constituted of a 50 inputs connector block (National Instruments Corporation, Austin TX, CB-50) connected to an A/D board (National Instruments Corporation, Austin TX, DAQCard-1200) with the corresponding cable (National Instruments Corporation, Austin TX, PSH27-50F-D).

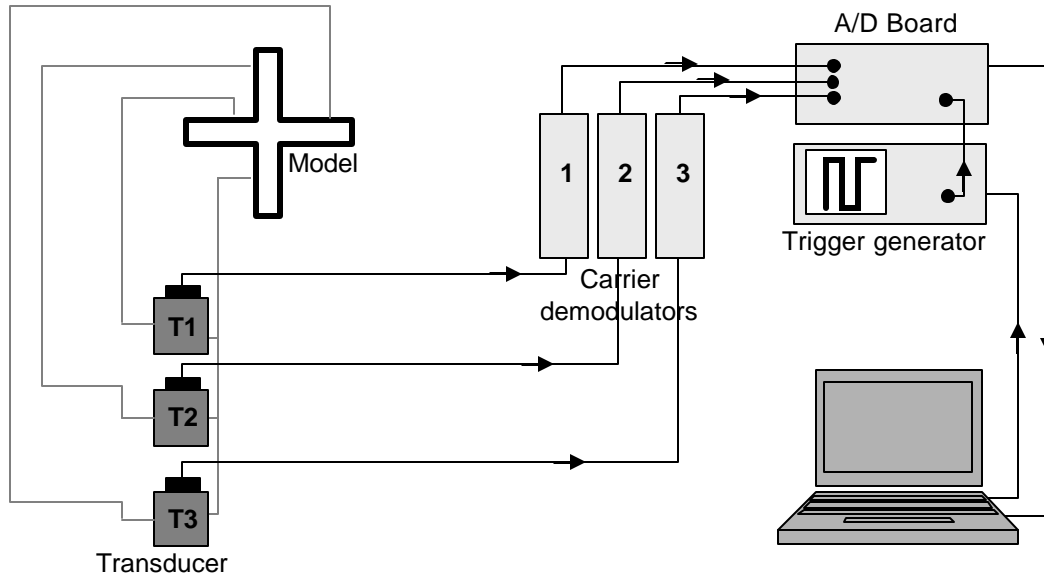


Figure 4.3.3: Experimental set-up for the pressure drop measurements

4.3.2.4 Data acquisition software

The data were collected on a PC (Gateway 2000) using DAQAnnal, a LabVIEW (LabVIEW 5.1, National Instruments Corporation, Austin TX) based in-house software. Data were acquired using the triggered data acquisition mode with 4 channels. The trigger was generated with a pulse generator controlled by the data acquisition PC using terminal.exe.

4.3.2.5 Data processing software

Data processing was done in two different steps. The raw data were first converted to Microsoft® Excel 2000 spreadsheets using DAQAnnal (LabVIEW 5.1, National Instruments Corporation, Austin TX). All the statistical analysis and power loss calculations, see Section 5.2.1, were performed within Microsoft® Excel 2000.

4.3.3 Flow Visualization

4.3.3.1 Particle flow visualization

Ensley et al. [Ensley, 1999] and Ryu et al. [Ryu, 2001] had already performed particle flow visualization in the simplified glass models 1, 2 and 3 both to provide some insight into the flow structure in different TCPC geometries as well as some ground of validations for the numerical simulations. The same flow visualization technique was used in this study for models 1 to 4. Buoyant 40 *mm* Pliolite particles (Goodyear Chemicals, Akron, OH) were suspended in the solution of water glycerin. The model was illuminated along the centerline with a sheet of 200-Watt incandescent light and digital video images were recorded over the range of flow conditions described in Section 5.3.

4.3.3.2 Dye flow visualization

In the anatomical models as well as in models 5 and 6 another flow visualization technique was necessary. The important mixing and the complex flow behavior were too complicated for particle flow visualization to provide an easy understanding of the flow. For that reason, streak-lines were generated from the inlets of the different models, which enabled an easy tracking of a given fluid element as it went through the connection. The streak-lines were generated by injecting a mixture of liquid soap and dark pigments (Mars Black Dry Pigments, Gamblin Artists Colors Co., Portland, OR) in the venae cavae by the mean of catheters. The viscous mixture was forced through the catheters with a mechanical piston syringe. Video images were acquired at 500 frames/second with a high speed CCD camera (Model A504K, Basler AG, Ahrensburg, Germany). A schematic of the experimental set-up is provided Figure

4.3.4. If the camera was shooting from the anterior side, a halogen lamp illuminated the model from the posterior side. A sheet of white paper was put between the halogen lamp and the model to act as a light diffuser and prevent the video images from being overexposed.

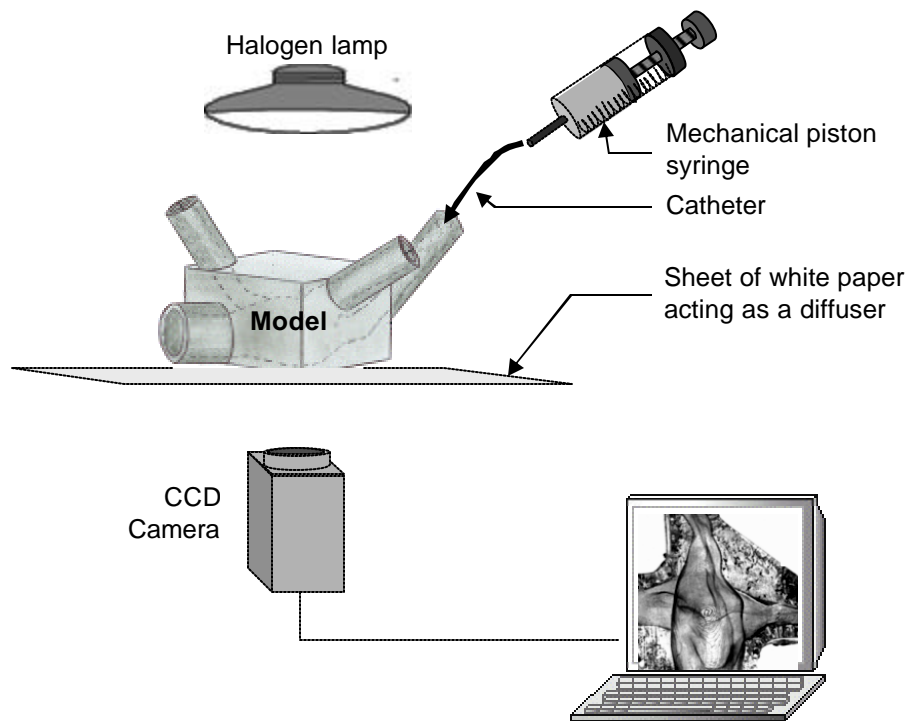


Figure 4.3.4: Set-up used for the flow visualization using dye injection.

4.3.4 2D Digital Particle Image Velocimetry (DPIV)

4.3.4.1 Theory of operation

DPIV technique has proven to be a valuable method in the study of fluid dynamics as it is a non invasive and is able to acquire instantaneous 2D velocity through a whole plane. The working fluid is seeded with micron size particles which are illuminated by a high energy sheet of laser light while a charged coupled device (CCD) camera records images of the illuminated flow field. In order to ensure that each image acquisition will represent an instantaneous snapshot of the flow field and that there is no significant particle motion during the exposure time, very short aperture time is required. To overcome the mechanical limitations of the aperture system on the camera, a pulsed laser-light with short pulse duration is used. Q-switched Nd:Yag lasers produce short duration (10ns) high-energy (50mJ to 100mJ) pulse of green light (532nm). The pulse energy is short enough to freeze hypersonic flows and the pulse energy is sufficient to illuminate sub-micron particles in the air, which make the Nd:Yag laser a well suited source of light for DPIV applications.

DPIV then uses a statistical approach (correlation processing) to give the average displacement, and subsequently the average velocity, of the particles within an interrogation spot. The two major correlation processes are the single-frame multiple-exposure autocorrelation and the double-frame single exposure cross-correlation. Each of these processing techniques presents advantages and drawbacks and will not serve the same purposes.

a. Single-frame autocorrelation

Autocorrelation is used with multiple exposure images and is best suited for very high speed flows. The scattered light from several exposures of the particles is recorded on a single image. This image is then subdivided into interrogation windows and autocorrelation is performed for each single one of them.

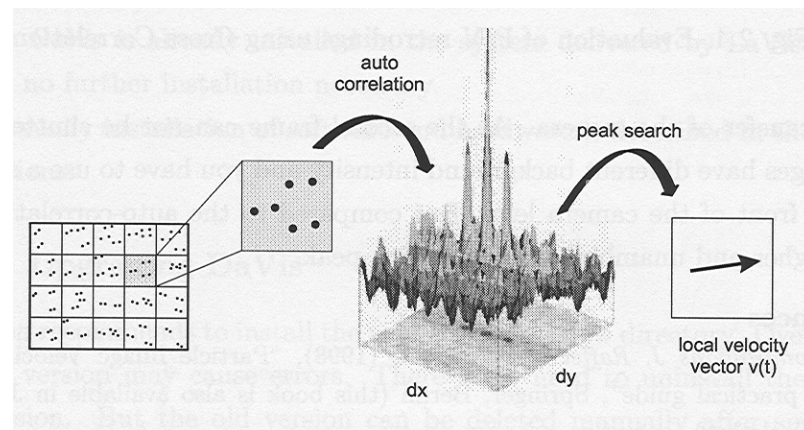


Figure 4.3.5: PIV vectors calculation using Single-frame autocorrelation [DaVis FlowMaster Software, LaVision GmbH, Goettingen, Germany]

Because the correlation is performed using the same image twice, maximum correlation is obtained for a zero-displacement, when each particle is correlated with itself. The autocorrelation peak should be the second highest peak. However, if the particle displacement is too small, the autocorrelation peak will not be distinguishable from the central zero-displacement peak. Special attention should be paid to ensure that

all particles cover a minimal distance. The autocorrelation function is symmetrical with respect to zero: each displacement peak has a peak of equal intensity in the opposite direction. One peak is the peak between the first and second particle image, the forward velocity, while the other is the distance between the second and first particle image, the backward velocity. If there are no negative velocities in the flow, then the correct peak can be selected by choosing amongst the positive displacements only. If there are flow reversals image shifting should be used to resolve the directional ambiguity. Finally, the auto-correlation peaks are small when compared to those obtained using cross-correlation. In models such as ours where there is a high noise, this increases the possibility that the correlation peaks completely disappear in the background.

b. Double-frame cross-correlation

Two-frame cross correlation uses two image frames with one pulse of light on each frame, and computes the velocities as a results of tracking the particles from one frame into the other. This method presents several advantages: first there is no ambiguity in the velocity direction, as there would be with autocorrelation, then zero-velocities can be measured and finally this is the correlation technique that has the highest signal to noise ratio.

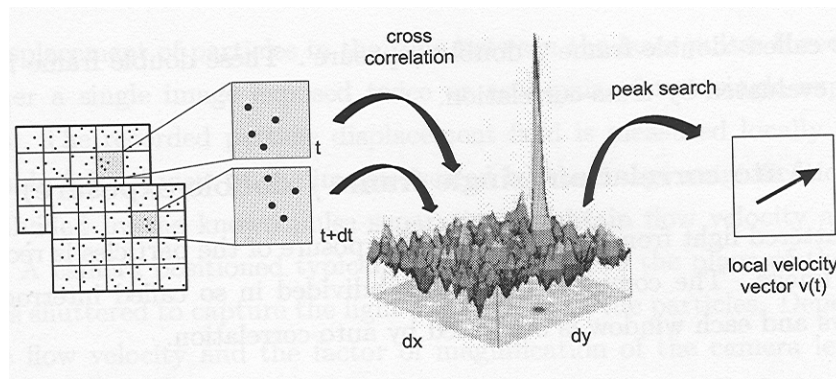


Figure 4.3.6: PIV vectors calculation using double-frame cross-correlation [DaVis FlowMaster Software, LaVision GmbH, Goettingen, Germany]

The limitation of using double-frame cross-correlation is the effective image-acquisition rate. The particles should move less than a fourth of the interrogation window in the time interval that separates the first and the second frame, which may be achieved by adjusting either the interrogation window or the time interval. The typical acquisition rate of a high resolution CCD camera is 30frames/s, which makes the double frame cross correlation not very practical for high-speed flows, since it would require larger interrogation windows and thus decrease the spatial resolution. A technique called “frame straddling” is used to overcome this limitation. As is shown in Figure 4.3.7, the laser beam is pulsed at the end of the first exposure and then at the start of the second exposure. This allows short time intervals between pulses so that high velocity flows can be captured. However Nd:Yag lasers use a flash-lamp to produce the energy that is converted into the laser beam and can only fire at about 10Hz. Frame-straddling is thus achieved with either two pulsed lasers or one double pulsed laser.

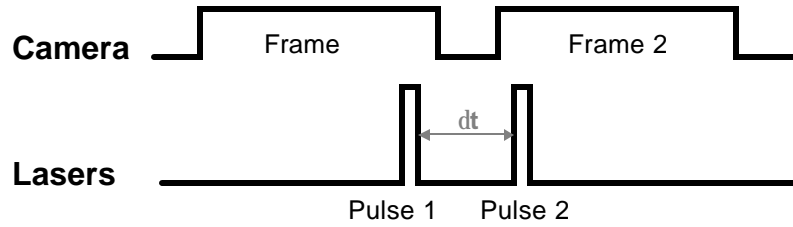


Figure 4.3.7: frame straddling: the laser beam is pulsed at the end of the first exposure and then at the beginning of the second exposure.

In this study, we did not have to deal with supersonic flows, and had a relatively high background noise. We thus used a double-frame cross correlation algorithm with a two-lasers configuration. The beams from the two lasers have to be combined into a collinear beam. Even though it may be more complicated to align than a double-pulsed laser, a two single-pulsed lasers configuration presents the advantages of allowing for any pulse separation as well as for maximum laser pulse power. Indeed, because it fires the Q-switch twice during a single flash-lamp discharge, the pulse energy of a double-pulsed laser is a decreasing function of the time between pulses. The maximum time between pulses with a double-pulsed laser is about 200 μ s, which is appropriate for velocities of 1m/s and higher, but would have been too short for our purposes.

4.3.4.2 DPIV hardware

The DPIV measurements that are shown in this study were performed using two different commercial DPIV systems for data acquisition: first a TSI Incorporated (Shoreview, MN) system that was then changed and upgraded to a LaVision (LaVision

GmbH, Goettingen, Germany) system. The first system was used for the DPIV data acquisition on the intra-atrial TCPC, while the latter system served to study the bilateral SVC. The LaVision software was used to process all the DPIV data sets presented in this study (no matter which system they had been acquired with).

a. Lasers

The two 17mJ pulsed Nd:Yag lasers (model miniYAG S/N 5505 and 5506, New Wave Research Inc, Fremont CA) were used with both systems. The two laser beams were combined using the TSI model 610010 Beam Combination Optics. An articulated arm with a set of mirrors conducted the laser beams up to the experimental set-up. The laser sheet was optimized with the combination of a cylindrical and a spherical convergent lens placed in series in the laser head.

The cylindrical lens controls the light-sheet height divergence angle, and the spherical lens controls the light-sheet thickness, as shown in Figure 4.3.8. In our system the spherical lens had a focal length of -12.7mm (TSI model 610081), and the 25mm diameter spherical convergent lens had a focal lens of +500mm (TSI model 610062). When optimized this configuration produced a light-sheet of approximately 90mm high and 0.3 mm at the waist. For optimum accuracy the laser should thus be set 500mm away from the center of the experimental model so that the laser sheet would be the thinnest possible. Additionally the laser head was mounted onto a traverse system so as to accurately control the location of the plane that was being imaged.

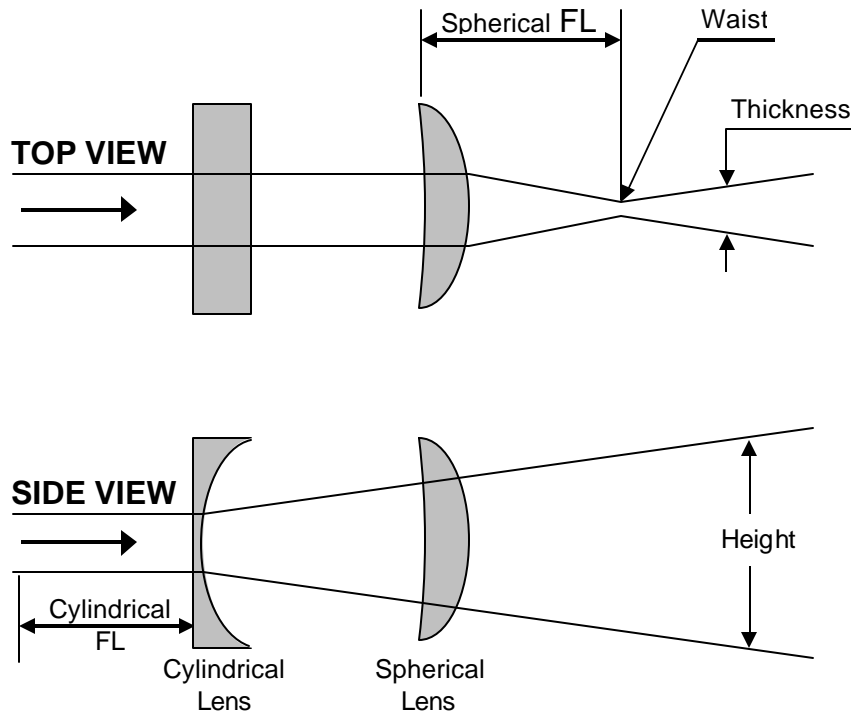


Figure 4.3.8: DPIV Laser light-sheet optics

b. TSI Incorporated (Shoreview, MN)

A schematic of a typical DPIV set-up is provided Figure 4.3.9. The TSI Incorporated system consisted of a data acquisition software package (TSI, Insight 3.34), a computer controlled synchronizer (TSI model 610032), interfaced with the two 17mJ pulsed Nd:Yag lasers (model MiniYag, New Wave Research, Fremont CA) and a CCD camera (TSI model 630046 PIVCAM 10-30). The camera used to record the images had a resolution of 1008*10018 pixels and was focused normal to the illuminated plane. It was equipped with an AF Micro Nikkor 60mm lens (Nikon, Melville, NY).

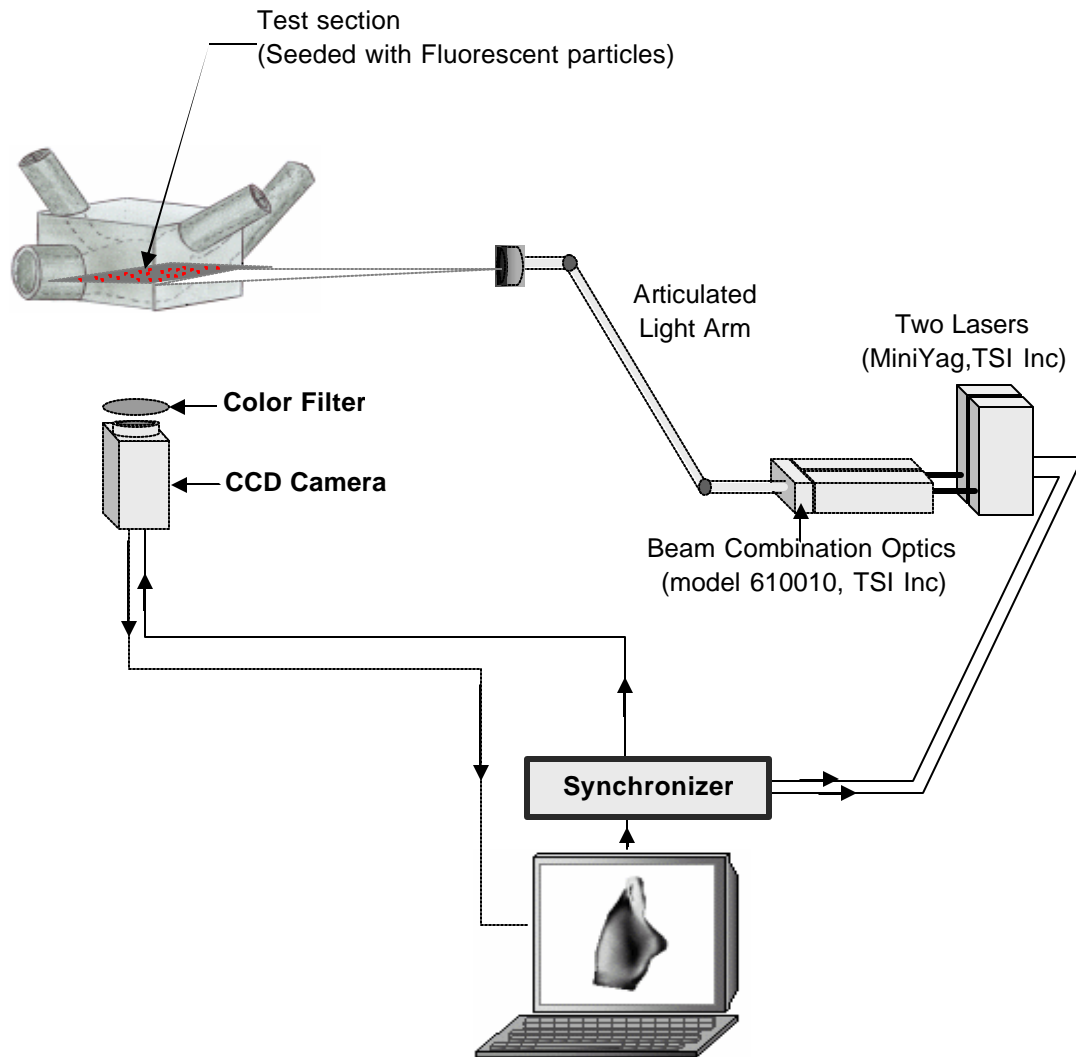


Figure 4.3.9: General DPIV set-up. In our set-up the CCD camera was located underneath the model, which required extreme caution in order to avoid any spill. Using a set of mirrors may be more appropriate as it would allow the experimenter to image from the same location without endangering the hardware.

c. LaVision (LaVision GmbH, Goettingen, Germany)

The DPIV system was upgraded during the performance of this study. The upgraded DPIV system included a data acquisition software package (Davis, version 6.2 to version 7.0) with 2D and 3D PIV/PTV capabilities, a programmable timing unit (Model 1108013), two 1600*1200pixels CCD cameras (Model 1101MPRO), an A/D converter (Model 1108033) and a new system computer (Model 1104004) with direct to disk high speed storage system (Model 1104101). All the specifications for the new hardware may be found in Appendix A.

This new system provided improved spatial and time resolution. The spatial resolution of the computed velocity fields was also improved by the ability of the software to perform cross-correlation computations in multiple passes using decreasing interrogation window size. This however significantly increased the processing time, which should be overcome in future works thanks to the distributed data processing (Network license, 1105NET).

d. Flow seeding

For optimal image quality, the fluid was seeded with fluorescent particles (MF/RhB, size range: 2.5 to 5 μ m, supplier: Microparticles GmbH, Berlin, Germany). A red color filter ($\lambda = 570$ nm) was used to cut off the laser beam reflections on the model surfaces while still allowing the fluorescent particles to shine through.

4.3.5 Laser Doppler Velocimetry (LDV)

Laser Doppler velocimetry (LDV) was used to measure velocities along the centerline of each vessel of the intra-atrial anatomical model. The exact location of the LDV measurements are displayed Figure 5.2.6.

LDV is a non-invasive laser technique used to measure fluid velocity accurately by detecting the Doppler frequency shift of laser light that has been scattered by small particles moving with the fluid. Contrary to DPIV, which provides an instantaneous snapshot of the velocity field throughout an entire plane, LDV is a point-by-point measurement technique and is thus much more tedious for area investigation. However it provides much higher spatial and temporal resolution than the available DPIV systems. Therefore, while DPIV was used to provide an overall understanding of the flow field, LDV was used to give further insight into the unsteadiness of the flow that had previously been observed in flow visualization. LDV could also have provided 3D velocity information. However the optical quality of the side surfaces did not allow for the third velocity component to be acquired. Thus, only 2D LDV measurements were performed. A summary of the LDV system is provided Figure 4.3.10. The following subsections describe the different components as well as the working theory of the 2D LDV set-up.

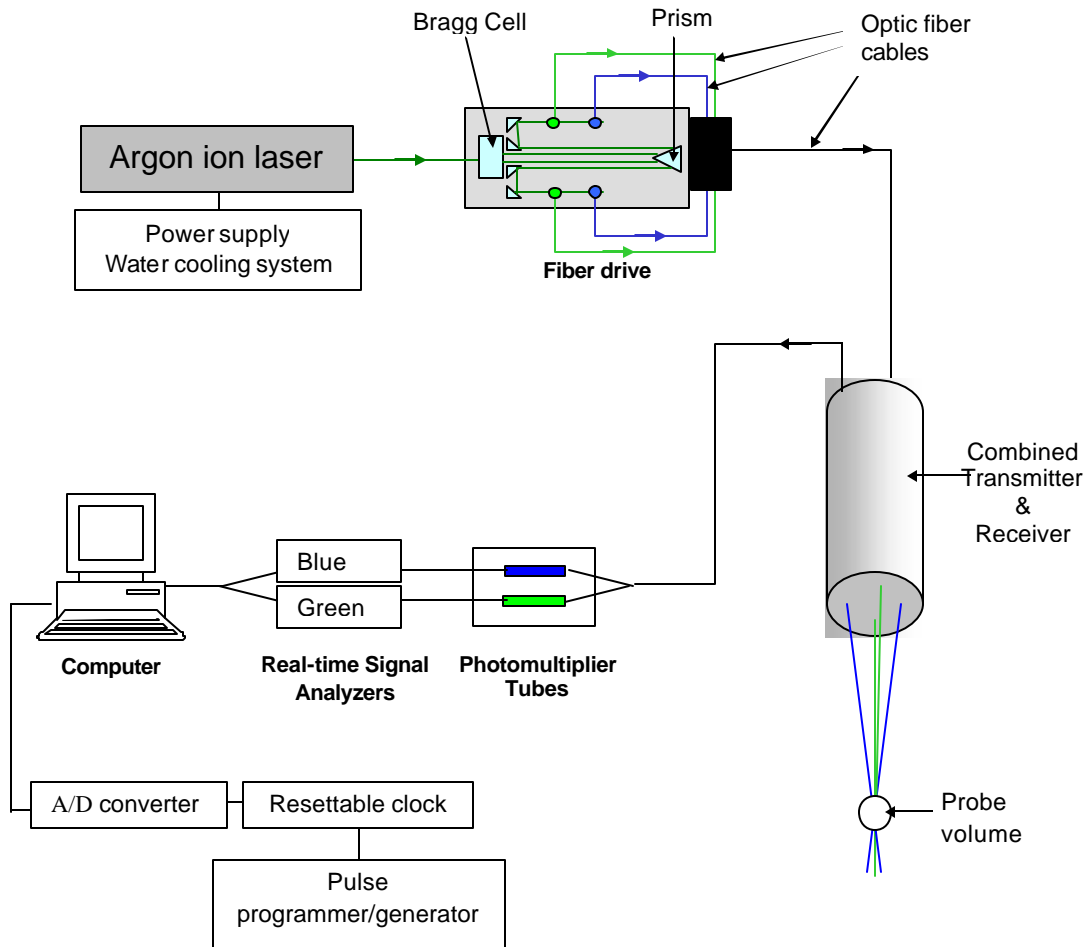


Figure 4.3.10: Schematic of the 2D LDV system

4.3.5.1 Laser

A 5 W multi-line argon-ion gas laser (Innova 70, Coherent, Santa Clara, CA) was used to produce the primary laser beam. The intense primary laser beam was then directed towards a fiber drive (Model FBD 1340, Aerometrics Inc., Sunnyvale CA). A Bragg Cell within the fiber drive split the incoming laser into two parallel beams of equal intensity but of different frequency. A frequency shift was added to one beam of each focal pair; one beam (called the zero order beam) had the frequency of the incident

beam while the other (called the first order beam) was shifted 40 MHz in frequency. The two beams were then separated into individual colors by two dispersion prisms. The four more powerful beams were directed into four fiber optic couplers, two green beams (with a wavelength of 514.5 nm), and two blue beams (488 nm). The couplers linked the fiber drive with a coupled transceiver-receiver (Model XRV 1204, TSI Inc, Shoreview, MN) via a series of fiber optic cable. A 100 mm focal length lens was used to transmit the beams towards the interrogation region of the model.

4.3.5.2 Flow seeding

The flow was seeded with neutrally buoyant silicon carbide particles (Model 10081, TSI Inc, St Paul, MN) with a nominal diameter of 1.5 μm . The solution was filtered regularly through a 5 μm filter cartridge (Model C1, US Filter Plymouth Product, Warrendale, PA) to remove any contaminants.

4.3.5.3 LDV measurement principle

The intersection of two coherent beams created a probe volume with the shape of an ellipsoid of revolution. The overall resultant probe volume is the region formed by the intersection of the one, two, or three ellipsoid volumes depending on the number of dimensions that are being acquired. When a particle flows across the probe volume, the laser-light is scattered from within the probe volume and recorded back by the receiver. This phenomenon is known as a Doppler burst. Because the beams are coherent sources, the intersection of a pair of beams creates interference fringes (pattern of bright and dark bands of light) and the intensity of the refracted light subsequently alternates between a

zero- and a peak- intensity as the particle goes across destructive (dark) and constructive (bright) fringes. The intensity of the refracted light varies in a Gaussian fashion as the particle goes from the one side of the probe volume to the other. A characteristic Doppler burst is illustrated in Figure 4.3.11.

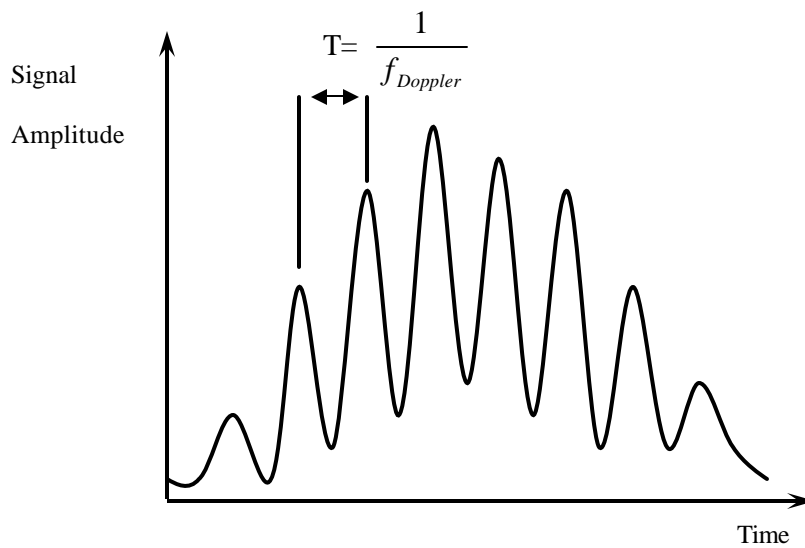


Figure 4.3.11: Doppler pulse obtained from light scattered by particle [Simon, 2004]

The velocity of the particle can then be calculated by multiplying the distance between the fringes with the frequency at which the particle crossed them. The velocities computed with such a technique only depend on the properties of light: The spacing between fringes in the probe volume solely depends upon the laser wavelength and the

angle between the paired beams, while the Doppler frequency is obtained from the Doppler burst signal. Subsequently no calibration of the LDV system is required.

In order to measure multiple velocity components of a given particle, the probe volumes formed by each beam pair were aligned in such a way that they intersected at the same spatial location and were positioned orthogonal to each other. By doing so, the particles flow through both probe volumes simultaneously and both X and Y velocity components could be acquired.

The frequency shift introduced by the Bragg Cell to the input beams offsets the Doppler frequency, thereby moving the zero velocity away from the zero frequency. This in turn allowed particles of near-zero velocity to generate Doppler burst and enabled the distinction between positive and negative velocities.

Finally the time required for a particle to go across the probe volume, called gate time, is recorded for each particle to be used further down the road as a weight for the data averaging process.

4.3.5.4 Signal acquisition

The Doppler bursts were captured by the coupled transceiver-receiver (Model XRV 1204, Aerometrics Inc., Sunnyvale CA), amplified and converted into an analog signal by two photomultiplier tubes (Model RCM 2300 LS, Aerometrics Inc., Sunnyvale CA), which present the combined advantage of having a higher gain and signal to noise ratio than photodiodes or other similar devices.

Two real-time Signal Analysers (Model RSA1000 L, Aerometrics Inc., Sunnyvale CA) interfaced with a computer were used to process the signal using the Fast

Fourier transform method. Prior to the velocity computations, the 40MHz shift was removed and a low pass filter eliminated all high frequency noises. Data were recorded via Aerometrics System Software, Particle Acquisition and Analysis, Version 0.80.

Additionally, because all post-processing software packages had been designed for triggered pulsatile flow, data acquisition was triggered at 64Hz. A 16 bit resettable clock (TSI Inc, Shoreview, MN) was interfaced with the pulse duplicator and synchronized the data acquisition with the cycle time.

4.4 Computational Fluid Dynamics (CFD)

As stated in Specific aim 3, this study was designed to provide a tool for thorough CFD validation in complex geometries. Every experiment thus had a numerical counterpart. CFD of the different anatomies were studied under the same conditions as the experiments, namely incompressible, laminar flow with steady inflow conditions and rigid vessel walls. Calculations were carried with three different flow solvers: the first four simplified glass models (Model 1 to Model 4) were studied using the commercial CFD package CFD-Ace (Version 5, CFD Research Corporation, Huntsville, AL). The intra-atrial TCPC was studied using both the commercial CFD package FIDAP (Fluent Inc., NH) and a recently developed, in-house, high-resolution unsteady flow solver, which will be subsequently referred to as the *in-house code*. This section briefly describes these different CFD tools.

4.4.1 CFD-Ace (Version 5, CFD Research Corporation, Huntsville, AL)

Numerical results on the first four simplified glass models can be found in literature [Liu, 2004; Ryu, 2001]. All four models were meshed using CFD-GEOM (CFD Research Corporation, Huntsville, AL). Ryu et al. used unstructured grids only while Liu et al. [Liu, 2004] compared the numerical solutions obtained for Model 4 with both structured and unstructured grids. The calculations were carried out using the commercial code CFD-Ace (Version 5, CFD Research Corporation, Huntsville, AL). To ensure that the code would capture secondary flows, second order-order up-wind differencing with 10%-30% blending with first-order up-wind differencing was used to discretize the convective terms.

4.4.2 FIDAP (Fluent Inc., NH)

The FIDAP computations were conducted by Pekkan et al. [Pekkan, 2004] on the intra-atrial geometry. They were aimed at exploring the accuracy with which a state-of-the-art commercial code can predict the general flow patterns and in particular the energy losses for various flow splits and Reynolds numbers.

4.4.2.1 Numerical scheme

The parallelized segregated finite-element solver FIDAP (Fluent Inc., NH) with the SIMPLER-like pressure projection algorithm [Haroutunian, 1993] was used in conjunction with the conjugate gradient (CG) and conjugate gradient squared (CGS) iterative solvers for symmetric and non-symmetric linear equations with Gauss-Seidel and diagonal preconditioning, respectively. Petrov-Galerkin pressure stabilization was activated for the 4-node linear unstructured tetrahedrons [Hughes, 1986]. The streamline

upwind scheme [Hughes, 1979], which enabled better-than-first-order accuracy in the cross-stream direction is utilized to discretize the convective terms. The overall accuracy of this scheme, however, was only first-order.

4.4.2.2 Convergence

All simulations with FIDAP converged to a steady-state solution starting from a zero initial guess. The residuals leveled off after approximately 800 iterations, as the velocity residuals decreased by three orders of magnitude and the pressure residuals decreased by four orders of magnitude. The iteration process was continued, however, for 3000 iterations to ensure that convergence was indeed achieved and that no long-time instabilities develop. Convergence criteria for the CG and CGS systems were 0.01 and 0.001 times the residual convergence criteria with an appropriate number of inner iterations, respectively. All jobs were run in parallel with 2- or 4- CPU nodes in linux (2.8GHz) and Sun (450MHz) machines with 2 to 4 GBytes memories. Mesh partitioning was done through PMETIS [Karypis, 1997] and DOMECC [Farhat, 1995] schemes with little difference in CPU time. For the medium grid a typical convergence requires 32 CPU hours. Steady inflow boundary conditions are specified at the IVC and SVC.

4.4.2.3 Grid generation

An unstructured grid was generated in Gridgen (Pointwise Inc). A systematic grid refinement study was carried out using three gradually refined grid sets with 64,000 to 340,000 tetrahedral elements, respectively (see Figure 4.4.1 for a typical view of the FIDAP computational mesh).

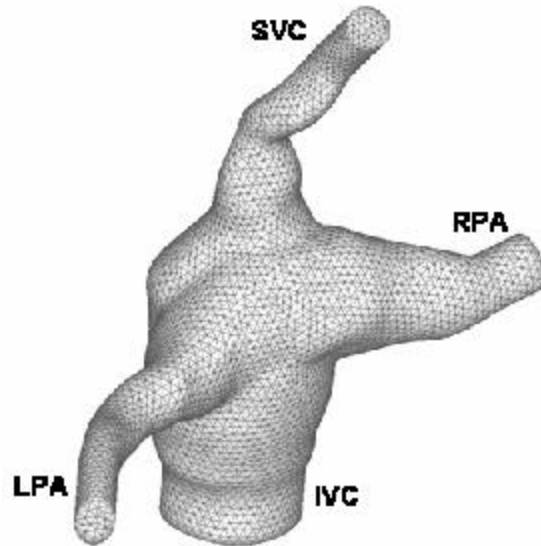


Figure 4.4.1: Typical view of the FIDAP computational mesh, generated with Gridgen on the intra-atrial TCPC geometry

4.4.2.4 Boundary conditions

The total cardiac output is split as 60 to 40 between the IVC and SVC. At both vena cavae the inflow velocity profile is specified as fully-developed. To obtain the specific fully-developed velocity profile, auxiliary steady CFD solutions are performed over the inlet entrance lengths (since the anatomic vessel cross-sections were not exactly circular, the actual fully developed flow profile is an unknown). Computations with the uniform plugflow velocity profile did not reproduce the experimental flow field. Reasonable agreement with experimental results was only achieved when the fully-developed flow profiles were implemented. Outflow through PA's are modeled using pressure boundary conditions. To specify the correct split, a set of auxiliary runs, as

shown in Figure 4.4.2 were performed to map the pressure and PA split characteristics of the connection [Liu, 2004].

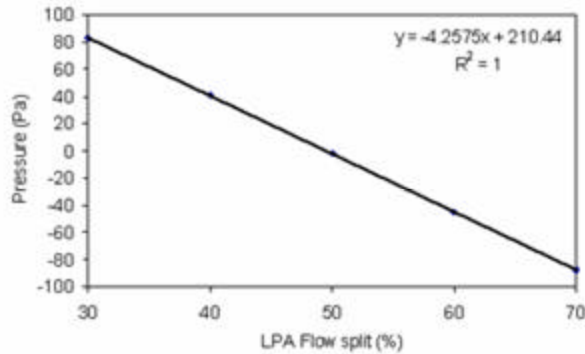


Figure 4.4.2: Correlation between the pressures imposed at the boundaries and the PA flow split for correct PA flow split specification.

4.4.3 In-House Flow Solver

As is discussed in Chapter VI and VII, despite a great success in predicting the overall pressure loss in the TCPC region, FIDAP failed to reproduce the complexity and flow instabilities that were observed in the experiments in the intra-atrial TCPC. The simulations with the in-house code were conducted by Liang Ge. They were prompted by the inconsistency between the experimental observations and numerical simulations.

4.4.3.1 Numerical scheme

The numerical method was that developed by Ge et al. [Ge, 2003] for simulating flows in mechanical, prosthetic heart valves. It employed domain decomposition with overset (Chimera) meshes [Ge, 2003; Tang, 2003] to discretize arbitrarily complex, multi-connected domains with domain-structured, body-fitted meshes. The governing equations were discretized on a non-staggered grid in strong-conservation form using second-order accurate numerics. Namely, three-point, second-order accurate central-differencing plus third-order, fourth-difference, matrix-valued artificial dissipation is used for the convective terms while central differencing was used for the remaining terms in the governing equations. The discrete equations were integrated in time using a dual-time-stepping, artificial compressibility technique in conjunction with a block, approximate-factorization iterative algorithm for rapid convergence during each physical time-step.

4.4.3.2 Convergence

It is important to point out that, unlike the commercial code, running the in-house code in a steady-state mode failed to yield converged solutions. Based on our past experience with this code, failing to obtain a converged steady-state solution typically meant that the physical flow was likely to be inherently unstable and flow unsteadiness was to be anticipated. For that reason the code was run in an unsteady mode, using the dual-time iterative algorithm to converge the velocity and pressure residuals by approximately two to three orders of magnitude per physical time step. Upon switching to

the unsteady mode of the code, we found that a complex, unsteady solution naturally emerged, which exhibited many of the attributes of the laboratory flow.

4.4.3.3 Grid generation

A structured grid constituted of three overset blocks (LPA arm, RPA arm and IVC/SVC conduit) with a total of 1.18 million nodes. The meshes in each sub-domain were generated using the Gridgen (Pointwise Inc, TX, USA) commercial grid-generation software. A typical view of the overset mesh is shown in Figure 4.4.2. For geometry as complex as that studied in this work, generating a good quality block structured mesh typically requires considerably more effort than generating the unstructured mesh used by FIDAP.

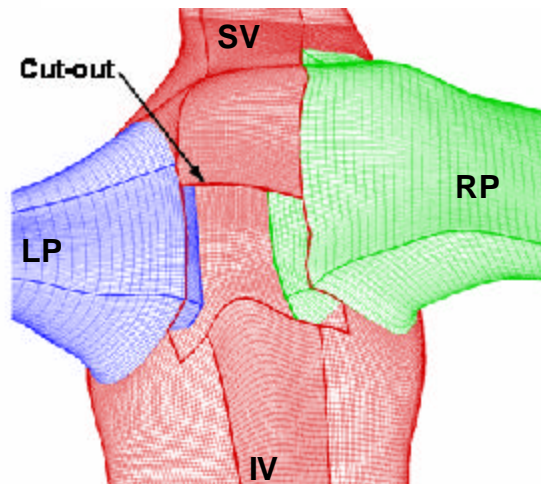


Figure 4.4.3: Typical view of the overset mesh used with the in-house code. A cut-out is provided on the SVC-IVC block surface to show the intersecting LPA and RPA blocks.

4.4.3.4 Boundary conditions

The flow profile and flow rates were specified for both inlets. The handling of the outlets was slightly more complex. Initial outlet flow rates were set to zero. For the following iterations, the computations at time step $n+1$ for the nodes closest to the outlets were carried using the flow information for the outlet nodes at time step n (Figure 4.4.4-a) instead of a fully implicit scheme. The values for the outlet nodes at time step $n+1$ were then obtained by extrapolating those of the neighboring nodes at $n+1$ (Figure 4.4.4-b) and then multiplied by the correction factor Q^* so as to obtain the desired flow split $Q_{Desired}$, where Q^* was computed as follows:

$$Q^* = \frac{Q_{Desired}}{Q_{Extrapolated}} \quad (\text{Equation 4.4.1})$$

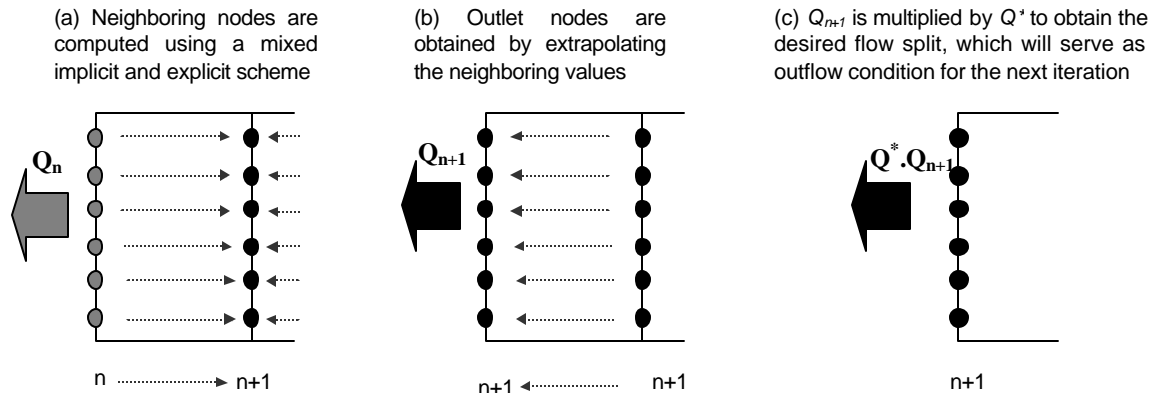


Figure 4.4.4: Outlet flow conditions for the in-house flow solver. Q_n is the outlet flow rate at time step n and Q^* the correction factor computed according to Equation 4.4.1 and applied so as to obtain the desired flow split.

CHAPTER V

METHODS AND PROTOCOLS

This Chapter will cover in turn: (i) the methodology that was developed to manufacture patient specific models of the TCPC, (ii) the protocols used for the acquisition of the experimental data and their processing, (iii) the CFD validation methodology, and, finally, (iv) the different flow conditions under which the experiments and CFD simulations were run. Some sections of this chapter are written with thorough details so as to be used as a user manual.

5.1 Anatomical Model Manufacturing Methodology

5.1.1 Model Construction Overview

As discussed in Chapter II, several studies have already succeeded in generating experimental models that accurately replicate the blood volume of a given vessel. A successful strategy is described by Bale-Glickman et al. [Bale-Glickman, 2003]. In their study, the first step was to obtain a digital representation of the blood volume. It was then manufactured using the stereolithographic technology with a water-soluble resin. The transparent experimental model was then obtained by casting Splygard® around the water-soluble rapid-prototype. This approach is a long and tedious process. The methodology that is described in the following paragraphs was meant to reduce the manufacturing time while keeping the same accuracy as the previously developed techniques.

The overall reconstruction process, going from patient data to the numerical and experimental models, is illustrated by the flow diagram in Figure 5.1.1. In this study MRI scans were the source of patient anatomy information. However this methodology may be generalized to other types of medical imaging.

5.1.2 Patient Data Acquisition

Children who had undergone a Fontan surgery were imaged via MRI. Axial 2D images were acquired covering the whole span of the connection and used for the 3D reconstruction. Sagittal and coronal images (Figure 5.1.2.) improved the segmentation process whenever the anatomy was ambiguous as they provided an extra source of information. Scans were obtained using two different types of pulse sequences. The earlier scans, such as the one that was used for the intra-atrial TCPC, used a spin echo sequence in which blood appears black while other tissues appear as shades of gray (Figure 5.1.2, A to C). Gradient echo sequences, which were used in later in this study for the bilateral SVC, generate images where flowing blood appears white. This provides a much better contrast between fluids and tissues (Figure 5.1.2, A' to C') and is thus more adapted for blood-vessel segmentation.

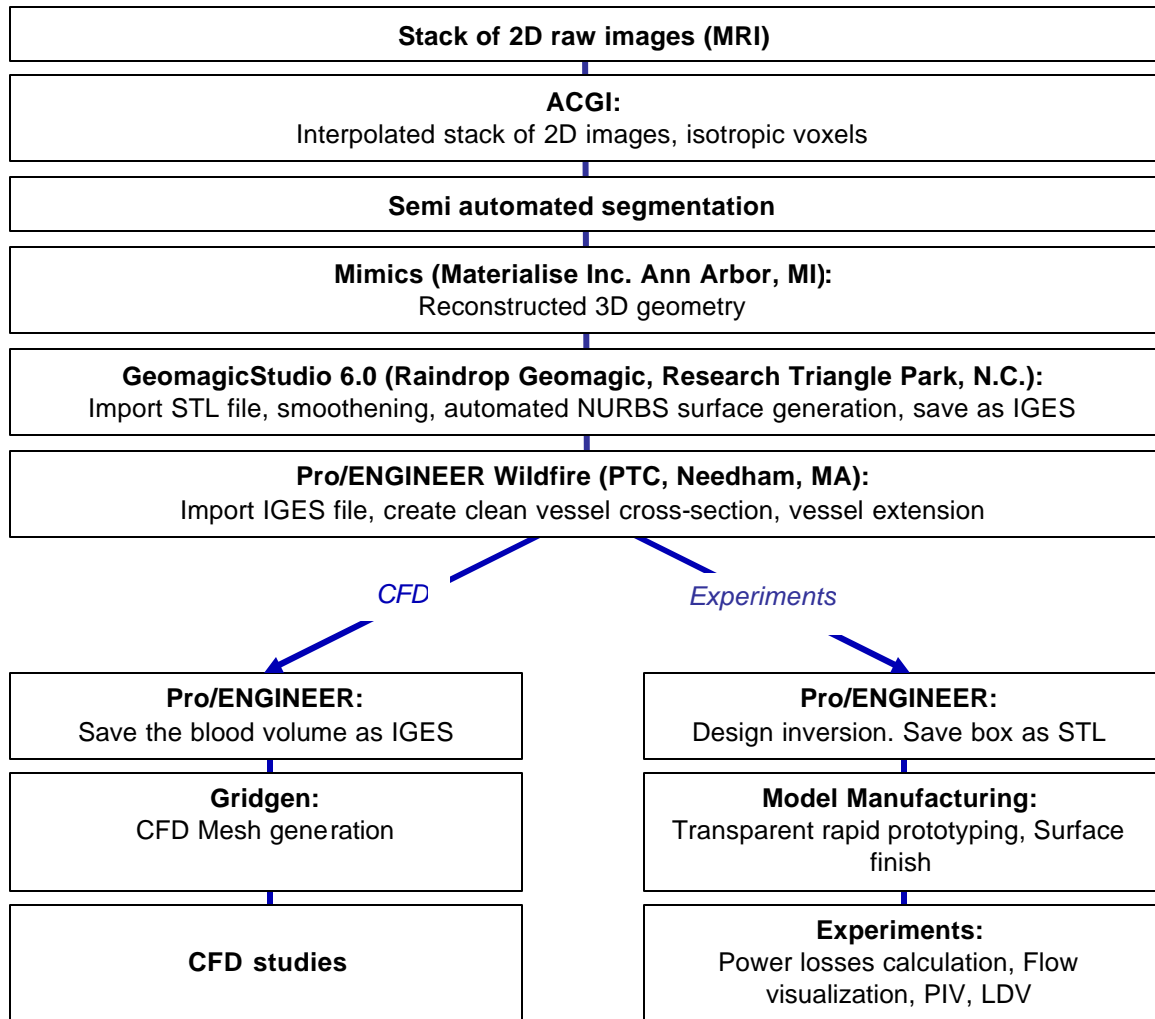


Figure 5.1.1: Work flow of the methodology for anatomical model manufacture.

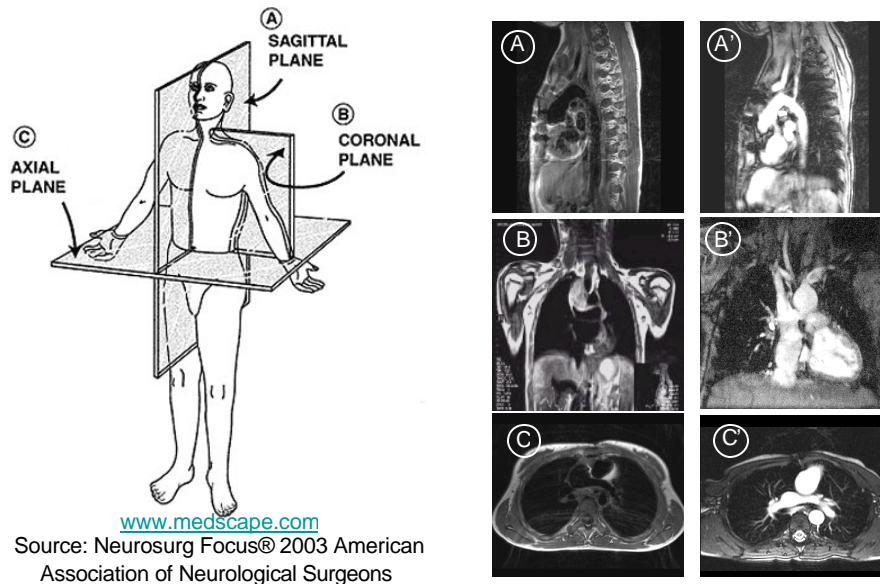


Figure 5.1.2: Orientation of the MRI planes and two series of illustrating MR images. Spin echo images (A to C) offer a high spatial resolution and decreased artifact from biomedical implants. Their clinical use includes cardiac tumors, vessel wall abnormalities. Gradient echo sequences are faster and provide a better contrast between vascular and non-vascular structures (A' to C'). They are typically used to delineate cardiovascular anatomies.

5.1.3 Anatomical Geometry Reconstruction

The spatial resolution of the MRI scans typically ranged from 0.5mm to 1mm, while slice thickness varied from 5mm to 8mm. In order to overcome the out-of-plane sampling limitations, the stack of axial MRI images was enhanced using an adaptive control grid interpolation technique [Frakes, 2003]. The enhanced data set was entirely composed of isotropic voxels. The vessels of interest were segmented from the enhanced data set using a semi-automated in-house code [Frakes, 2003]. A special case of region growing called shape element segmentation was used to isolate the vascular area of interest in multiple image planes with high consistency. The segmented images were then

imported into Mimics (Materialise Inc. Ann Arbor, MI) where the 3D representation of the TCPC was ultimately generated.

5.1.4 Design Inversion

Mimics (Materialise Inc. Ann Arbor, MI) is a reverse engineering tool aimed at medical and industrial applications and was designed to interface between CT or MR imaging and computer aided design (CAD), rapid prototyping, or finite element analysis. The 3D reconstruction generated within Mimics can be exported to the stereolithographic machine shop as STL surfaces, or to numerical simulations as IGES polylines or Point Clouds. In our case, however, an extra step was necessary as the design had to be inverted prior to manufacturing. A major bottleneck was encountered when attempting to export the data from Mimics to a CAD software package to perform the design inversion: IGES polylines can easily be imported into any CAD software package, but they only provide the contour lines of the segmented data set in each plane. STL surfaces on the other hand provide a full 3D representation of the reconstructed anatomy, but are difficult to import. In this study, the two aforementioned pathways were tested; the major steps, advantages and disadvantages of both processes are reviewed in the following sections.

5.1.4.1 Exporting the reconstructed blood volume

a. Using IGES polylines: the intra-atrial TCPC

The first methodology used IGES polylines and was tested on the intra-atrial model. In this model the venae cavae were essentially axially oriented, while the pulmonary arteries were essentially sagittally oriented. Two sets of polylines were

generated from Mimics: one in the axial orientation to accurately reconstruct the venae cavae and the other one in the sagittal orientation for the pulmonary arteries. Both were then imported into I-DEAS 9.0 (EDS, Plano TX). The venae cavae and pulmonary arteries were, respectively, reconstructed using the axial polylines and the sagittal polylines only. A surface was fitted onto the axial and sagittal sets independently, using the “surface swift” option in I-DEAS 9.0. Both volumes were then unified into a single object which was the solid representation of the intra-atrial TCPC and on which further design operations could be performed.

b. Using STL surfaces: the bilateral SVC

STL surfaces were obtained by triangulating the original surface. The accuracy of such a representation depends on the maximal size of the triangles as well as on the tolerance of the curvature, both of which can be manipulated by the user. The two major issues that were faced with STL surfaces were: (i) not all CAD software packages allow for STL data importing; and (ii) most packages consider STL data as a set of disconnected triangles and not as a closed volume. Both of these issues were encountered using I-DEAS and subsequently GeomagicStudio 6.0 (Raindrop Geomagic, Research Triangle Park, N.C.) and Pro/ENGINEER Wildfire (PTC, Needham, MA) were used in this approach.

The major advantages of GeomagicStudio 6.0 were that it creates water-tight NURBS-surfaces in a single user-operation and within a couple minutes. Additionally these may then be exported as either STEP or IGES files, which are both compatible with Pro/ENGINEER Wildfire. GeomagicStudio also allows for basic Boolean operations,

originally designed for reverse engineering applications where only small modifications are needed.

Figure 5.1.3 shows the bilateral SVC at different stages of the process. The STL surface of the reconstructed bilateral SVC was imported from Mimics into GeomagicStudio 6.0. The model was first smoothed in the polygon phase before automatically fitting a NURBS surface in the shape phase. The default settings were used for both operations. This surface was imported into Pro/ENGINEER Wildfire as a STEP file format for the final design operations.

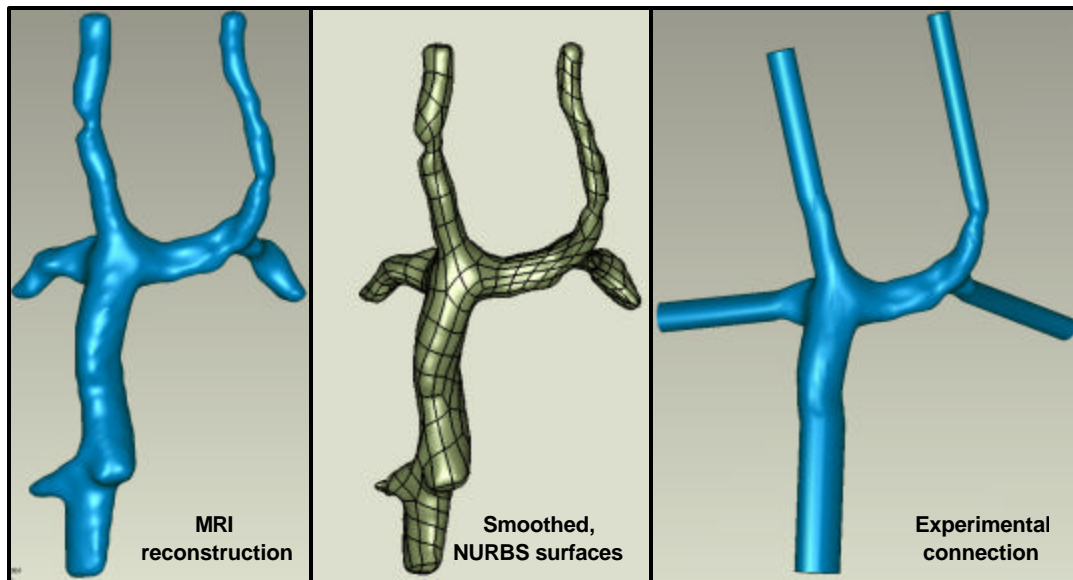


Figure 5.1.3: Anatomical bilateral SVC at different stages of the reconstruction: (a) As was reconstructed in Mimics (Materialise Inc. Ann Arbor, MI); (b) After automatic NURBS surfaces fitting in GeomagicStudio 6.0 (Raindrop Geomagic, Research Triangle Park, NC); (c) After vessel extension in Pro/ENGINEER Wildfire (PTC, Needham, MA).

c. Method comparison

The two methodologies were compared based upon the ease of use and their accuracy. The accuracy was evaluated as the average deviation between the geometry that was reconstructed with Mimics and the one that was finally obtained with either I-DEAS 9.0 or Pro/ENGINEER Wildfire.

Exporting the blood volume as IGES polylines allowed us to overcome the difficulty of importing STL surfaces into CAD software packages. However, while this methodology could be applied to the intra-atrial TCPC, it could not be used as a universal methodology as diverging vessels are not tolerated by the surface fitting operation. This would have become an issue when reconstructing more complex geometries such as a bilateral SVC, interrupted IVC, or a carotid artery bifurcation. Moreover, as is shown in Figure 5.1.4, the standard deviation between the starting and final geometries was 0.7mm, which is relatively poor considering that SVC vessel diameter is only 5mm.

Combined use of GeomagicStudio 6.0 and Pro/ENGINEER Wildfire allowed us to completely circumvent the difficulties first encountered when importing STL files into a CAD software package. This methodology was both fast and accurate. The blood volume was out-putted from Pro/ENGINEER Wildfire in about 10 minutes and the standard deviation from the original file was 0.02mm. This accuracy was more than sufficient for our application as the accuracy of our SLA machines was 0.1mm and the accuracy of the initial reconstruction 0.6mm.

However, as this process was implemented on other TCPC geometries, it became apparent that STEP files were not systematically identified as watertight surfaces once they had been imported into Pro/ENGINEER Wildfire. This problem was overcome

by exporting the files from GeomagicStudio 6.0 to Pro/ENGINEER Wildfire in IGES format. This is the final process, which is summarized in Figure 5.1.1 and worked for all geometries and the accuracy of the geometry was independent of the model complexity.

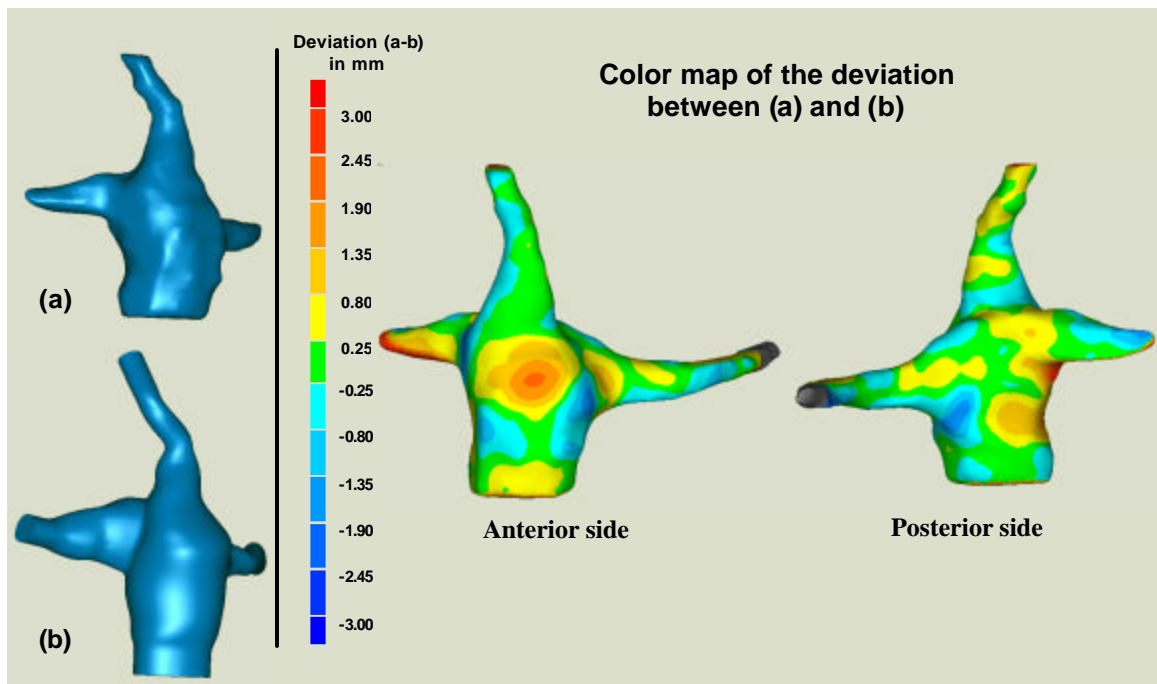


Figure 5.1.4: Comparison of the intra-atrial TCPC at the beginning and at the end of the reverse engineering process. (a) The TCPC as it was reconstructed in Mimics (Materialise Inc. Ann Arbor, MI); (b) the same with vessel extension imported into IDEAS 9.0 (EDS, Plano TX); (c) Color maps of the deviation between the final and original geometries.

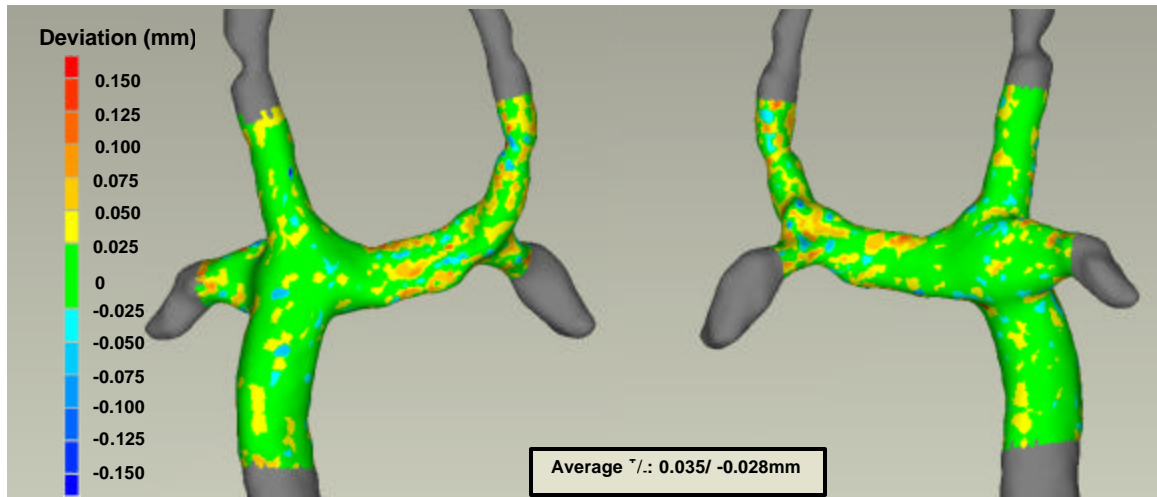


Figure 5.1.5: Quantitative comparison of the final blood flow versus the original reconstruction of the anatomical bilateral SVC. Green regions correspond to the areas where both models overlapped exactly while red and blue regions show higher divergence.

5.1.4.2 Design of the experimental box

Once the TCPC blood volume had been successfully imported into a CAD software package, the design was inverted and the experimental model designed.

First, clean vessel cross-sections were obtained by cutting each of the vessels orthogonally to their axis. These cross-sections were then used as a basis to extrude the PAs and VCs over a distance sufficient for both numerical and experimental purposes. While at this step the extended lumen model could be transferred to grid generation for further numerical studies, the actual experimental model was generated by Boolean subtraction of the extended TCPC lumen from a solid box. The main constraints for box design were to avoid image distortion and laser light scattering when performing PIV. Angled surfaces were moved away from the region of interest. The geometry was

designed to provide outer surfaces facing the camera and the laser that were flat and orthogonal to the desired acquisition and laser beam axes respectively.

Stereolithographic manufacturing techniques generate construction supports under all overhanging surfaces. Thus, had the model been constructed as a single block, supports would have been built throughout the entire blood volume. Though easy to remove, these supports significantly alter the inside surface and would have impaired both the optical quality and the geometrical accuracy of our model. Therefore, the box was split into two parts along the axis of the vessels. Figure 5.1.6 illustrates our recommendations for the design of the different surfaces.

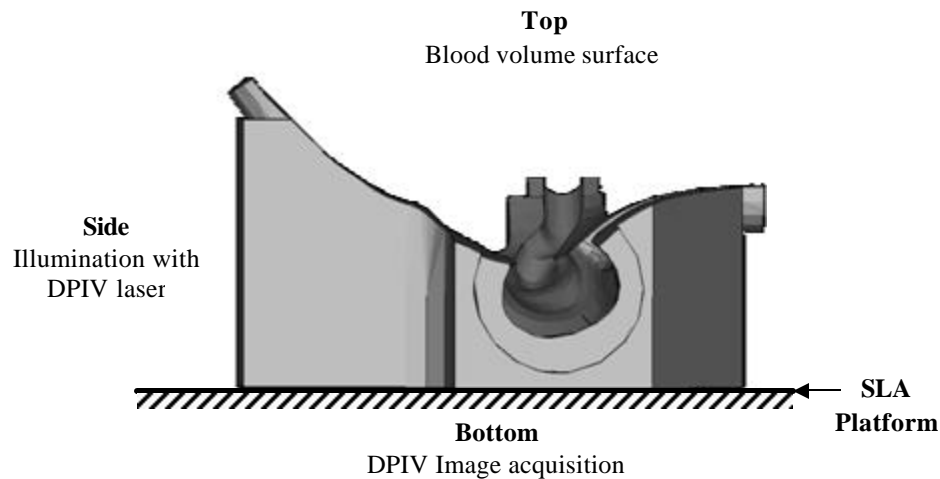


Figure 5.1.6: Model in the SLA machine as the anterior half is being manufactured. Terminology used to describe the orientation of the model (bold). Recommendations for the design and orientation of the model in correlation with the experimental use.

5.1.5 Model Manufacturing

The models were manufactured using stereolithography in a SLA® 250 system, using transparent resins SL 5510 and SL 7510 (Renshape ® Solutions, Cambridge, United Kingdom) for the intra-atrial TCPC and the bilateral SVC models, respectively. The build accuracy was set to 0.004 inches (0.1mm).

As stated previously all three models (the two anatomical models as well the RP 1D-offset reference model, Figure 5.1.6) were built in two halves to avoid the generation of construction supports throughout the entire blood volume during the manufacturing process. This also allowed for the polishing of the inner surfaces. The two halves were glued back together using commercial epoxy glue.

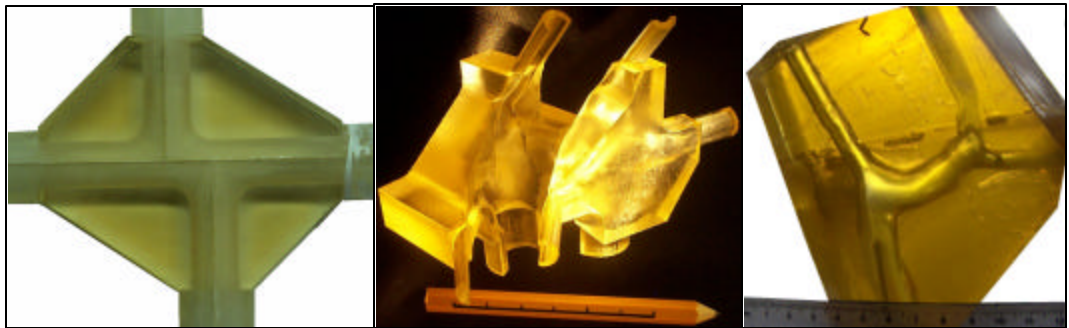


Figure 5.1.6: Rapid prototypes, from left to right: simplified Model 1 (control), anatomical intra-atrial, anatomical bilateral SVC.

In order to preserve the optical quality of the resin, no chemical curing was performed after the build. RP models are manufactured in layers that are deposited from the bottom to the top of the prototype, as it is oriented in the SLA machine, Figure 5.1.6.

Optimal surface quality and transparency is obtained for the top surface and the components were oriented so as to have the inner surfaces (the vessel walls) facing the top. On all other surfaces, the stereolithographic layers generated small ripples that increased the surface roughness and reduced the quality of the images obtained through these surfaces.

These issues were overcome with careful polishing; using wet sandpaper of decreasing grain size (400 followed by 600) and then using coarse (Armor All No.7 Rubbing Compound, The Clorox Company, Oakland, CA) and fine (Armor All No.7 Clearcoat Polishing Compound, The Clorox Company, Oakland, CA) polishing compounds. Any typical polishing compound could be used to perform this task. The surface roughness decreased from $R_a = 10.0 \mu\text{m}$, coming out of the SLA® machine, to $R_a = 0.3 \mu\text{m}$ after polishing.

All the three models presented in this study were polished on the outside, whereas only the anatomical bilateral SVC was polished on the inside. Given the small dimensions of the intra-atrial model (SVC diameter of 4.5mm) geometrical accuracy was prioritized over lower surface roughness and the inner surfaces of the experimental model were left as built. The RP control model was not polished in order to assess the impact of surface roughness on the power losses.

Finally a transparent acrylic paint (Rust Oleum “Gloss Clear 1901”) was sprayed over the outer surfaces of all models to improve optimal transparency. However, slight blurring still remained on the side surfaces that were orthogonal to the SLA platform (see Figure 5.1.6). Therefore, the RP models should be designed to allow the surfaces through which PIV images will be acquired to face the bottom of the SLA

machine. Accordingly the side surfaces will be the ones through which the model will be illuminated (Figure 5.1.6).

5.2 Experimental Methods

5.2.1 Power Losses Calculation

5.2.1.1 Pressure drop measurements

Static pressure measurements were made at the wall of each vessel 10 cm away from the center of the connection in the simplified models and 5 cm away from the original TCPC geometry in the anatomical RP models. Three (four for the bilateral SVC) multiple range pressure transducers (Validyne Engineering Corp. Northridge, model DP15) were used to measure the pressure, referenced to the inferior vena cava, within each branch.

The data were acquired at 500Hz for 10s and averaged to produce a single value for the static pressure. To remove any transducer bias at each flow setting (a given total flow rate and flow splits), the transducers were rotated and measurements performed by each of the differential pressure transducers. Finally to maximize accuracy and ensure repeatability, each experiment was repeated eight times.

5.2.1.2 Statistical treatment

The aforementioned data acquisition methodology yielded 24 pressure measurements per location, for each flow split and flow rate. These were processed in three passes within Microsoft® Excel 2000. Examples of the Microsoft® Excel 2000 spreadsheets are provided in Appendix B.

a. Regional median filtering

The mean and standard deviation of all 24 measurements were computed. In the first pass, all pressure data more than two standard deviations away from the mean were removed and in the second pass, the data were screened for consistency. Within a data set (e.g. first repetition at 1L/min with a 30/70 RPA/LPA flow split, Table 5.2.1), if more than half of the pressure measurements coming from the same transducers (e.g. T1) were detected as outliers in the first pass, the remaining pressure measurements coming from that transducer were removed. Similarly for each repetition (e.g. first repetition at 1L/min), if more than half of the pressure measurements coming from the same transducer and location (e.g. T1, SVC pressure) were detected as outliers in the first pass, the remaining pressure measurements for that transducer and location were removed.

b. Data replacement and interpolation

The third pass aimed at replacing the removed outliers, whenever the remainder of the corresponding dataset was consistent enough to be used. The mean of the filtered pressure measurement was computed for each flow condition. Considering a given data point that had been removed as an outlier in one of the two previous passes, if more than half of the pressure measurements acquired by that same pressure transducer for that data set (e.g. first repetition at 1L/min with a 30/70 RPA/LPA flow split, Table 5.2.1) had not been considered as outliers, the data set was considered valid: The removed outlier was replaced with the filtered average and the corresponding power loss were computed. Otherwise the outlier was not replaced nor the corresponding power loss computed. Table 5.2.1 illustrates the filtering and interpolation process at a given flow rate and flow split.

Table 5.2.1: Filtering and interpolation process illustrated for a given data set (example given: Transducer 1 at 1L/min, 60/40 IVC/SVC, 30/70 RPA/LPA, Repetition 1). Original pressure measurements (P), removed data (-) and average of the pressure measurements remaining after filtering (Ave)

Number of outliers	After 1 st Pass			After 2 nd Pass			After 3 rd Pass			Computing power losses
	SVC	RPA	LPA	SVC	RPA	LPA	SVC	RPA	LPA	
0	P	P	P	P	P	P	P	P	P	Yes
1	-*	P	P	-	P	P	Ave	P	P	Yes
2	-*	-*	P	-	-	P	-	-	P	No
3	-*	-*	-*	-	-	-	-	-	-	No

**Outliers are determined with respect to the mean and standard deviation of the pressure measurements done at 1L/min, 60/40 IVC/SVC, 30/70 RPA/LPA by all three transducers through the eight different repetitions.*

c. Impact on the computed power losses

There was no significant difference in the power losses computed using the aforementioned method and those computed without filtering out any data point, but the standard deviation associated with these computed values was systematically smaller when using the median filtering method. This improvement in the dispersion of the data was especially noticeable when the pressure drops across the models were small. Taking Model 1 as an example, the p-value associated with the difference between the two methods was superior to 0.2 at 2 L/min and superior to 0.6 at higher flow rates, while the standard deviations obtained with the median filtering method were 50% lower than those obtained without filtering at 2 L/min and 10% lower at higher flow rates.

5.2.1.3 Power loss calculation

Both the static pressure, $P_{i\text{ Measured}}$, taken at the wall of each vessel and the volumetric flow rate, Q_i , were used to determine the total power losses associated with the different flow conditions in each one of the TCPC models. Prior to any experiment, differential pressures were acquired with still fluid in the loop (P_{i0}). This P_{i0} value was subtracted from all subsequent pressure measurements so as to remove pressure head bias introduced by small changes in the model elevation. Accordingly, the static pressure drops, $P_{i\text{ Static}}$, used in power loss calculations were calculated using the following formula:

$$P_{i\text{ Static}} = P_{i\text{ Measured}} - P_{i0} \quad (\text{Equation 5.2.1})$$

Using Bernoulli's theorem, the total pressures, $P_{i\text{ Total}}$, were computed as follows:

$$P_{i\text{ Total}} = P_{i\text{ Static}} + P_{i\text{ Kinematic}} = P_{i\text{ Static}} + \frac{1}{2} \mathbf{r} \left(\frac{Q_i}{A_i} \right)^2 \quad (\text{Equation 5.2.2})$$

where \mathbf{r} is the density of the working fluid and A_i the hydraulic diameter at the measurement location.

Power losses, \dot{E}_{Loss} , were then computed by an integrated control volume energy balance:

$$\dot{E}_{\text{Loss}} = \sum_{\text{Inlets}} P_{i\text{ Total}} \cdot Q_i - \sum_{\text{Outlets}} P_{i\text{ Total}} \cdot Q_i \quad (\text{Equation 5.2.3})$$

Throughout this study, the significance of the difference in efficiency between two different TCPC designs is assessed using an unpaired Student t-test. Differences with a p-value inferior to 0.05 were considered significant.

5.2.1.4 Friction loss correction

One additional correction was performed on the differential pressure measurements in the intra-atrial model. For both experimental and CFD studies, only the power losses occurring in the same connection area were considered. However, as we mentioned earlier, experimental pressures were acquired 5 cm away from the original MRI data, they were thus corrected for the extra losses that occurred in the PVC pipes outside the TCPC connection itself.

According to Bernoulli's equation, the energy loss of an incompressible and inviscid fluid in a pipe between two points A and B, $\Delta_{A \rightarrow B} E$, can be expressed as follows:

$$\Delta_{A \rightarrow B} E = \Delta_{A \rightarrow B} (rg \cdot h) + \Delta_{A \rightarrow B} P_{Static} + \Delta_{A \rightarrow B} \left(\frac{rV^2}{2} \right) = 0 \quad (\text{Equation 5.2.4})$$

where g is the gravitational force and h the elevation of the pipe.

The assumptions behind Equation 5.2.4 are that

- 1- The fluid is incompressible
- 2- The fluid is inviscid
- 3- The flow is fully developed

Assumption 1 was the only assumption to really hold in our case. Assumption 2 was obviously incorrect since we used a viscous fluid. Assumption 3 was more than questionable as in the PAs, the flow was not fully developed and unsteady under certain flow conditions. In the VCs, sufficient entrance length was provided upstream of the measurement points for the caval inlet flows to be considered fully developed. Therefore

Assumption 3 holds in the VCs, but not for the outlet flows in the PAs. However the outlet flows never reached fully developed turbulence either and modeling them as such would have been erroneous too. Formulas for fully developed laminar flow provided a satisfying compromise and were used to carry the calculations, despite the limitations aforementioned.

Bernoulli's equation conserves energy. As Assumption 2 did not hold, a viscous dissipation term was added to account for the mechanical energy that is converted into heat in the viscous boundary layer along the pipe walls:

$$\Delta_{A \rightarrow B} E = \Delta_{A \rightarrow B} (\mathbf{r}g \cdot h) + \Delta_{A \rightarrow B} P_{Static} + \Delta_{A \rightarrow B} \left(\frac{\mathbf{r}V^2}{2} \right) + \int_A^B \frac{\lambda}{D(x)} \frac{\mathbf{r}V(x)^2}{2} dx = 0 \text{ (Equation 5.2.5)}$$

where $D(x)$ and $V(x)$ are respectively the diameter of the pipe and the flow velocity at x and λ the friction factor.

Equation 5.2.5 was then simplified according to the following considerations:

1- Since our pressure measurements were corrected for head pressure effect, h was assumed constant along the pipe, therefore:

$$\Delta_{A \rightarrow B} (\mathbf{r}g \cdot h) = 0 \text{ (Equation 5.2.6)}$$

2- As stated in Equation 5.2.2, the static pressure and the kinematic term both contribute to the total pressure P_{Total} :

$$\Delta_{A \rightarrow B} P_{Total} = \Delta_{A \rightarrow B} P_{Static} + \Delta_{A \rightarrow B} \left(\frac{\mathbf{r}V^2}{2} \right) \text{ (Equation 5.2.7)}$$

3- The last term was simplified by assuming we had a fully developed laminar flow in the piping, and that the nominal pipe diameter $D(x)$ was constant:

$$\int_A^B \frac{I}{D(x)} \frac{rV(x)^2}{2} dx = L_{A \rightarrow B} \cdot \frac{I}{D} \cdot \frac{rV^2}{2} \quad (\text{Equation 5.2.8})$$

where I is the friction factor and $L_{A \rightarrow B}$ the algebraic length of the pipe between the two points A and B. $L_{A \rightarrow B} > 0$ if the fluid flows from A to B, and $L_{A \rightarrow B} < 0$ otherwise.

Incorporating these simplifications into Equation 5.2.5, we obtained:

$$\Delta_{A \rightarrow B} P_{Total} = L_{B \rightarrow A} \cdot \frac{I}{D} \cdot \frac{rV^2}{2} \quad (\text{Equation 5.2.9})$$

The friction factor I is both a function of the Reynolds number in the pipe and of the relative roughness. In these flows I is dominated by the Reynolds number term and was obtained analytically according to the formula for laminar flows:

$$I = \frac{64}{Re} \quad (\text{Equation 5.2.10})$$

Finally the corrected pressures, $P_{i \text{ friction}}$ in the power losses computations, were obtained as follows:

$$P_{i \text{ Friction}} = P_{i \text{ Measured}} + L_{Exp.Meas. \rightarrow Anat.Geom.} \cdot \frac{64}{Re \cdot D} \cdot \frac{rV^2}{2} \quad (\text{Equation 5.2.11})$$

where $L_{Exp.Meas. \rightarrow Anat.Geom.}$ is the algebraic distance between the point where the experimental pressures were acquired and the limits of the anatomical model before the vessels were elongated.

As an example, using these equations in the intra-atrial model under the following flow conditions: 1L/min with a 30/70 RPA/LPA flow split and a 5 cm length

extension, we obtained a correction of 0.04mmHg, 0.58mmHg, 0.14mmHg and 1.02mmHg in the IVC, SVC, RPA and LPA respectively. These corrections reduce the computed power loss from 19.8mW down to 17.6mW.

5.2.1.5 Equal pulmonary vascular resistance (EPVR)

Efficiency of the TCPC is obtained over a wide range of operating conditions through pressure and flow rate measurements. In a child, however, the pulmonary flow split may not be imposed. Instead, it is the resistance encountered by the blood flow going to either lung that dictates the pulmonary flow split. The focus of this section is thus to characterize the pulmonary flow split and the corresponding efficiency that would be achieved in a child that would have undergone the TCPC surgery under study.

The physiological pulmonary flow split can be computed for each model at a given cardiac output using the linear Darcy's model. Darcy's law establishes a relationship between pressure drops and total flow rates for steady-state flows going through a porous media. Given the small dimensions of the capillaries, this model is considered valid for capillary lung flows. Therefore:

$$R * Q_{LPA} = P_{LPA} - P_{PV} \quad (\text{Equation 5.2.12})$$

$$R * Q_{RPA} = P_{RPA} - P_{PV} \quad (\text{Equation 5.2.13})$$

where R is the pulmonary vascular resistance assuming it is the same for both lungs, Q_{LPA} and Q_{RPA} are the flow rates through the LPA and the RPA in L/min, and P_{LPA} , P_{RPA} and P_{PV} are the pressures in the LPA, RPA and in the pulmonary venous return referenced to the IVC and expressed in mmHg. Subtracting Equation 5.2.13 from Equation 5.2.12, we obtain the following relation:

$$R * (Q_{LPA} - Q_{RPA}) = P_{LPA} - P_{RPA} \quad (\text{Equation 5.2.14})$$

Pressure differences between the two pulmonary artery branches are known from the experimental measurements as a function of flow split, Q_{RPA} . A linear regression L_1 is fitted to the experimental pressures differences. Thus, the left hand side (LHS) can be computed as a function of flow split for a specific total cardiac output and pulmonary vascular resistance R .

Pulmonary vascular resistance is usually expressed in Wood units, where 1 Wood unit is equal to 1 mmHg/(L/min) and is defined as follows:

$$R = \frac{PAP_{Mean} - PAWP}{CO} \quad (\text{Equation 5.2.15})$$

where PAP_{Mean} and $PAWP$ respectively are the mean pulmonary artery pressure and the pulmonary artery wedge pressure expressed in mmHg while CO is the cardiac output expressed in L/min. A normal baseline for R is usually comprised between 1 and 3 Wood units [Ibrahim, 1995], most studies consider as values lower than 2 Wood units as normal PVR [Fratz, 2003; Wilson, 1997]. An average PVR value of 1.8 Wood units was chosen to conduct our calculations, but a variation in the value retained for R only had a small impact on the EPVR point: in the case displayed in Figure 5.2.1 the EPVR point associated with a PVR of 1, 1.8 and 3 Wood units corresponded to a pulmonary flow split of 59.8/40.2 RPA/LPA, 59.2/40.8 RPA/LPA and 58.4/41.6 RPA/LPA, respectively. These flow split values meaning that a child with an intra-atrial connection such as the one studied here would see about 60% of his blood going to the right lung while only hardly more than 40% went to the left lung.

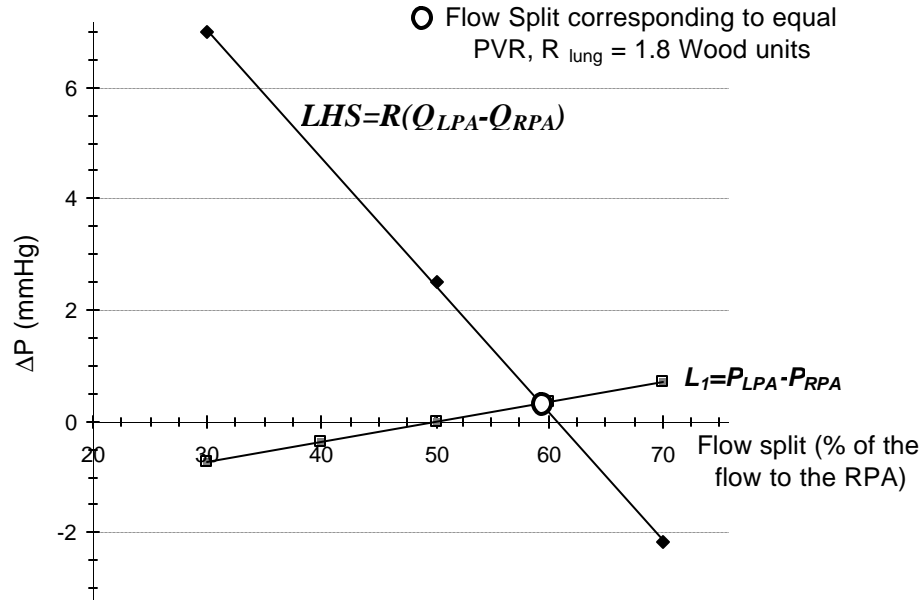


Figure 5.2.1: L_1 and LHS as a function of the pulmonary flow split, in the anatomical intra-atrial model at 1L/min. Visual determination of the EPVR point: L_1 and LHS intersect at the pulmonary flow split corresponding to equal pulmonary vascular resistance $R = 1.8$ Wood unit.

5.2.2 Digital Particle Image Velocimetry (DPIV)

5.2.2.1 Interrogation sites

DPIV measurements were performed both in the intra-atrial TCPC and in the bilateral SVC models. Both models were imaged along the coronal planes. The laser head was positioned 500mm away from the model so that the waist of the laser sheet would fall in the middle of the acquisition plane minimizing the width of the laser sheet. The camera was positioned along the anterior-posterior axis such that the image acquisition plane was orthogonal to the laser sheet minimizing image distortion and associated systematic errors. To achieve perpendicularity, we mounted the laser head, model and

camera on the same rigid structure made out of 80/20 (80/20 Inc., Columbia City, IN). The advantages of using 80/20's product line to build DPIV rigs include the fact that the parts are made out of aluminum which does not corrode, that they are sturdy, easy to clean, and allow the experimenter to quickly and reliably add 80/20 parts or custom material handling devices such as the camera and laser mounts. The model was fixed, while the camera and laser head were mounted on traverse systems so as to accurately locate different imaging planes and maintain the relative orientation of the laser sheet.

Both the intra-atrial TCPC and the bilateral SVC were imaged from the anterior side (Figure 5.2.2 and Figure 5.2.4). Because of its small dimensions, the entire span of the intra-atrial TCPC was contained within a single image. Six different planes were imaged along the posterior-anterior axis, as shown in Figure 5.2.3. The outer surface on the anterior side of the model was used as a reference. The first acquisition plane was taken at 5mm and the last one at 18mm.

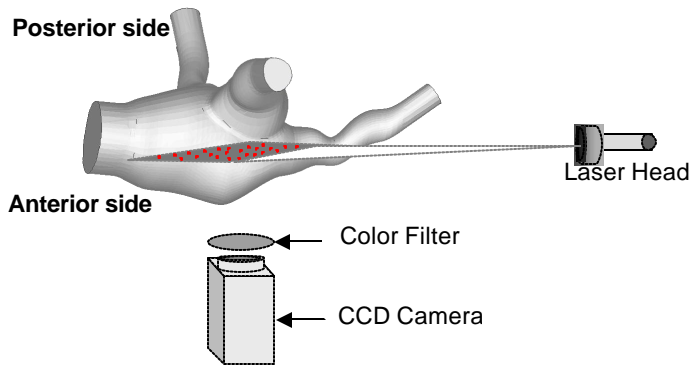


Figure 5.2.2: DPIV set-up for the intra-atrial TCPC. The DPIV images were acquired from the anterior side while the laser was located on the right side.

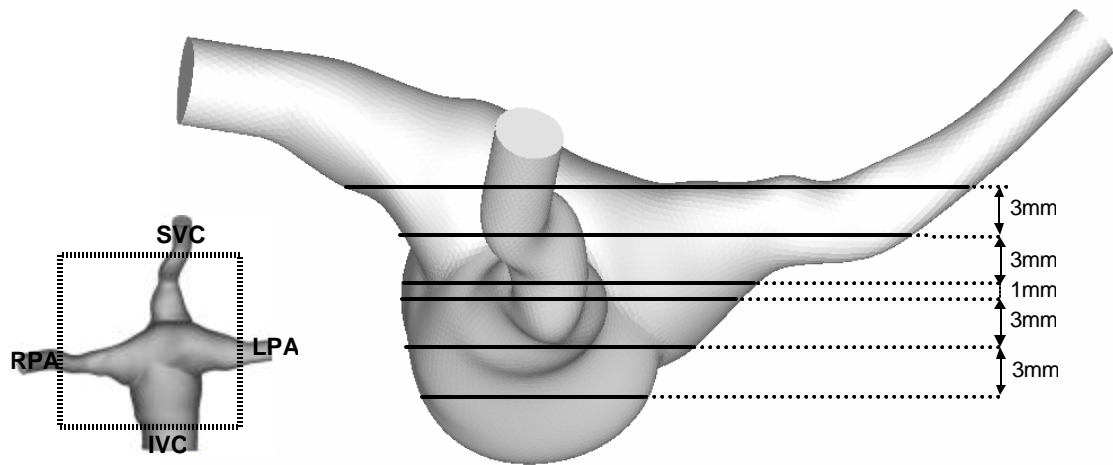


Figure 5.2.3: DPIV interrogation planes viewed from the top (Right). The domain that was imaged is highlighted on the posterior view (Left).

The bilateral SVC was much larger than the intra-atrial TCPC; imaging the whole connection decreased the spatial resolution. Additionally, the lasers were only just powerful enough to illuminate the whole model. Therefore the connection was imaged first as a single image and then split into three different regions, focusing on each of the venae cavae, that were imaged independently. Figure 5.2.4 shows the general DPIV set-up for the bilateral SVC, while Figures 5.2.5 to 5.2.7 display the location of the different interrogation regions and the number of planes that were acquired at each location along the anterior-posterior axis.

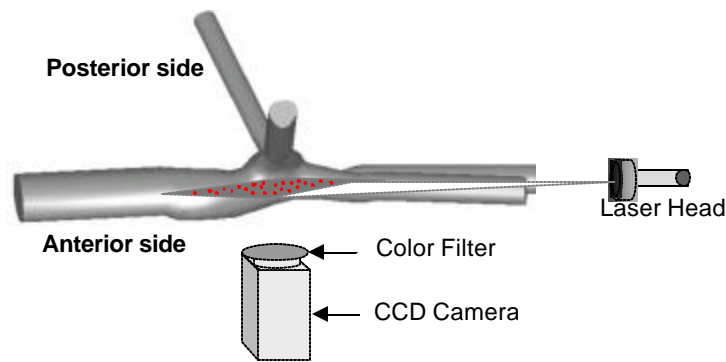


Figure 5.2.4: General DPIV set-up for the bilateral SVC. The DPIV images were acquired from the anterior side while the laser shot from the left or the right side of the model.

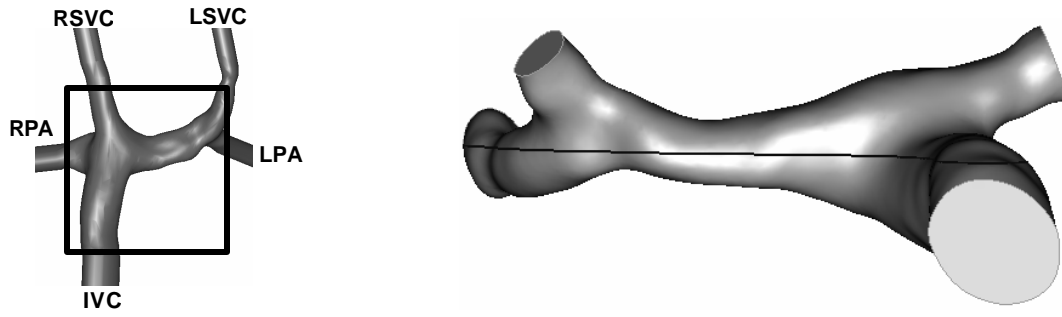


Figure 5.2.5: DPIV interrogation sites for the anatomical bilateral SVC. The whole domain was imaged at once for one single plane.

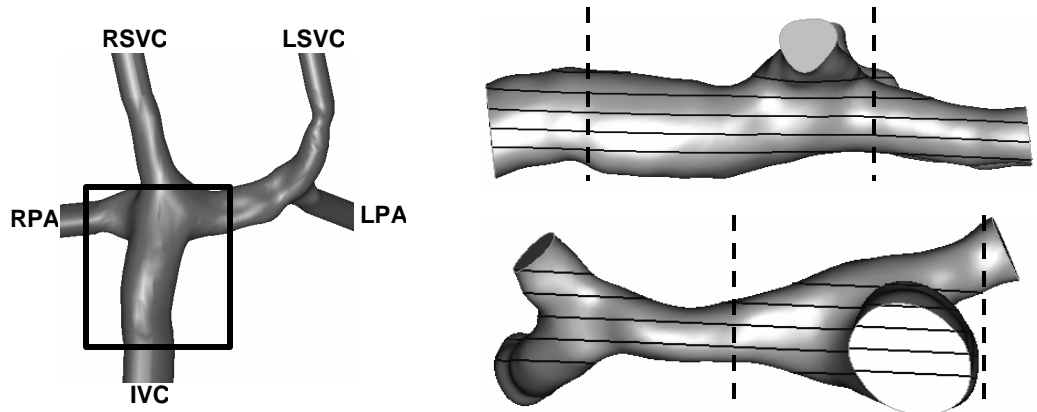


Figure 5.2.6: DPIV interrogation sites for the anatomical bilateral SVC, focusing on the IVC flow. 5 planes separated by 2.5mm were imaged throughout the IVC.

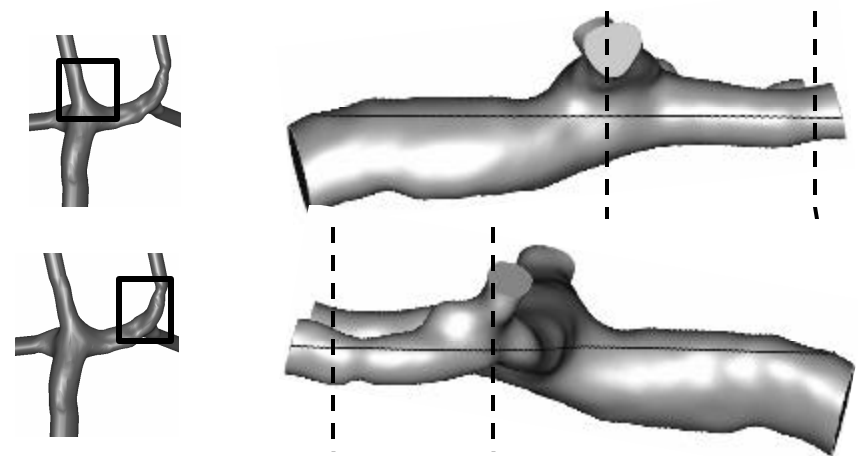


Figure 5.2.7: DPIV interrogation sites for the anatomical bilateral SVC, focusing on the RSVC and LSVC flow. Solely the median plane was imaged in the SVCs.

5.2.2.2 Validation of the DPIV measurements in transparent RP models

In addition to the anatomical models, DPIV was also performed on a straight pipe made out of the rapid-prototyping resin. This served as a validation study to check if the background noise that was observed in all RP models, affected the accuracy of the cross-correlation as well as the identification of the internal surfaces, which was used when calibrating the cameras (see Section 5.2.2.3). In order to conduct the spatial calibration, the pipe was made large enough for a calibration target to be conveniently inserted. The calibration target, a metal ruler, was located inside the tube coincident with the acquisition plane. The model was then filled with the working fluid and images of the ruler were acquired using the standard acquisition techniques.

DPIV measurements were made along the central plane of the pipe and validated against both total flow rate measurements and LDV point measurements. The LDV measurements were taken at the center of the pipe and the total flow rate measurements were obtained with a transonic flow probe. As is discussed further in the Results and Discussion chapters, this validation study demonstrated that accurate DPIV results could be obtained in RP models despite the background noise.

5.2.2.3 Parameters for data acquisition

a. Image calibration

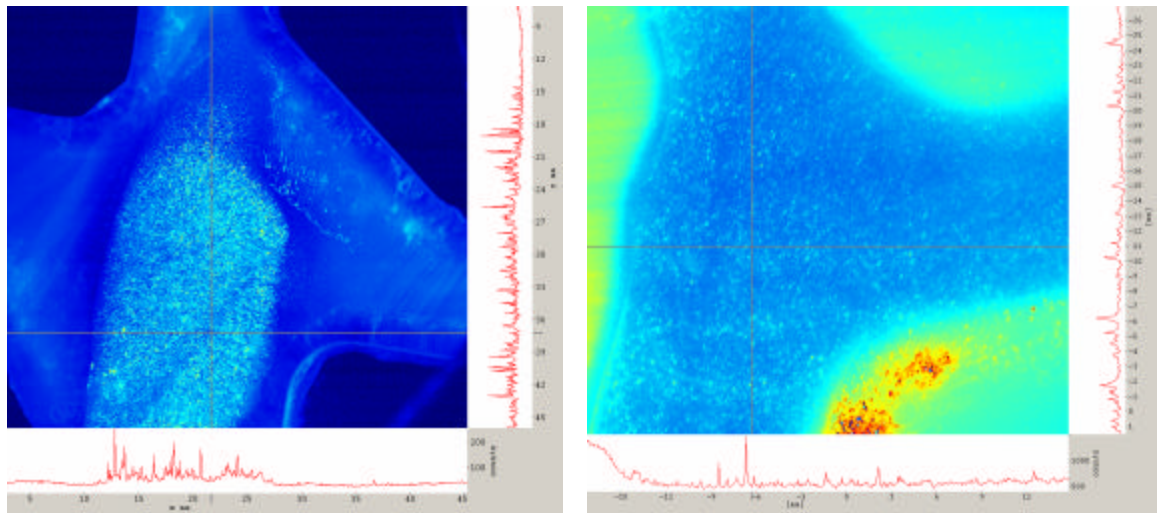
The DPIV images were scaled for each acquisition plane using a simple two-point calibration. A known dimension of the model (usually a vessel diameter) was chosen as a reference. This technique has shown a great accuracy when used with acrylic models where the walls of the model, and subsequently the diameter of the model, can

very be very clearly identified. In our RP models the background noise was much higher and the exact location of the walls was not as clear. A series of diameter measurements was thus taken and the average distance in pixels vs. the actual distance in mm was used to compute the scaling factor.

b. Illumination of the test section

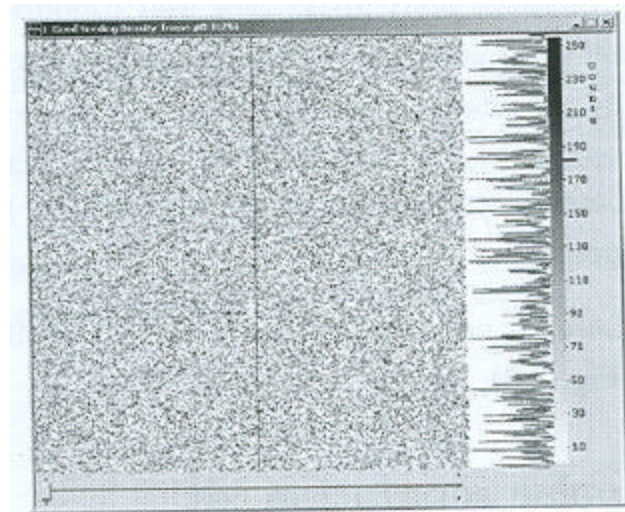
Laser power and camera aperture were adjusted to avoid CCD chip saturation and optimize the image contrast. The satisfying settings were determined based on the image intensity profiles, Figure 5.2.8. In order to minimize the laser light reflections on the model, a color filter ($\lambda=570 \text{ nm}$) was used to cut off the internal reflections of the laser beam ($\lambda=532 \text{ nm}$) on the model while still allowing the light refracted by the fluorescent particles ($\lambda_{\text{emission}} = \text{nm}$) to shine through.

Nd:Yag lasers require two signals to create a laser pulse; the first one triggers the flash lamp and the second one opens the Q-switch that pulses the laser. In DaVis 6.2.2 (LaVision GmbH, Goettingen, Germany), the default values for Q-switch delays are $186\mu\text{s}$ for the maximal power and $400\mu\text{s}$ for the minimal power. In our set-up, both lasers contained very similar energy, controlling the camera aperture and changing the percentage of laser power in use by the same amount for both lasers should thus have been sufficient to obtain the optimal settings. However one of the laser beams was not Gaussian, resulting in increased clipping losses and uneven light sheet. Therefore the Q-switch delays were manipulated individually to obtain similar illumination from the two lasers, and the aperture of the camera and the % of laser power in use were adjusted next.



(a) Intra-Atrial

(b) Bilateral SVC



(c) Sample Data from

Figure 5.2.8: Typical DPIV images and intensity profiles obtained in the anatomical intra-atrial model (a) and in the bilateral SVC (b). As a ground of comparison Figure (c) shows the optimal seeding and contrast recommended in the DPIV manual (LaVision GmbH, Goettingen, Germany). Such a quality could not be achieved in the RP models.

c. Optimal δt and number of frames

Test-images were acquired and processed using a single-pass standard correlation with a window size of 32×32 pixels so as to optimize the separation time between two consecutive frames, δt . The results were displayed as displacements in pixels and the best-suited δt was considered to be the one when the mean displacement was about 5 to 7 pixels, with a reasonably smooth field.

300 double-frame images were acquired for each location and flow condition. As is shown in Figure 5.2.9, the variation between the average velocity magnitudes obtained with 200 and with 300 frames was less than 5% and the variation between 250 and 300 frames was less than 2.5%. It was thus considered that sufficient convergence of the average was achieved with 300 frames. Moreover when acquiring more than 300 double frames (which could have been possible) storage becomes a serious issue. Thus the sample size of 300 was tradeoff between improved accuracy and storage space.

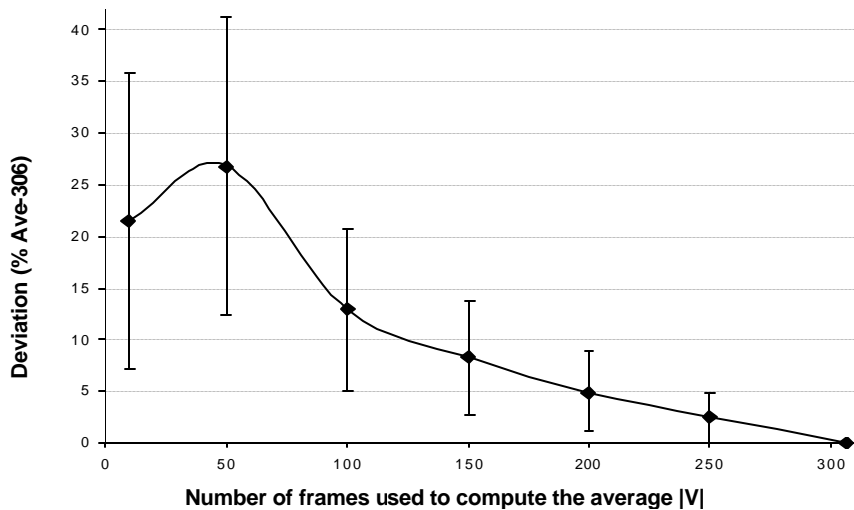


Figure 5.2.9: Convergence of the DPIV measurements

5.2.2.4 Vector calculation

a. Processing algorithm

The data were processed using DaVis 6.2 (LaVision GmbH, Goettingen, Germany). This software uses a central differential scheme, which is accurate to the order $(\Delta t)^2$ [Wereley, 2001]. The velocity at time t is computed using particle images at time $t - \Delta t/2$ and $t + \Delta t/2$:

$$V(t) = \left. \frac{dX}{dt} \right|_{t=t} = \frac{X(t + \Delta t/2) - X(t - \Delta t/2)}{\Delta t} + \frac{(\Delta t)^2}{24} \left. \frac{d^3 X}{dt^3} \right|_{t=t} + \dots \text{(Equation 5.2.16)}$$

Two correlation functions can be used within DaVis 6.2 (LaVision GmbH, Goettingen, Germany) to compute the particle image displacement: the standard and the normalized correlation. The standard algorithm is 5 times faster than the normalized one, but biases the displacements towards a (0,0) displacement. The normalized correlation on the other hand induces no zero-displacement bias, and will effectively compensate for varying background intensities and signal density, but is far slower.

In this study we used the standard correlation function with multiple iterations and decreasing interrogation window size. When performing a multi-pass correlation, the algorithm uses the information of the previous pass (Velocity vectors: $V_N(x)$), to compute the current vector field (Velocity vectors: $V_{N+1}(x)$). The velocity vector V_{N+1} in $X(t)$ is computed using the central differencing scheme, where the position $X(t - \Delta t/2)$ is obtained by shifting the first interrogation window by $-V_N(x)/2$ and $X(t + \Delta t/2)$ by shifting the second interrogation window by $+V_N(x)/2$. This iterative process ensures that the same particles are correlated with each other, even if the interrogation window is smaller than the maximal displacement. This allows for increased spatial resolution. Additionally after

the initial pass, the cross-correlation only calculates the velocity fluctuations around the mean value from the previous passes. The magnitude of these fluctuations should be small. The zero-displacement bias of the standard correlation function now acts in our favor by filtering out the large, and most likely erroneous, fluctuations.

b. Interrogation window size

The rules of thumb for choosing the appropriate window size for a single-pass correlation [Keane, 1990] are that:

- ❑ The final interrogation window should be the smallest possible to resolve small flow structures and to ensure that the average velocity in each window properly represents the motion of the particles throughout the entire interrogation spot.
- ❑ Each interrogation window should contain more than 10 particle images.
- ❑ The window size should be at least 4 times the maximum particle image displacement.

When using a multi-pass cross-correlation these conditions translate into:

- ❑ The starting window size (typically 32*32 or 64*64 pixels) should be larger than 4 times the maximum particle image displacement
- ❑ The final interrogation window (typically 16*16 pixels) should be larger than 4 times the velocity fluctuations around the mean velocity, and contain more than 10 particles.

The size of the starting interrogation window and the choice for δt are thus closely linked, while the final interrogation window relates to the density of the flow seeding as well as to the dispersion of the velocity vectors.

In this study, all the images were processed going from an initial window size of 32*32 pixels down to a 16*16 pixels window with a 50% window overlap to satisfy the Nyquist sampling limit.

c. Mask

A mask corresponding to the solid boundary of the model was defined for each different plane and applied to the images before the cross-correlation. This reduced the processing time by avoiding the calculation of spurious vectors outside the blood volume.

d. Vector post-processing

Validity checks and post-processing techniques can be used at each step of the vector calculation: on each correlation window, on the intermediate vector field, on the final vector field.

Multi-pass post processing

The intermediate passes in the DPIV correlation are used as reference vector fields for the subsequent correlations. Thus, if spurious vectors are not removed in the intermediate passes, the error will propagate to the following correlations with smaller interrogation windows as the right particles are not matched anymore. The intermediate vector fields were screened for outliers using the regional median filter setting in DaVis 6.2.2 “strongly remove and iteratively replace”. This median filter functions in four passes:

1. First, the average and standard deviation of its eight neighbors are computed for every vector in the flow field. If a vector falls more than a certain number (2 in this study) of standard deviations away from the computed mean, it is considered as an outlier and is removed.

2. The second pass eliminates all vectors that do not have a certain number (typically between 3 and 8) of valid neighboring vectors.
3. The third pass looks to replace as many of the removed vectors as possible. Since all spurious vectors should have been removed, the deviation around the average of remaining neighbors should be smaller than in pass 1; the insertion criteria may thus be looser than the removal one and was set to 3 standard deviations for this study. For all locations, the four first correlation peaks are stored in a buffer. If the first correlation peak does not satisfy the median criteria, the other three highest correlation peaks are checked.
4. The fourth pass finally throws away any group with less than 3 vectors, which effectively removes small groups of spurious vectors that have not been detected in passes 1 or 2.

Finally a smoothing function (1*Smooth 3*3) was used to fill up all the empty spaces with the average of the neighboring vectors.

Final vector field post-processing

In order to preserve the final results, no extra post-processing was performed after the final pass. The currently active mask was applied again for a nicer image display.

5.2.2.5 Summary of the acquisition and processing parameters used for this study

Table 5.2.3: Summary of the acquisition and processing parameters used for this study

Acquisition parameters	<ul style="list-style-type: none"> • 300 double-frame images • δt tested for each flow condition and acquisition plane, Table 5.2.1 and Table 5.2.2
Image Preprocessing	<ul style="list-style-type: none"> • None
Vector Calculation parameter	<ul style="list-style-type: none"> • User defined mask • Standard I1*I2 cross-correlation function with multi-pass processing with decreasing window size and 50% window overlap • No image correction • Camera calibration set prior to data processing, vectors displayed in m/s
Initial Reference vector Field	<ul style="list-style-type: none"> • No initial reference vector field, nor constant window shift • No restrictions on the vector range and position
Correlation function	<ul style="list-style-type: none"> • Standard I1*I2 for all passes • None of the other options was selected
Multi-pass Post-processing	<ul style="list-style-type: none"> • Median filter: strongly remove and iteratively replace • Remove if $> 2r_{ms}$ and insert if $< 3 r_{ms}$ of neighbors
Vector Post-processing	<ul style="list-style-type: none"> • Apply currently active mask

5.2.3 Laser Doppler Velocimetry

5.2.3.1 Interrogation sites

A cross-section of each vessel of the intra-atrial model was selected, see Figure 5.2.10. The cross-sectional area of two venae cavae was mapped using 2D or 1D LDV depending on the beam coincidence. Because of the high curvature of the vessels, LDV measurements were only performed along the centerline of the two PAs. Figure 5.2.10 shows the location of the four cross-sections within the model, and the LDV mapping. To map the measurement locations for each cross-section, the LDV probe was first located in what was a rough estimate of the center of the cross-section. This point was used as a reference. In order to locate the reference point properly, the LDV probe was then moved in the anterior-posterior directions until the anterior and posterior walls had been located (points where the data acquisition rate was null even in 1D). The same thing was then done with the left and right walls (for the caval cross sections) or the superior and inferior walls (for the pulmonary cross-sections).

5.2.3.2 Data acquisition

Because of the optical limitations of the model, only 2D or 1D LDV measurements were performed. The blue and green laser beams were coupled within the two-component transceiver. The transceiver was positioned on the anterior side of the model when scanning the venae cavae and on the posterior side of the model for the pulmonary arteries. The transceivers were also coupled to the receiver, and were thus used in the backscatter position.

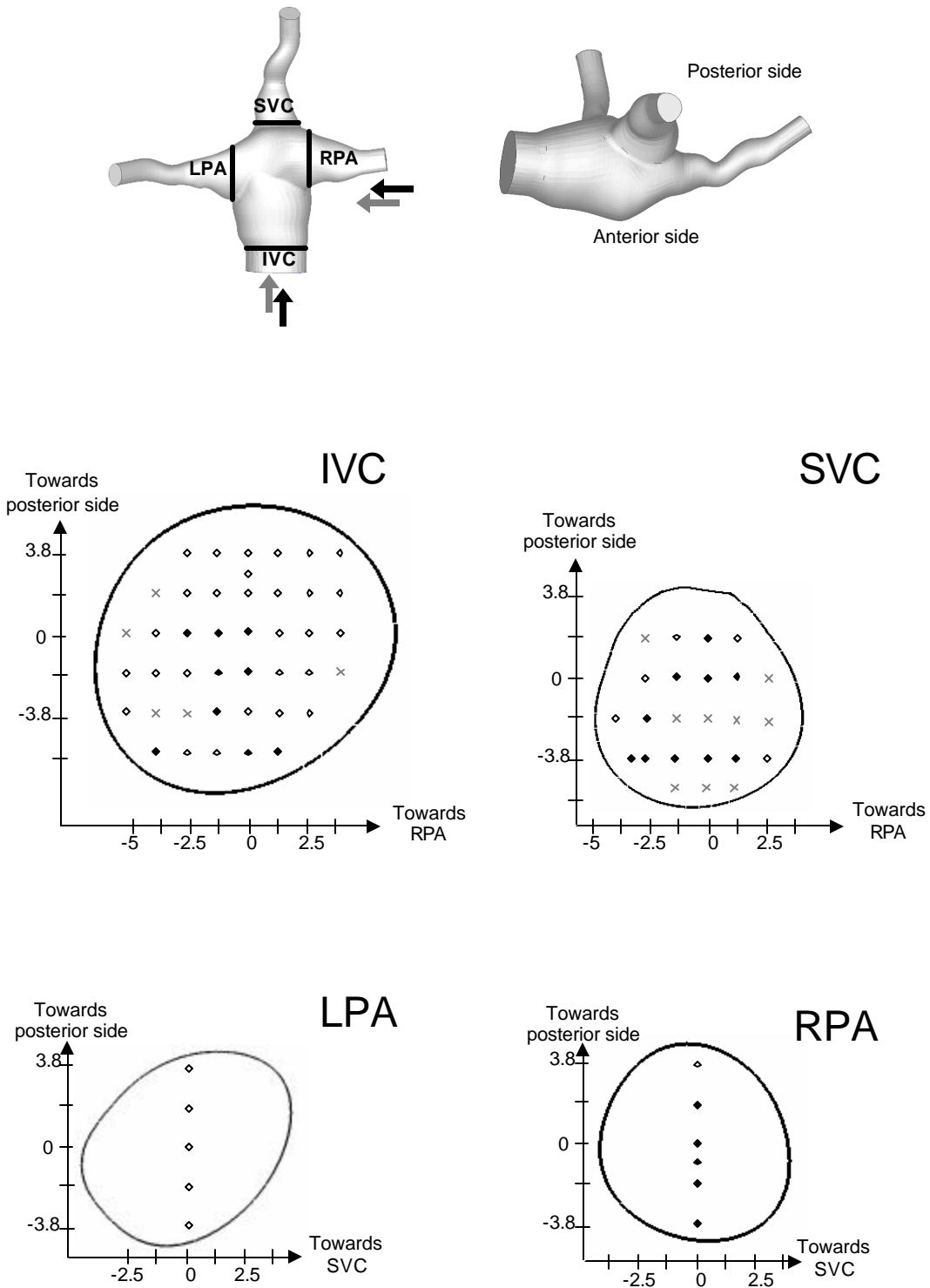


Figure 5.2.10: LDV interrogation sites for the anatomical intra-atrial model. The arrows show the direction from which the PA and VC cross-sections were viewed. \diamond : data acquired in 1D, $?$: data acquired in 2D, \times : rejected data (data acquisition rate under 0.5Hz). All the distances are given in mm.

In all of the experiments, measurements were acquired in coincident mode. In order for a Doppler burst to be recorded as a valid data point in coincident mode, it must be received by both channels at the same time. In addition to these data, the gate-time, which is the time needed by a particle to fly through the LDV probe volume (Figure 5.2.11), was recorded for each particle. The minimum signal to noise ratio was set to 65%. Additionally, to ensure that all velocity components were acquired simultaneously for each measurement, the gate scale was set at 1. This meant that two individual Doppler pulses, detected one by the first probe and one by the second probe, had to be less than one gate time apart to be considered as coincident and be recorded. The rate at which the LDV probe scanned for particles was set to 5 MHz.

At each location, a minimum of 500 points was acquired for statistical significance. If the data-sampling rate was particularly low, a minimum of 200 points was acquired to ensure the statistical significance of the computed average.

5.2.3.3 Data processing

The data were processed using an ensemble averaging method [Simon, 2004]. This method involved weighting individual measurements with the particle gate-time, calculating the statistics of the measurement population, filtering outliers, and calculating the each velocity component according to the following formula:

$$\overline{u_M} = \left(\frac{\sum_{i=1}^N u_{M i} G_{M i}}{\sum_{i=1}^N G_{M i}} \right)_{filtered} \quad (\text{Equation 5.2.16})$$

Where N is the total number of points acquired at the location M that fulfilled the statistical filtering conditions, u_{Mj} is the instantaneous velocity at the location M and G_{Mi} is the gate-time associated with velocity u_{Mi} .

The velocity magnitude was then obtained by:

$$\bar{V}_M = \sqrt{(\bar{u}_M)^2 + (\bar{v}_M)^2} \quad (\text{Equation 5.2.17})$$

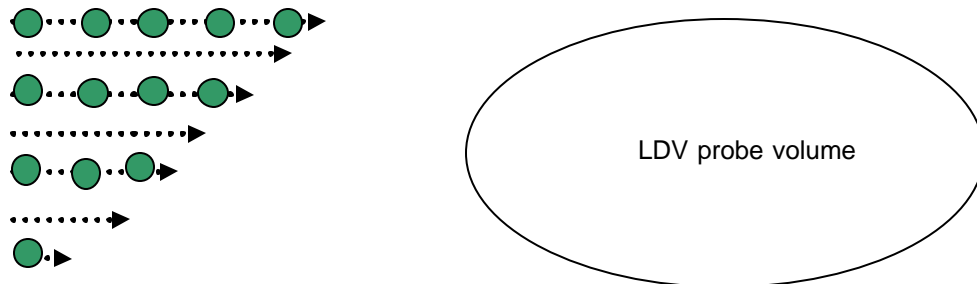


Figure 5.2.11: [Simon, 2004] Velocity bias in LDV measurements. Arrows indicate velocity magnitude. The particles at the bottom of the probe volume flow slower than those at the top, there will thus be fewer of them flowing across the probe volume in a given acquisition time, and more of the faster ones. On the other hand the slower particles will take longer to flow across the probe volume (longer gate-time). Weighing the measured velocities by the gate-time is thus a way to remove the velocity bias.

5.3 CFD Validation Methodology

CFD simulations of the different TCPC geometries were compared to their experimental counterpart for validation. The simulations were run under conditions similar to the experiments using incompressible viscous fluid, rigid walls and identical flow splits. The boundary conditions for CFD used steady, laminar and fully developed inlet flows and constant pressure for the outlets. The purpose of this validation was to determine the most appropriate and cost-effective CFD tool depending on the parameter of interest. Three different levels of accuracy were considered:

- The time averaged power loss calculated over the connection control volume
- The time-averaged velocity field
- The instantaneous velocity field

5.3.1 Control Volume Power Losses

In the simplified models 1 to 4, the experimental and CFD control volumes used to compute the power losses both extended 10cm from the center of the connection. For the anatomical intra-atrial model, we only considered the losses occurring within the original geometry. As described in Section 5.2.1.4, the experimental pressure drops were acquired 5cm up- and down- stream of the connection geometry and were corrected for extra tubing length prior to comparison.

5.3.2 Average Flow Field

The CFD and DPIV results were both imported into Tecplot 9.0 (Tecplot Inc., Bellevue, WA) for comparison. DPIV provided quantitative planar 2D flow information. Since the exact frequency of the DPIV data acquisition was unknown, only the average flow fields were used for validation and compared to time-averaged CFD results. CFD results provided 3D velocity information over the entire blood volume. Six CFD planes were extracted from the whole 3D velocity field corresponding to the orientation and height of the six DPIV acquisition planes as described in Table 5.3.1. Since the thickness of the laser beam was of about 1mm, the CFD planes that were retained for comparison were chosen within 0.5mm of the theoretical location. The CFD velocity vectors were projected on the DPIV acquisition planes and the in-plane components were finally compared to the 2D DPIV measurements.

Table 5.3.1: Height of DPIV acquisition planes and coordinates of the corresponding CFD planes.

CFD (coordinates given for the Tecplot files)		DPIV
Plane Normal	Intercept Y = 0.0273; Z = 0.0536	Laser height (mm)
X=- 0.9952 Y= 0.0965 Z= 0.0173	X = 0.0035	5.0
	X = 0.0065	8.0
	X = 0.0095	11.0
	X = 0.0105	12.0
	X = 0.0135	15.0
	X = 0.0165	18.0

5.4 Experimental Flow Conditions

5.4.1 Experimental Flow Measurements

For all experiments the flow rates going through the vessels were measured using rotameters and controlled with a series of ball valves. The original calibration curve for the rotameters, provided by the manufacturer, was obtained in water, which is less dense than the fluids used in these experiments. Thus, all the rotameters were recalibrated with water/glycerin and water/glycerin/NaI using a stopwatch method. At a given flow rate, the fluid was collected in a bucket over a period T , timed with a stopwatch. The volume of collected fluid, V , was measured using a glass beaker. The true flow rate, $Q_{Measure}$, was then determined using the regular formula:

$$Q_{Measure} = \frac{V}{T} \quad (\text{Equation 5.4.1})$$

Five different flow rates were tested throughout the range of each rotameter. For each flow rate, the reading on the rotameter was compared to the average of five stopwatch measurements. The trend was linear for all flowmeters ($R^2 > 0.98$).

5.4.2 Motivation for the Tested Flow Conditions

5.4.2.1 Total flow rate

The flow conditions for each TCPC model were chosen to be representative of the physiologic *in vivo* conditions, as well as to provide a comparison with previous *in vitro* studies on similar models. The average cardiac output of an infant is 2L/min at rest and may rise up to 4L/min during exercise [Guyton, 1997]. This range shifts towards higher flow rates as the child grows and the average cardiac out-put of an adult is 4L/min

increasing to 6L/min during active exercise. However, patients who have undergone a Fontan surgery can only sustain limited exercise and are unlikely to achieve typical exercise cardiac outputs.

The higher cardiac outputs of 6L/min were still simulated in the simplified glass models to provide additional comparison between the models. If a general trend between the glass models can be seen at lower flow rates, then typically the differences are amplified as the flow rate increases.

For the bilateral SVC, the experimental flow rates were based upon the *in vivo* flow measurements acquired in the MRI scanner. The child had a 2L/min cardiac output with 1.1L/min coming through the IVC and 0.45L/min through both venae cavae. Since those flow conditions were that of the child sedated in the MRI scanner, additional runs simulating exercise conditions were performed at 3 and 4L/min, with the same flow splits.

For the intra-atrial TCPC no MRI velocity data were acquired. However, given the high resistances that were observed both experimentally and numerically, even at flow rates as low as 1L/min, flow rates above 3L/min were considered unrealistic. The intra-atrial TCPC was thus tested for 1, 2 and 3L/min only. Model 6, whose design was the closest to the intra-atrial TCPC, also demonstrated high resistance and was run at the same flow rates as the intra-atrial TCPC. The design of Model 5 was intermediate between the simplified geometries and Model 6. It was run at flow rates, ranging from 1 to 6 L/min, so as to enable the comparison with the glass models.

5.4.2.2 Caval flow ratio

Previous investigations [Salim, 1995] argue that the caval flow ratio varies with age, going from 50/50 IVC/SVC in an infant, to typical ratios of 60/40 IVC/SVC in adults and children older than 6.6 year-old (although ratios of 75/25 have been observed in adults). This average 60/40 value was used for all the glass models as well as for the anatomical intra-atrial model. The child whose intra-atrial connection was modeled was 13 years old; as no other information was available, a 60/40 IVC/SVC was estimated to be a reasonable caval flow split for a 13 years-old child. For the bilateral SVC, the caval flow split was based on the *in vivo* data from the MR scanner with 55% of the total flow going to the IVC and 22.5% to each one of the SVCs.

5.4.2.3 Pulmonary flow ratio

Pulmonary flow ratio is dependent upon activity, health, left and right lung morphologies and is thus highly variable. As a consequence, a wide range of pulmonary flow ratios was tested for each model, going from 70/30 to 30/70 RPA/LPA by 10% increments. At 1L/min the pulmonary flow ratio was varied by 20% increments because 0.1L/min, a 10% increment, was close to the resolution of our rotameters.

5.4.3 Experimental and Numerical Flow Settings

Pressure drops and the subsequent power loss calculations were performed for all the flow conditions described above. Other experimental techniques were used over a smaller range of flow conditions either because they were qualitative (such as the flow visualization) and were thus only mildly affected by changes in the flow rates; or because

they were very time consuming (LDV and PIV). Tables 5.4.1 to 5.4.7 give the flow conditions that were tested in each model.

5.4.3.1 Pressure drop measurements

Table 5.4.1: Flow rates at which the pressure drops measurements and the subsequent power loss calculations were conducted. For each total flow rate, the pulmonary and caval flow ratios were varied according to Table 5.4.2.

		Tested Cardiac output (L/min)					
		1	2	3	4	5	6
Simplified Models	Design 1 Glass & RP, 2, 3, 4		v		v		v
	Design 5	v	v	v	v		v
	Design 6	v	v	v			
Intra-atrial TCPC		v	v	v			
Bilateral SVC			v	v	v		

Table 5.4.2: Pulmonary and caval flow ratios at which the pressure drops measurements and power loss calculations were conducted for each total flow rate (Table 5.4.1)

		Flow Splits	
		IVC/SVC	LPA/RPA
Simplified Models	Design 1 Glass & RP, 2, 3, 4	60/40	30/70 to 70/30 • by 20% increments at 1L/min • by 10% increments at 2L/min and higher
	Design 5	60/40, 50/50 and 40/60	
	Design 6	60/40	
Intra-atrial TCPC		60/40	
Bilateral SVC		55% IVC 22.5% LSVC and RSVC	

5.4.3.2 Flow visualization

Table 5.4.3: Flow rates at which flow visualization was performed. Caval flow ratio was fixed at 60/40 IVC/SVC and pulmonary flow ratio varied between 70/30, 50/50 and 30/70 LPA/RPA.

		Tested Cardiac output
Simplified Models	Design 4	4L/min
	Design 5	3L/min
	Design 6	1L/min
Intra-atrial TCPC		1L/min
Bilateral SVC		2 and 4L/min

5.4.3.3 DPIV

Table 5.4.4: Flow rates at which PIV measurements were taken with the corresponding caval and pulmonary flow ratios.

	Total Cardiac output	Flow Splits	
		IVC/SVC	LPA/RPA
Simplified Model 1 [Ensley, 2001]	4L/min	60/40	30/70, 50/50 and 70/30
Intra-atrial TCPC	1 and 3L/min	60/40	
Bilateral SVC	2 and 4L/min	55% IVC 22.5% LSVC & RSVC	

5.4.3.4 LDV

Table 5.4.5: Flow rates at which LDV measurements were taken with the corresponding caval and pulmonary flow ratios.

	Total Cardiac output	Flow Splits	
		IVC/SVC	LPA/RPA
Intra-atrial TCPC	1 and 3L/min	60/40	50/50

5.4.3.5 CFD

Table 5.4.6: Flow solvers and flow conditions that were used for the CFD simulations.

		Flow solver	Flow conditions
Simplified Models	Model 1, 2, 3	CFD-Ace [Healy, 2001; Ryu, 2000]	Steady mode 4L/min
	Model 4	CFD-Ace [Liu, 2004]	60/40 IVC/SVC 30/70 to 70/30 LPA/RPA
Intra-atrial TCPC		FIDAP [Pekkan, 2004]	Steady mode 1, 2 and 3L/min 60/40 IVC/SVC 30/70 to 70/30 LPA/RPA
		FIDAP [Pekkan, 2004]	Transient mode 1 and 3L/min 60/40 IVC/SVC 50/50 LPA/RPA
		In-house [Pekkan, 2004]	Unsteady mode 1L/min 60/40 IVC/SVC 50/50 LPA/RPA

5.4.3.6 Summary

Table 5.4.7: Summary of all the experiments and numerical simulations that were conducted in our laboratory. v refers to the experimental work that was conducted for this study.

		Q (L/min)	Power Losses	Flow Visualization	PIV	LDV	CFD
Simplified Models	Design 1, Glass	2	v	-	-	-	[Healy, 2001]
		4	v	-	-	-	-
		6	[Ensley, 2000] v	[Ensley, 2000] -	[Ensley, 2000] -	-	[Ryu, 2000] -
	Design 1, RP	2	v	-	-	-	-
		4	v	-	-	-	-
		6	v	-	-	-	-
	Design 2, 3	2	v	-	-	-	-
		4	v	[Ryu, 2000]	-	-	[Ryu, 2000]
		6	v	-	-	-	-
	Design 4	2	v	-	-	-	-
		4	v	v	-	-	[Liu, 2004]
		6	v	-	-	-	-
	Design 5	1	v	-	-	-	-
		2	v	-	-	-	-
		3	v	-	-	-	-
		4	v	v	-	-	-
		5	v	-	-	-	-
	Design 6	1	v	v	-	-	-
2		v	-	-	-	-	
3		v	-	-	-	-	
Anatomical Models	Intra- atrial TCPC	1	v	v	v	v	[Pekkan, 2004]
		2	v	-	-	-	
		3	v	-	v	v	
	Bilatera l SVC	2	v	v	v	v	-
		3	v	-	-	-	-
		4	v	v	v	v	-
			v	v	v	v	-

CHAPTER VI

RESULTS

The results are organized into four primary sections, namely: (1) method validation studies, (2) simplified TCPC models 1 through 6, (3) anatomical intra-atrial TCPC and (4) anatomical bilateral SVC. Figure 6.0.1 shows a schematic of the orientation of the TCPC models in the figures displayed throughout this chapter.

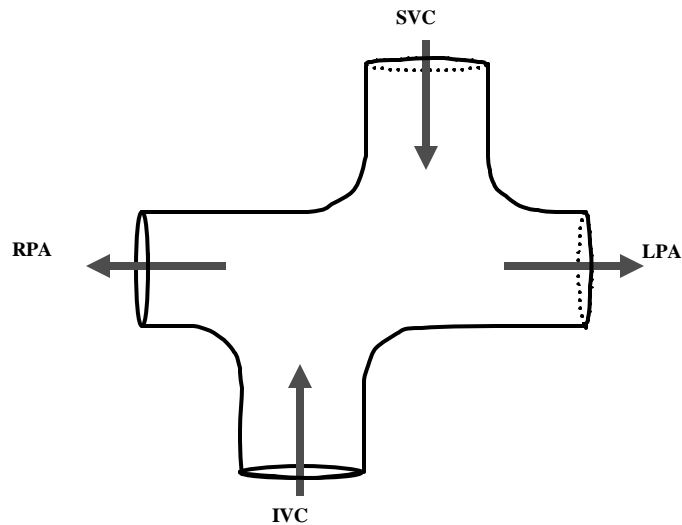


Figure 6.0.1: Schematic showing the spatial configuration that will be used to describe the results from each different technique and for each model. All the models, except for Model 4, were imaged from the anterior side, as though facing the patient: with the LPA on the right hand side and the RPA on the left.

6.1 Validation of the Methods

6.1.1 Static Pressure Measurements

In order to validate our experimental set-up and the accuracy of our static pressure measurements, a preliminary study was conducted by achieving a fully developed laminar pipe flow and measuring the pressure drop between two points A and B separated by 0.5 m. With a fully developed flow, the total and in static pressures are equal so that the analytical expression for the static pressure drop between the A and B can be obtained from the expression for $\Delta_{A \rightarrow B} P_{iTotal}$ derived in Section 5.2.1.4:

$$\Delta_{A \rightarrow B} P_{Static} = L_{B \rightarrow A} \cdot \frac{I}{D} \cdot \frac{\rho V^2}{2} \quad (\text{Equation 6.1.1})$$

where I is the friction factor, D the pipe diameter, ρ the fluid density, V the bulk flow velocity and $L_{A \rightarrow B}$ the algebraic length of the pipe between the two points A and B. $L_{A \rightarrow B} > 0$ if the fluid flows from A to B, and $L_{A \rightarrow B} < 0$ otherwise.

The pressure drops between A and B, $\Delta_{A \rightarrow B} P_{Exp}$, were measured for different flow rates and with three different transducers. The corresponded friction factors f_{Exp} were computed using Equation 6.1.1. As is shown in Figure 6.1.1, the experimental results were in good agreement with the theoretical expression for the friction factor in the laminar regime, which is $I = \frac{64}{Re}$. This observation validated the pressure measurement set-up.

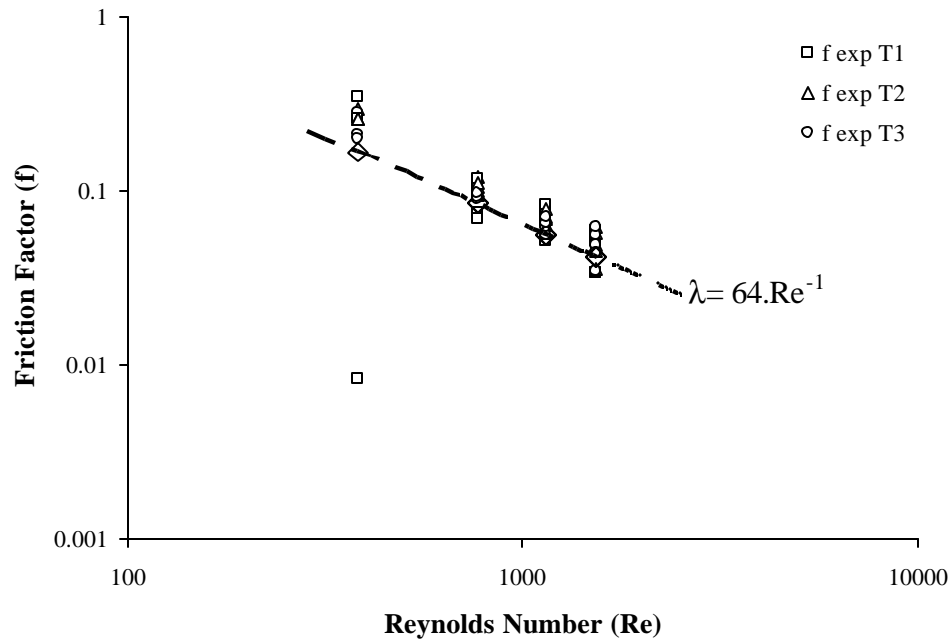


Figure 6.1.1: Experimental friction factors obtained for three different pressure transducers, T1, T2 and T3. The dashed line displays the theoretical values for the friction factor in the laminar regime.

6.1.2 Impact of the Surface Roughness

As described in Section 5.1, RP models are built in layers and in two halves, which result in higher surface roughness than that of regular glass models. The surface roughness can be significantly lowered down by carefully polishing the inner surface. However in small models, polishing may either not be feasible or endanger the geometrical accuracy of the model. Since the CFD simulations were run using smooth vessel walls, a comparative study was performed on a simple geometry, the reference Model 1.

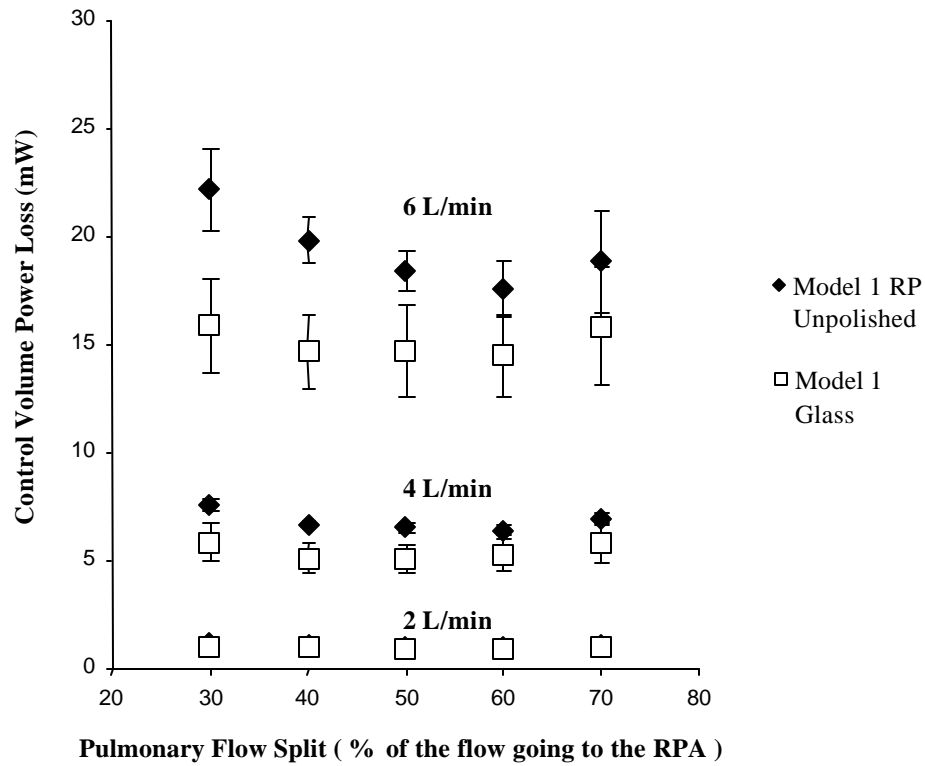


Figure 6.1.2: Comparative power losses in Model 1, depending on the manufacturing method. Power losses in the unpolished rapid prototype were systematically higher than in the handcrafted glass model.

Figure 6.1.2 compares the hydrodynamic control volume power losses as a function of flow split between the unpolished rapid prototype for Model 1 and the glass model. The power losses corresponding to 50% flow split for the unpolished RP model were 1.05, 6.53, and 18.43 mW at 2, 4, and 6 L/min respectively. These losses can be seen to be systematically higher than the losses in the glass model (0.94, 5.10, and 14.69 mW respectively). These differences were found to be significant at 4 and 6 L/min ($p < 0.05$) with an average increase in power loss between 25 to 30%.

6.1.3 Suitability of the RP Models for Quantitative Optical Flow Measurements

Using dye flow visualization, transparent RP resins enabled for good quality qualitative flow assessment. However, as was mentioned in Chapter V, when performing quantitative DPIV measurements, an important background noise was observed in the images acquired through transparent RP resins. In order to evaluate whether this affected the accuracy of the DPIV cross-correlation process, we considered a fully developed flow going through a straight pipe of one inch in diameter and built out of the same transparent RP resin as the bilateral SVC model (Vantico Renshape 7510) and confronted the DPIV measurements against two well established techniques, LDV and ultrasonic flow probe measurements.

Utmost care had been paid to ensure fully developed profile with our experimental set-up. However as can be observed in Figure 6.1.3, the DPIV vector fields nearly fitted the parabolic profile expected from a fully developed laminar flow, but not quite. A slight asymmetry in the in the profile was observed with lower velocities in half that was further away from the laser beam. Possible sources of explanations include asymmetries in our set-up despite our efforts, and uneven illumination of the test section. As the laser power was dissipated as the laser beam traveled across the fluid. Such observation was also done in the acrylic models run in our laboratory, but had a higher impact here, as the transparent RP resins absorbed more power to start of with. With lower contrast and intensity, DPIV cross-correlation leads to higher RMS values and a higher deviation from the expected value.

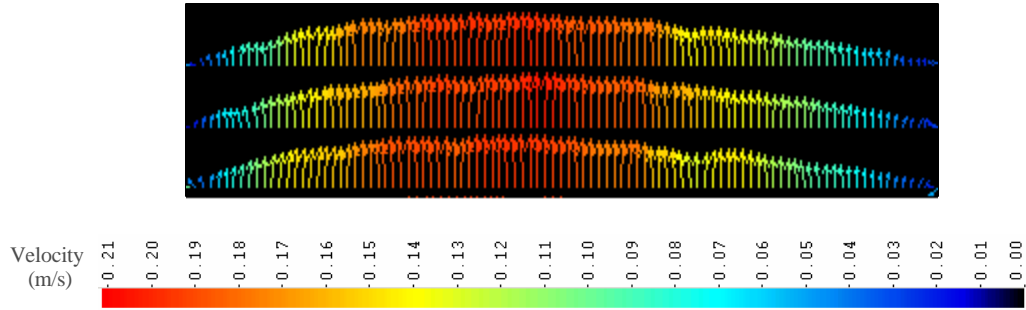


Figure 6.1.3: Fully developed velocity profile in a one-inch pipe

The flow velocities along the centerline were measured for ten flow rates ranging from 1.5 to 9 L/min using DPIV and LDV respectively. When considering fully developed laminar pipe velocity profiles, the maximum velocity is located along the centerline of the pipe and is worth 1.5 times the bulk flow velocity. Figure 6.1.4 compares the DPIV and LDV velocities at the center of the pipe against the corresponding theoretical velocity computed as follows:

$$V_{Theor} = \frac{1.5 * Q_{Transonic}}{60 \cdot 1000 \cdot \pi R_{Pipe}^2} \quad (\text{Equation 6.1.3})$$

where V_{Theor} is the theoretical centerline velocity in m/s, $Q_{Transonic}$ the total flow rate measured by the Transonic flow probe in L/min, and R_{Pipe} the diameter of the pipe (0.0127m).

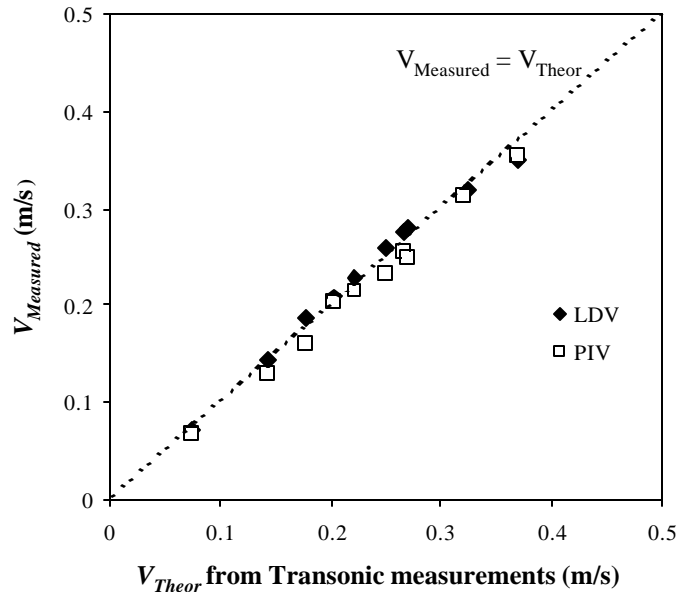


Figure 6.1.4: Comparison of the velocity along the centerline of the RP pipe measured using DPIV and LDV and computed after the total flow rates measured with the ultrasonic flow probe. The DPIV and LDV results are plotted as a function of V_{Theor} , while dotted line represents the theoretical values V_{Theor} .

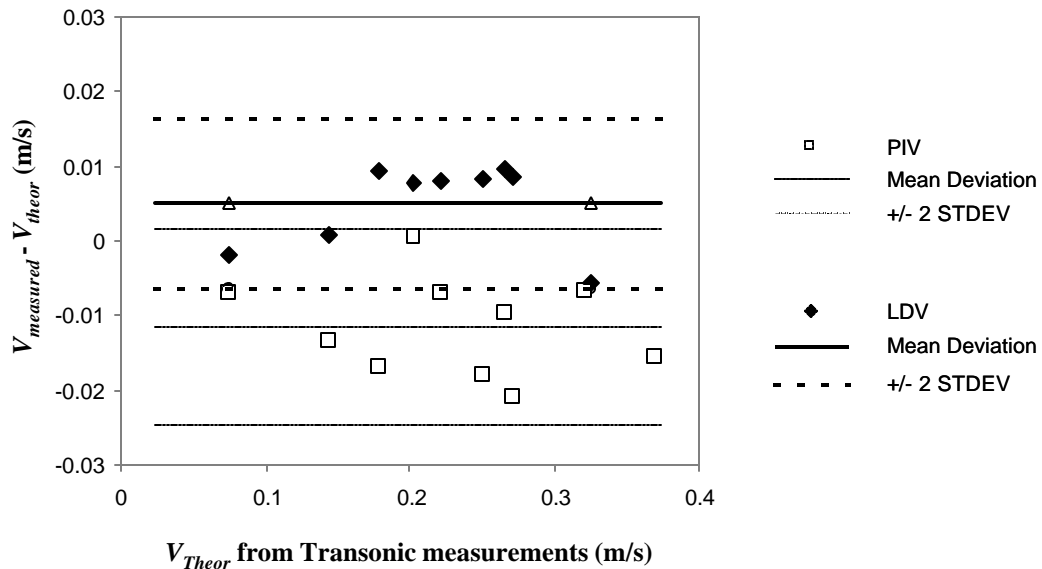


Figure 6.1.5: Comparison of velocity bias of the LDV and DPIV techniques along with the mean and 95% confidence intervals of the respective bias. The velocities computed with the ultrasonic flow measurements are taken as reference. The continuous lines provide the mean bias while the dashed lines picture the 95% confidence interval (2 standard deviations away from the corresponding mean)

As is illustrated in Figure 6.1.5, both LDV and transonic flow probe measurements were in close agreement, with a mean bias of +0.005 m/s, which corresponded to a mean error in the velocity measurements of 3.1%. Both these techniques measured higher velocities than the DPIV measurements. DPIV measurements thus underestimated the flow velocities by a mean bias of -0.012 m/s. However, the DPIV measurements remained within 10% of V_{Theor} over the tested flow range and the mean error in the velocity measurements was of 5.6%. These results were encouraging in the sense that velocities within 10% accuracy were achievable using the DPIV technique despite the presence of background noise. However, it should be kept in mind that the DPIV results that shown later will more than likely underestimate the true velocities.

6.2 Simplified Models

Models 1 through 6 were built to provide a further understanding of the individual contribution of different geometrical features to the global flow field that was observed in the anatomical intra-atrial model and supported the numerical validation effort. As a brief reminder of the geometric characteristics of all six models, Model 1 and 2 featured constant diameters (13.34 mm), Models 3, 4 and 5 featured more anatomical diameters based on the design proposed by Ryu et al. [Ryu, 2000] and Model 6 reproduced the hydraulic diameters of the anatomical intra-atrial model. Models 1, 3, 5 and 6 were planar, while Models 2 and 4 were not; and finally Models 1 through 4 included a one-diameter caval offset, while Models 5 and 6 featured no caval offset.

6.2.1 Flow Visualization

6.2.1.1 Models 1 and 2 [Ensley, 2000; Ryu, 2000]

Flow visualization had already been performed in Model 1 [Ensley, 2000], 2 and 3 [Ryu, 2000]. This section will briefly review their results as they provide some ground of understanding for the subsequent power loss behavior. In their article, Ryu et al. describe the flow structure in Model 1 as follows: at 4 L/min, when 70 % of the flow was directed toward the RPA (Figure 6.2.1), the “fluid entering the connection from the IVC flowed dominantly toward the RPA. The SVC flow impinged on the inferior aspect of the LPA just distal to IVC-to-LPA flare. A large area (~10 mm in diameter) of flow having a clockwise rotation encompassed the entire central region of the connection between caval inlets. This central recirculation appeared to be propelled by the IVC inflow on the RPA side and by the SVC inflow on the LPA side.” At equal pulmonary flow split conditions (Figure 6.2.2) a portion of the IVC inflow was directed toward the LPA. The recirculation region was smaller (~8mm) and moved from the superior aspect of the RPA toward the inferior aspect of the LPA just distal of the IVC-to-LPA flare. When most of the flow (70%) was directed to the LPA (Figure 6.2.3), “about an equal amount of the IVC inflow was directed towards both PA’s.” The recirculation region created was even smaller (~5mm) and still located distal of the IVC-to-LPA flare. Finally, helical flow was observed in the PA’s, irrespective of the RPA/LPA flow split.

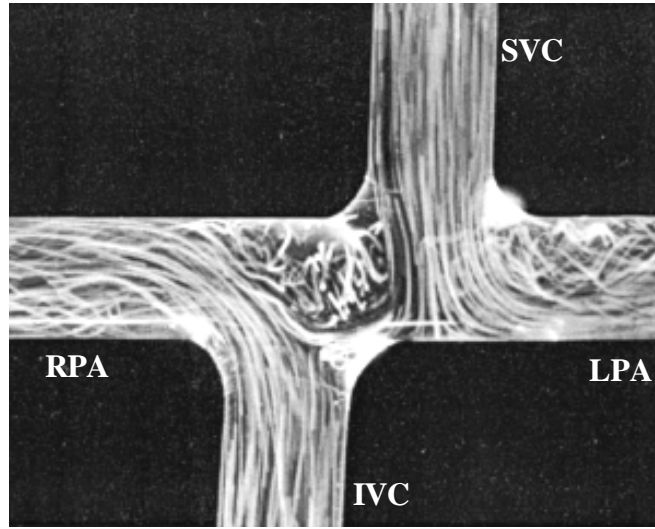


Figure 6.2.1: Model 1. Qualitative flow visualization at 4L/min and with a pulmonary flow split of 70/30 RPA/LPA [Ensley, 2000]

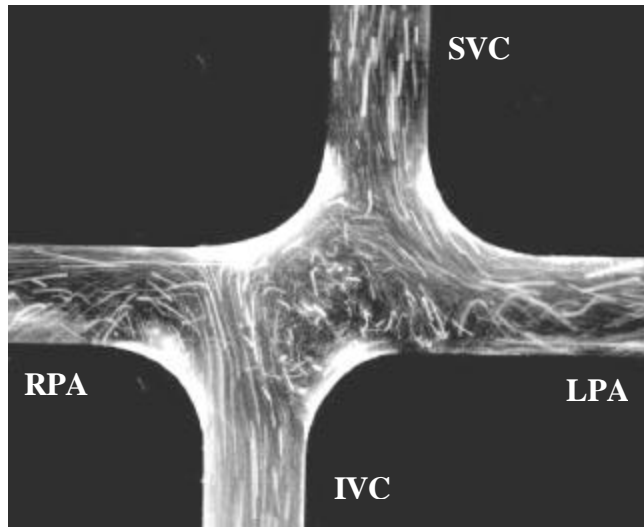


Figure 6.2.2: Model 1. Qualitative flow visualization at 4L/min and with a pulmonary flow split of 50/50 RPA/LPA [Ensley, 2000]

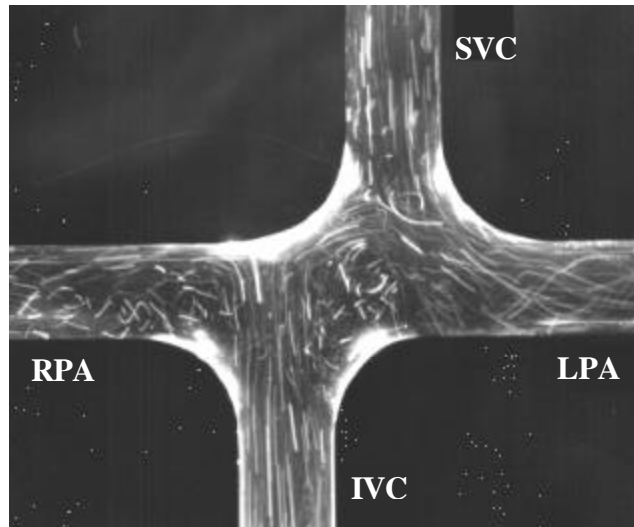


Figure 6.2.3: Model 1. Qualitative flow visualization at 4L/min and with a pulmonary flow split of 30/70 RPA/LPA [Ensley, 2000]

The aforementioned flow characteristics were also observed in the three subsequent models (Model 2, 3 and 4). The caval offset forced the recirculation region and there was no visible difference between the flow field in Model 2 and that of Model 1 [Ryu, 2000].

6.2.1.2 Models 3 and 4

If the overall flow behavior in Models 3 and 4 was very similar to what was seen in Models 1 and 2, the change in vessel diameters slightly yielded slight modifications in the relationship between the IVC and SVC flows. Due to a smaller vessel diameter, the SVC flow was faster and contained more kinetic energy in Model 3 than in Model 1. At 70/30 RPA/LPA (Figure 6.2.4), it impinged on the inferior aspect of the LPA before splitting between both PA's and part of it went down 3 to 4mm into the IVC. The recirculation region induced by the IVC and SVC streams was wider than in

Model 1 (~12 mm). Similarly to Models 1 and 2, directing more flow to the LPA (Figure 6.2.5) decreased the size of the recirculation region and moved it from the distal part of the SVC-to-RPA flare to the inferior aspect of the LPA distal of the IVC-to-LPA flare (Figure 6.2.5). This in turn pushed the location of impingement of the SVC stream further into the LPA away from the junction.

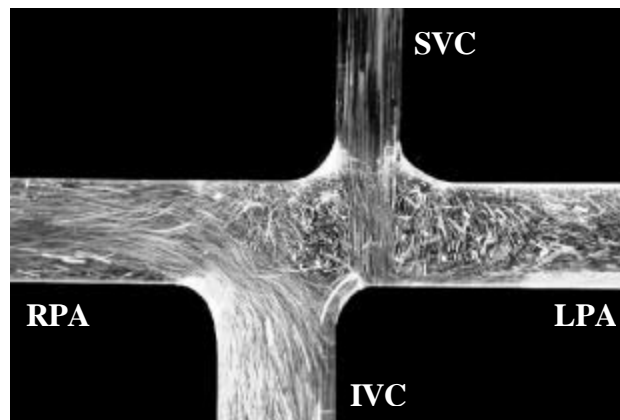


Figure 6.2.4: Model 3. Qualitative flow visualization at 4L/min and with a pulmonary flow split of 70/30 RPA/LPA [Ryu, 2000]

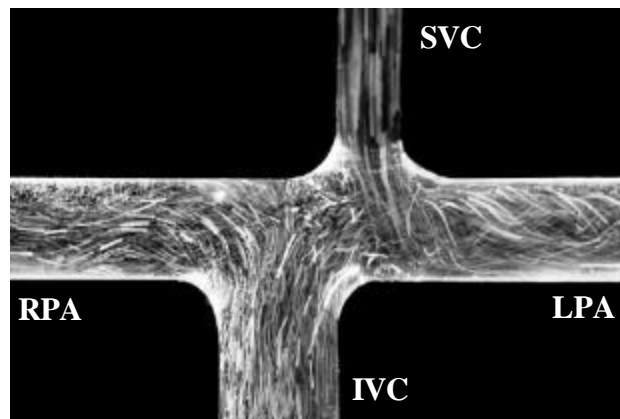


Figure 6.2.5: Model 3. Qualitative flow visualization at 4L/min and with a pulmonary flow split of 30/70 RPA/LPA [Ryu, 2000]

The flow field observed in Model 4 was comparable to that of Model 3. However the curvature in the PA's appeared to cause stronger helicity just after the connection. When most of the flow was directed to the LPA (Figure 6.2.7), the central recirculation region located just distal of the IVC-to-LPA flare combined with a stronger helical pattern in the LPA, pushed the SVC stream even further into the LPA than in Model 3, and there was no clear impingent point.

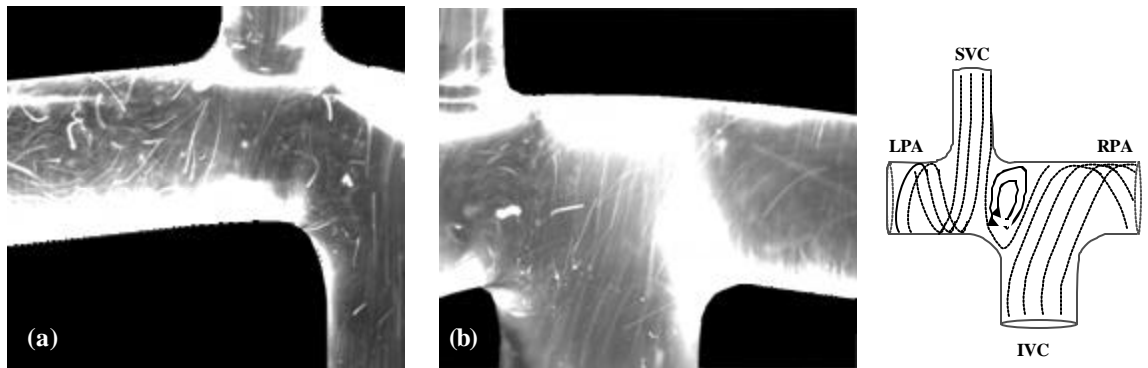


Figure 6.2.6: Model 4. Qualitative flow visualization at 4L/min and with a pulmonary flow split of 70/30 RPA/LPA. Unlike all the others, these images were acquired from the posterior side, with the LPA on the left (a) and the RPA on the right (b).

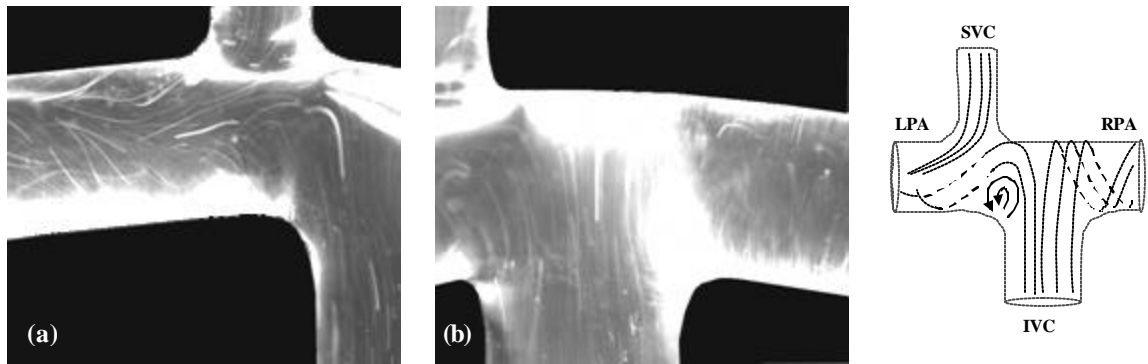


Figure 6.2.7: Model 4. Qualitative flow visualization at 4L/min and with a pulmonary flow split of 30/70 RPA/LPA. Unlike all the others, these images were acquired from the posterior side, with the LPA on the left (a) and the RPA on the right (b).

6.2.1.3 Model 5

In contrast to Models 1 through 4, Models 5 and 6 had no caval offset. Previous studies [Ensley, 1999; Sharma, 1996] have already demonstrated that the absence of caval offset lead to increased flow disturbance. As shown in Figure 6.2.8, the caval flows collided in the center of the connection, leading to a stagnation plane. This region was characterized by slight flow instabilities. At equal pulmonary flow split, the IVC and SVC streams oscillated and were alternatively directed towards the LPA and RPA so that the same streakline was observed to lead to both PA's at the same time (Figure 6.2.8). Leaving the inflow colliding region, the flow then swirled helically towards the PA's. Both venae cavae appeared to contribute equally to each one of the pulmonary arteries. Depending on the pulmonary flow split the caval flows were directed preferably towards the left or the right side of the connection (Figure 6.2.9).

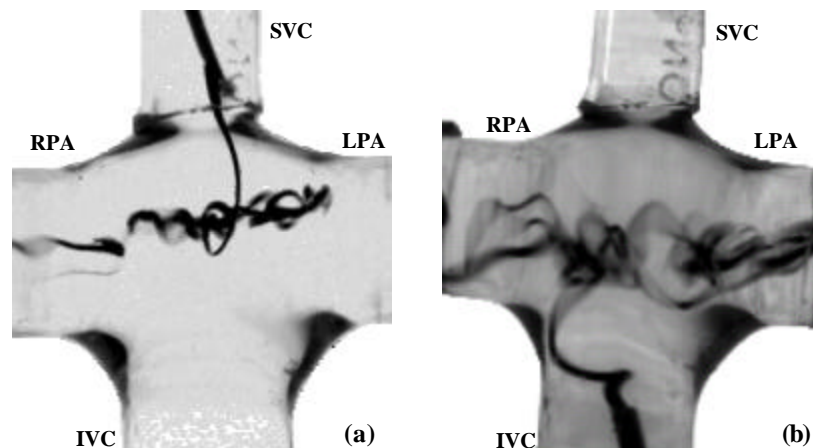


Figure 6.2.8: Model 5. Qualitative flow visualization 4L/min and with a pulmonary flow split of 50/50 RPA/LPA. Dye injected (a) from the SVC and (b) from the IVC.

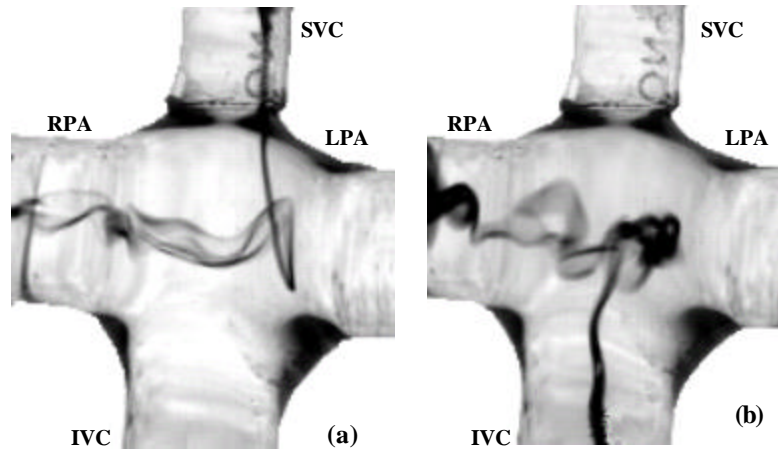


Figure 6.2.9: Model 5. Qualitative flow visualization at 4L/min and with a pulmonary flow split of 70/30 RPA/LPA. Dye injected (a) from the SVC and (b) from the IVC.

6.2.1.4 Model 6

In Model 6, the colliding caval flows no longer generated a stable stagnation. Instead, the SVC flow went down into the connection initiating an important recirculation throughout the entire connection that distributed the flow to the two pulmonary arteries (Figures 6.2.10 and 6.2.11).

With 70% of the flow going into the LPA, the IVC stream went all around the pouch, making a 270° turn before entering the LPA (Figure 6.2.10-a). The SVC stream aimed straight at the LPA anastomosis site. Figure 6.2.10-b shows the SVC stream spiraling down into the connection before entering the LPA (it doesn't really aim straight rather the flow here is spiraling). The dye trajectory exhibited sensitivity to initial conditions as shown in Figure 6.2.10-c where the trajectory spirals down followed by joining the recirculating flow in the connection before finally entering the LPA. It is at equal pulmonary flow split that the counterclockwise recirculation was most clearly identified. It occupied the entire connection area, and was driven by the IVC stream on

the right side (Figure 6.2.11-a) and by the SVC stream on the left side (Figure 6.2.11-b). After recirculating throughout the pouch, the two caval flows were split between the LPA and RPA. At 70/30 RPA/LPA, the identification of the recirculation region was no longer so clear. The SVC stream went directly into the RPA without further mixing (Figure 6.2.12-a) while the IVC stream contributed to both pulmonary flows. The IVC flow either went directly into the LPA (Figure 6.2.12-b) or flowed into the RPA after going first through an instable flow region (Figure 6.2.12-c). Finally, due to the bulgy aspect of the connection, the mixing of the caval flows was not two- but rather three-dimensional through all flow conditions. The high velocity flow coming out of the SVC pushed the IVC stream towards one side of the connection and then initiated 3D mixing (Figure 6.2.13) before entering the PA's with a helical pattern.

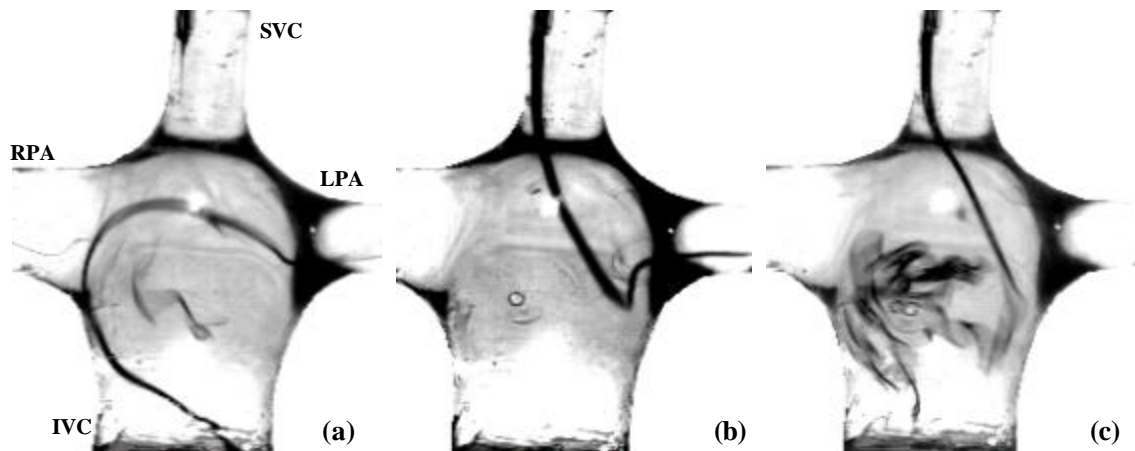


Figure 6.2.10: Model 6. Qualitative flow visualization at 1L/min and with a pulmonary flow split of 30/70 RPA/LPA.

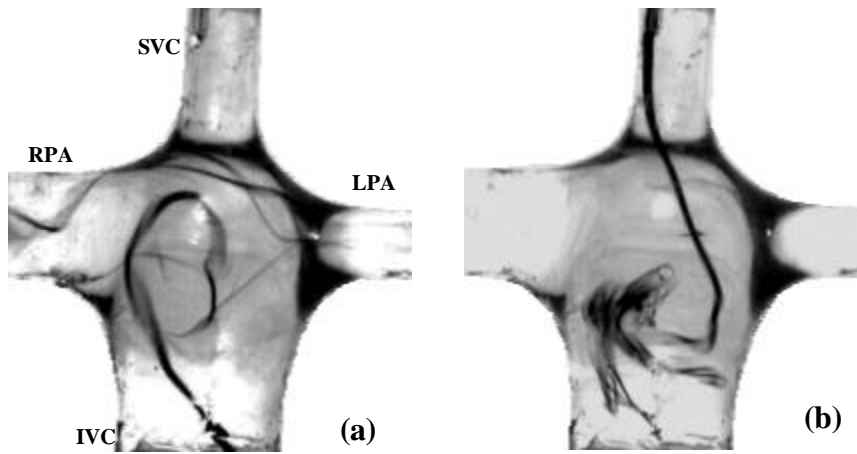


Figure 6.2.11: Model 6. Qualitative flow visualization at 1L/min and with a pulmonary flow split of 50/50 RPA/LPA.

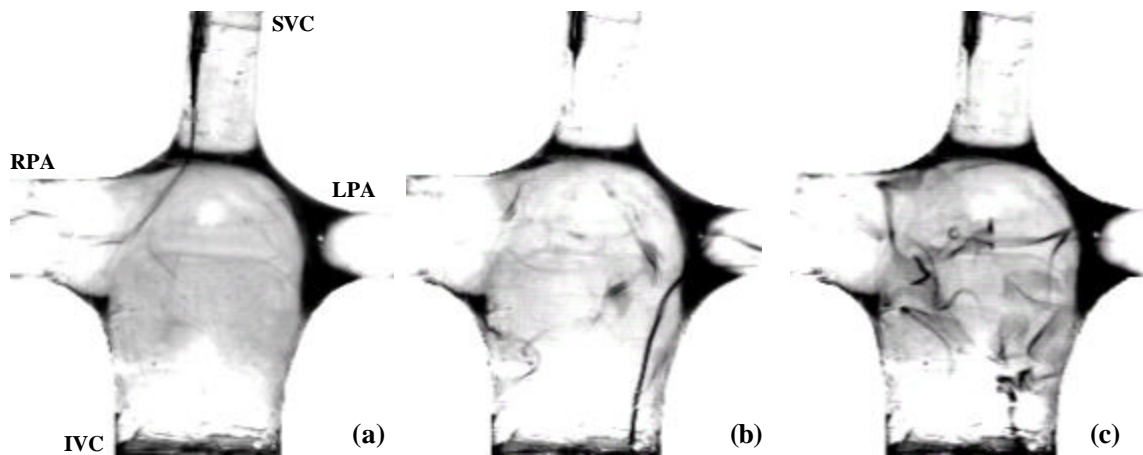


Figure 6.2.12: Model 6. Qualitative flow visualization at 1L/min and with a pulmonary flow split of 70/30 RPA/LPA



Figure 6.2.13: Model 6. Qualitative flow visualization at 1L/min and with a pulmonary flow split of 70/30 RPA/LPA seen from the side. The recirculation region occupied the entire connection region, leading to important 3D mixing of the caval flows.

6.2.2 Experimental Pressure Drops and Power Losses

6.2.2.1 General comments

This section will only display the results that appeared to be the most relevant to the discussion. However, the processed power loss and pressure data for all simplified and anatomical models may be found in Appendix C. Figure 6.2.15 displays the power loss plot for Model 1 at different cardiac outputs as a typical example of the results that were obtained in the simplified glass models. The figure shows the measured power losses as a function of pulmonary flow split (30/70 to 70/30 LPA/RPA) for three total flow rates (i.e. cardiac outputs of 2, 4, and 6 L/min). The red line corresponds to the power losses corresponding to equal lung resistance. This means that a child with equal left and right lung resistance ($R_{Lung} = 1.79$ Wood units) whose TCPC design would exactly reproduce that of Model , would see an equal share of his blood going to the left and right lung irrespective of his total cardiac output. In all of the simplified glass models, the EPVR points also corresponded with the point of minimal energy dissipation.

Figure 6.2.14 shows the measured pressure in SVC, LPA, and RPA relative to the pressure in the IVC as a function of flow split for Model 1 at 2 L/min. The trends observed in the figure correspond well with the flow visualization observations in all models. The pulmonary pressures decreased as more flow was directed through the corresponding PA. In models with identical LPA and RPA diameters (Models 1 to 5), the LPA and RPA pressure curves had nearly symmetric behavior and crossed at about 50/50 LPA/RPA. Models 1 to 4 included a 13.3 mm caval offset, with the SVC oriented towards the LPA. In all these models the SVC pressure decreased as more flow was directed to the RPA (and less to the LPA). This decrease in SVC pressure combined with the increase in LPA pressure lead to an even smaller SVC-to-LPA pressure drop, which correlated well with the lower LPA/RPA flow ratio. Such a behavior did not hold true in models such as Model 5 and 6 where a caval offset was absent.

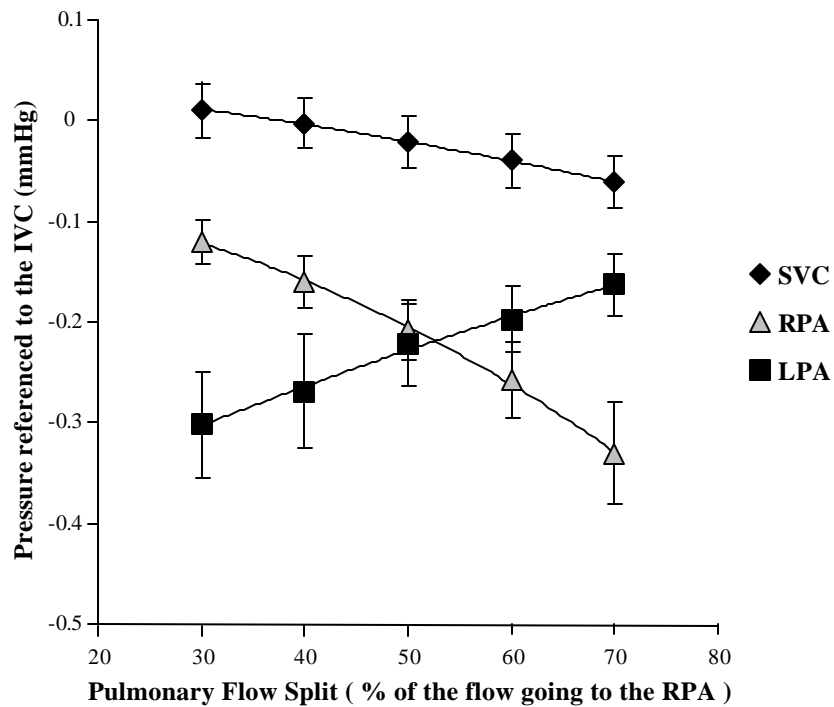


Figure 6.2.14: Pressure in SVC, RPA and LPA with respect to that in the IVC measured in Model 1 at 2 L/min.

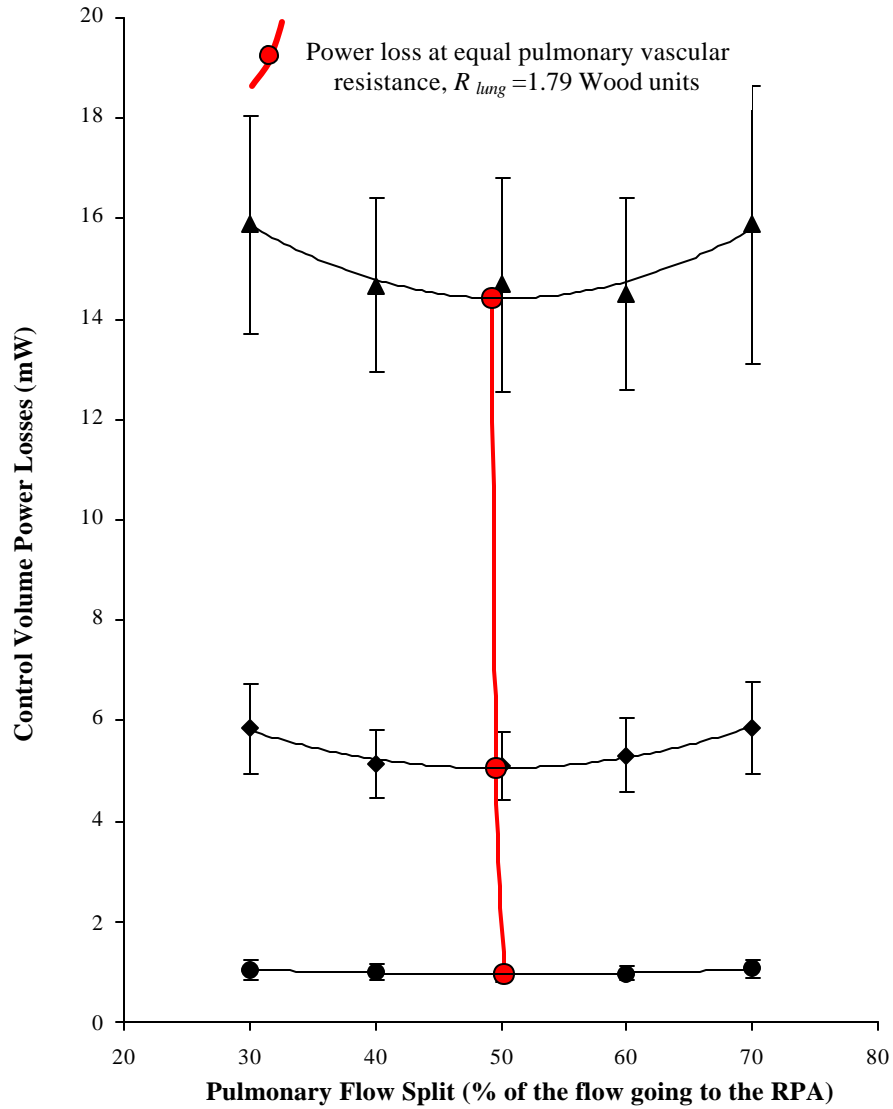


Figure 6.2.15: Power losses measured in Model 1 at 2, 4 and 6L/min. The power loss points were fitted with a second-degree polynomial curve. The EPVR points, described by the red line, corresponded to a 50/50 LPA/RPA flow split irrespective of the total flow rate.

6.2.2.2 Model 1

In order to provide some ground of comparison with earlier studies, Model 1 was run as a control and compared to the flared 14 mm-offset model previously studied by Ensley et al. [Ensley, 1999]. Both earlier and current measurements followed the same pattern (see Figure 6.2.16). Energy dissipation was minimal at a 50/50 LPA/RPA flow split and steadily increased as the pulmonary flow split tended towards either 30/70 or 70/30 LPA/RPA. Ensley et al. had observed a higher sensitivity to pulmonary flow split than what was measured here. However, except at 50/50 LPA/RPA, the power losses measured in Model 1 showed no significant difference ($p>0.1$) with the earlier data. The two set-ups were thus considered to be equivalent, so that the results from this study could be combined with those obtained by Ensley et al. for a further understanding of the TCPC hemodynamics.

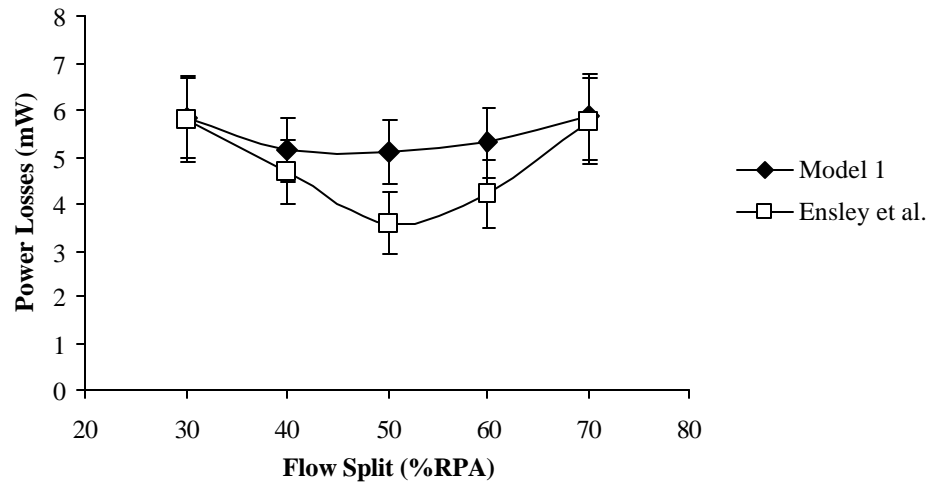


Figure 6.2.16: Comparison of the control volume hydrodynamic power losses obtained at 4L/min in this study in the simplified glass Model 1 with previous results by Ensley et al. [Ensley, 2001]

As can be observed from Table 6.2.1 as well as from Figure 6.2.14, the EPVR point for Model 1 corresponded to a 50/50 pulmonary flow split, irrespective of the total flow rate. The EPVR point also coincided with the lowest energy dissipation point.

The pressure difference between the IVC and SVC was close to zero at 2 and 4L/min and only started increasing under exercise conditions, at 6L/min. The pressure drops towards either of the lungs remained lower than 1mmHg in the resting state and only reached 1.1 mmHg at 6 L/min. These pressure drops are on the order of those that a surgeon would aim for, i.e.: less than 1 to 1.5 mmHg pressure drop between the IVC baffle and the opening of the pulmonary arteries. However, the pressures here were measured much further apart, 10 cm up- and down-stream of the connection, than they are measured during surgery. The pressure drop at the connection site must thus be less than those reported here.

Table 6.2.1: Pressure drops and power losses corresponding to equal pulmonary vascular resistance conditions ($R_{Lung} = 1.79$ Wood units) for Model 1 at 2, 4 and 6L/min.

Q_{Total} (L/min)	%RPA	Pressure with reference to the IVC (mmHg)			Power Loss (mW)
		SVC	RPA	LPA	
2	50	-0.02	-0.21	-0.23	0.95
4	50	0.01	-0.60	-0.49	5.06
6	49	0.17	-1.10	-0.81	14.42

6.2.2.3 Model 2

Model 2 featured the same vessel diameters as Model 1 but the PA's were curved towards the posterior side. Table 6.2.2 shows that the EPVR point corresponded to a 50/50 LPA/RPA flow split irrespective of the flow rate similar to the findings in Model 1. Though by a small amount, the static pressures in the SVC were lower than in the IVC; about -0.16 mmHg at 4 L/min and -0.34 mmHg at 6 L/min. The pressure drops observed in the LPA and RPA were nearly equal. Finally the power losses at 2, 4 and 6 L/min, were on average 15 to 20% higher than in Model 1. This difference was significant ($p < 0.05$) except at 2L/min at 50/50 and 40/60 RPA/LPA ($p > 0.15$).

Table 6.2.2: Pressure drops and power losses corresponding to equal pulmonary vascular resistance conditions ($R_{Lung} = 1.79$ Wood units) for Model 2 with flow rates ranging from 2 to 6 L/min.

Q_{Total} (L/min)	%RPA	Pressure with reference to the IVC (mmHg)			Power Loss (mW)
		SVC	RPA	LPA	
2	50	-0.03	-0.25	-0.25	1.02
3	50	-0.08	-0.45	-0.42	2.79
4	50	-0.16	-0.74	-0.72	6.15
5	50	-0.29	-1.03	-1.01	10.43
6	50	-0.34	-1.32	-1.32	16.53

6.2.2.4 Model 3

Model 3 was planar with more physiologic caval diameters (smaller SVC, 8 mm in diameter, and wider IVC, 15 mm in diameter). When compared to Model 1 or 2 this change in dimensions affected neither the pulmonary pressure drops nor the EPVR point, which still was 50/50 LPA/RPA for all flow splits (see Table 6.2.3). However, the major impact of the change in caval diameter was on the pressure difference between the IVC and SVC. While in Model 1 the static pressure in the SVC was nearly equal to that of the IVC, in Model 3 it is 1.44 mmHg higher than the IVC at 4 L/min and 2.32 mmHg higher at 6 L/min. This translated into a significant increase in power losses by 140 to 160%.

Table 6.2.3: Pressure drops and power losses corresponding to equal pulmonary vascular resistance conditions ($R_{Lung} = 1.79$ Wood units) for Model 3 with flow rates ranging from 2 to 6 L/min.

Q_{Total} (L/min)	%RPA	Pressure with reference to the IVC (mmHg)			Power Loss (mW)
		SVC	RPA	LPA	
2	50	0.64	-0.20	-0.22	2.46
3	50	0.90	-0.30	-0.30	5.64
4	50	1.44	-0.49	-0.51	12.52
5	51	1.89	-0.77	-0.86	23.19
6	51	2.32	-1.00	-1.04	35.98

6.2.2.5 Model 4

Models 3 and 4 had identical dimensions; however, Model 3 was planar while Model 4 featured curved PA's that formed a 120° angle pointing towards the posterior side. The EPVR point was again observed at 50/50 LPA/RPA for all flow splits and the pulmonary pressures were of the same order as in Model 3. The pressure in the SVC, on the other hand, was 30 to 50% higher than in Model 3 for the same flow rates. As a result, the power losses in Model 4 showed a significant 15 to 30% increase ($p < 0.05$) at 3 L/min when compared to those in Model 3. The power losses were 140 to 160% higher when compared to those observed in Model 2.

Table 6.2.4: Pressure drops and power losses corresponding to equal pulmonary vascular resistance conditions ($R_{Lung} = 1.79$ Wood units) for Model 4 with flow rates ranging from 2 to 6 L/min.

Q_{Total} (L/min)	%RPA	Pressure with reference to the IVC (mmHg)			Power Loss (mW)
		SVC	RPA	LPA	
2	50	0.83	-0.17	-0.19	2.61
3	50	1.21	-0.34	-0.33	6.68
4	50	2.19	-0.59	-0.55	15.81
5	50	2.99	-0.79	-0.75	27.54
6	50	3.66	-1.20	-1.06	44.56

6.2.2.6 Model 5

Model 5 had the same vessel diameters as the two previous models, Models 3 and 4. It was planar, had no caval offset and featured a connection site with a higher inner diameter. The pulmonary pressures were of the same order as those measured in the two previous models and the EPVR point corresponded again to a 50/50 RPA/LPA flow split for all flow rates.

Whereas the SVC pressure decreased with increasing RPA/LPA flow ratio in Models 1 to 4, which all featured a caval offset, the SVC pressure in Model 5 followed a parabolic trend with a minimum value around 50/50 LPA/RPA (see Figure 6.2.17). The SVC pressure at the EPVR point was 20 to 50% and 50 to 65% lower than in Model 3 and 4 respectively. However, the power losses observed in Model 5 were higher than in both Model 3 and 4. There was a significant 20 to 45% increase with respect to Model 3 for 3L/min and higher. The difference in energy dissipation between Model 4 and 5 was only significant for 5 and 6L/min where the losses in Model 5 were on average 10 and 25% higher than in Model 4.

Table 6.2.5: Pressure drops and power losses corresponding to equal pulmonary vascular resistance conditions ($R_{Lung} = 1.79$ Wood units) for Model 5 with flow rates ranging from 1 to 6 L/min.

Q_{Total} (L/min)	%RPA	Pressure with reference to the IVC (mmHg)			Power Loss (mW)
		SVC	RPA	LPA	
1	50	0.11	-0.11	-0.10	0.37
2	50	0.29	-0.42	-0.38	2.63
3	50	0.51	-0.60	-0.60	6.53
4	50	1.02	-1.28	-1.16	17.32
5	50	1.38	-1.71	-1.55	29.62
6	50	1.83	-2.33	-2.33	50.28

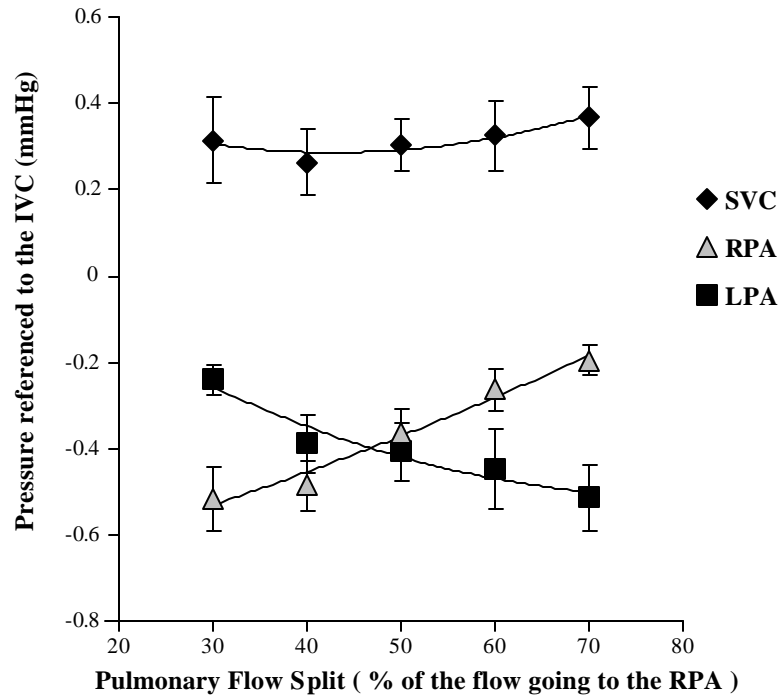


Figure 6.2.17: Pressure drops measured in Model 5 at 2L/min.

6.2.2.7 Model 6

Model 6 had a design similar to that of Model 5. The vessels were co-planar, and the pouch-like connection site actually had the same inner dimensions as that of Model 5. The differences in design between the two models were that Model 6 had smaller vessel diameters and most importantly that the LPA diameter (5 mm) differed from that of the RPA (8 mm).

As can be observed from Figure 6.2.18, the pressure in the LPA (ranging between -4.8 mmHg and -14.4 mmHg at 2 L/min) was much lower and showed a greater dependence on the pulmonary flow split than that in the RPA (ranging between -1.0 mmHg and -3.4 mmHg at 2 L/min). As more flow went to the LPA, the LPA pressure

dropped at a higher rate and the SVC pressure steadily increased, so as to increase the overall VC-to-LPA pressure drop. However, at 1 and 2 L/min, the variation in the SVC pressure with respect to the flow split was not significant ($p>0.15$), which may be due to the fact that the pouch-like connection site reduced the correlation between the caval and pulmonary flows.

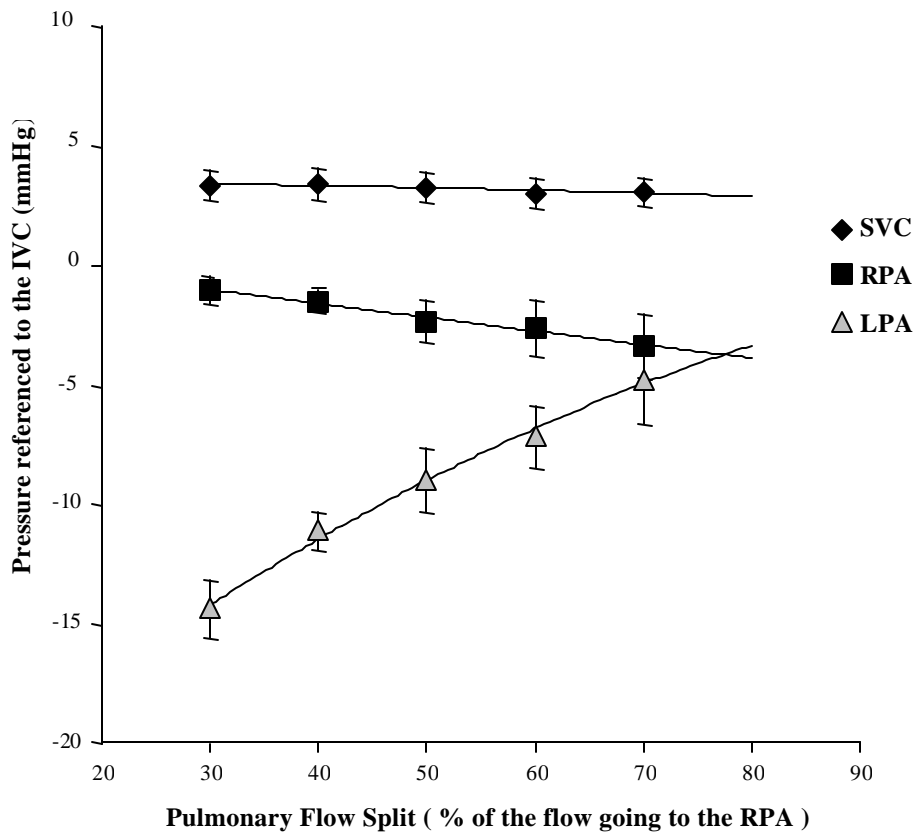


Figure 6.2.18: Pressure drops measured in Model 6 at 2 L/min.

The magnitude of the RPA and SVC pressures in Model 6 were about 5 to 10 times those in Model 5 for the same flow conditions, while the magnitude of the LPA pressures in Model 6 was as high as 70 times higher than in Model 5 at 30/70 RPA/LPA. As a result, the power losses observed in Model 6 were one order of magnitude higher than those observed in Models 1 to 5 and were highly dependent upon the pulmonary flow ratio. Minimal losses occurred at 70/30 RPA/LPA, and were 55-65% lower than those measured at 30/70 RPA/LPA (Figure 6.2.19). At 3 L/min, when more than 50% of the flow was directed through the LPA, the flow in the LPA was turbulent ($Re > 2300$). RPA flow remained in the laminar regime throughout all flow conditions. The EPVR point no longer corresponded to a 50/50 RPA/LPA flow split irrespective of the total flow rate; instead, it corresponded to a 62/38 RPA/LPA flow split at 1 L/min going to an even more unbalanced flow split of 70/30 RPA/LPA at 2 and 3 L/min (Table 6.2.6).

It is worthwhile to point out that the EPVR corresponds to equal lung resistance, and thus does not necessarily match the point where both LPA and RPA pressures are equal. If this held true for Model 1 to 5, it was no longer the case for Model 6. At 2 L/min, the EPVR point was found to correspond to a 70/30 RPA/LPA flow split, while the pulmonary pressures only became equal at 79/21 RPA/LPA (Figure 6.2.18).

Table 6.2.6: Pressure drops and power losses corresponding to equal pulmonary vascular resistance conditions ($R_{Lung} = 1.79$ Wood units) for Model 6 at 1, 2 and 3 L/min.

Q_{Total} (L/min)	%RPA	Pressure with reference to the IVC (mmHg)			Power Loss (mW)
		SVC	RPA	LPA	
1	62	0.74	-0.54	-1.54	2.52
2	70	3.00	-3.02	-5.22	20.48
3	70	4.27	-6.43	-9.00	54.23

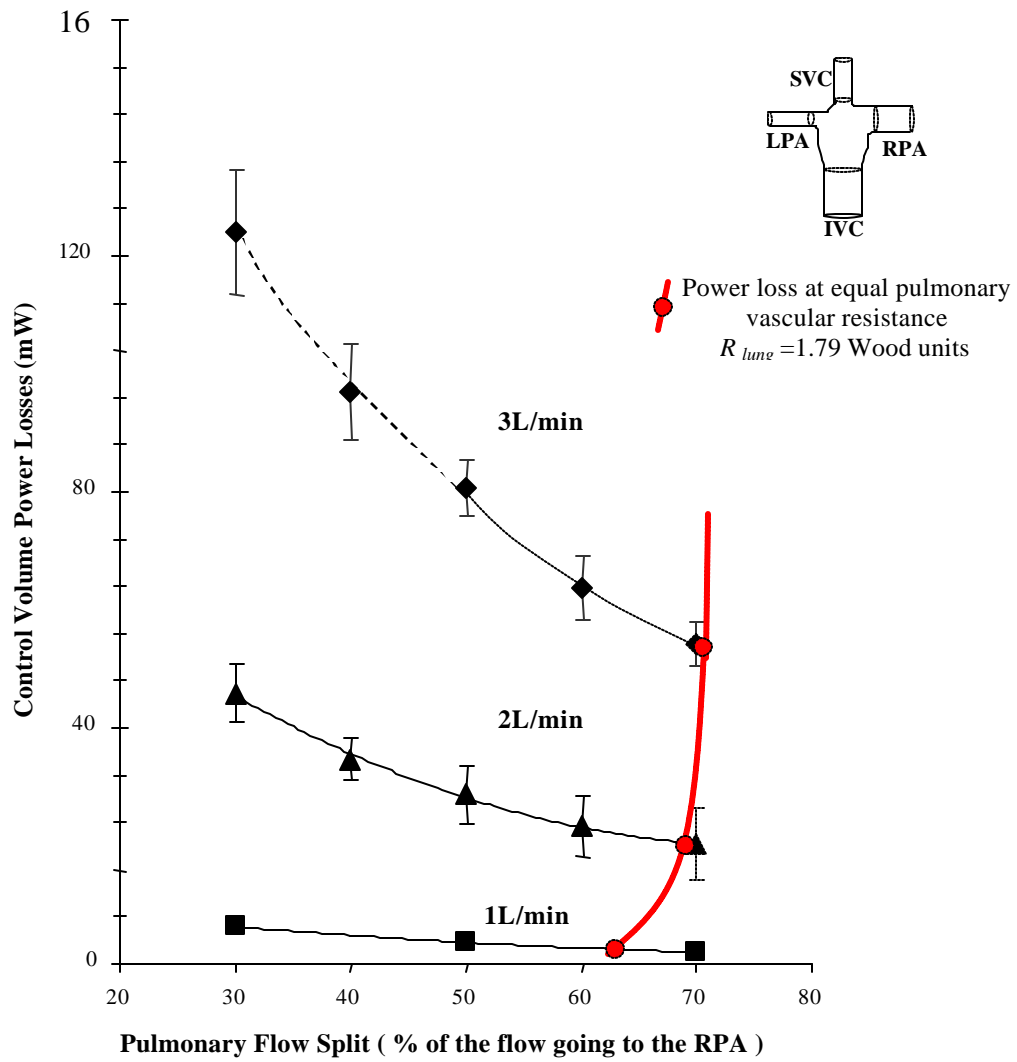


Figure 6.2.19: Power losses observed in Model 6 at 1, 2 and 3L/min. The dashed lines denote the regions where the flow became turbulent in the LPA, while the red line describes the power losses at EPVR. Power losses and EPVR points were fitted with a second order polynomial curve.

6.3 Anatomical Intra-Atrial Model

6.3.1 Power Losses

The power losses observed in the anatomical intra-atrial model (Figure 6.3.1) were two orders of magnitude higher than those observed in Models 1 to 5 and twice as high as those observed in Model 6. They demonstrated a high sensitivity to pulmonary flow split, increasing at an always-faster rate as the amount of the flow going to the LPA increased. Minimum power losses were observed when 60-70% of the flow was directed into the RPA and were 30-40% lower than those occurring at a 30/70 RPA/LPA flow split for the same total cardiac output. The EPVR points fell within the minimum power loss region, going from a 59/41 RPA/LPA split at 1L/min to a 65/35 RPA/LPA split at 3L/min.

For flow regime assessment, Reynolds numbers were computed based upon the hydraulic diameters 2cm away from the connection. Caval flow remained in the laminar regime for all flow rates ($Re < 1800$). At 3L/min, LPA flow became turbulent ($Re > 2300$) when 50% of the total flow or more was directed to the LPA. Similarly, the RPA flow became turbulent at 3L/min when more than 60% of the flow was directed to the RPA. The pulmonary flow splits at which one the PA flow is turbulent, are represented with a dashed line in Figure 6.3.1.

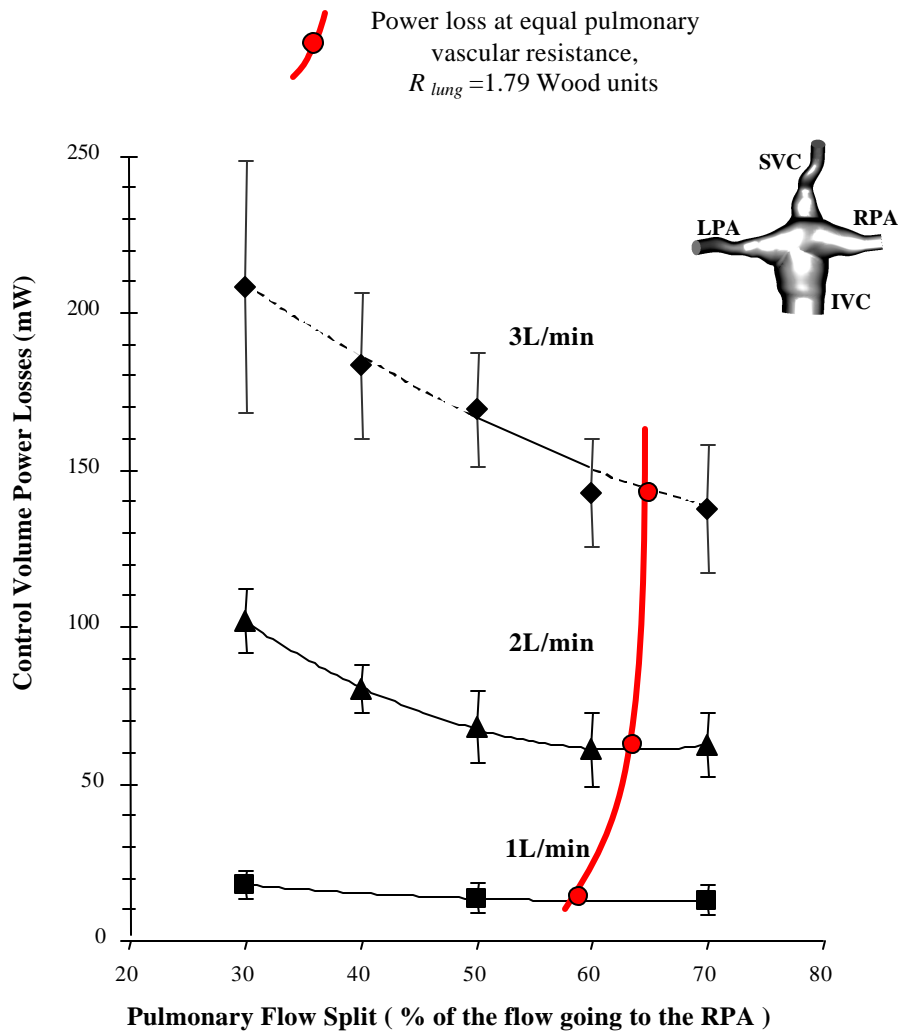


Figure 6.3.1: Power losses observed in the anatomical intra-atrial model at 1, 2 and 3L/min. The dashed lines denote the regions where the flow became turbulent either in the LPA (3L/min, %RPA < 50%) or in the RPA (3L/min, %RPA > 60%), while the red line describes the power losses at EPVR. Power losses and EPVR points were fitted with a second order polynomial curve.

Table 6.3.1: Pressure drops and power losses corresponding to equal pulmonary vascular resistance conditions ($R_{Lung} = 1.79$ Wood units) for the anatomical intra-atrial model at 1, 2 and 3 L/min.

Q_{Total} (L/min)	%RPA	Pressure with reference to the IVC (mmHg)			Power Loss (mW)
		SVC	RPA	LPA	
1	59	-0.72	-5.95	-6.34	12.78
2	64	4.86	-11.82	-12.74	60.86
3	65	6.18	-18.67	-19.91	141.19

6.3.2 Qualitative Flow Field Assessment

Flow visualization (Figures 6.3.2 and 6.3.3) underscored the enormous complexity of the flow in the anatomical intra-atrial TCPC even for flow rates well within the laminar flow regime (Re ranging from 300 to 800 at 1L/min). To better appreciate the complexity and dynamical richness of the flow in this region, the complete video recording from the flow visualization experiment at 1L/min is attached as Animations 6.3.1 and 6.3.2. At higher flow rates, 3L/min, the unsteadiness was too intense to allow for good quality flow visualization. Both in the experiments and in the numerical simulations this complex unsteady flow emerged naturally, without any imposed external forcing other than ambient laboratory disturbances present in any experiment and numerical disturbances due to truncation and other discretization errors, respectively.

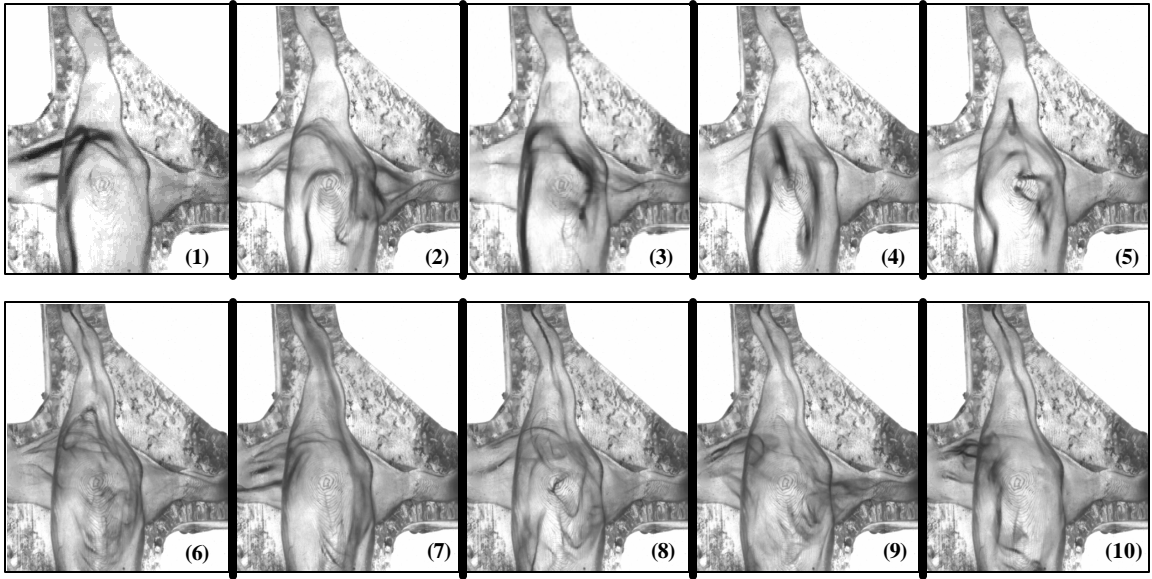


Figure 6.3.2: Qualitative flow visualization of the anatomical intra-atrial model at 1L/min and with a pulmonary flow split of 70/30 RPA/LPA. (1) to (5): dye injected in the SVC; (6) to (10): dye injected in the IVC.

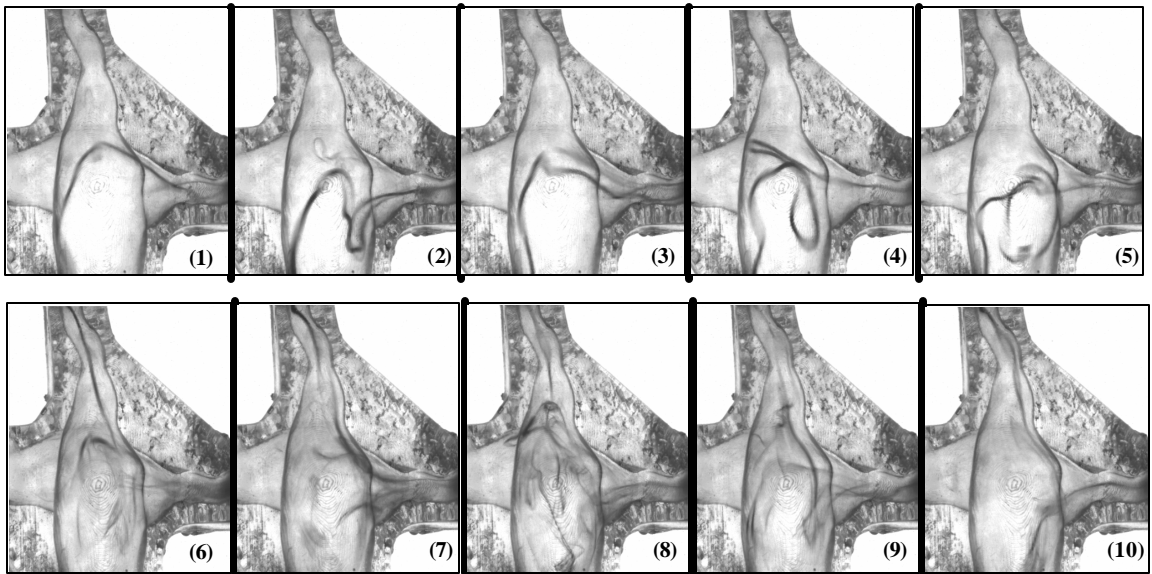
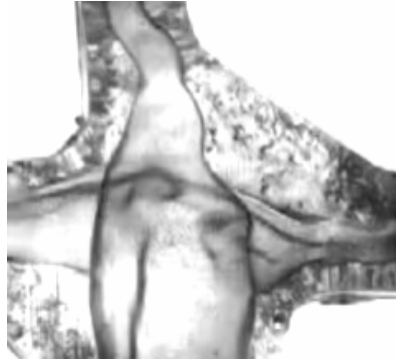
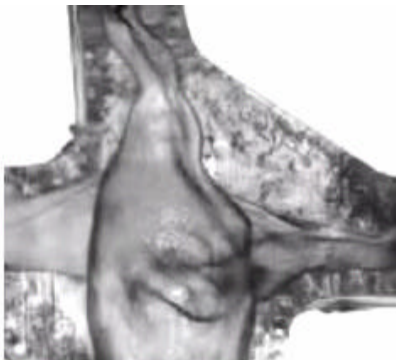


Figure 6.3.3: Qualitative flow visualization of the anatomical intra-atrial model at 1L/min and with a pulmonary flow split of 30/70 RPA/LPA. (1) to (5): dye injected in the SVC; (6) to (10): dye injected in the IVC.



Animation 6.3.1: Flow visualization of the anatomic intra-atrial model at 1 L/min, with a 60/40 IVC/SVC and 70/30 RPA/LPA flow split. Dye injected within the IVC stream. (MOV, 82K, de_zelicourt_diane_a_200412_mast_anim631_intraatrial_fv.mov)



Animation 6.3.2: Flow visualization of the anatomic intra-atrial model at 1 L/min, with a 60/40 IVC/SVC and 70/30 RPA/LPA flow split. Dye injected within the SVC stream. (MOV, 43K, de_zelicourt_diane_a_200412_mast_anim632_intraatrial_fv.mov)

Figures 6.3.2 and 6.3.3 clearly show complex, rotational flow patterns and intense unsteadiness of the flow in the connection region. The SVC stream (Figures 6.3.2 and 6.3.3, (1) to (5)) was directed towards the anterior wall of the pouch and went far down into the connection area, while the flow towards the posterior wall showed less disturbance and was dominated by the IVC flow (Figures 6.3.2 and 6.3.3, (6) to (10)). The onset of the unsteadiness appeared to be the result of flow instability at the saddle point in the center of the connection where the IVC and SVC collided and divided laterally into the LPA and RPA. The instability manifested itself in the form of seemingly random meandering of the flow. There were instants in time during which IVC flow from the anterior side entered the connection region, recirculated, and exited almost exclusively through the LPA as in Figure 6.3.2-(1). At other moments, flow from the same region was almost equally divided within the LPA and RPA, Figure 6.3.2-(2), or entered the RPA in its entirety, Figure 6.3.2-(3). As can be seen from Figures 6.3.2 and 6.3.3, similar chaotic meandering was observed for the SVC flow.

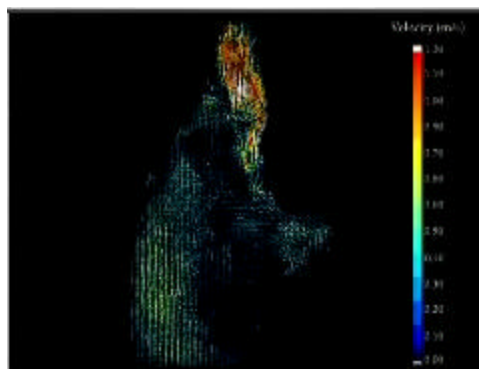
Similar instabilities were observed in simplified geometries [Bolzon, 2002; Khunatorn, 2003]. Bolzon et al. numerically calculated the onset of instability to be at $Re=1100$, for their larger (SVC and IVC diameter =11.2 mm) idealized model having caval offset. Here, the extra volume of the pouch set up an additional spatial degree of freedom, thus allowing the flow instability to become clearly visible and prevail for all flow conditions. The frequency and overall complexity of the flow increased with increasing flow rates and Reynolds numbers. Despite much higher power losses, there was slightly less disturbances at 30/70 RPA/LPA (Figure 6.3.3, (1) to (5)) than at 70/30 RPA/LPA (Figure 6.3.2, (1) to (5)).

The IVC was fairly large. It stood in the sagittal plane as the RPA and connection area and went straight up towards the pouch. The SVC had a tortuous shape and curved path. Additionally, it enlarged towards the anastomosis location. This divergent geometric configuration resulted in a flow separation region (Figures 6.3.2 and 6.3.3, (6) to (10)) with fast flow on one side and slow recirculating flow on the other. Coming all the way back up towards SVC, the IVC flow was occasionally observed to reside in this recirculation region (Figure 6.3.2 (4) or 6.3.3 (8)). In the same fashion as the SVC, the IVC became wider towards the anastomosis creating a large pouch. An IVC flow recirculation could thus have been expected in the opening of the IVC. Instead, due to its higher kinetic energy content, the SVC stream overrode the IVC stream going far down into the IVC and swirling clockwise along the anterior wall. The higher kinetic energy content resulted from the smaller dimensions of the SVC, while the clockwise orientation of the swirl resulted from the orientation of the SVC, which directed the SVC stream towards the left and anterior aspect of the connection.

Finally, the flow in the PA's was characterized by a helical pattern through all the different flow splits. The helix within the LPA was tighter than within the RPA. This was believed to be due to the faster tapering of the LPA vessel, which accelerated the flow into the LPA. The smoother RPA connection, led to a wider helical pattern. This remark is of importance as the tighter the helical pattern, the longer the distance the fluid will have to travel along the vessel wall. This may in turn result in increased energy dissipation in the LPA as a result of wall friction.

6.3.3 Quantitative Flow Field Assessment

Quantitative information on the flow fields was obtained using DPIV, LDV and CFD results. The DPIV measurements underscored once again the high instabilities observed throughout the entire connection (Animation 6.3.3). However, the maximum sampling rate of our DPIV hardware (~ 15 double-frames/s) was not high enough for us to perform a frequency analysis of the flow instabilities. Additionally, no periodicity could be identified in the observed instabilities; we thus only considered the time-average DPIV velocity fields. Those revealed that the SVC flow exited the vein as a high velocity jet, and dove down into the IVC along the left anterior wall before going back up along the right anterior wall (Figure 6.3.4-a). The IVC flow became more dominant towards the posterior side. Along the posterior wall (Figure 6.3.4-d), the flow was completely governed by the IVC stream. The intermediate planes that are shown in Figures 6.3.4-b and 6.3.4-c, exhibited the recirculation region within the connection, as well as the flow separation in the SVC previously observed in the flow visualization studies.



Animation 6.3.3: Instantaneous DPIV velocity fields of the anatomic intra-atrial model at 3 L/min and for the following flow splits: 60/40 IVC/SVC and 70/30 RPA/LPA. The plane being imaged corresponds to the laser height of 12 mm. (MOV, 1,635K, de_zelicourt_diane_a_200412_mast_anim633_intraatrial_piv.mov)

As will be discussed in Chapter VII, the time-average velocities obtained via DPIV were systematically lower than those computed numerically. In order to check whether there was any bias in the experimental measurements, additional 2D-LDV data were acquired on the two inflows and outflows. Similarly to the DPIV measurements these 2D-LDV data quantified the sagittal velocities. Results for the IVC and SVC are displayed in Figure 6.3.5. The SVC flow came down the anterior wall. Peak SVC velocities were of about 1.0 m/s and were directed towards the left-anterior aspect of the connection. Flow reversal was observed along the posterior aspect of the SVC, with flow going back up into the SVC at 0.2 m/s. The IVC flow on the other hand was skewed towards the right hand side of the pouch, due to the important recirculation that was taking place within the connection area. IVC velocity magnitude was of about 0.5 m/s. Reverse flow of the same order of velocity magnitude (0.4 m/s) was observed along the left-anterior aspect of the IVC cross-section. These findings correlated well with the flow structure and velocity magnitude observed in DPIV, with the high velocity jet entering the pouch through the SVC and going far down into the IVC along the left-anterior wall.

LDV measurements were also performed in the RPA and LPA. However, the resulting velocity magnitudes were not consistent with the DPIV measurements, or even a rough estimate of what the velocity magnitudes should have been. For example, at 3 L/min with a 50/50 RPA/LPA flow split, the velocity in the LPA was expected to be higher than 1 m/s. The LDV measurements for this flow condition yielded velocity magnitudes lower than 0.2 m/s. The fact that we used 2D LDV and did not acquire all three velocity components was not sufficient to explain such an underestimation of the

velocity magnitudes. The error in these LDV measurement was believed to result from the difficult optical access to the Pa's. As a result, the data acquisition rates in these vessels did not exceed 1 Hz, which may have biased the resulting LDV velocity measurements.

LDV and DPIV experiments were run independently and yielded similar velocity magnitudes and flow fields in the IVC and SVC, which was encouraging for the reliability of our optical measurements through the transparent RP resin. However, as was the case in the PA's, the limited transparency of the RP resins may severely impair the quality of the data. A cautious design of the *in vitro* models is thus required so as to provide optimal optical access to the measurement locations. In our case, the model was originally meant to allow for DPIV measurements, with two flat surfaces on the anterior and posterior side of the model. As a result the LDV laser beam had to go across a thick RP wall before reaching the PA's, which resulted in low data acquisition rates.

Due to optical limitations, only the sagittal velocity fields could be acquired using the DPIV or the LDV systems. Validated CFD results (see Chapter VII) were thus used to provide further information on the flow structures in the coronal and axial directions (Figure 6.3.6-e and -f), as well as to estimate the total velocity magnitude, including all three velocity components (Figure 6.3.6-a to -d), which could not be captured through 2D DPIV. Because of a smaller vessel diameter, the SVC stream was of 5 to 6 times faster than the one coming out of the IVC. Similarly, due to smaller vessel dimensions, the LPA stream two times faster than the RPA stream at 50/50 RPA/LPA.

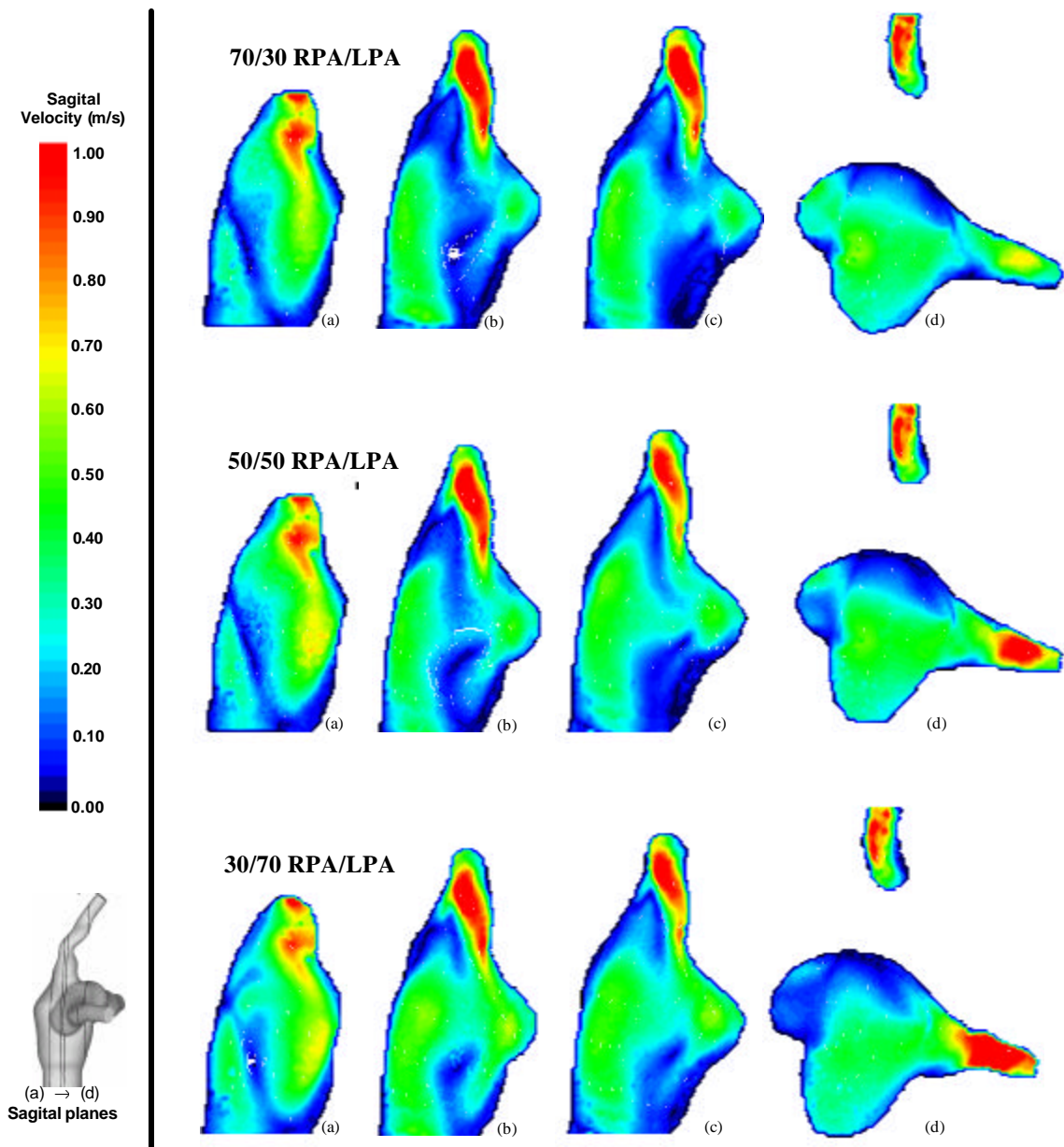


Figure 6.3.4: Quantitative assessment of the flow field using DPIV at 3L/min with varying pulmonary flow splits. The data acquisition planes are indexed from the most anterior (a) to the most posterior (d), and correspond to the laser heights 8 mm, 11 mm, 12 mm and 18 mm (Table 5.3.1).

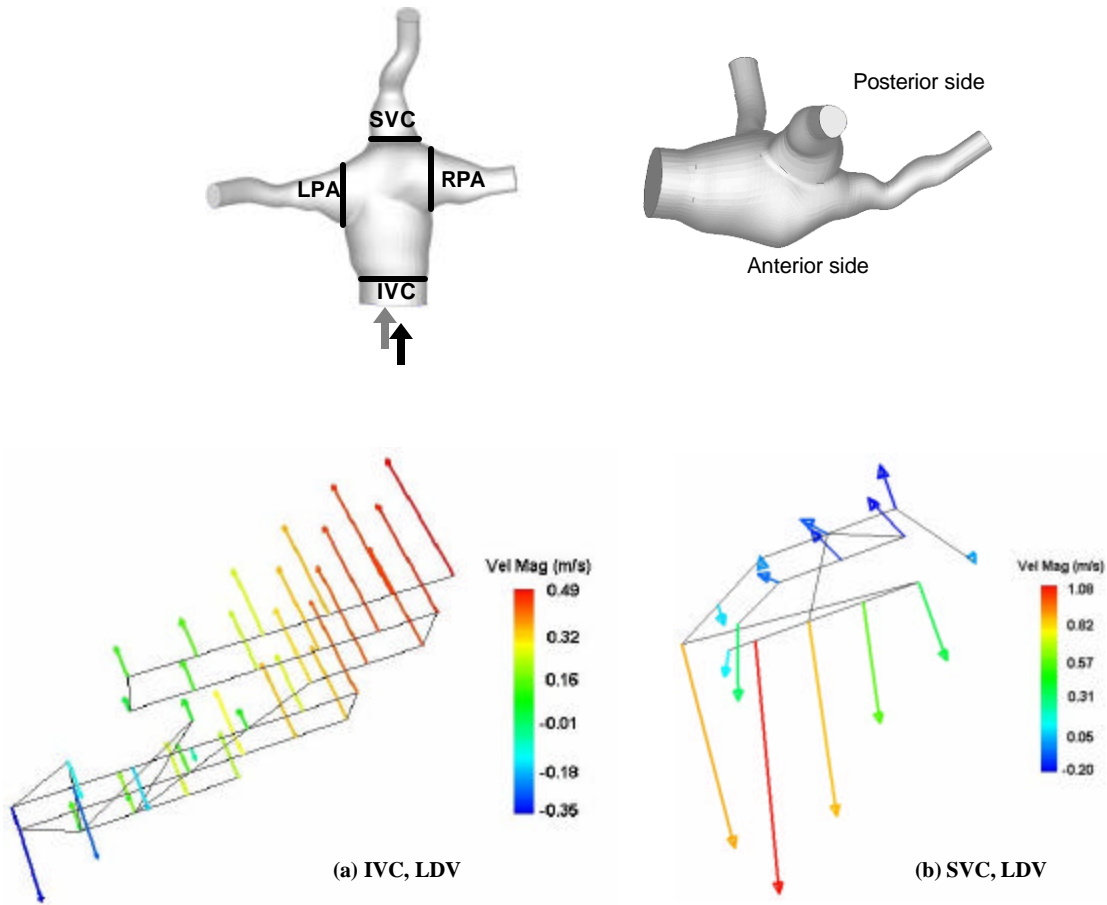


Figure 6.3.5: Quantitative assessment of the IVC and SVC flow profiles using LDV at 3L/min. The arrow shows the angle under which the two cross-sections are viewed. (a) Out-of-plane IVC velocity component. (b) 2D sagittal SVC velocities.

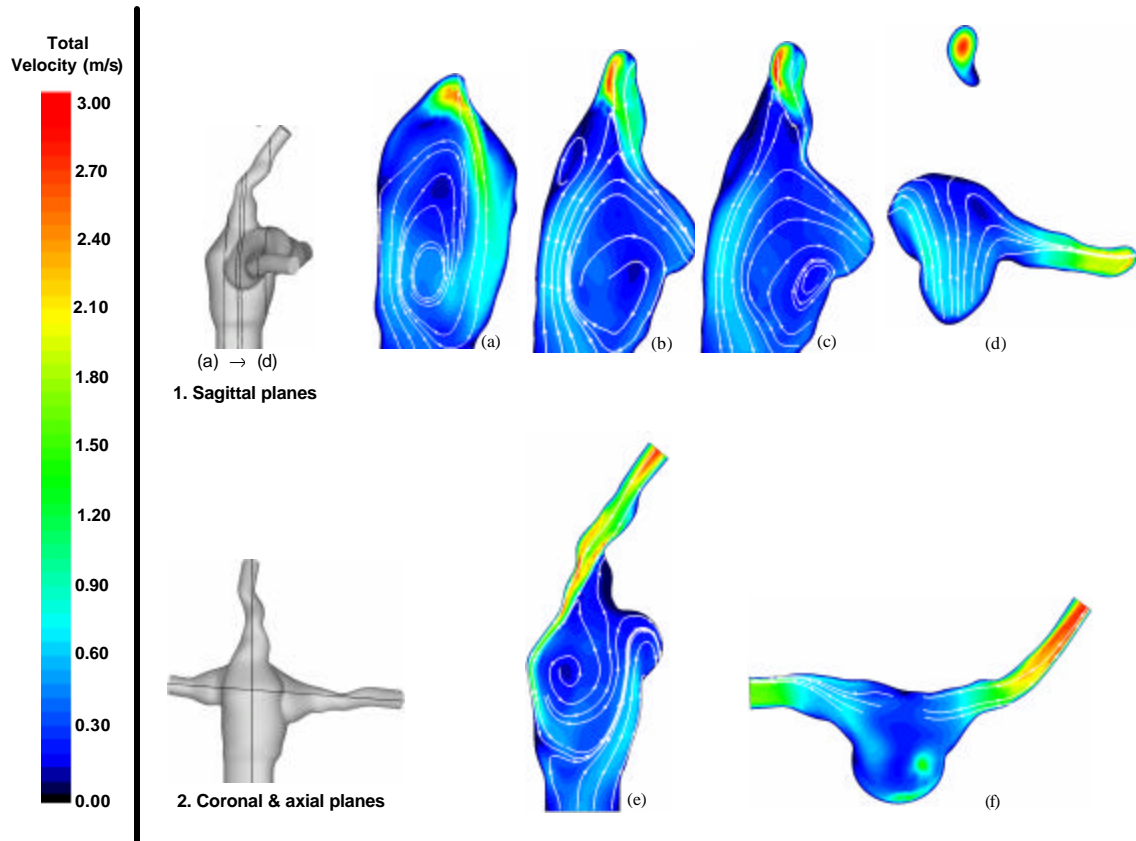


Figure 6.3.7: Assessment of the total velocity using CFD (1st order-accurate, Fidap) at 3L/min; pulmonary flow split: 50/50 LPA/RPA. The location of the imaged planes is shown in Schematics 1 and 2. The sagittal planes are indexed from the most anterior (a) to the most posterior (d). They correspond to the CFD plane heights of 6.5 mm, 9.5 mm, 10.5 mm and 16.5 mm (Table 5.3.1) and are the numerical counterpart of the experimental flow fields shown in Figure 6.3.4.

6.3.4 Flow Structure Summary

Because of the highly three-dimensional nature of the flow in the connection region, it is very difficult to convey its complete structure with a few instantaneous snapshots or video animations from one particular view angle. For that reason we analyzed both the laboratory observations and numerical flow fields from different angles and compiled the main flow features in the sketches shown in Figure 6.3.7.

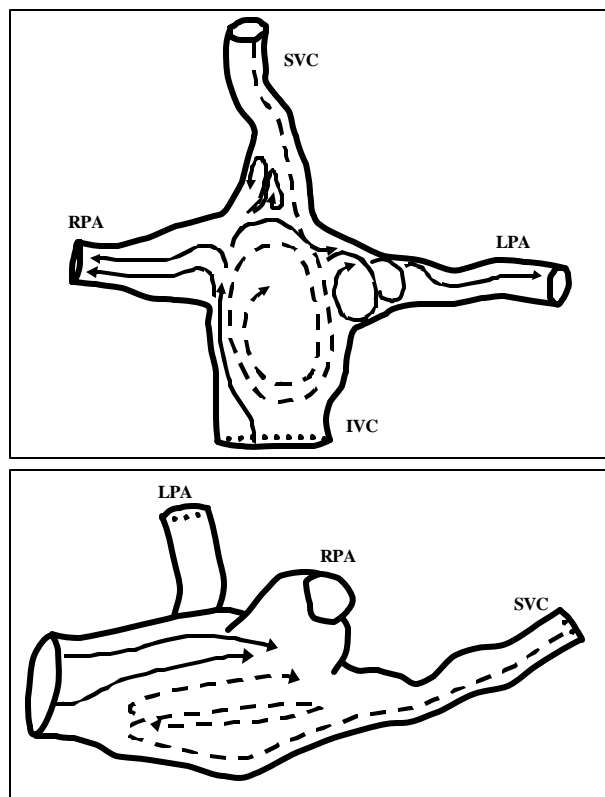


Figure 6.3.7: Schematic of the flow structure observed in the anatomical intra-atrial model at 1L/min. The SVC flow was 5 to 6 times faster than the IVC stream and recirculated deep down into the IVC. Flow separation was observed in the SVC. A stagnation point appeared at the end of the full turn of the recirculating SVC flow and was located at the RPA inlet proximal to the SVC. Pulmonary flow followed a helical pattern.

6.4 Anatomical Bilateral SVC Model

Following the same protocol as the one previously developed for the anatomical intra-atrial model, an anatomical bilateral SVC with an extra-cardiac conduit was also studied. The main geometric characteristics of this second anatomical model were that: (i) there were three flow inlets, (ii) the vessel diameters were bigger than that of the anatomical intra-atrial TCPC studied earlier, with an IVC diameter of about 12 mm, while the SVCs were about 8 mm in diameter, (iii) the IVC faced the RSVC while the LSVC and IVC were offset by 49 mm, (iv) the extra-cardiac conduit yielded a smooth geometry for the IVC track and all VCs were coplanar. Qualitative and quantitative characterization of the resulting flow field is provided in the subsequent sections.

6.4.1 Pressure Drops and Power Loss

Figure 6.4.1 shows the pressure drops across the bilateral SVC model at 2L/min as a typical example of the pressure behavior through this model. There was no statistically significant difference between the three caval pressures through all flow conditions. As was expected, the pulmonary pressures decreased as more flow was forced through the corresponding PA. However, except at 70/30 RPA/LPA, the LPA pressure remained lower than that of the RPA for all the tested pulmonary flow splits, meaning that a higher IVC-to-PA pressure drop was needed to drive the flow through the LPA than through the RPA. Accordingly the EPVR point favored right lung perfusion and corresponded to an RPA/LPA flow split of approximately 60/40 (Table 6.4.1). The EPVR point did not depend on the total cardiac output, going from 61/39 RPA/LPA at 2 and 3 L/min to 62/38 RPA/LPA under exercise conditions at 4L/min.

Interestingly the EPVR point did not match with the minimum energy dissipation point. Similarly to the LPA pressure (Figure 6.4.1), the power lost across the bilateral SVC connection highly depended upon the pulmonary flow split that was imposed. At 2, 3 and 4 L/min, energy dissipation was minimal for a 70/30 RPA/LPA flow split where it was, respectively, 59, 64 and 48 % lower than at a 30/70 RPA/LPA pulmonary split and 10 to 15% lower than at the corresponding EPVR point (Figure 6.4.2). Power losses at the EPVR point in the anatomical bilateral SVC model were one order of magnitude higher than those observed at the EPVR point and for the same flow rates in the simplified glass Model 1, but only 110 to 200 % higher than in Model 3 and about half of those observed in the anatomical intra-atrial model (80 to 90% lower).

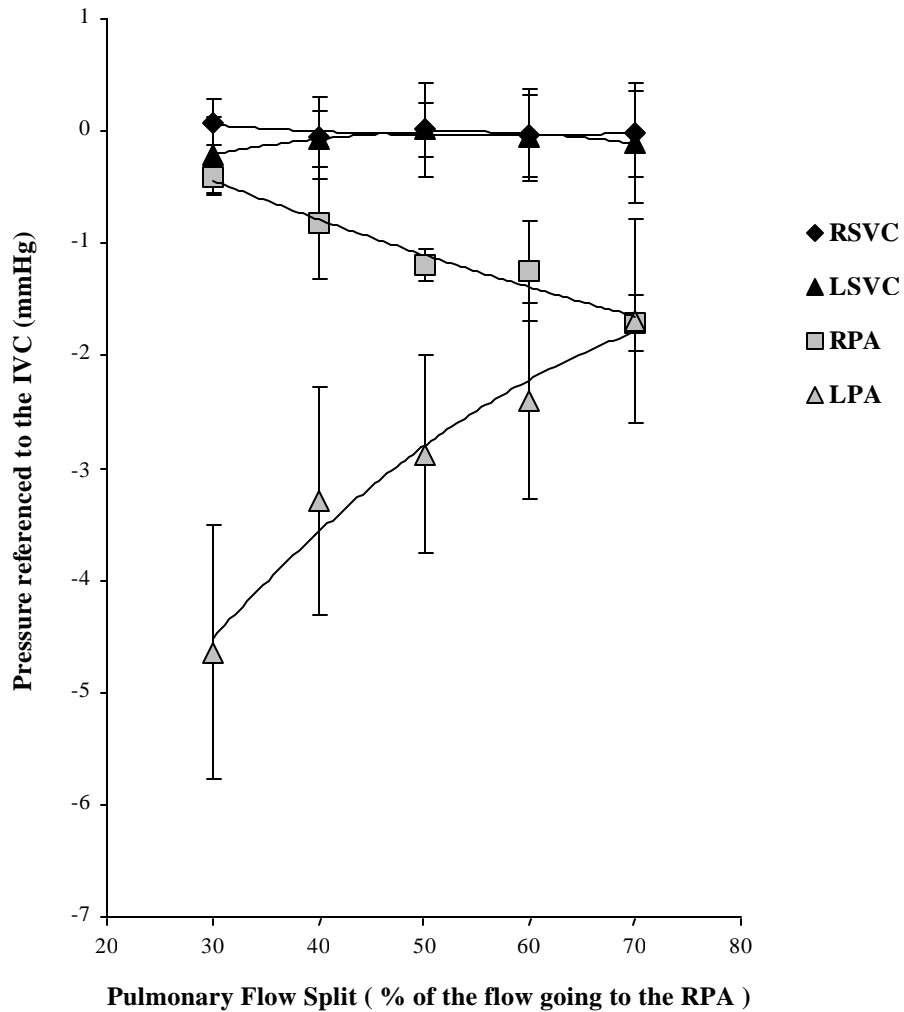


Figure 6.4.1: Pressure measurements for the anatomical bilateral SVC at 2L/min, the measurements were taken in the RSVC, LSVC, RPA and LPA with respect to the IVC.

Table 6.4.1: Pressure drops and power losses corresponding to equal pulmonary vascular resistance conditions ($R_{Lung} = 1.79$ Wood units) for the anatomical bilateral SVC model at 2, 3 and 4 L/min.

Q_{Total}	%RPA	Pressure with reference to the IVC (mmHg)				Power Loss (mW)
		RSVC	LSVC	RPA	LPA	
2	61	-0.03	-0.04	-1.42	-2.29	5.63
3	61	0.10	0.18	-2.37	-3.40	11.95
4	62	-0.12	0.01	-5.14	-7.00	37.87

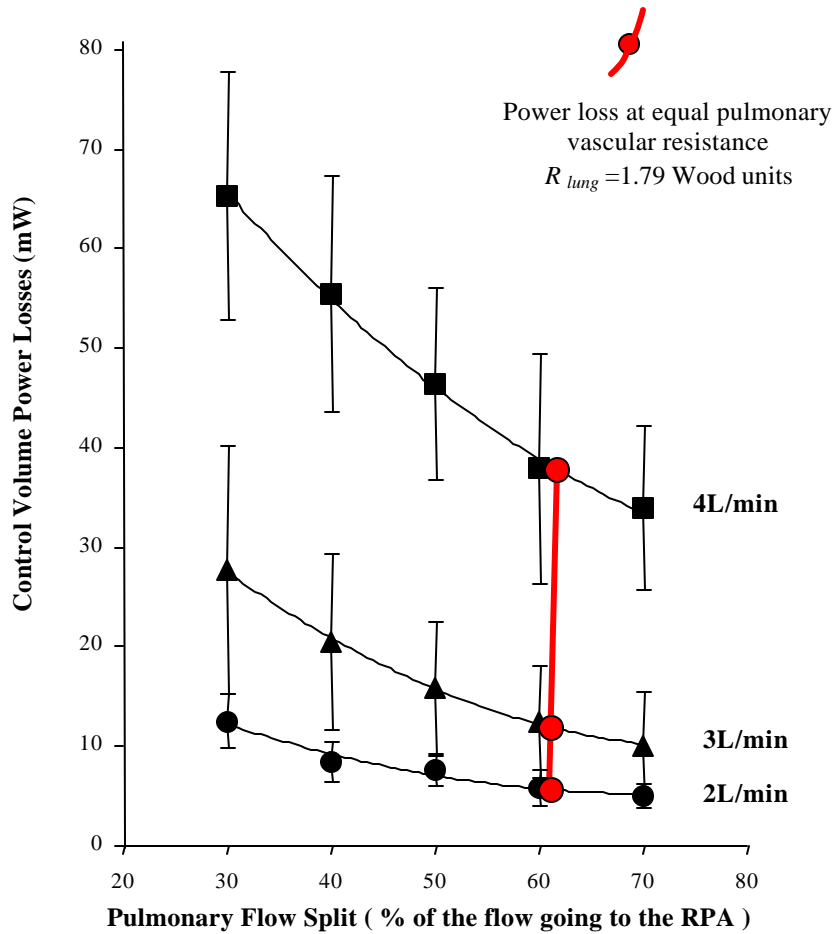


Figure 6.4.2: Hydrodynamic power losses measured in the anatomical bilateral SVC model at 2, 3 and 4 L/min. The power losses at equal pulmonary resistance, which are described by the red line, corresponded to a pulmonary flow split of about 60/40 RPA/LPA irrespective of the total flow rate.

6.4.2 Qualitative Flow Structure

Flow visualization was performed at 2L/min for three different pulmonary flow splits: 70/30, 50/50 and 30/70 RPA/LPA. Run under steady flow conditions, this TCPC connection was characterized by smooth and steady flow fields. The only disturbances were observed at the point where IVC and RSVC flow collided before going into the PA's. When most of the flow was directed to the RPA, IVC and RSVC flows went nearly exclusively into the RPA, while the LPA was perfused with the LSVC flow (Figure 6.4.3). IVC flow went smoothly into the RPA (Figure 6.4.3-a) while the RSVC flow made a 270° turn before entering the RPA (Figure 6.4.3-b), which sometimes generated slight disturbances and flow recirculation along the posterior aspect of the RPA at the anastomosis site (Figure 6.4.4). Streaklines were very seldom observed in between the two SVCs: since all of the LSVC flow, which is to say 22.5% of the total cardiac output, went into the LPA, there was very little contribution from either the IVC or the RSVC to the LPA flow.

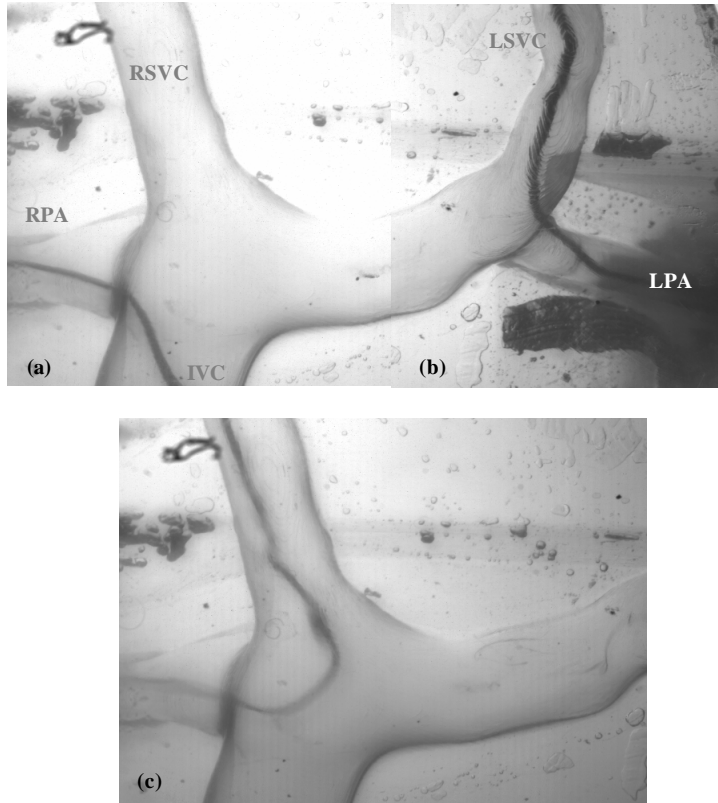


Figure 6.4.3: Qualitative flow visualization of the anatomical bilateral SVC model at 2L/min and with a pulmonary flow split of 70/30 RPA/LPA. The dye was injected in turns from the IVC (a), from the LSVC (b) and finally from the RSVC (c).

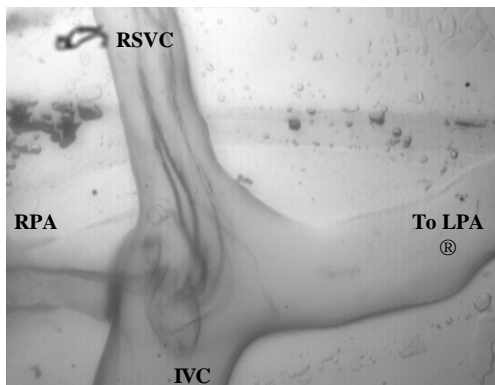


Figure 6.4.4: At a pulmonary flow split of 70/30 RPA/LPA, flow recirculation and slight disturbances were observed in the RSVC stream along the posterior aspect of the RPA-IVC-RSVC anastomosis.

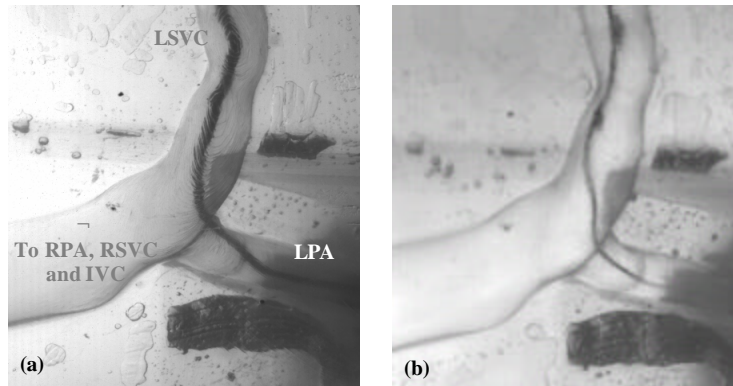


Figure 6.4.5: The LSVC flow was steady for all pulmonary flow splits. It followed the same flow path irrespective of whether most of the flow went into the RPA (a), or into the LPA (b).

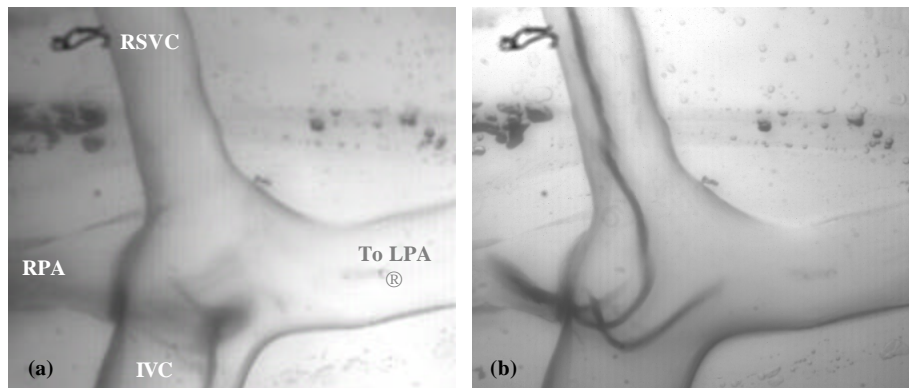


Figure 6.4.6: Qualitative flow visualization of the anatomical bilateral SVC model at 2L/min and with a pulmonary flow split of 50/50 RPA/LPA. The dye was injected in turns from the IVC (a) and from the RSVC (b).

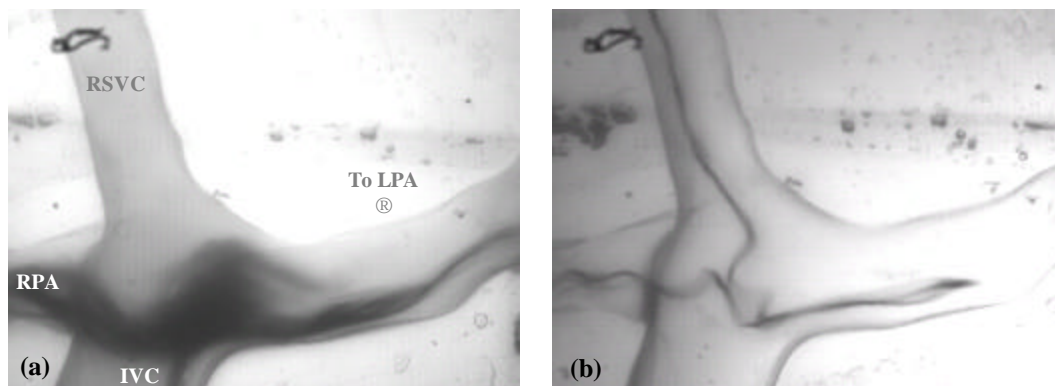
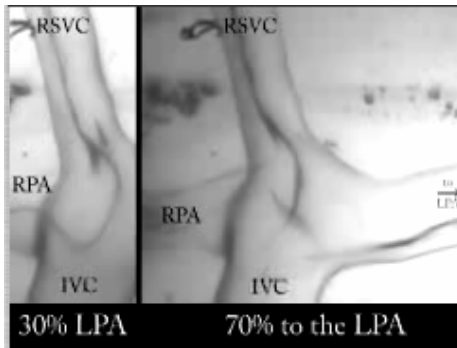
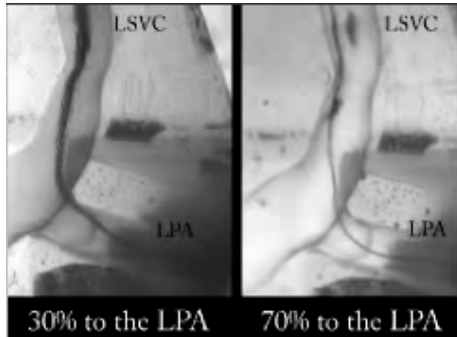


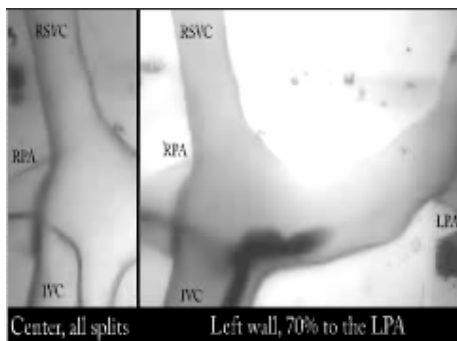
Figure 6.4.7: Qualitative flow visualization of the anatomical bilateral SVC model at 2L/min and with a pulmonary flow split of 30/70 RPA/LPA. The dye was injected in turns from the IVC (a) and from the RSVC (b).



Animation 6.4.1: Flow visualization of the anatomic bilateral SVC model at 2 L/min. The dye is injected at the center of the RSVc stream. There was no noticeable difference between the flow behavior at 30/70 RPA/LPA and at 70/30 RPA/LPA. (MOV, 158K, de_zelicourt_diane_a_200412_mast_anim641_bilateral_fv.mov)



Animation 6.4.2: Flow visualization of the anatomic bilateral SVC model at 2 L/min. The dye is injected at the center of the LSVc stream. There was no noticeable difference between the flow behavior at 30/70 RPA/LPA and at 70/30 RPA/LPA. (MOV, 149K, de_zelicourt_diane_a_200412_mast_anim642_bilateral_fv.mov)



Animation 6.4.3: Flow visualization of the anatomic bilateral SVC model at 2 L/min. The streaklines observed when injecting the dye at the center of the IVC (Left) were the same irrespective of the flow rate. The streaklines (Right) obtained when injecting the dye along the left side of the IVC demonstrated higher flow disturbances than the central flow. (MOV, 184K, de_zelicourt_diane_a_200412_mast_anim643_bilateral_fv.mov)

Contrary to the RSVC stream, the LSVC stream was perfectly stable. This held true for all pulmonary flow splits with no significant change in the LSVC flow path (Figure 6.4.5). As more flow was directed to the LPA, IVC and RSVC flows split between the two PA's. At 70/30 RPA/LPA, the IVC stream was oriented towards the RPA even before reaching the connection site (Figure 6.4.3-a). At the equal pulmonary flow split, the IVC stream went straight into the connection (Figure 6.4.6-a) where it collided into the RSVC stream, yielding a stagnation region in the middle of the connection. Similarly, the RSVC stream first collided into the IVC stream before splitting into both PA's (Figure 6.4.6-b). Most of the IVC and RSVC flows still went into the RPA. The IVC and RSVC flow behavior at a 30/70 RPA/LPA flow split was similar to what they were at 50/50 RPA/LPA. IVC and RSVC streams collided before splitting into the PA's yielding a stagnation region at the center of the connection site (Figure 6.4.7). The major difference was that for that flow split, the section in between the two SVCs was obviously perfused with both IVC and RSVC flows.

6.4.3 Quantitative Flow Structure

Quantitative analysis of the flow field using DPIV confirmed what had been observed by flow visualization. As can be observed from Animations 6.4.1, 6.4.2 and 6.4.3, the flow field was nearly steady, except in the region where IVC and RSVC streams collided. When 70% of the flow was directed to the RPA (Figure 6.4.8), a vast majority of the IVC stream went into the RPA. Part of it entered the RPA directly, while the rest merged with the incoming RSVC stream and then recirculated in the connection area before entering the RPA. The DPIV plane imaged in Figure 6.4.8, roughly went

through the middle of all three VCs. At that height the RSVC was the only one to contribute to the right-to-left flow. In addition to the fact that hardly any flow went from the RSVC and IVC towards the LPA, it was found that the flow in between the two SVCs was slow (about 0.06m/s) when compared to the other flow streams (0.12 to 0.18 m/s). At 50/50 and 30/70 RPA/LPA (Figures 6.4.9 and 6.4.10), the colliding region between the IVC and RSVC streams could clearly be identified. At equal pulmonary flow splits, mean flow velocity was uniform throughout the entire connection (about 0.1m/s) while, at a 30/70 RPA/LPA flow split, high velocities (0.37 m/s) were observed in between the two SVCs.

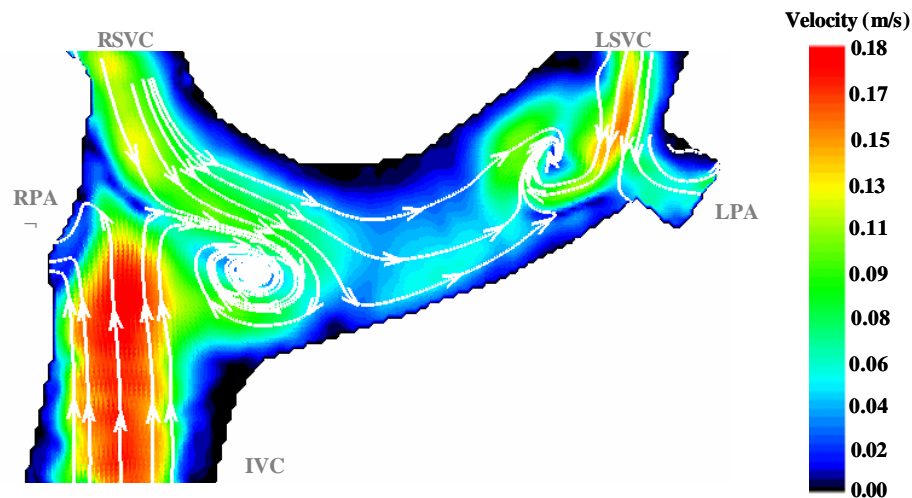


Figure 6.4.9: Quantitative assessment of the flow field through the entire bilateral SVC model using DPIV at 2L/min with a 70/30 RPA/LPA flow split.

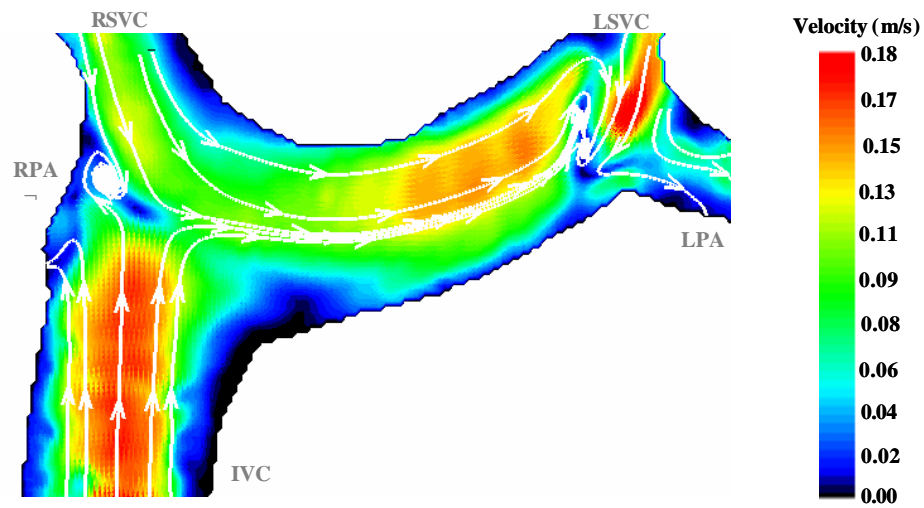


Figure 6.4.10: Quantitative assessment of the flow field through the entire bilateral SVC model using DPIV at 2L/min with a 50/50 RPA/LPA flow split.

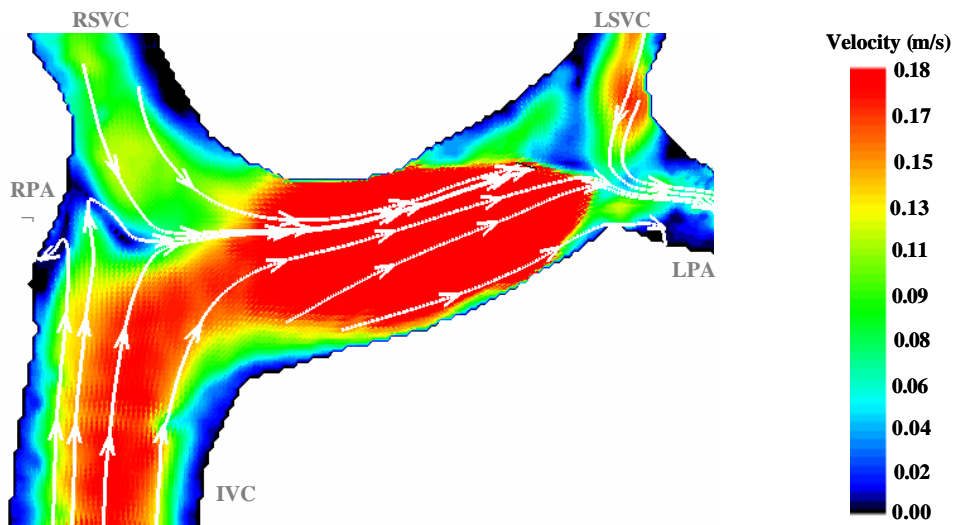


Figure 6.4.11: Quantitative assessment of the flow field through the entire bilateral SVC model using DPIV at 2L/min with a 30/70 RPA/LPA flow split.

The LSVC flow went exclusively to the LPA. Varying pulmonary flow splits only affected the IVC and RSVC flow fields. In order to characterize the relative contribution of the two caval flows to each one of the PA's, several planes were acquired going from the anterior (Figures 6.4.11-a to 6.4.13-a) to the posterior (Figures 6.4.11-e to 6.4.13-e) aspect of the IVC-RSVC-RPA connection site. At 70/30 RPA/LPA, the anterior side of the connection was dominated by the IVC stream (Figure 6.4.11-b), half of which went to the RPA while the other half went to the LPA. Going towards the posterior side of the connection, an increasing share of both IVC and RSVC flows went to the RPA. A clockwise recirculation region was identified at the IVC-to-MPA flare (Figure 6.4.11-c), which finally occupied the entire connection region along the posterior wall and redirected the RSVC flow towards the RPA.

At 50/50 RPA/LPA (Figure 6.4.12), a stagnation point was identified in the middle of the connection where IVC and RSVC streams collided, along the entire anterior-posterior axis. Both IVC and RSVC streams contributed to the LPA and RPA flows. At 30/70 RPA/LPA on the other hand, the only contribution to RPA flow seemed to be coming from the IVC as all the streamlines emanating from the RSVC were directed towards the LPA. It should be pointed out at this stage, that the path that would actually be followed by a particle or a blood cell launched in this connection is not described by the streamlines but by the streaklines, which were qualitatively acquired via flow visualization. Due to the flow instabilities that were observed at the inflow colliding point, streaklines and streamlines did not coincide, and as can be observed in Figure 6.4.7-b, some flow emanating from the RSVC was still seen to enter the RPA. It is thus important to keep in mind that the streamlines extracted from the averaged DPIV flow

fields can only provide an overall idea of the caval flow distribution between the two PA's but not an exact one.

Finally, when focusing on the LSVC region, a recirculation region was identified, facing the LPA. This recirculation was driven by the LSVC flow (Figure 6.4.14-a) and progressively disappeared as more flow came in from the IVC and RSVC (Figure 6.4.16-a). Flow in the LSVC itself was not affected by the change in flow pattern at its anastomosis site (Figures 6.4.14-b to 6.4.16-b). There was a small stenosis in the LSVC, which translated in a 50% increase in peak flow velocity, going from 0.13 m/s upstream of the stenosis up to 0.19 m/s at the stenosis site.

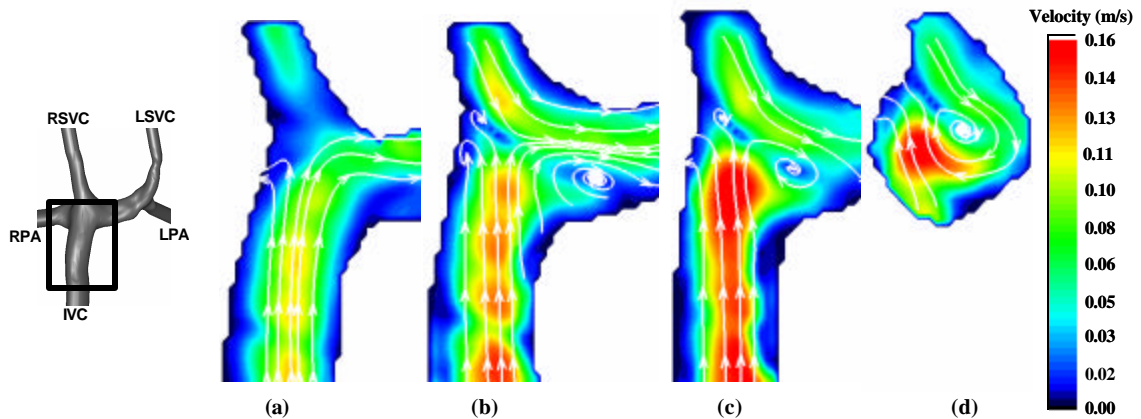


Figure 6.4.12: Quantitative assessment of the flow field using DPIV at 2L/min with a 70/30 RPA/LPA flow split and focusing on the IVC anastomosis site. The data acquisition planes were 2.5 mm apart (Figure 5.2.6) and are labeled from the most anterior (a) to the most posterior (d).

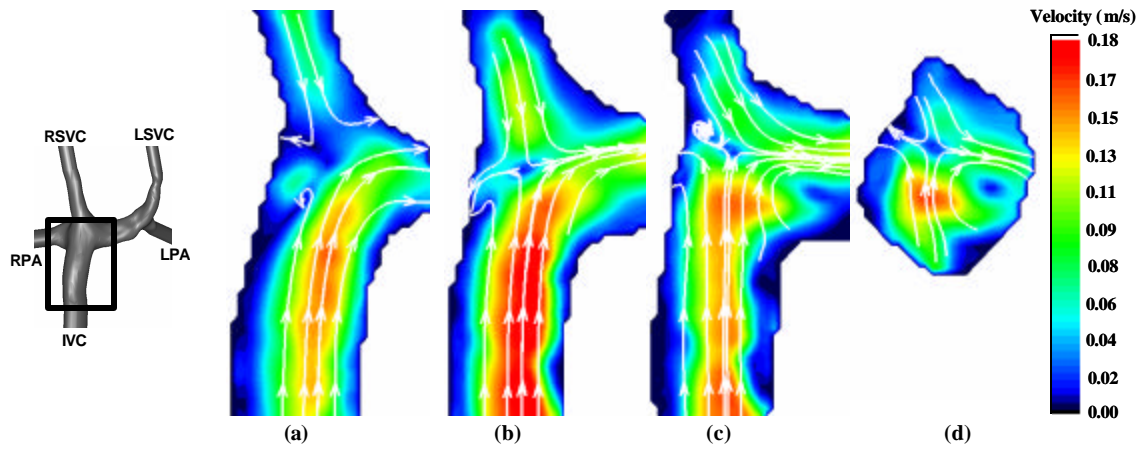


Figure 6.4.13: Quantitative assessment of the flow field using DPIV at 2L/min with a 50/50 RPA/LPA flow split and focusing on the IVC anastomosis site. The data acquisition planes were 2.5 mm apart (Figure 5.2.6) and are labeled from the most anterior (a) to the most posterior (e).

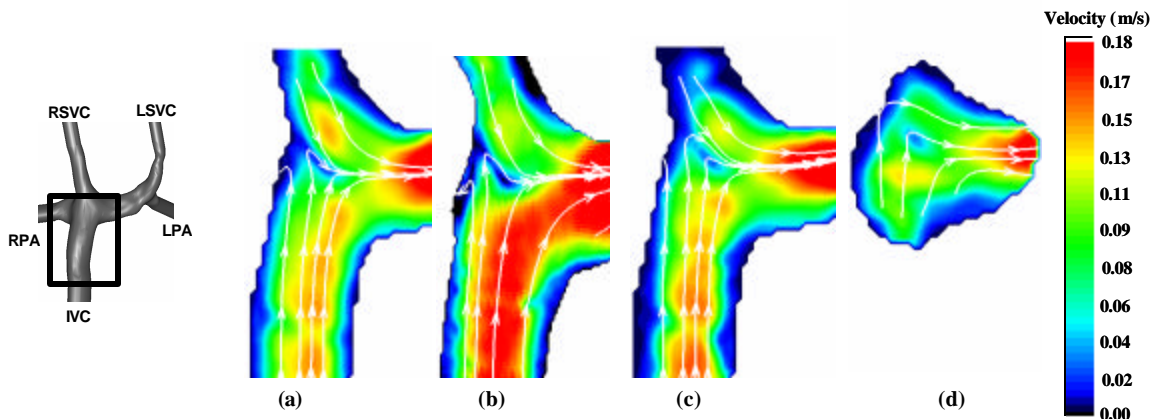


Figure 6.4.14: Quantitative assessment of the flow field using DPIV at 2L/min with a 30/70 RPA/LPA flow split and focusing on the IVC anastomosis site. The data acquisition planes were 2.5 mm apart (Figure 5.2.6) and are labeled from the most anterior (a) to the most posterior (e).

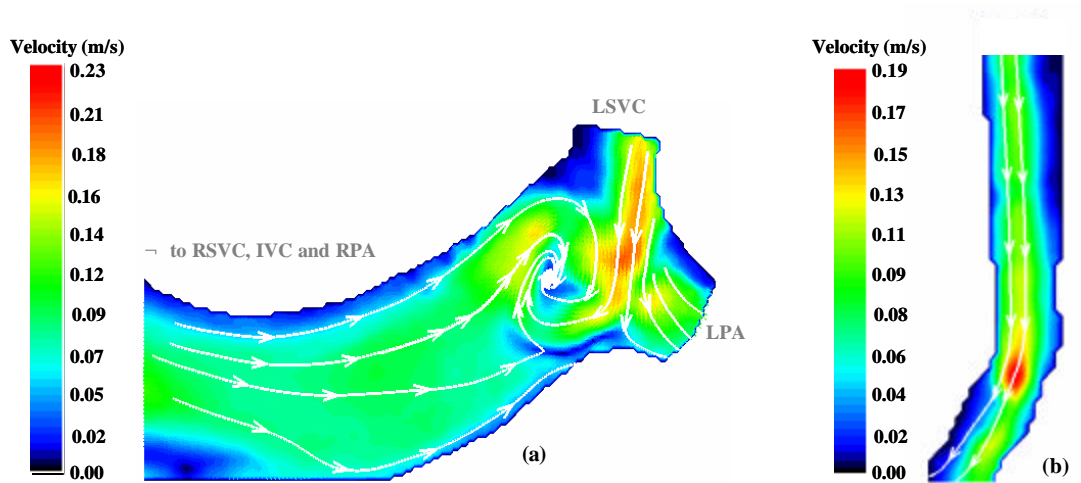


Figure 6.4.15: Quantitative assessment of the flow field using DPIV at 2L/min with a 70/30 RPA/LPA flow split and focusing on the LSVC anastomosis site (a) and on the LSVC vessel (b).

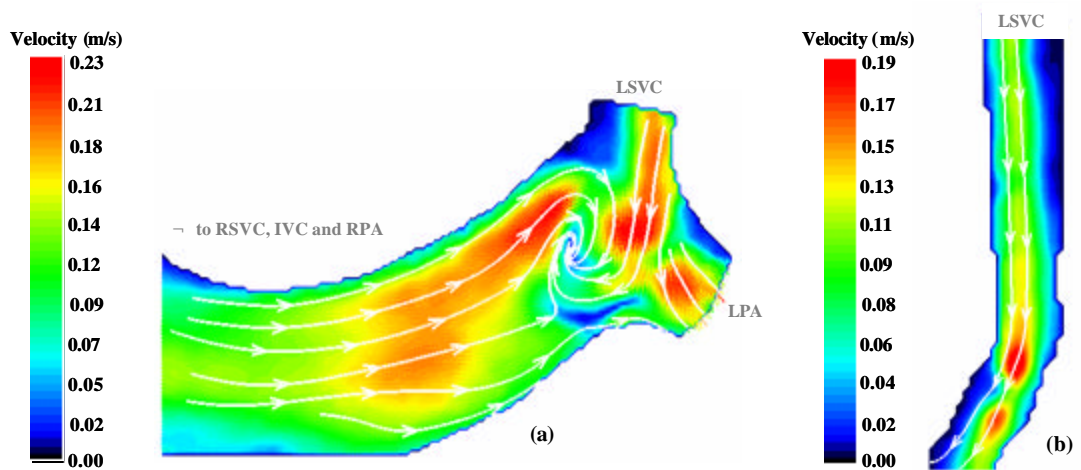


Figure 6.4.16: Quantitative assessment of the flow field using DPIV at 2L/min with a 50/50 RPA/LPA flow split and focusing on the LSVC anastomosis site (a) and on the LSVC vessel (b).

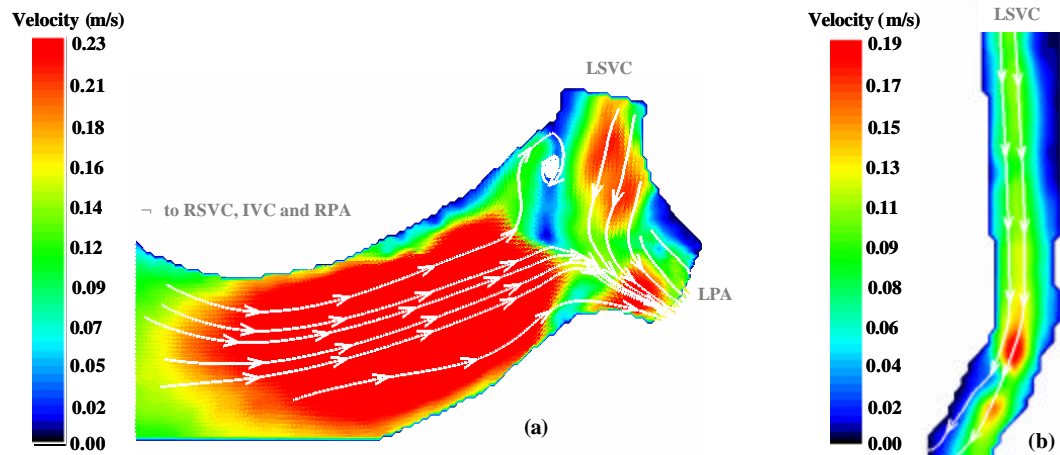


Figure 6.4.17: Quantitative assessment of the flow field using DPIV at 2L/min with a 30/70 RPA/LPA flow split and focusing on the LSVC anastomosis site (a) and on the LSVC vessel (b).

6.4.4 Flow Structure Summary

All the aforementioned flow characteristics are summarized in Figure 6.4.18 and Figure 6.4.19 for the 70/30 RPA/LPA and 30/70 RPA/LPA flow splits, respectively. It should be pointed out that, relying on the computed EPVR point, the physiological flow split should correspond to 60/40 RPA/LPA, flow split at which the flow field should be close to that described in Figure 6.4.18 and where only little flow travels in between the two SVCs. This may in turn lead to medical complications due to the uneven repartition of hepatic blood coming from the IVC or to the presence of slow flow motion regions, which will be discussed further in Chapter VIII.

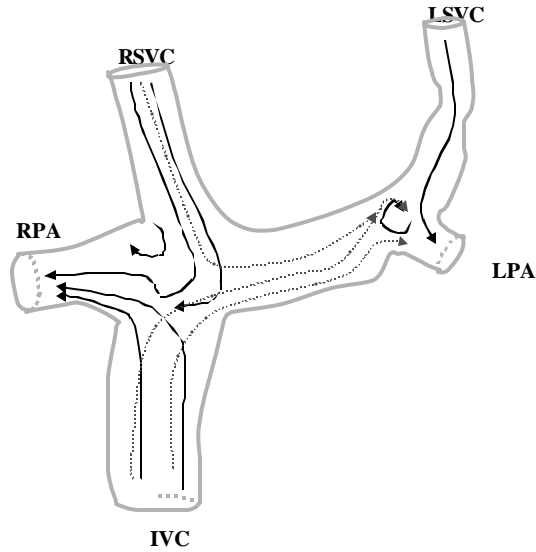


Figure 6.4.18: Schematic of the flow structure observed in the anatomical bilateral SVC model at 2L/min with a 70/30 RPA/LPA flow split. LSVC flow went exclusively to the LPA, while the vast majority of the RSVC and IVC flows went to the RPA. Only a little amount of fluid slowly came from the IVC and RSVC, along the anterior wall, across the intermediate PA section. Two recirculation regions were identified, facing the opening of each one of the PA's.

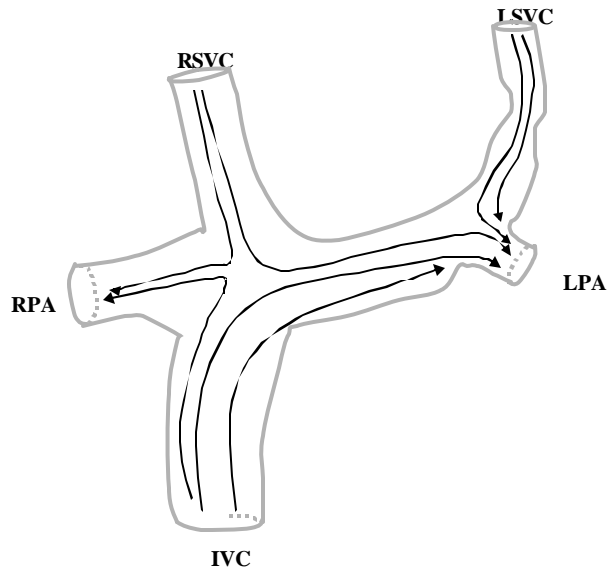


Figure 6.4.19: Schematic of the flow structure observed in the anatomical bilateral SVC model at 2L/min with a 30/70 RPA/LPA flow split. LSVC flow went exclusively to the LPA, together with the vast majority of the RSVC and IVC flows. IVC and RSVC flows collided before splitting into both PA's, yielding a stagnation region. Both RSVC and IVC contributed to RPA flow. The flow across the intermediate PA section was twice as fast as in the IVC.

CHAPTER VII

DISCUSSION

As was presented in Chapter VI, this study combined the use of experimental and numerical results to analyze the velocity fields of six simplified TCPC prototypes and two anatomic models, enabling a better understanding of the effects of connection geometry and pulmonary flow split on the fluid mechanics and efficiency of a given TCPC design. The work was part of a broader multi-center research program whose long-term goals are: (i) to develop reliable numerical methods that would enable a complete characterization of the *in vivo* hemodynamics of the TCPC and facilitate surgical planning; and (ii) to combine the knowledge gained from *in vitro*, *in vivo* and CFD results to improve the efficiency of the TCPC.

The recent developments in medical imaging techniques combined with the latest advancements in numerical methods for solving the Navier-Stokes equations have created unprecedented opportunities for developing CFD tools that would meet patient-specific surgical planning objectives. However, for CFD to reach its full potential and gain the trust and confidence of medical practitioners, there is a pressing need for physics-driven numerical modeling and comprehensive numerical model validation.

There were thus two main motivations to this study: (i) get a better understanding of the TCPC hemodynamics through anatomical models and simplified geometries, (ii) propose a combined CFD and *in vitro* approach that would enable the development of reliable CFD tools. In this Chapter we will thus first discuss the

manufacturing methodology, then analyze the TCPC hemodynamics and the determining geometrical parameters, and finally focus on the suggested CFD validation methodology.

7.1 Manufacturing Methodology

The RP manufacturing methodology described in Chapter V is a rapid process to produce experimental models that reproduce any computer-designed geometry within a small tolerance (0.1mm with our RP hardware) and also meet all optical requirements for flow visualization, DPIV and/or LDV. Specifically, anatomic configurations can be reconstructed from digital medical images and then directly converted to a solid experimental model and a CFD grid.

7.1.1 Geometric Accuracy

In this study, anatomic configurations were reconstructed from MRI. Two different levels are thus to be considered when evaluating the geometric accuracy of the RP manufacturing methodology: First the accuracy of the anatomic reconstruction and then the accuracy with which the experimental model and the CFD mesh reproduced the reconstructed three-dimensional geometry.

As is detailed in Section 5.1, the MR images were interpolated and segmented using in-house codes, while the final three-dimensional flow volume was generated within Mimics (Materialise Inc. Ann Arbor, MI). Frakes et al. state that combined use of their interpolation and segmentation codes brings the reconstructed geometry within 0.6mm of the original anatomic configuration [Frakes, 2003]. The smoothing occurring within Mimics cannot be exactly quantified nor completely turned off. For a better

control over the accuracy of the anatomic reconstruction, an in-house code is currently being developed.

Using both Geomagic Studio 6.0 (Raindrop Geomagic, Research Triangle Park, N.C.) and Pro/ENGINEER Wildfire (PTC, Needham, MA) for further design operations, the blood volume of the digitized experimental model, which was also used for the numerical simulations, laid within 0.02 mm of the Mimics reconstruction (Figure 5.1.5). Finally, the accuracy of our SLA hardware was of 0.1 mm so that, overall, the experimental models were within 0.7 mm of the true anatomic configuration and within 0.1 mm of their numerical counterpart. The anatomic reconstruction step was the major source of error of the proposed methodology and was mainly dictated by resolution of the MR images, which in turn depended upon MRI hardware and software. Subsequently, even though the RP manufacturing methodology achieved satisfactory convergence between experimental and numerical models, there may be a higher deviation between those models and the original patient's anatomy. As will be discussed further in Section 7.2, the diameter of the vessels was found to govern the amount of energy that was dissipated across the connection. A small deviation between the dimensions of the true anatomy and those of the reconstructed geometry may thus lead to a high error in the predicted power losses. This is a limitation that should always be kept in mind when considering the relevance and clinical significance of the results obtained from either experimental or numerical studies. Both of these will provide useful information, but may not exactly reflect the patient-specific hemodynamics.

7.1.2 Material Properties

7.1.2.1 Surface roughness

With the manufacturing accuracy used in this study, namely 0.1 mm, the “as is” inner-surface roughness was measured to be $R_a = 10.0 \mu\text{m}$ and could be further reduced to $R_a = 0.3 \mu\text{m}$ after careful polishing. However, given the small dimensions of the intra-atrial model (SVC diameter of 4.5mm) geometric accuracy was prioritized over lower surface roughness and the inner surfaces of the experimental model were left as built.

In order to assess the impact of the surface roughness on the power losses, Model 1 was built using both glass and unpolished RP materials. The RP grooves were shown to yield constantly higher power losses, but had no significant effect in the laminar regime.

7.1.2.2 Optical measurement accuracy

Using appropriate image acquisition techniques, such as dye flow visualization instead of particle flow visualization, or fluorescent DPIV particles instead of silicon carbide particles, transparent RP resin models enabled both qualitative flow visualization as well as quantitative laser measurements techniques.

Provided the refractive index of the working fluid accurately matched that of the RP resin, we were able to obtain LDV and DPIV measurements that matched the qualitative flow visualization observations (Sections 6.3 and 6.4). Comparative measurements on a fully developed laminar pipe flow demonstrated that the velocities measured with either of these techniques yielded a small bias in the measured velocities,

but stayed within 10% of the expected velocity that was computed based upon the ultrasonic flow rate measurements.

However, as was observed in both the LDV and DPIV experiments, the RP resins absorbed and refracted part of the laser power, which lead to lower LDV data acquisition rates than what was seen in acrylic models and impaired the outcome of the DPIV cross-correlation. For the DPIV measurements, these hurdles were circumvented by the combined use of fluorescent particles and a color filter. As for the LDV measurements, low data acquisition rates were suspected to induce some bias in the computed velocities. Of major concern were the regions where the laser beams went across thick walls, such as to access the PA's in the intra-atrial model. In these regions, even though we were able to obtain coincident laser beams for 2D LDV measurements, the data acquisition rates in 2D were so low that some of the LDV data were acquired in 1D or not considered at all. Designing thin walls close to the measurement regions is thus critical to ensure the quality of the quantitative laser measurements.

This study demonstrated that quantitative optical measurements through transparent RP resins were feasible, but that careful model design was a crucial step in order to ensure optical access to the measurement regions.

7.1.3 Suitability for CFD Validation and Cardiovascular Studies

Because it minimizes the number of steps between the computational model and the experimental prototype, the RP manufacturing methodology is very well suited for CFD validation in complex geometries. Such an approach calls for obtaining DPIV measurement in an anatomic TCPC prototype and comparing the resultant average vector

fields to their numerical counterparts. With respect to cardiovascular studies, one limitation might be the model rigidity. Sylgard as described by Yedavalli et al. [Yedavalli, 2001], could provide a certain amount of compliance, like other latex or silicone based materials, Kerber et al. [Kerber, 1989]. However, for real-life surgical planning or studies involving large sets of experimental models, faster model production is a critical issue. The methodology described here reduces production time from over a week to one or two days (Table 7.2.1), and the routine accuracy of RP machines is sufficient even for models of relatively small dimensions (on the order of mm). Additionally, manufacturing multiple models at the same time may further reduce the production costs. The importance of those work flow-enhancing characteristics in the context of time critical, high volume studies cannot be overstated.

Table 7.2.1: Comparison of Transparent Model Alternatives

Prototype	Cost	Model Complexity	Production Time	Geometric Accuracy	Optical Qualities
Glass	Low (140 \$)	Limited	Short † (3 to 4 hours)	Poor † (2 to 3mm)	Very Good
Stereolithography with Sylgard (Dow Corning©)	High †† (550\$)	Acceptable	Long (7 to 8 days)	Medium (0.1 to 0.4 mm)	Good
Direct Stereolithography with no Chemical Process	High (455 \$)	Good	Medium (RP: 13 hours + polishing: 1 day)	High (max 0.15 mm)	Acceptable

† Complexity dependent

†† Price including both RP and Sylgard costs

The orders of magnitude provided here are based on the cost and production time estimates that were obtained for the particular TCPC geometry shown in this study. Geometric accuracy represents the difference between the manufactured model and the corresponding TCPC geometry as it is reconstructed in Mimics (Materialise Inc. Ann Arbor, MI)

7.2 TCPC Hemodynamics

As has been summarized in the results section, the flow in the anatomic intra-atrial model was highly three-dimensional and unsteady, despite the carefully maintained steady inflow conditions. Concordant with these complex flow features, the power losses that were measured in the intra-atrial TCPC were two orders of magnitude higher than those first found by Ensley et al. in their simplified glass models [Ensley, 1999]. Previous results as well as those obtained in the six glass models were used in an effort to try and break down the contribution of each geometric parameter to the global flow field. The knowledge gained from these simple geometries also served to understand some of the flow characteristics of a completely different TCPC template: an extra-cardiac bilateral SVC.

7.2.1 Relative Impact of Vessel Diameters and Connection Design on the Power Loss

The power losses for Model 1 to 6 at 2 L/min are displayed together with those for the anatomic intra-atrial model in Figure 7.2.1. This plot underscores the predominant impact of vessel diameter upon the order of magnitude of the energy dissipation, while the impact of the design of the connection itself seems more marginal. The most striking example being, the relationship between the losses observed in Model 6 when compared to those of the intra-atrial model. Model 6 mimicked the vessel diameters and pouch dimensions of the anatomic intra-atrial model, but was still very simple when compared to the complexity of the anatomical intra-atrial TCPC. However, the power losses observed in both models were on the same order of magnitude. Similarly, the characteristic power loss curves for the simplified glass models grouped themselves

together based on vessel dimensions: first Model 1 and 2 had power losses of the same order of magnitude, then Model 3, 4 and 5 and finally Model 6.

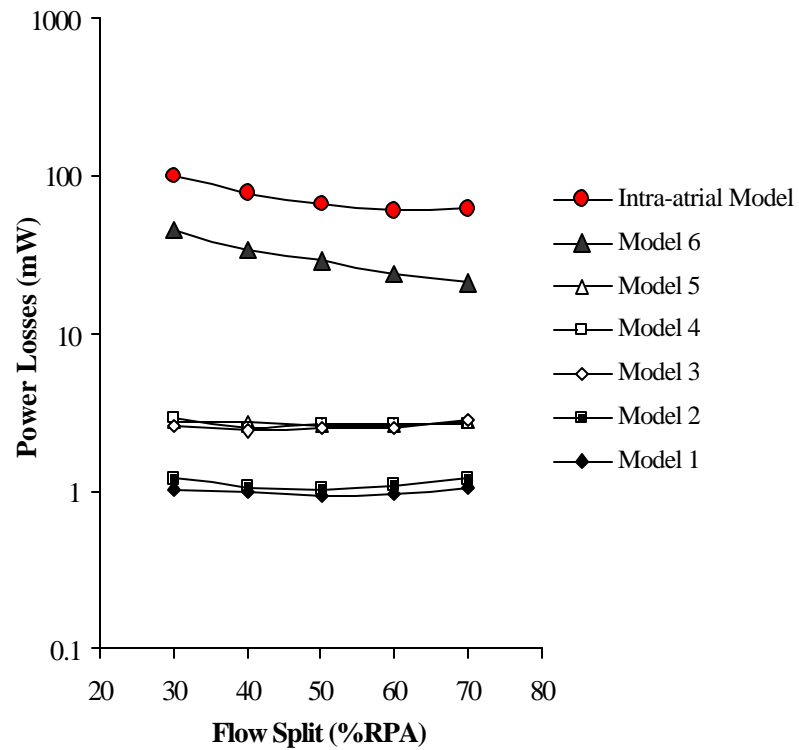


Figure 7.2.1: Power losses in the simplified glass models and in the anatomic intra-atrial model at 2L/min, with a fixed 60/40 IVC/SVC flow split and varying RPA/LPA flow splits.

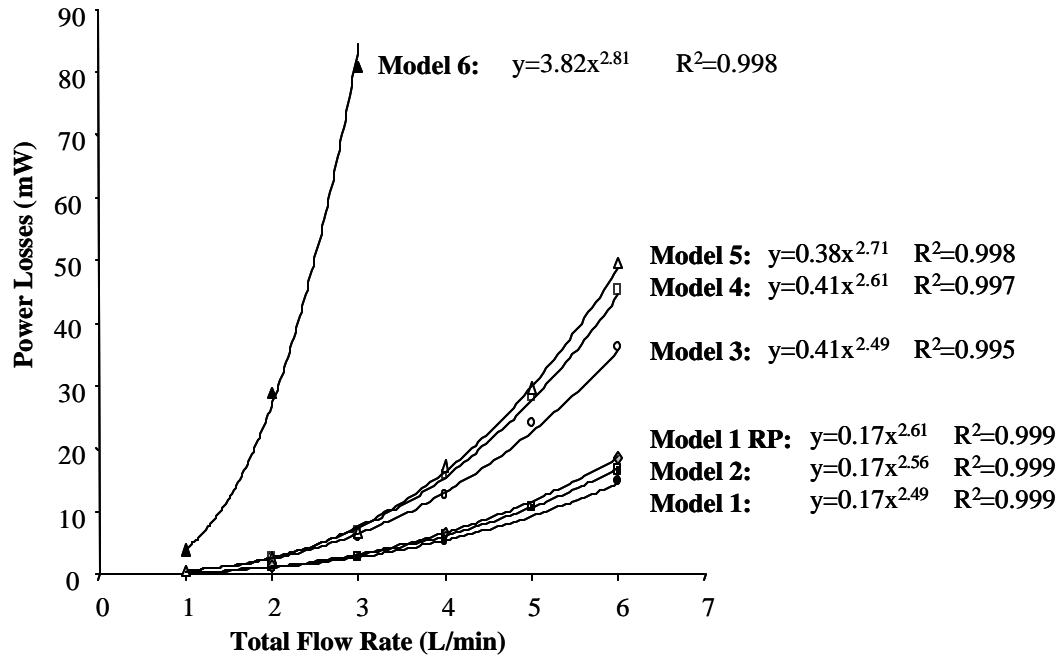


Figure 7.2.2: Power losses in the simplified models at 60/40 IVC/SVC and 50/50 RPA/LPA as a function of the total flow rate.

In an effort to try and identify any clearer relationship between the model dimensions and the corresponding power losses, the losses across the connection were plotted as a function of the total flow rate forced through that connection. To make our discussion clearer, we will focus on a single pulmonary flow split, 50/50 RPA/LPA (Figure 7.2.2). However, similar conclusions could have been drawn from other pulmonary flow splits and the results for the five different pulmonary flow splits (ranging from 30/70 to 70/30 RPA/LPA) can be found in Appendix D. Fitting a power law ($y(x) = b \cdot x^a$) upon the power losses measured across the simplified models for flow rates between 1 and 6 L/min, we observed a strong correlation between the multiplication

factor, \mathbf{b} , and the dimensions of the models and between the power, α , and the connection design (Figure 7.2.2). \mathbf{b} was of ~ 0.17 for Models 1 and 2, ~ 0.4 for Models 3, 4 and 5 and ~ 3.8 for Model 6. \mathbf{a} laid between 2.5 and 3 and increased with the complexity of the connection design. In Models 1 and 3, which were planar and included a caval offset, the energy dissipation varied as $Q_{Total}^{2.49}$. In Models 2 and 4, which included a caval offset but were non-planar, the energy dissipation varied as $Q_{Total}^{2.56}$ and $Q_{Total}^{2.61}$, respectively. In Model 5, which had no caval offset and a connection region (18 mm in diameter) that was wider than any of the connecting vessels (13.3 mm for the PAs), the energy dissipation varied as $Q_{Total}^{2.71}$. In Model 6, which had smaller vessel diameters (5 mm for the LPA and SVC) connecting to a wide pouch (18 mm in diameter), the energy dissipation varied as $Q_{Total}^{2.82}$.

The correlation between geometry of TCPC and the two aforementioned parameters α and β , suggests that a simple law may be used to provide a quick estimate of the losses in a given TCPC geometry. When considering pipe flows, there are two major sources of energy dissipation: viscous dissipation along the pipe walls and dissipation due to sudden pipe expansion or contraction.

Simplifying the problem to its utmost point, the venae cavae and pulmonary arteries could be considered as straight pipes with a characteristic diameter D_i , while the anastomosis sites within the TCPC could be approximated as sudden pipe expansions or contractions, between the connecting vessel and the connection area.

The purpose of such an approach would not be to establish a rigorous fluid dynamic model, for which powerful CFD models are required, but rather to identify a set

of parameters that would characterize a given TCPC geometry and allow for a fast estimate of the order of magnitude of the associated power losses. The following paragraphs detail possible approaches for wall friction and sudden pipe expansion analyses. However, as will be detailed in subsequent paragraphs, additional experimental data are needed and no clear conclusion could be drawn from this study alone.

Wall friction along a straight pipe with a fully developed laminar flow

Under the assumptions in Section 5.2.1.4, namely:

- viscous and incompressible fluid,
- fully developed and laminar flow,
- and constant diameter vessels

the pressure drop, $P_{Viscous}$, due to viscous dissipation along the vessel walls between two points A and B is given by:

$$\Delta_{A \rightarrow B} P_{Viscous} = L_{B \rightarrow A} \cdot \frac{I}{D} \cdot \frac{\rho V^2}{2} \quad \text{(Equation 7.2.1)}$$

where $L_{A \rightarrow B}$ the algebraic distance between A and B ($L_{A \rightarrow B} > 0$ if the flow goes from A to B and $L_{A \rightarrow B} < 0$ otherwise), D the nominal pipe diameter, ρ the density of the fluid, V the bulk flow velocity and I the friction factor, which is given by:

$$I = \frac{64}{Re} \quad \text{(Equation 7.2.2)}$$

Plugging Equation 7.2.2 back into Equation 7.2.1 we obtain the following expression for $\Delta_i P_{Viscous}$:

$$\Delta_i P_{Viscous} = \frac{8L_i \cdot \rho n}{\rho} \cdot \frac{Q_i}{R_i^4} \quad \text{(Equation 7.2.3)}$$

where i indicates a specific vessel (IVC, SVC, LPA or RPA), Q_i the flow rate going through that vessel, R_i the vessel diameter, ν the kinematic viscosity, and L_i the algebraic distance at which the pressure measurement was taken (with $L_i > 0$ for the inlets and $L_i < 0$ for the outlets). For the simplified glass models all of the pressure measurements were taken 10 cm away from the connection. The energy lost by viscous dissipation can finally be written as:

$$\dot{E}_{Viscous} = \sum (\Delta_i P_{Viscous} \cdot Q_i) = K_{Viscous} \cdot Q_{Total}^2 \quad (\text{Equation 7.3.5})$$

where

$$K_{Viscous} = \frac{8 \nu}{\rho} \sum \frac{L_i \cdot \%_i^2}{R_i^4} \quad (\text{Equation 7.3.6})$$

and where $\%_i$ is the percentage of the total flow rate that went through vessel i . For fixed inlet and outlet flow splits, the contribution from the viscous dissipation to the overall power losses can thus be expressed as a function of the total flow rate squared, Q_{Total}^2 , and a factor $K_{Viscous}$ that would only depend upon the vessel diameter.

Sudden pipe expansion

The contribution from the pipe fitting dissipation, to the overall power losses is more complex. As a general rule the pressure drop due to a sudden change in vessel diameter is expressed as:

$$\frac{\Delta_i P_{Expansion}}{\rho} = K_{i Expansion} \frac{Q_i^2}{2g} \quad (\text{Equation 7.3.7})$$

where $K_{i Expansion}$ depends upon the pipe diameter prior and after the pipefitting and the Reynolds number. The resulting contribution to the overall power losses is thus given by:

$$\dot{E}_{Expansion} = \sum (\Delta_i P_{Expansion} \cdot Q_i) = \sum \left(\frac{\rho \cdot K_{i Expansion}}{2g} \cdot Q_i^3 \right) \quad (\text{Equation 7.3.8})$$

This contribution is much more complex to model than the previous one as each one of the K_i Expansion has to be determined, which requires an extra pressure measurement at the center of the connection so as to be able to isolate the pressure drops taking place at each one of the connection sites.

Additional contributions

The approach presented above results in two dissipative terms: the energy dissipated through viscous dissipation along the vessel walls, which behaved as Q^2 , and the energy dissipated through flow separation, which roughly behaved as Q^3 . This could correlate with the fact that in Model 6, where small vessels were connected to a large pouch, α was closer to 3, while it was of the order of 2.5 in smoother geometries such as Model 1.

None of the simplified TCPC geometries yielded losses that behaved as Q^2 . Instead, α was always larger than 2.5. This could be due to the flow separation that was observed in the PAs of all the simplified models, as well as it could be due to the helical pattern of the pulmonary flow, which increased the amount of wall friction along the vessel walls. If flow separation was responsible for most losses, a slow tapering from the pouch to the PAs may yield significantly lower power losses for similar PA diameters. If viscous dissipation turned out to be the predominant energy loss factor, greater care should be taken to try and prevent the onset of helical flows. When looking at the results displayed in Figure 7.2.2, there was a higher variability in the multiplication factors β than in the exponents α : β went from 0.17 for Model 1 up to 3.8 for Model 6, while

α only varied between 2.5 and 2.8. This could suggest a predominant effect of wall friction. However, no clear conclusion could be drawn at this stage.

7.2.2 Correlation Between Geometric Features and Flow Structures

If the exact design of the connection area only had a marginal impact on the power losses when compared to that of the vessel diameter, it had a major impact on the flow structures at the connection site and in the arteries.

7.2.2.1 Vessel flaring and caval offset

Previous investigations by Ensley et al. demonstrated that the optimal design for the TCPC included flaring the vessel anastomosis sites to minimize flow separation along the pulmonary walls, and offsetting the VC's to prevent direct collisions of the inflows [Ensley, 1999]. Accordingly, all the simplified glass models studied were flared at the vessel anastomosis sites, and the VC's were offset by one pulmonary diameter in Models 1 through 4. Concurring with Ensley et al. Model 5, which did not feature any caval offset, demonstrated power losses 20 to 45% higher than Model 3 due to the direct the caval inlet collision and resulting flow disturbances.

7.2.2.2 Pouch

In addition to the absence of caval offset, Model 5 also included a pouch-like connection. In previous studies that modeled no caval offset, the flow at the connection site was primarily two-dimensional [Ensley, 1999]. In Model 5, the wider connection site

provided an extra degree of freedom and 3D flow patterns appeared where the caval flows collided.

7.2.2.3 Curvature

The clearest effect of the non-planar feature was the asymmetric PA flow patterns observed in the flow visualization and even more clearly identified in the CFD simulations. Considering the secondary pulmonary flow structures within a planar TCPC model, Khunatorn et al identified two counter-rotating vortices in the PA's that were perfectly symmetric to one another [Khunatorn, 2003]. Similarly, Liu et al. [Liu, 2004] identified two counter-rotating vortices in the PA cross-section of the non-planar Model 4, but those were no longer symmetric and the asymmetry became stronger as the PA flow split was more unbalanced. Asymmetrical flow patterns were also identified in the connection area itself [Liu, 2004; Ryu, 2001]. Overall pulmonary curvature only translated into a 10-20% increase in power loss between Models 1 and 2 and a 15-30% increase in power loss between Models 3 and 4. However, the subsequent flow asymmetries had a major impact on the distribution of the energy dissipation and of the strain rates along the vessel walls; higher values being expected on the posterior side of Models 2 and 4 than on their anterior side [Ryu, 2001].

7.2.2.4 Vessel diameters

As was discussed in Paragraph 7.2.1, the diameter of the vessels was directly correlated with the amount of energy dissipated within the TCPC as most of it was dissipated through wall friction. Additionally flow visualization revealed that varying the

VC diameter ratios or the PA diameter ratios yielded major differences in the observed flow fields.

a. Caval diameters

The SVC flow rate accounted for 40% of the total flow rate in all the models. However since the SVC area was smaller in Models 3 and 4 than in Models 1 and 2, the corresponding SVC velocities were significantly higher: 0.53 m/s for Models 3 and 4 at 4 L/min, versus only 0.198 m/s for Models 1 and 2. As a result, the SVC stream contained more energy in Models 3 and 4 than in Models 1 and 2 and impinged on the inferior aspect with increased strength. Accordingly, Ryu et al. observed higher strain rates and thus higher rates of energy dissipation at the SVC impingement point in Model 3 than in Models 1 and 2 [Ryu, 2001]. Additionally, while in Models 1 and 2 the recirculation region always remained at the center of the connection, in Model 3 and 4, the high energy SVC stream went down into the IVC when most of the flow was directed towards the RPA (Figures 6.2.4 and 6.2.6).

b. Pulmonary diameters

Uneven PA diameters were modeled in the simplified glass Model 6 together with a pouch-like connection and no caval offset, the two latter geometric features being also modeled in Model 5. Contrary to Model 5, an important counterclockwise recirculation was noted in the connection site of Model 6 (Figures 6.2.10 to 6.2.13) due to the difference between the LPA and RPA diameters.

Additionally, computing the EPVR points of each model underlined that uneven pulmonary diameters lead to uneven lung perfusion. While the functioning point of Model 5 was at about 50/50 RPA/LPA for all flow rates, the anatomic model and

Model 6 clearly favored right lung perfusion. Moreover, the slope of the power loss curves was more negative as the total flow rate increased, meaning that a variation in the LPA/RPA ratio had an increased impact upon the amount of energy that was dissipated in the pouch. Accordingly, at higher cardiac outputs, lung perfusion was found to be even more unbalanced: in the Model 6 the EPVR point corresponded 62/38 RPA/LPA at 1L/min versus 70/30 RPA/LPA at 3L/min.

7.2.3 Fluid Mechanics in Anatomic TCPC's

7.2.3.1 Intra-atrial connection

The main geometric characteristics of the intra-atrial connection considered in this study were the absence of caval offset, a pouch-like connection and small, non-planar vessels with flared connections. As discussed in Paragraphs 7.2.2.1 and 7.2.2.2, the absence of caval offset combined with the pouch-like connection led to three dimensional flow disturbances at the inflow collision region. The combination of small SVC/IVC and small LPA/RPA diameter ratios had been observed to cause important flow recirculation in Model 6. Concordantly, due to the smaller diameter of the SVC, the SVC stream entered the pouch five to six times faster than the IVC flow, went far down into the IVC inducing a strong recirculation region throughout the entire connection. The orientation of the SVC elevated the strength and three dimensionality of this recirculation region one step further, by directing the SVC stream first towards the left-anterior aspect of the connection rather than towards its center.

The connection area was significantly wider than all of the connecting vessels so that both the LPA and RPA were tapered to transition from the pouch diameter down

to the pulmonary diameters, which were 4.2 mm and 5.1 mm for the LPA and RPA, respectively. The LPA tapered down at a faster rate than the RPA such that, 1 cm away from the connection, the LPA/RPA diameter ratio was of 0.6 (corresponding to an LPA and an RPA diameter of 5 mm and 8 mm respectively), while it was roughly 0.8 two centimeters away from the connection.

The smaller dimensions and the faster tapering of the LPA led to an unbalanced lung perfusion that favored RPA flow; situation which worsened with increasing cardiac output: the EPRV point for the anatomic intra-atrial model corresponded to 59/41 RPA/LPA at 1L/min versus 65/35 RPA/LPA at 3L/min. Interestingly, due to the geometry of the connection area, the EPVR points corresponded to the pulmonary flow splits at which the flow within the connection showed the most disturbance with a strong mixing of both IVC and SVC streams (Figure 6.3.2).

Numerical results and experimental flow visualization studies confirmed the presence of significant helicity in the PA's of the anatomic model. This helicity could be a major factor for the high power loss as it increased the friction along the vessel walls. Accordingly, the CFD pressure map (Figure 7.4.1) demonstrated that most of the pressure drops and subsequently most of the power loss occurred at the entrance of the PA's. Helical pulmonary flow as a result of the colliding caval flows has been observed in most TCPC models, from the simplest idealized glass models to more sophisticated numerical models [Bolzon, 2002; Migliavacca, 1999; Ryu, 2001] and may not be completely preventable. It may also have a positive impact as it minimizes pulmonary flow separation and prevents the formation of stagnation regions. However, in the anatomic case studied here, the impact of helicity on the power loss was brought to an even higher

level due to the rapid tapering of the pulmonary arteries, which accelerated the flow along the walls.

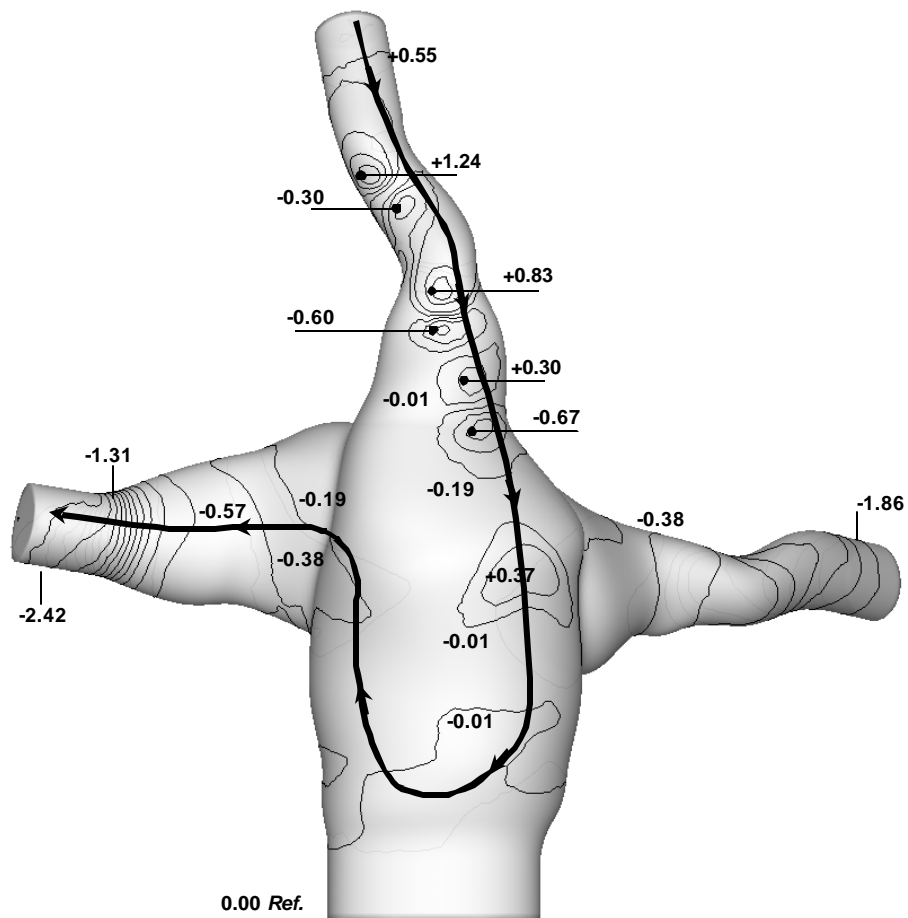


Figure 7.4.1: Pressure distribution in the anatomic intra-atrial model at 1L/min; inlet flow split: 60/40 IVC/SVC; outlet flow split: 70/30 RPA/LPA. Pressures are given in mmHg. IVC pressure was chosen as the reference. [de Zélicourt, 2004]

The SVC diameter increased towards the connection site, which led to flow separation with a high velocity jet on one side and a stagnation region on the other side (Figure 6.3.7). Stagnation regions are not desirable as they favor thrombus formation. The high energy SVC stream was noted to push the IVC flow towards the posterior side while going far down into the pouch thereby preventing stagnation from occurring behind the IVC anastomosis. The pouch bulged more on the anterior side than on the posterior side. We are unsure as to why the “pouch” existed in the first place. It may well be related to surgical technique and could have resulted from a hemi-Fontan procedure. However once present, it did lead to the recirculation region as shown and we believe that it would lead to further deformation of the wall and in turn even stronger recirculation, mixing and unsteadiness.

Similar to what was observed in the anatomic model, Khunatorn et al. [Khunatorn, 2003] observed some small perturbations within the inlet flows of their scaled-up simplified *in vitro* model, despite steady inflow conditions. The flow instabilities described for the anatomical intra-atrial model were exacerbated by the complexity of the geometry. The magnitude and the frequency of the fluctuations increased with the total flow rate (i.e.: cardiac output), which correlated well with the increase in power loss and measurement uncertainty at the higher flow rates. While they lead to increased power losses and may generate greater shear stresses resulting in platelet activation, flow instabilities also enhance blood mixing, which may be desirable.

7.2.3.2 Bilateral SVC connection

The second anatomic model that was studied, an extra-cardiac bilateral SVC, featured smooth vessels with flared connections and caval diameters on the order of those of the simplified glass Models 3, 4 and 5, while the pulmonary arteries were of significantly smaller diameter (about 5 mm). This anatomic configuration yielded power losses that were one order of magnitude lower than those of the anatomic intra-atrial model and a smooth flow field. The only flow disturbances that were observed in this model resulted from the collision of the IVC and RSVC streams. The remainder of the connection was characterized by quasi-steady flow.

In the anatomical intra-atrial model, the SVC diameter nearly doubled in the vicinity of the connection area. This fast tapering of the SVC generated a flow separation region at the SVC anastomosis site. In this anatomical bilateral SVC model, there was not as much of a diameter mismatch between the connection area and the vessels. Additionally, the rate at which the vessels were increased from the original vessel diameter up to the dimensions of the connection area was slow, so that no flow separation region was identified in the venae cavae. Interestingly, the PA diameters of the bilateral SVC model 2 cm downstream of the anastomosis site were of the same order as that of the intra-atrial TCPC, but the resulting pressure drops at the EPVR were two to three times lower than in the anatomic intra-atrial TCPC. This was believed to be due to the design of the PA anastomosis. In the bilateral SVC model the diameter of the anastomosis site was only 50-60% larger than the diameter of the corresponding PA and the vessels were slowly tapered down to their final dimensions. In the intra-atrial model, on the other hand, the diameter of the anastomosis site was about twice the diameter of

the connecting PA's and the vessels quickly tapered down to their final diameter, which accelerated the flow and reinforced the helical pattern. The tapering rate of the vessels may thus be a parameter of importance. In a human body, other organs such as the lungs or the aortic arch, constrain the surgeon's freedom of action. However, clinicians should try and taper the vessels as slowly possible in order to minimize flow acceleration and the onset of flow separation regions.

Despite the fact that the IVC and RSVC were curved towards the LPA (Figure 4.1.4), this connection design was shown to favor right lung perfusion. As has been detailed earlier, most of the energy was dissipated through wall friction. Accordingly, forcing the flow through an extra length of vessel in between the right and left SVCs was unfavorable. A tradeoff between this extra length of vessel and the increased flow rate through the RPA resulted in an EPVR point of that corresponded to a 60/40 RPA/LPA flow split irrespective of the total flow rate. In the anatomic intra-atrial model, the unbalanced lung perfusion was due to the uneven pulmonary diameters and became even more unbalanced as the flow rate increased. In the bilateral SVC anatomy, the unbalanced lung perfusion resulted from the offset between the RSVC and IVC on one side and the LSVC on the other. As a result more energy was required to force some of the incoming IVC and RSVC flows towards the LPA than what was needed to direct it into the RPA. However, contrary to the intra-atrial TCPC, the EPVR point showed no dependence upon the total cardiac output. Intuitively the energy needed to drive the blood through an extra-length of vessel should behave as Q^2 , so that with increasing total flow rates, it should be increasingly advantageous to direct the blood into the RPA rather than forcing it first through the intermediate section and then into the LPA. However, because

this intermediate section of vessel had a much bigger diameter (~15 mm) than the PAs themselves (~5 mm), this effect was counter-balanced by the fact that increasing the share of the flow going through one of the PAs drastically increased the viscous dissipation taking place in that vessel.

The LSVC flow represented 22.5% of the total incoming flow and was entirely directed to the LPA. Subsequently, at the EPVR point only 17.5% of the flow went through the intermediate vessel section, resulting in low flow regions. Additionally, assuming that IVC and RSVC flows contributed to the LPA flow equally, this implied that the IVC accounted for 22% and 81% of the LPA and RPA flows, respectively. If the exact contribution of hepatic flow to the development of the pulmonary vascular structure is still unclear, the contribution of the IVC flow to either lungs may still be a criteria of importance as the exclusion of hepatic blood was demonstrated to be strongly correlated with pulmonary venous malformation [Justino, 2001; Pike, 2004; Srivastava, 1995].

Finally the IVC and RSVC were sutured directly opposite to one another, resulting in the collision of the IVC and RSVC streams before they were split between the PA's. Caval flow collision yielded slight instabilities proximal to the RPA anastomosis. As the connection dimensions remained more uniform than in the intra-atrial model, these instabilities appeared to be of a lower frequency and magnitude than in the intra-atrial TCPC. When most of the flow was directed to the RPA, a flow recirculation region was identified proximal to the RPA anastomosis that was due to the curvature in the IVC and RSVC vessels that directed the caval flows towards the LPA. The caval flow thus had to make a full turn before entering the RPA (Figure 6.4.18).

7.3 CFD Validation

7.3.1 Motivation

With state-of-the-art computational capabilities, and through substantial efforts, the most sophisticated CFD solution can be produced for a given cardiovascular fluid mechanics problem. Alternatively, a combined experimental and computational approach requires a balanced emphasis on the research resources and avoids the tendency of jumping into the most complex computational model before sorting out the fundamental concerns. An illustration was provided by the anatomic intra-atrial TCPC flows that turned out to be intrinsically transient and transitional. Accordingly, for any unexplored anatomic morphology, most of the flow features and underlying flow physics will initially be unknown. CFD verification and validation [Coleman, 2003; Freitas, 2002] then becomes an important requirement for the TCPC research, as well as for all applications of computational cardiovascular fluid dynamics. Particularly, these requirements should not be ignored in clinical applications of CFD that involve human subjects. This is even more critical when CFD is aimed at surgical planning. Likewise, physicians and surgeons who may plan on applying any computer-generated result or act as end-users of a clinical CFD tool, should be aware of CFD validation concepts and the possible numerical uncertainties. CFD is a breakthrough in medicine that is most valuable when applied in the appropriate manner.

As was detailed in Section 2.5.3.3, CFD simulations have first been used on simplified TCPC geometries and then on increasingly complex and realistic models. However, as has been emphasized in recent editorial remarks [Metcalf, 2003; Migliavacca, 1999], there is a pressing need for rigorous model validation with detailed

laboratory data, for CFD to realize its full potential as a powerful clinical tool for patient-specific modeling. This section will thus detail the combined experimental and numerical *in vitro* analysis methodology proposed in Section 5.3 differentiating between three levels of accuracy:

- **The simplified control volume power losses, which are time-averaged and integrated over the whole control volume.**
- **The time-averaged velocity field**
- **The detailed physics of the flow**

Presenting the results in this fashion is intended to underscore an important finding of this work. Namely that even though a reasonable description of time-averaged flow quantities can be obtained using commercially available CFD models, predicting the details of the physics of the flow field is a far more challenging and demanding task that requires considerably more careful and sophisticated numerical modeling.

7.3.2 Power Losses

7.3.2.1 Simplified glass models 1 to 4

CFD simulations for the simplified Models 1 through 3 had been performed prior to this study [Healy, 2001; Ryu, 2001]. This paragraph thus reports on an *a posteriori* evaluation of the numerical results for Models 1 to 3 [Ryu, 2001] and Model 4 [Liu, 2004] as it allows for the assessment of three different methods used to compute the numerical power losses:

1. the full control volume equation, given by

$$\dot{E}_{Loss} = - \int_{CS} [P_{Static} + \frac{1}{2} \mathbf{r} \cdot \mathbf{u}_k \mathbf{u}_k] \mathbf{u}_i n_i dS \quad (\text{Equation 7.3.1})$$

where CS is the control surface, ρ the fluid density, P_{Static} the static fluid pressure, u_i the components of the velocity vectors, n_i the components of the outward surface normal vector of the control surfaces and dS the differential surface area element on the control surface.

2. the simplified control volume given by:

$$\dot{E}_{Loss} = \sum_{Inlets} P_{iTotal} \cdot Q_i - \sum_{Outlets} P_{iTotal} \cdot Q_i \quad (\text{Equation 7.3.2})$$

which was also used in the experimental calculations and is detailed in Section 5.2.1.3

3. the viscous dissipation approach:

$$\dot{E}_{Loss} = \int \mathbf{m} \mathbf{f} dV \quad (\text{Equation 7.3.3})$$

which was motivated by the fact that it could also be used *in vivo* as a non invasive means of assessing the power losses within the TCPC based on MR velocity information [Frakes, 2004; Healy, 2001] and where \mathbf{m} is the fluid dynamic viscosity in kg/m s, and \mathbf{f} the local rate of mechanical energy dissipation given by:

$$\mathbf{f} = \frac{1}{2} \left(\frac{\partial u_i}{\partial x_j} + \frac{\partial u_j}{\partial x_i} \right)^2 \quad (\text{Equation 7.3.4})$$

The resulting CFD power losses obtained for Models 1 to 4 at 4 L/min are displayed together with their experimental counterpart in Figures 7.3.1.

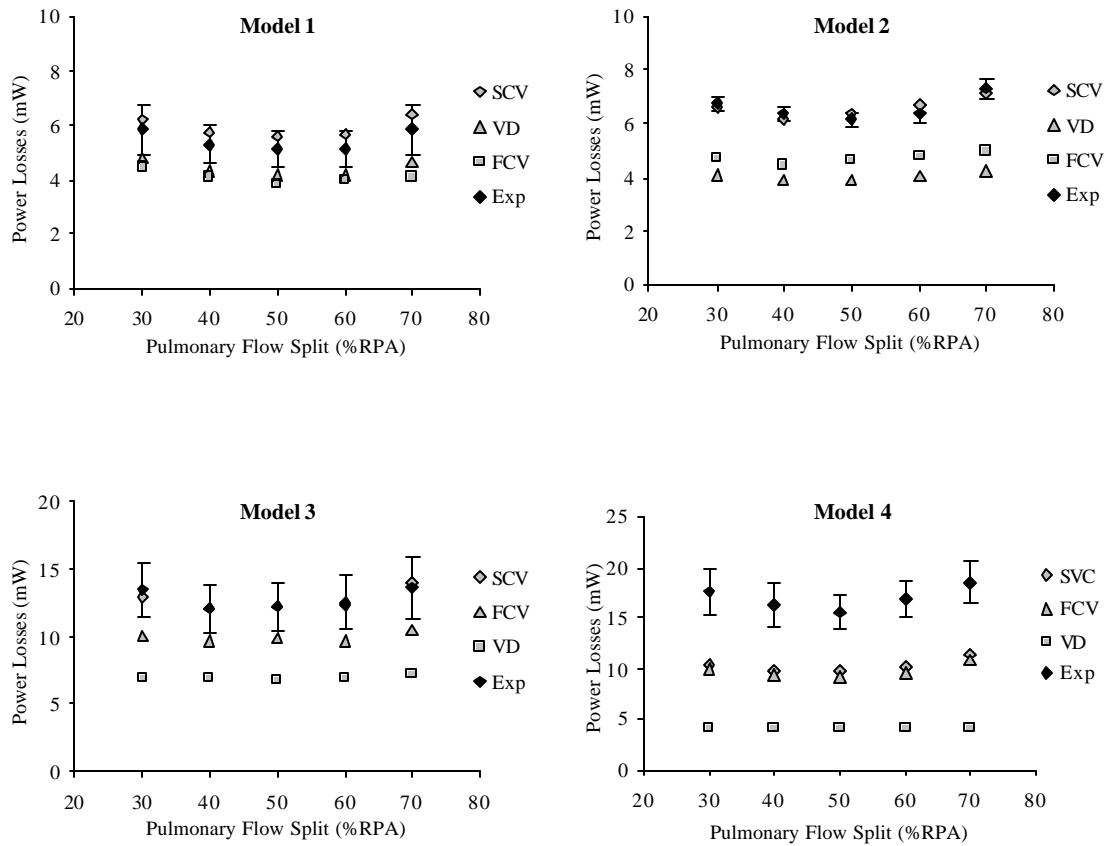


Figure 7.3.1: Experimental (Exp) and numerical power loss results for Models 1 to 3 [Ryu, 2001] and 4 [Liu, 2004] at 4L/min, with a fixed caval flow split of 60/40 IVC/SVC. The computational power losses were obtained using structured meshes and either the simplified control volume (SCV), the full control volume (FCV) or the viscous dissipation (VD) approach.

Results obtained using the simplified control volume approach were the closest match to the experiment data and fell within the 95% confidence interval (1 standard deviation) for Models 1 to 3. On average, the energy losses obtained with the FCV approach were 40% lower than those obtained with the SCV approach, while the results obtained using the velocity gradient based dissipation method were 13 to 35% lower (except for Model 1) than those obtained with the FCV analysis. Even though Healy et al. [Healy, 2001] had found the difference between the VD and FCV methods to be insignificant in Model 1, those two methods yielded drastically different results as the complexity of the model increased. Possible sources of explanation include the fact that as it is based on velocity gradients, the VD approach is very sensitive to the grid size and shape as well as on the accuracy of the numerical scheme, and that converged numerical solutions guarantee mass and momentum conservation, but not energy conservation [Liu, 2004].

Finally, all the results displayed here were run using structured CFD meshes. Liu et al. also assessed the impact of the mesh structure upon the computed power losses and flow structures within Model 4 (Figure 7.3.2). This study was motivated by the fact that structured mesh generation can be very tedious on complex anatomic geometries. The same method for power loss computations used on different meshes was found to yield significantly different results: the energy losses from FCV and SCV were higher in the unstructured model whereas the VD method yielded high losses in the structured model. Liu et al. pointed out the fact that structured grids can capture more vortices, and thus more dissipative flow structures, to explain the second scenario, but could not satisfyingly back up their observation for the SCV and FCV behavior.

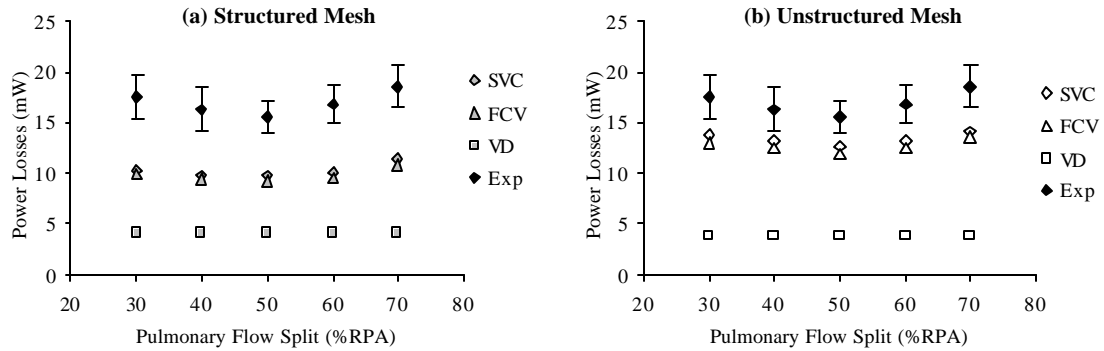


Figure 7.3.2: Numerical power loss results for Model 4 [Liu, 2004] using (a) structured and (b) unstructured meshes. The computational power losses were obtained at 4L/min, with a 60/40 IVC/SVC flow split using either the simplified control volume (SCV), the full control volume (FCV) or the viscous dissipation (VD) approach. The experimental data (Exp) are provided as a ground for comparison.

7.3.2.2 Anatomic intra-atrial model

Figure 7.3.3 displays both the experimental and the numerical (steady-state with FIDAP) simplified control volume power losses at 1, 2 and 3 L/min for the anatomic intra-atrial TCPC. Both computational and experimental data demonstrated similar trends of energy loss as a function of RPA/LPA split. At 1 and 2 L/min, the numerical results obtain with a medium or a fine mesh fell within the 95% (1 standard deviation) confidence interval of the experimental data so that there was no statistical difference between the experimental and CFD results. At 3 L/min, transient flow was observed in the PA's for all flow conditions except between the 50/50 and 60/40 RPA/LPA flow splits. These steady-state simulations were only meant to address laminar flow regimes so that only the results for the 50/50 and 60/40 RPA/LPA flow splits were taken into consideration. The results obtained using a fine mesh fell within the 95 to 98% (1 to 2

standard deviations) confidence interval of the experimental data, showing that this model was reaching its limits.

Figure 7.3.3 also shows the results of the grid refinement study with FIDAP. For the 1 L/min case all three meshes yield essentially identical results, which implies that even the coarsest mesh is adequate to establish a grid independent numerical solution for this case, at least insofar as the integral power losses are concerned. For the other two cases, however, the coarse mesh tends to overpredict the losses, but as the grid is refined the numerical solutions clearly converge toward a grid insensitive solution, which is in good agreement with the experimental measurements.

As seen in Figure 7.3.3, for the highest cardiac output (3 L/min) condition the numerical simulations agreed well with the measurements only within a relatively narrow band of flow splits. This discrepancy should be attributed to the fact that for this condition transition to turbulence becomes very likely within the pulmonary arteries. Based on the vessel hydraulic diameter, the Reynolds number calculated for both pulmonary arteries is close to 2300 for most of the pulmonary flow split range. The SVC flow, on the other hand, turns out to be relatively less critical as compared to the PA—for example, at 3L/min, 60/40 IVC/SVC split, the SVC Reynolds number reaching 1900. Operating conditions corresponding to turbulent flow are shown with dashed lines in the hydrodynamic power loss map of Figure 7.3.3. Since all numerical simulations in this work assumed laminar flow, it is not surprising that the predicted power losses begin to deviate substantially from the measurements for conditions in the turbulent flow regime. Work is currently under way to carry out turbulent flow calculations using traditional

steady Reynolds-average Navier-Stokes (RANS) model and other more-advanced unsteady statistical turbulence models.

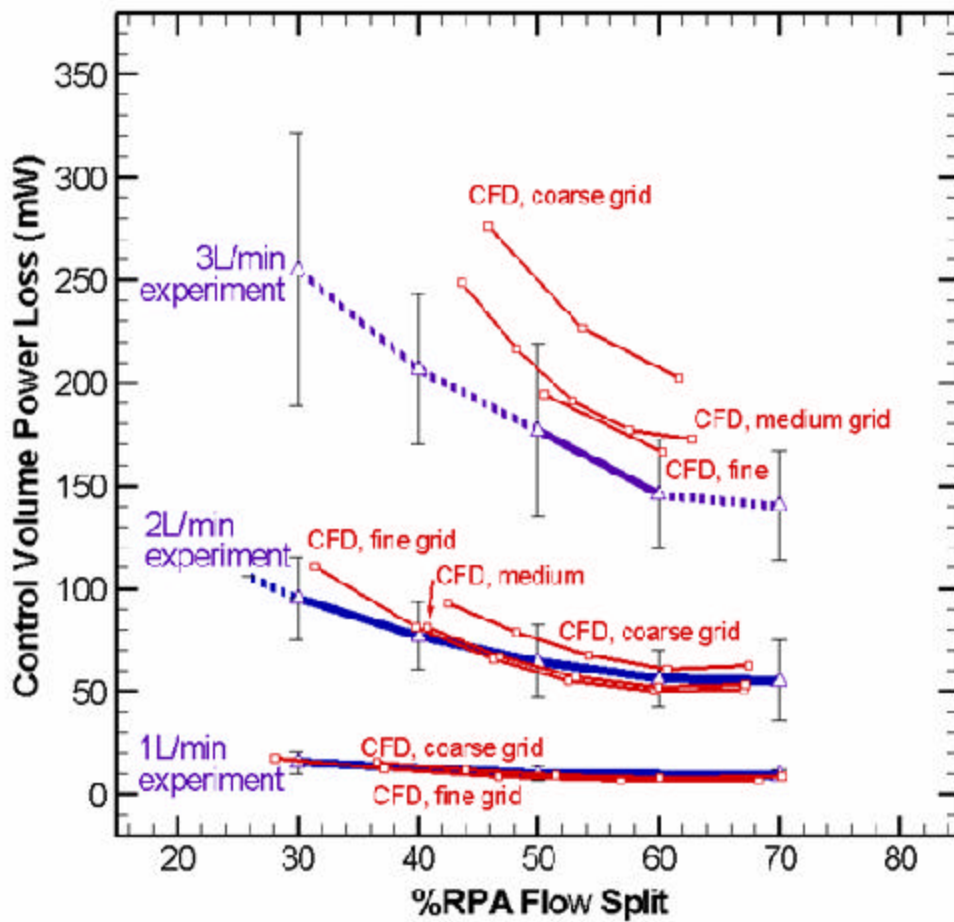


Figure 7.3.3: Grid size verification and experimental comparison of the steady-laminar CFD model. Dashed lines denote conditions where Re_{LPA} or $Re_{RPA} > 2300$ i.e. flow should be fully developed turbulent at one of the pulmonary arteries. [Pekkan, 2004]

7.3.3 Mean Velocity Field

The second step of our validation process focused on the calculated mean velocity fields, which were compared with the time-averaged velocity magnitude measurements obtained via DPIV. As we have previously mentioned, both the DPIV experiments and flow visualizations revealed a complex, unsteady flow field for all cases considered in this work. The experimental mean velocity fields were thus obtained by averaging 300 instantaneous DPIV velocity fields. On the numerical side, no averaging was conducted on the FIDAP computations (since only steady-state results were obtained in this work), while the instantaneous flow fields obtained with the in-house code were averaged over a time interval comparable to that used in the DPIV experiments.

During the numerical verification studies, the velocity profile of inflow boundary conditions was found to have a strong effect on the calculated flow field. Keeping the IVC velocity profile fully developed, two different inflow velocity profiles, plug and fully developed flow, were specified at the SVC. Despite the fact that they both had the same average flow rate, they still yielded significantly different flow fields in the TCPC as shown in Figure 7.3.4—the results shown in this figure were obtained using FIDAP on the medium mesh. Specifying plug flow velocity distribution at IVC or SVC may be a practical CFD modeling option, especially for anatomic flows, but introduces considerably less vorticity into the flow than parabolic fully developed profiles. Inflow vorticity is redistributed via vortex skewing and intensified via stretching and, thus, its intensity could greatly affect the intensity and structure of secondary flow and the distribution of momentum throughout the connection region (see Figure 7.3.4). All subsequently reported results have been obtained using fully-developed inlet profiles as

this boundary condition corresponded more closely to the experimental set-up and yielded results with closer agreement with the experimental measurements.

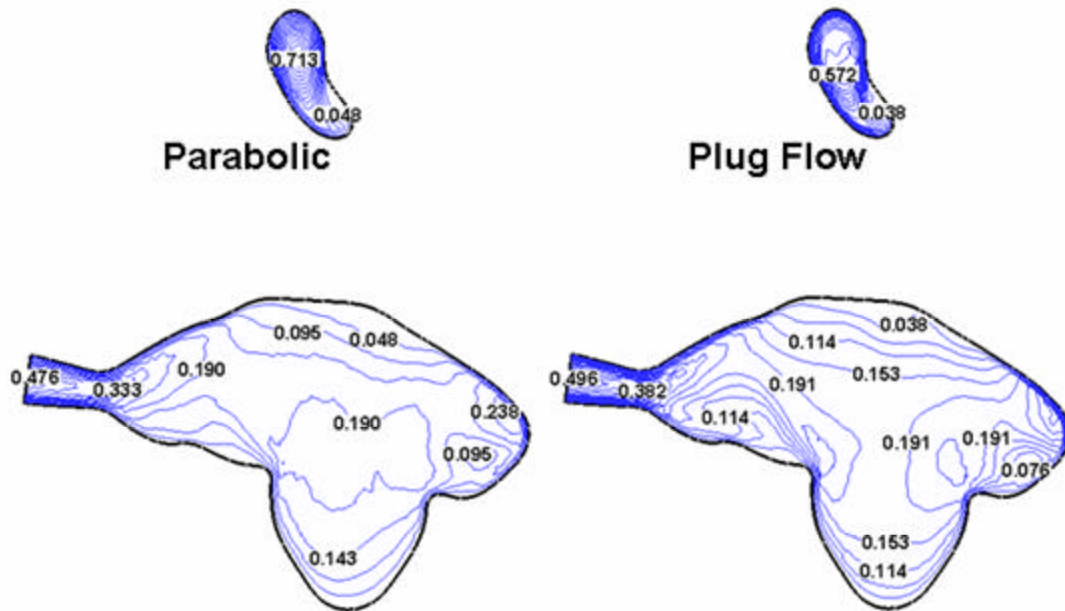


Figure 7.3.4: Axial velocity component contours (m/s) in the mid coronal plane, showing the influence of two SVC inflow boundary condition profiles on the calculated flow field.

Figure 7.3.5 compares the time-averaged DPIV measurements at 1 L/min with a 50/50 LPA/RPA flow split to the steady-state FIDAP results and the time-averaged results obtained with the in-house code. It is important to point out that unpolished inside model surfaces introduced a background noise effect on the DPIV cross correlation, which resulted in systematically lower velocity magnitudes than CFD (max 15%), for

slices farther away from the DPIV camera. Both CFD predictions appeared to capture most of the experimental trends with reasonable accuracy. This level of agreement is indeed remarkable if one takes into account the complexity of the flow and the fact that the two numerical results were obtained using entirely different numerical methodologies and grid structures.

Comparisons similar to those presented in Figure 7.3.5 but with a 3 L/min total cardiac output are also shown in Figure 7.3.6. For this case, however, computations have been carried out only with FIDAP. The general flow patterns for this case are very similar to those shown in Figure 7.3.5 and the numerical simulations are also in reasonable qualitative and quantitative agreement with the measurements. Thus, the results shown in this section clearly demonstrate that if only time-averaged flow quantities are of interest either FIDAP or the in-house code would be sufficient to obtain results of reasonable engineering accuracy. In fact, FIDAP would be the model of choice for this case since its first-order spatial accuracy allows for a steady-state solution to be obtained at only a fraction of the time required to obtain results with the unsteady, in-house flow solver. As we will subsequently show, however, this conclusion was drastically altered when we focused attention on the unsteady characteristics of the flow field.

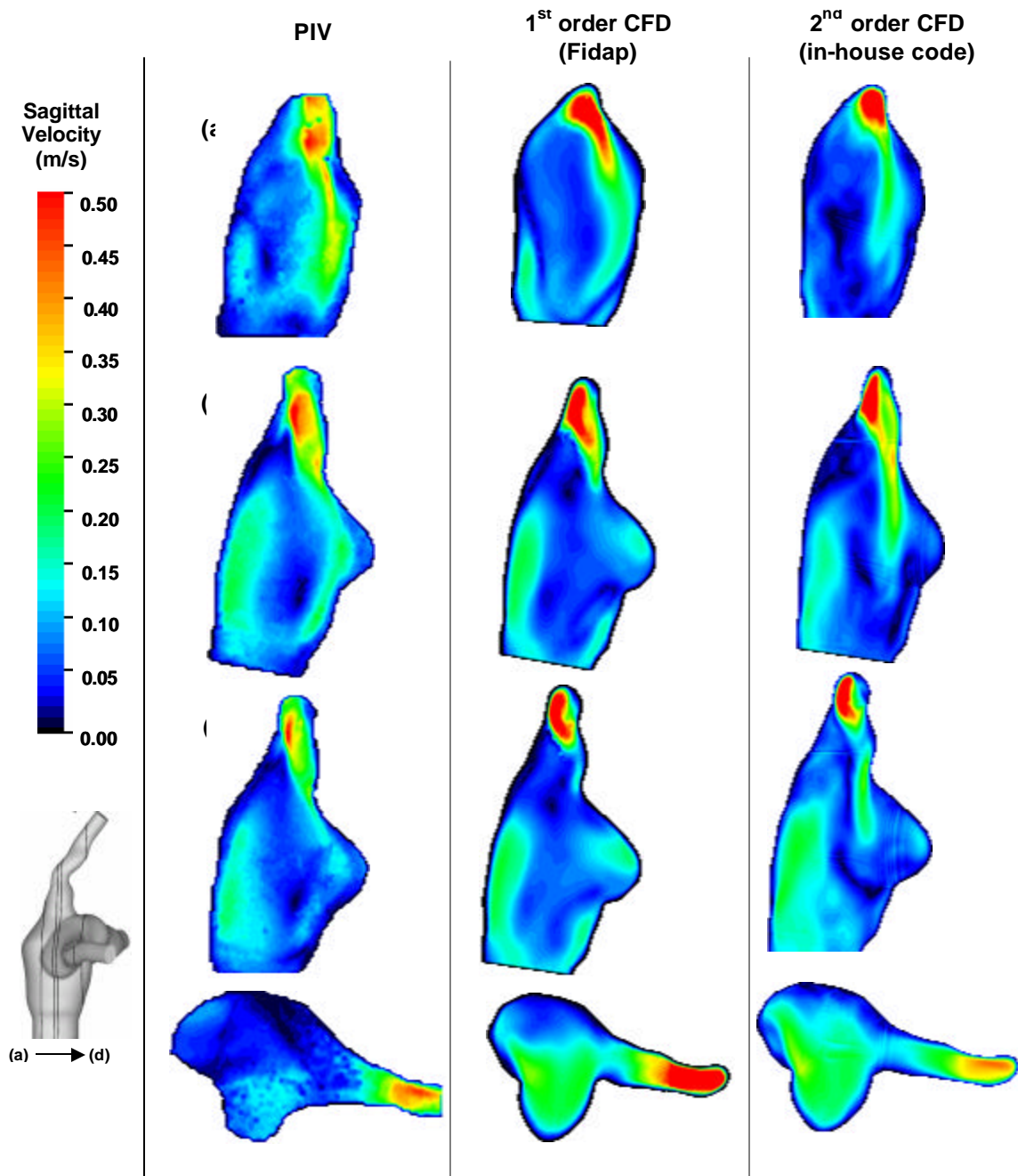


Figure 7.3.5: Quantitative assessment of the flow field using PIV, CFD 1st and 2nd order accurate at 1L/min; inflow split: 60/40 IVC/SVC; outflow split: 50/50 LPA/RPA. The data acquisition planes are indexed from the most anterior (a) to the most posterior (d), and correspond to the laser heights 8 mm, 11 mm, 12 mm and 18 mm (Table 5.3.1). [Pekkan, 2004]

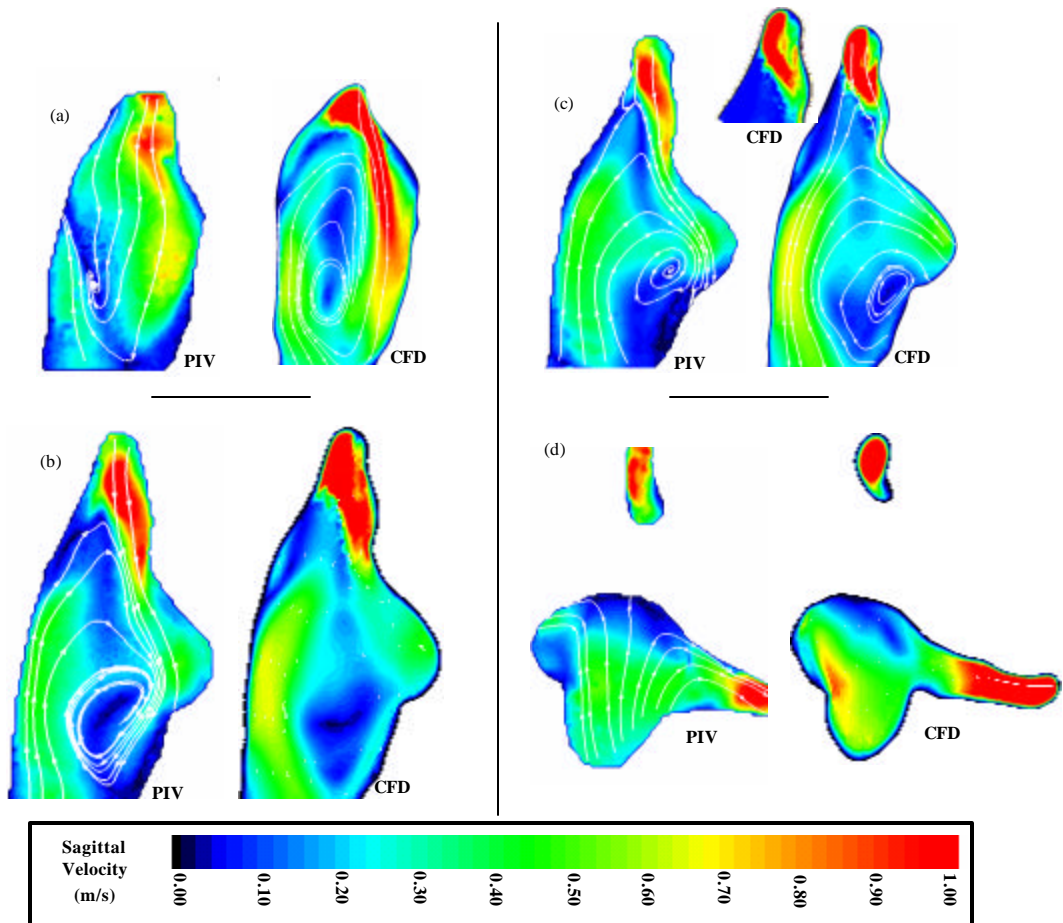
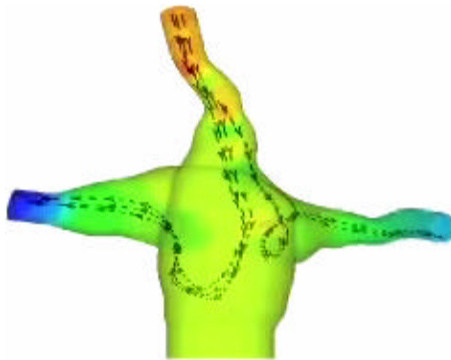


Figure 7.3.6: Quantitative assessment of the flow field using PIV and CFD. Flow conditions: 3L/min, 60/40 IVC/SVC, 50/50 LPA/RPA. The data acquisition planes are indexed from the most anterior (a) to the most posterior (d), and correspond to the laser heights 8 mm, 11 mm, 12 mm and 18 mm (Table 5.3.1). [Pekkan, 2004]

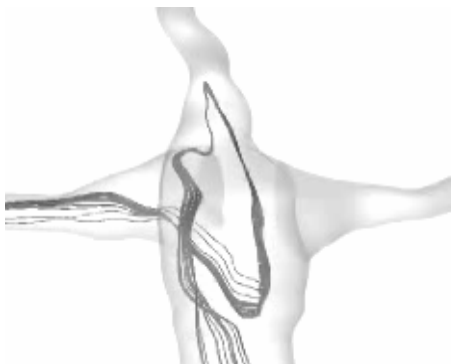
7.3.4 Detailed Physics of the Flow Field

As discussed in Section 6.3, flow visualization underscored the complexity of the flow in the anatomic TCPC even for flow rates well within the laminar flow regime (Re 300 – 800, 1 L/min total cardiac output). The complexity and dynamic richness of the flow in this region can be better appreciated through the flow visualization video recordings attached as Animations 6.3.1 and 6.3.2. The simulations run with the commercial code FIDAP converged towards a steady state solution and thus failed to capture the important instabilities observed within the connection area (Animation 7.3.1). As can be seen from Animation 7.3.2 and from Figure 7.3.7, which displays several snapshots from the flow visualization experiments and the unsteady numerical simulations with the in-house code (visualized in terms of instantaneous streamlines), the in-house code captured the complex flow features with reasonable accuracy. This finding is particularly encouraging since the mean-flow comparisons shown in the previous section established that the simulated unsteady flow is in good qualitative agreement with the measured time-averaged flow. It should be pointed out, however, that a more comprehensive validation of the in-house code is required insofar as the unsteady features of the flow is concerned. Comparisons need to be made for the spectral content of the simulated and measured flows (temporal frequencies of the flow) and the intensity of the unsteadiness (Reynolds-stresses). This validation, however, will require highly resolved unsteady measurements, which due to current limitations in our DPIV instrumentation are not possible. The dominant frequency of the oscillations as observed in the flow visualizations and CFD calculations were of the same order as the data acquisition

capability of our standard DPIV set-up. Work is currently under way to address these difficulties.



Animation 7.3.1: Animated streamlines of the numerical solution obtained for the anatomical intra-atrial model with the commercial flow solver FIDAP (Fluent Inc., NH). This solution converged towards a steady state and thus failed to capture the complexity of the flow within the connection area. (MOV, 11K, de_zelicourt_diane_a_200412_mast_anim731_cfd_fidap.mov)



Animation 7.3.2: Animated streamlines of the numerical solution obtained for the anatomical intra-atrial model with the in house flow solver. Flow conditions: 1L/min, 60/40 IVC/SVC and 50/50 RPA/LPA flow splits. The in-house code captured the complex flow features observed in the experiments with reasonable accuracy. (MOV, 114K, de_zelicourt_diane_a_200412_mast_anim732_cfd_inhouse.mov)

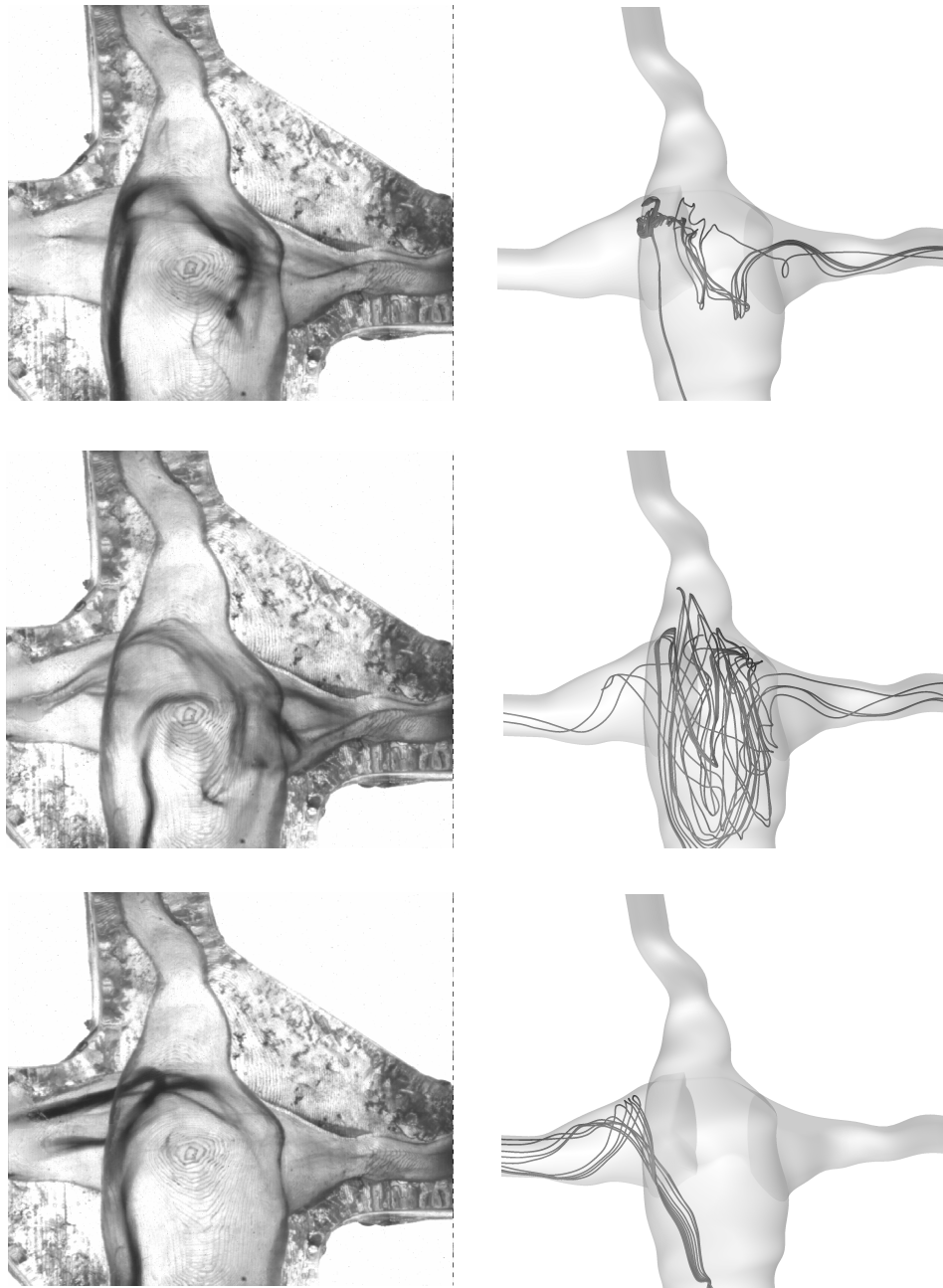


Figure 7.3.7: At 1 L/min, flow visualization (left) showed that the TCPC flow was dominated by complex, unsteady, and highly 3D flow structures. Using 2nd order accurate transient simulations those were also captured in CFD (right).

7.3.5 Modeling Issues and Comparison Criteria

Firstly, a basic but crucial consideration is that for a CFD validation campaign to have any relevance, it should be performed on a model with a complexity relevant to the CFD simulations that will be conducted in the future using the same code. CFD codes that provided satisfying results on simplified geometries might not be suited for more complex patient-specific geometries. This is critical for the surgical applications of CFD. The quality of the validation campaign should always be kept in mind as a possible limitation when considering the relevance and clinical implications of a numerical study.

Another basic but important consideration is that the approximations inherent to any numerical scheme or the discrete grids used to represent a continuous flow domain are not the only possible sources of divergence between experimental and numerical results. These may also arise from experimental measurement errors or from discrepancies between experimental and CFD modeling. This is of particular relevance in cases such as the one studied here where the efficiency of the connection has been shown to be highly dependent on the geometry and where the flow structure has shown a great sensitivity to inflow conditions [Pekkan, 2004]. In our case, the experimental and numerical processes were kept in close interaction in order to ensure that both were conducted under the same conditions, namely:

- incompressible viscous fluid,
- rigid walls,
- steady, laminar and fully developed inlet flows,
- and identical flow splits and total flow rates.

Additionally, the experimental model was manufactured using stereolithography so as to be a close replica of the computational one, both geometries replicating each other within 0.1 mm.

Then, the comparison parameters should be chosen with care. As shown in Figure 7.3.1, power loss computations conducted on the same mesh but with different methods yielded significantly different results even on simplified TCPC geometries [Liu, 2004; Ryu, 2001]. CFD and experimental power losses were in closer agreement when computed using the same approach, namely the simplified control volume method. Similarly, the averaged DPIV flow fields were compared to either steady or time-averaged CFD solutions.

Transparent resins proved to be practical for flow visualization and DPIV experiments. In this study, the inner surfaces of the experimental intra-atrial model were left “as is” with no inside polishing, in order not to accidentally alter the anatomy. This decision affected the optical quality of the experimental model. Although useful DPIV data was acquired, the observed velocity values in the slices that were further away from the DPIV camera were systematically lower. Slight light scattering was observed through the model. Fluorescent particles, color filter, and background noise filtering was used to improve the DPIV image quality. In general CFD solutions showed more complex flow features than DPIV. DPIV vectors are obtained by averaging the particle displacements over an interrogation window. The size of this interrogation window is what determines the spatial resolution of the DPIV flow fields and in our case, the finer flow structures identified in the CFD simulations, such as the peak velocity regions or small vortices, were smaller than the spatial resolution of the DPIV measurements. Furthermore, the

highest velocity peaks were located close to the SVC wall. The quality of the DPIV acquisition in these regions was thus limited due to partial volume effects. Additionally, the difference in magnitude between the high velocity SVC stream and its neighboring stagnation region or low velocity IVC stream, limited the choice for the optimal laser pulse separation, δt . This in turn stands as a limit for the resolution of the computed velocity fields. Finally, while the CFD results display velocity fields in a plane that has no thickness, the DPIV results represent the flow behavior averaged over the entire thickness of the laser sheet. With our hardware the thinnest possible laser thickness was of ~ 0.5 mm, which was of the same order as the characteristic dimensions of the intra-atrial connection. It would thus be erroneous to assume that the flow was uniform across the laser beam thickness. The CFD planes that were compared against the DPIV data were taken so as to approximately fall in the middle of the DPIV laser sheet. However, as is shown in Figure 7.3.6-c, shifting the CFD planes by only 0.5 mm, which corresponds to the typical laser thickness, revealed additional flow details. It may thus be relevant for the CFD validation process to average the CFD data not only over time but also over the thickness of the laser beam. Validated CFD results may then be used to display the flow fields in finer details than what may be achieved using DPIV.

Accurate though it may be, a validated CFD code does not guarantee anatomically accurate flow fields. The reconstruction process, leading from the patient MRI data to a CAD file for CFD grid generation is still a long and tedious task, with repeated approximations, which might endanger the final accuracy of the model. This is of prime importance for the physiological relevance of any numerical study to the cardiovascular field, especially in cases such as the one presented here, where the

efficiency of the connection has been shown to be highly dependent on the geometry. Thus, utmost care should be taken when reconstructing and designing the model. Some of the unique accuracy and uncertainty issues have already been highlighted in literature [Augst, 2003; Moore, 1999; Thomas, 2003], as a research area of its own. Reverse engineering and stereolithographic techniques are very useful for quantifying these errors. In our case, the experimental and CFD geometries laid within 0.1 mm of each other due to the optimal accuracy of our stereolithographic hardware. The differences between the reconstructed geometry and the true anatomy are more difficult to assess and are discussed in detail by Frakes et al. [Frakes, 2003].

The fluid dynamic instability, as described for the intra-atrial model, is exacerbated by the large connection area. For other morphologies, closer in shape to the idealized glass models, with more uniform vessel sizes and possibly including caval offset, smaller flow instabilities are expected and are expected to occur at higher Reynolds numbers. For their idealized model with no offset, Bolzon et al. [Bolzon, 2002] estimated the period of the observed instabilities to be $T = 0.39-0.29$ s., at $Re = 1600$ based on average PA flow, which is in the same order as our anatomic case where the period was observed to be about 0.1 s, but for a much lower Reynolds number $Re_{PA} = 670$. Likewise, a global instability index would be useful to define in order to compare different TCPC geometries. Clinically high levels of flow instabilities would severely increase the hydrodynamic power losses, while on the other hand, it will contribute to the beneficial hepatic blood mixing. As the total cardiac output increases, Reynolds numbers and the frequency of the fluctuations increase. This may signal the onset of transition to turbulence. Such a conclusion is consistent and correlates well with the increasing

experimental standard deviations and differences between steady, laminar first-order CFD and *in vitro* benchtop-data, as summarized in Figure 6.5.2.

7.4 Clinical Significance

The investigation of the simplified TCPC geometries demonstrated that the diameter of the connecting vessels, and of the pulmonary arteries in particular, was a parameter of prime importance. Helical pulmonary flow has been observed through all TCPC models, from the simplest to the anatomical geometries studied here. This secondary flow structure which is due to the fact that the flow has to operate a 90° turn to go from the VC's into the PA's, once again increases wall friction and subsequently viscous dissipation in the PA's. As a direct consequence the pulmonary diameter as well as the design of their anastomosis had a major impact upon the TCPC efficiency. In contrast, the exact design of the connection area had a lower impact upon energy dissipation. This observation concurred with previous findings by Ryu et al. [Ryu, 2001], who stated that most dissipation within the TCPC connection was actually due to wall friction. This statement, however, would benefit from further investigation.

The symmetry of the pulmonary artery diameters and of the design of the anastomosis sites were shown to have a drastic impact upon the hemodynamics, and more specifically upon lung perfusion. In models with equal RPA and LPA diameters (Models 1 to 5), the EPVR point corresponded to a 50/50 RPA/LPA flow split, irrespective of the total cardiac output or of the connection design (caval offset, pouch like connection, curved PA's). On the other hand, smaller LPA diameter and/or faster vessel tapering led

to an unbalanced lung perfusion that became even more unbalanced that the total cardiac output increased (under exercise conditions for example).

This observation is of prime importance as LPA stenosis was observed in 17 out of 37 of the TCPC reconstructions that were done in our laboratory (September 2004). For extreme cases, it may thus be relevant to consider additional palliative procedures aimed at balancing lung perfusion such as angioplasty, but also fenestrations of the IVC baffle whose potential benefits for Fontan patients with stenotic pulmonary arteries are currently under investigation. Since, most of the LPA stenosis cases are believed to result from the compression of the LPA by the reconstructed neo-aorta, other options to be investigated also include designing the Glenn or hemi-Fontan connections so as to force enough flow through the LPA for it not to be compressed. With an accurately validated CFD tool, these solutions and their resulting flow fields, could be explored prior to *in vivo* tests.

Considering the bilateral SVC another parameter came into play, the position of the IVC with respect to the two SVC's. The IVC and RSVC were both sutured one facing the other while the LSVC was offset by over 49 mm and very little flow was observed to travel through the vessel section comprised in between the SVC's. Subsequently, and despite its smooth vessels and anastomosis and its PA's of equal diameter, the extra-cardiac bilateral SVC led to the same kind of lung perfusion as the intra-atrial TCPC, with 60% of the flow going to the right lung under resting conditions. We believe that balanced lung perfusion could have been achieved if the IVC had been sutured in between the two SVC's, provided this was surgically feasible. Additionally

this may have brought the slight instabilities due to the colliding RSVC and IVC flows down to an even lower level.

The absence of caval offset in the anatomical intra-atrial model resulted in important flow turbulence, which was enhanced by the large connection area and may in turn lead to platelet activation or blood cell damage. The quantification of the maximum shear stresses across the connection would be needed prior to drawing any conclusion and would require further investigation. In a smoother connection, such as the bilateral SVC, lower levels of instability were observed, despite the colliding IVC and RSVC streams. However as was discussed in Chapter II, extra-cardiac connections provide no growth potential and may lead to conduit stenosis and thromboembolism [Haas, 2000; Petrossian, 1999; Tam, 1999]. It is also believed that intra-atrial connection may provide some pulsatility to the lungs, which would be more physiologic. The advantages of a smoother flow field should thus be clearly assessed and balanced with other *in vivo* and surgical considerations.

Ensley et al. had demonstrated that flaring the anastomosis sites had a positive impact upon the TCPC hemodynamics as it minimized flow separation in the pulmonary arteries and thus reduced the power losses [Ensley, 1999]. In this study however we demonstrated that if flaring of the vessels may show beneficial, it should still be used with caution. In the anatomical intra-atrial model, the asymmetrical tapering of the RPA and LPA led to an unbalanced lung perfusion that favored the right lung. The anatomical intra-atrial model also featured fast tapering of the venae cavae, which yielded flow separation and the creation of stagnant flow regions. Thus, there appears to be an optimal

flaring rate and the exact relationship between flare and secondary flow structures would be an interesting focus for future work.

Finally, this study underscored that CFD may be a breakthrough in medicine but only if applied in the correct way. Physicians and surgeons should be aware of CFD validation concepts and the possible numerical uncertainties so as to properly assess the reliability of any computer generated result and their clinical significance. This conclusion is all the more important that CFD arises as a convenient surgical planning tool.

CHAPTER VIII

LIMITATIONS OF THE STUDY

8.1 CFD and *In Vitro* Modeling

As with any study, there are several limitations to this work. First, there were limitations in the *in vitro* experimental modeling. This study was conducted using either rigid glass models or rigid RP models. It thus did not address the effects of compliance on the power losses and flow structure in an *in vivo* situation. In simplified glass models, where the pressure gradients are minimal, the visco-elastic properties of the vessels were expected to impact the local flow structure but only mildly affect the macroscopic fluid dynamics [Migliavacca, 1996; Oddou, 1978]. This may not hold true in anatomical TCPC models, which demonstrated higher pressure gradients. Along the same lines, all the experiments were run under steady flow conditions, which was an additional simplification. However, using rigid models and steady flow conditions was a necessary step in the CFD validation. Besides, the flow curve describing the flow pulsatility within the TCPC is still unknown and implementing an arbitrary flow curve would have been meaningless. A study is currently underway in our laboratory to try and assess the amount of pulsatility and of vessel dilation present in the TCPC based on patient MRI data. These patient data should thus be used in future CFD and experimental studies in order to assess the relevance of modeling compliance and pulsatility.

8.2 Geometric Accuracy

As was pointed out in Section 7.1, the manufacturing methodology detailed in this study presented the major advantages to provide transparent replica of any digital geometry, irrespective of its complexity, within a short time span. This allowed for the CFD and experimental models to be within 0.1 mm of one another, which was critical for CFD validation purposes. Frakes et al. estimated the accuracy of the TCPC reconstruction to be about 0.6 mm [Frakes, 2003], so that overall the experimental anatomical models presented in this study were within 0.7 mm of the original patient anatomy. As was discussed in Section 7.2, the dimensions of the vessels were a major factor in the determination of the power losses across the TCPC. Subsequently, the power loss values and velocity magnitudes shown in this study may not exactly reflect what would have been seen in the true patients' TCPC anatomies. However, provided the quality of the MR image was uniform throughout the entire connection, the reconstruction process preserves the proportions of the TCPC anatomies, so that the flow structures observed in the anatomical models should still reflect the anatomical flow structures. On the other hand, the magnitude of the velocities and of the power losses may deviate from what should have been observed with the exact vessel dimensions. Subsequently, if the results discussed in this study may underline some important features and help identify some crucial parameters, they should still be used with caution.

8.3 CFD Validation

This study also introduced a CFD validation methodology. As was observed in the anatomical intra-atrial model, flow instabilities appeared throughout the connection

due to the colliding inflows. An accurate CFD validation would thus call for time resolved experimental data and frequency analysis, which was not possible with our DPIV hardware but may be done using LDV results. However, LDV was not the initial focus of this study and our models had been specifically tailored for DPIV measurements. Thus, even though we were able to demonstrate the feasibility of the LDV measurements, we were not able to take full benefit of this measurement technique. With temporal CFD validation in mind, the anatomical RP models should be designed so as to allow for an easy optical access for the LDV laser beams into the regions of interest, such as the PA's or regions of high instability.

8.4 3D Velocity Measurements

Another current consideration is the difficulty in acquiring the three directional velocity data. The CFD results and the flow visualization observations indicated significant through plane velocities in the central region of the intra-atrial model and in the PA's of both anatomical models. One way to quantify these would have been to switch the data acquisition axis and image the models from the side surfaces. However, our RP models did not permit such measurements. This was due to the fact that RP models are built in layers, which introduces an additional blur to the side surfaces so that DPIV or LDV data could only be acquired through the top and bottom surfaces and not through the sides. Another way would be to acquire three-dimensional DPIV data. The DPIV system currently available in our laboratory has just been upgraded allowing for the acquisition of 3D-velocity data sets. However, the error associated with such

measurements still has to be quantified prior to deciding whether this technique may be used and trusted with our *in vitro* RP models.

8.5 Characterization of the TCPC Efficiency

Based on the complexity of the anatomical TCPC flow fields, additional parameters may be needed to provide a complete evaluation of the hydrodynamic performance of a given TCPC design. Parameters of interest include: IVC/SVC contributions to LPA and RPA flow, residence times of IVC and SVC streams, connection shear and pressure maps, dissipation field [Ensley, 1999; Frakes, 2004; Healy, 2001] and individual branch and connection pressure drop contributions. As the anatomic sizes and morphologies are quite variable in the TCPC, comparative analysis may require that performance parameters be scaled. Additionally, the transient flow in the TCPC necessitates the calculation of exact unsteady analogs of these parameters, instead of practical time averages of the steady definitions [Migliavacca, 2003]. A validated CFD model is a first step for the accurate calculation of these clinically important parameters, but as stated earlier, the CFD validation should be adapted to the parameters of interest and involve time-resolved experimental data.

CHAPTER IX

CONCLUSIONS

This study demonstrated the potential applications of the recent development in medical imaging, experimental laser techniques and in CFD modeling in the biomedical field. It underscored the need for a close interdisciplinary interaction between CFD modeling, *in vitro* experiments, but also with physicians and surgeons, in order to evaluate the accuracy and reliability of the computed parameters as well as their relevance and significance, to surgical planning.

9.1 Anatomical *In Vitro* Models (Specific Aims 1 and 3)

This study utilized transparent stereolithography to produce experimental models that reproduced any computer-designed geometry within a small tolerance and also meet all optical requirements for flow visualization, DPIV and/or LDV. Specifically, anatomic configurations were reconstructed from digital medical images and then directly converted to a solid experimental model and a CFD grid.

The accuracy of the reconstruction process was estimated to be 0.6 mm and that of our SLA hardware was of 0.1 mm so that, overall, the experimental models were within 0.7 mm of the true anatomic configuration and within 0.1 mm of their numerical counterpart. With the manufacturing accuracy used in this study the “as is” inner-surface roughness was measured to be $R_a = 10.0 \mu\text{m}$ and could be further reduced to $R_a = 0.3 \mu\text{m}$ after careful polishing. This study demonstrated that qualitative optical measurements

through transparent RP resins were feasible but that a careful model design was a crucial step in order to ensure optical access to the measurement regions.

Finally, because it minimizes the number of steps between the computational model and the experimental prototype, the RP manufacturing methodology is very well suited for CFD validation in complex geometries.

9.2 TCPC Hemodynamics (Specific Aim 2)

9.2.1 Summary of the Anatomical Flows

The absence of caval offset in the anatomical intra-atrial model resulted in important flow turbulence, which was enhanced by the large connection area. The smaller dimensions and the faster tapering of the LPA led to an unbalanced lung perfusion that favored RPA flow. The corresponding power losses were two orders of magnitude higher than those observed in simpler glass models (Models 1 through 5) and demonstrated a high sensitivity to pulmonary flow split.

The second TCPC template that was studied, an extra-cardiac bilateral SVC, featured smooth vessels with only slightly flared connections. This anatomic configuration yielded power losses that were one order of magnitude lower than those of the anatomic intra-atrial model and a smooth flow field with lower levels of instability. However, due to the fact that the IVC and RSVC faced one another while the LSVC was offset by 49 mm, this design too favored right lung perfusion.

9.2.2 Major Hemodynamic Parameters

Prototype TCPC connection geometries were investigated in an effort to better understand the underlying hemodynamics and find more efficient alternative for the current surgical palliation. It was shown that the diameter of the connecting vessels and of the pulmonary arteries in particular, was a parameter of prime importance. In contrast, the exact design of the connection area had a lower impact upon energy dissipation.

Helical pulmonary flow has been observed through all TCPC models, from the simplest to the anatomical geometries studied here. This secondary flow structure which is due to the fact that the flow has to operate a 90° turn to go from the VC's into the PA's, once again increases wall friction and subsequently viscous dissipation in the PA's. In addition to the viscous dissipation another major dissipative term related to the changes in diameters between the connection area and the connecting vessels. The combination of those two dissipative terms generated major energy dissipation in the pulmonary arteries. This observation correlated well with previous findings by Ryu et al. [Ryu, 2001]. As a direct consequence the pulmonary diameter as well as the design of their anastomosis had a major impact upon the TCPC efficiency.

The fast tapering of the LPA within the intra-atrial model had two major consequences: first (i) it accelerated the LPA blood flow and enforced its helical pattern, leading to an increased viscous dissipation, then (ii) it yielded a more sudden change in vessel diameters, and thus higher energy dissipation due to flow separation. As a result it was unfavorable to force the flow through the LPA and this intra-atrial design favored right lung perfusion. The anatomical intra-atrial model also featured fast tapering of the venae cavae, which favored flow separation and the creation of stagnant flow regions. If

flaring the vessels was shown to have a positive impact on the hemodynamics [Ensley, 1999], this study underlines that it should be kept within reasonable limits so as not to yield high pressure drops in the PA's nor flow separation in the VC's.

9.2.3 Equal Lung Perfusion

In addition to the characteristic power loss curves traditionally used to describe the efficiency of a given TCPC design, we focused on the physiological operating point of each TCPC design, trying to quantify the quality of the lung perfusion assuming that both lungs had an equal pulmonary vascular resistance (EPVR).

For the simplified glass models and the anatomical intra-atrial model, which all featured a single SVC, lung perfusion was dictated by the PA diameters and by the size of the anastomosis site. In models with equal RPA and LPA diameters (Models 1 to 5), the EPVR point corresponded to a 50/50 RPA/LPA flow split, irrespective of the total cardiac output or of the connection design (caval offset, pouch like connection, curved PA's). On the other hand, smaller LPA diameter and/or faster vessel tapering led to an unbalanced lung perfusion that became even more unbalanced that the total cardiac output increased (under exercise conditions for example).

Considering the bilateral SVC another parameter came into play, the position of the IVC with respect to the two SVC's. The IVC and RSVC were both sutured one facing the other while the LSVC was offset by over 49 mm. Very little flow was observed to travel through the vessel section comprised in between the SVC's so that, despite its smooth vessels and anastomosis and its PA's of equal diameter, the extra-cardiac bilateral

SVC led to the same kind of lung perfusion as the intra-atrial TCPC, with 60% of the flow going to the right lung under resting conditions.

9.3 CFD Validation Methodology (Specific Aim 4)

This study presented a combined experimental and numerical approach, which was illustrated for the case of the anatomical intra-atrial TCPC. The use of transparent stereolithography produced experimental *in vitro* models that were within 0.1 mm of their numerical counterpart and allowed quantitative and qualitative assessment of the experimental flow field for CFD validation.

A close interaction between the numerical and the experimental analyses avoids the tendency of jumping into the most complex computational model before sorting out the fundamental concerns. Accordingly the combined experimental and numerical analysis methodology differentiated between three levels of accuracy:

- The simplified control volume power losses, which are time-averaged and integrated over the whole control volume.
- The time-averaged velocity field
- The detailed physics of the flow

Presenting the results in this fashion underscored an important finding of this work: Namely that even though a reasonable description of time-averaged flow quantities can be obtained using commercially available CFD models, predicting the details of the physics of the flow field is a far more challenging and demanding task that requires considerably more careful and sophisticated numerical modeling.

CFD may be a breakthrough in medicine but only if applied in the correct way. This conclusion is all the more important that CFD arises as a convenient surgical planning tool. Physicians and surgeons who may plan on applying any computer generated result or act as end-users of a clinical CFD tool, should be aware of CFD validation concepts and the possible numerical uncertainties [Guide for the verification and validation of computational fluid dynamics simulations, 1998; Roache, 1998]. We introduced a validation methodology as a first step towards the accurate simulation of the TCPC hemodynamics. Knowing the strength and limitations of each CFD tools will enable us to optimize computational time and simulation accuracy. A reliable CFD tool may then enable for the complete hydrodynamic evaluation of the TCPC, including parameters that may not easily be quantified *in vitro*, as well as for surgical planning operations.

CHAPTER X

RECOMMENDATIONS FOR FUTURE WORK

10.1 Characterization of the Different TCPC Templates

This study has shown the feasibility of analyzing flow fields in anatomically accurate models using both numerical and experimental approaches. Future development of this work includes not only improving the experimental and numerical models, but also and above all taking advantage of the developed methodology to perform parametric studies that will provide a better understanding of the *in vivo* hemodynamics. This should be done using a combined *in vivo* (based on patient MRI data), *in vitro* and computational approach.

A major potential focus is to determine the geometric and flow characteristics common to the TCPC geometries based on analysis using similar templates. In particular, it would be relevant to perform a thorough comparison between the extra-cardiac and intra-atrial procedures and between the Glenn and hemi-Fontan procedures. This would include assessing the characteristic geometric features; comparing the amount of pulsatility based on MRI velocity data, long term patient outcomes; tracking exercise capabilities and analyzing flow field features, turbulence and energy dissipation within the connection. These data may be insufficient to decide in favor of one technique but should still provide the surgeons with better rational for choosing one over the other.

10.2 Flare and Secondary Flow Structures

As mentioned earlier in this study, excessive flaring of the vessels within the anatomical intra-atrial model studied here was suspected to be partly responsible for the high energy dissipation observed within that connection. However, this did not fully agree with previous findings by Ensley et al [Ensley, 1999] who had recommended flaring of the connections in order to obtain smoother flow fields and lower power losses. Thus, there may be a threshold, and the exact relationship between flare and secondary flow structures would be an interesting focus for future work.

10.3 Characterization of the Energy Dissipation

The correlation between geometry of TCPC and the rate of energy dissipation (Section 7.2.1) leads to think that a simple law may be used to roughly predict the losses in a given TCPC geometry. Simplifying the problem to its utmost point, the venae cavae and pulmonary arteries could be considered as straight pipes with a characteristic diameter D_i , while the anastomosis sites within the TCPC could be approximated as sudden pipe expansions or contractions, between the connecting vessel and the connection area. Relatively simple expressions usually used to express the power losses in pipes, could then be applied as a first approximation to determine the power losses within the TCPC.

If such a model could be established, it would enable for a rough but fast prediction of the losses across a given TCPC design while awaiting more detailed and accurate results from the CFD simulations. It would also help to break up the losses associated with the TCPC into the viscous dissipation along the vessel walls and the

dissipation associated to flow separation regions and flow disturbances within the pouch. CFD could be used in combination with *in vitro* experiments for that purpose.

10.4 Accuracy of the Anatomical Reconstruction

This study of the TCPC has shown the importance of the geometry on hemodynamic efficiency of the connection using a combined experimental and numerical approach to the fluid dynamics. The TCPC anatomies were reconstructed from patient MRI. This reconstruction process included interpolating the raw data, segmenting the vessels of interest, generating the three-dimensional blood volume and finally performing some design operations in order to adapt the true anatomy to meet the experimental and numerical needs. The exact deviation between the experimental or numerical models and the true patient anatomy was difficult to quantify due to the fact that we had little control upon the three-dimensional volume generation step. An in-house code is currently under investigation, which would allow us to better control the overall process.

10.5 Compliant TCPC Models

The experimental models were built using rigid transparent rapid prototyping resins, and the numerical simulations were run using rigid walls. An interesting area of development would be to model the wall elasticity both numerically and experimentally. Compliance may turn out not to drastically impact the macro scale flow features, but should influence the microstructures, which in turn may impact the interaction between the flow and the blood cells.

Studies using rigid experimental and numerical models were necessary as a first step towards a validated CFD tool. Similarly, if the numerical models should ultimately focus on modeling true vessel compliance, a first and compulsory stage would be to make sure that both *in vitro* experiments and CFD simulations model the same compliance for an appropriate CFD validation, no matter how physiologic the *in vitro* compliance is.

The general methodology to obtain transparent compliant experimental models is to use RP with *opaque* resins to obtain an accurate water-soluble negative of the flow passage and then encase it in transparent Sylgard© (Dow Corning Inc.). Another possible track to explore is the recently developed transparent visco-elastic stereolithographic resins. Issues such as the transparency of the material, its mechanical properties and whether or not it would allow for surface polishing will have to be taken into account. These resins are still under development, and they were shown in the RP laboratory as prototypes, but may have great potential for our applications.

Similarly several tracks could be explored to model compliance numerically, including using immersed boundary conditions techniques originally developed to simulate the movement of a swimming fish [Gilmanov, 2002] or the in-house 2nd order accurate code mentioned earlier in this study. This last option would also require the development of a general methodology to generate fine overset meshes, which may call for a greater number of blocks than what was used for this model.

10.6 Physiologic Flow Conditions

Along the same lines, it would be worthwhile to assess and model the flow pulsatility within the TCPC connection. Similar to the compliance stage, any pulsatile

CFD model should first be validated against *in vitro* experiments. A study is currently under way in our laboratory to quantify the amount of pulsatility present in the TCPC *in vivo* based on patient MRI data. This study should first demonstrate the relevance of modeling such pulsatility and also provide information about the exact flow waveform to be implemented. Numerically, patient flow information could even be implemented directly into the CFD model as boundary conditions. MRI pulmonary flow information could then be compared to CFD results for validation purposes.

The clinical data analysis may also provide some insights into the role of the respiratory pump upon TCPC pulsatility. By looking at the frequencies present in the flow waveforms, one may identify the different contributions of the cardiac and respiratory pumps. It may also be interesting to compare patient data acquired via MRI with or without breath-hold.

10.7 Comparison of 3D DPIV Measurements with MR Flow Measurements and CFD Results

CFD is the only technique presented in this study to provide three-dimensional (3D) flow information. However, previous studies have shown the promise of adaptive control grid interpolation [Frakes, 2004] to reconstruct full 3D flow information based on *in vivo* or *in vitro* flow. Thus, it would be interesting to perform a comparative study using CFD results and the reconstructed 3D MRI and 3D DPIV data. This would enable a validation of the simplifying hypothesis used in numerical and experimental modeling. It would also allow a more in depth evaluation of the viscous dissipation method as a non-invasive means of determining TCPC energy losses by comparing between different power loss computation methods both numerically and experimentally (using the

traditional simplified control volume approach with the flow and pressure data or the full 3D velocity information based on the reconstructed MRI velocity fields).

However, prior to performing this 3D DPIV reconstruction a preliminary study is needed to assess the feasibility and accuracy of the 3D DPIV measurements in TCPC geometries with RP models.

10.8 Temporal Resolution

For better characterization of the TCPC templates it may also be relevant to define new evaluation parameters. As was suggested in Chapter VIII, these parameters could include IVC/SVC contributions to LPA and RPA flow, residence times of IVC and SVC streams, connection shear and pressure maps, dissipation field [Ensley, 1999; Frakes, 2003; Healy, 2001] and individual branch and connection pressure drop contributions. Considering that colliding caval flows generate some unsteadiness within the connection area from the simplest to the most complex models, characterization of this unsteadiness may be relevant both from the clinical aspect, as it may impact the amount of blood cell damage, and from the CFD validation point of view. Another possible parameter could thus be to provide a phase portrait of the central flow region of each TCPC model under study, which would allow for the distinction between designs leading to laminar, periodic, quasi periodic or chaotic flows. Such a study would involve an optimal temporal resolution on the experimental side, which may be achieved using laser Doppler velocimetry provided the models were designed for it.

10.9 Development of the CAD Interface for Surgical Planning

Finally, as this study aims to develop a surgical planning tool, an area of interest may be the development of an easy-to-use design tool for the surgeons to modify the TCPC geometry and perform some virtual surgeries. Preliminary work in this direction is currently under way in collaboration with the computer science department of the Georgia Institute of Technology, but further development may be needed.

APPENDIX A

LAVISION INC. DPIV EQUIPMENT

A.1 Hardware

Table A.1: List of the DPIV hardware (LaVision GmbH, Goettingen, Germany)

MODEL NUMBER	HARDWARE DESCRIPTION
1101MPRO	Double Image cross-correlation CCD cameras: 1600*1200 pixel resolution, progressive scan CCD, 30 frames/sec, >10-bit digital output (configurable), interframe time < 500ns, includes high speed digital camera interface and cable, multiformat lens adapter
1108013	Programmable Timing Unit (PTU): 16 output channels, 2 input triggers, 50ns time resolution, external and internal trigger capability, 100ns minimum time interval, PCI bus, board integrated TTL I/O – for programmable input and output triggers, 3 input channels, 20 output channels. Compatible with high speed triggering operation for 1000's triggers/sec for time resolved DPIV.

Table A.1: continued

MODEL NUMBER	HARDWARE DESCRIPTION
1108033	A/D converter: for external signals, 12-bit dynamic range, 50kHz sampling rate, 8 channels, integrated sampling control and data logging with images
1104101	On-line direct to disk storage controller and disks: Data acquisition from one or more cameras, RAID mode 0 (fast) requires 1*PCI II interface, standard 4*120GB HD, full capability with dual processor system.
1104004	System Computer: industrial PC with 19" rack mount, including 2*P4 processors, 5*free PCI II slots, 1GB RAM, 80GB harddisk, RW/CD/DVD ROM, 1.44MB floppy drive, 19" monitor, Windows 2000
1108196	Scheimplug camera Lens Adaptater: for F-mount camera lenses, full 360 degree adjustability
1002061	Stereo PIV Calibration target: dual plane, dual sided target, 100*100mm
1108193	Camera rail mount: 500mm optical rail with slider and 3D axis gear head

A.2 Software

Table A.2: List of the DPIV software (LaVision GmbH, Goettingen, Germany)

MODEL NUMBER	SOFTWARE DESCRIPTION
1105011	2D PIV/PTV software package: cross- and auto-correlation image processing algorithms (second-order correlation, deformed window correlation, multi-pass correlation), particle tracking (PTV) algorithms, advanced vector post-processing
1105012	3D PIV/PTV software upgrade: image acquisition and analysis for stereoscopic PIV, includes all necessary image calibration software
1105NET	5 users / Network License: includes distributed computing functionality for multiprocessor analysis on LAN. This allows up to 5 users to operate separate copies of DaVis on LAN or to operate one copy of DaVis as a master process for distributing data for processing on other machines on the network. Netsafe.

APPENDIX B

MICROSOFT® EXCEL 2000 SPREADSHEET USED FOR POWER LOSS COMPUTATION

A template of the Microsoft® Excel 2000 files used to compute the power losses associated with each TCPC template is provided together with this thesis (*Template.xls*). So as to make the subsequent explanations clearer, we will use:

- *Model 1* as an example of the model under study
- *3 L/min, 30/70 RPA/LPA* as flow rate conditions
- *Template.xls* to designate the Microsoft® Excel 2000 file where all the computations will be done.

B.1 Going from the Raw Data to Microsoft® Excel 2000

B.1.1 Raw Data Nomenclature

The pressure data were collected on a PC (Gateway 2000) using DAQAnnal, a LabVIEW (LabVIEW 5.1, National Instruments Corporation, Austin TX) based in-house software. The raw .DAT files were then converted into Microsoft® Excel 2000 spreadsheet within DAQAnnal. These raw data files were named and saved according to the following nomenclature:

- Nomenclature for the folder names:

Model name / Total flow rate / Repetition number

- Nomenclature for the raw data file names:

% of flow to the LPA_permutation number_transducer designation

so that *Model 1/3L/3Lno1/701T1.xls* contained the raw data recorded by the first transducer at 3 L/min and 30/70 RPA/LPA during the first experiment repetition and the first transducer permutation.

Each one of these raw data file contained 5000 values, acquired at 500Hz and which corresponded at one single data point.

B.1.2 Import Macro

Using the systematic nomenclature aforementioned, a Microsoft® Excel 2000 macro opened each one of the raw data file, averaged the 5000 values contained in there and copied the average and standard deviation into *Template.xls*. A sample of this macro is provided below:

Open the raw data file:

```
ChDir "C:\Model-Name\3L\3Lno1"
Workbooks.OpenText Filename:="C:\Model-Name \3L\3Lno1\301T1.xls",
  Origin:=xlWindows, StartRow:=1, DataType:=xlDelimited,
  TextQualifier:=xlDoubleQuote, ConsecutiveDelimiter:=False, Tab:=True,
  Semicolon:=False, Comma:=False, Space:=False, Other:=False,
  FieldInfo:=Array(Array(1, 1), Array(2, 1), Array(3, 1), Array(4, 1), Array(5, 1),
  Array(6, 1), Array(7, 1), Array(8, 1), Array(9, 1), Array(10, 1), Array(11, 1),
  Array(12, 1), Array(13, 1), Array(14, 1), Array(15, 1), Array(16, 1), Array(17, 1),
  Array(18, 1), Array(19, 1), Array(20, 1))
```

Compute the average and standard deviation:

```
Range("V1").Select
ActiveCell.FormulaR1C1 = "=AVERAGE(RC[-20]:R[499]C[-2])"
("W1").Select
```

```
ActiveCell.FormulaR1C1 = "=STDEV(RC[-21]:R[499]C[-3])"
```

Copy and paste into the power loss computation spreadsheet (template.xls):

```
Range("V1:W1").Select  
Selection.Copy  
Windows("Template.xls").Activate  
Range("H7").Select  
Selection.PasteSpecial Paste:=xlValues, Operation:=xlNone, SkipBlanks:=False,  
Transpose:=False
```

Close the raw data file:

```
Windows("301T1.xls").Activate  
ActiveWorkbook.Close
```

B.2 Power Loss Computation

Template.xls is organized as follows:

B.2.1 Summary

A Summary spreadsheet (Figure B.1), where all the parameters necessary for the power loss computations should be entered, and where all the results are summarized

- Model characteristics:
 - o Model name
 - o Vessel dimensions
- Transducer characteristics:
 - o Calibration factor
- Flow characteristics:
 - o Total flow rates

- Flow splits
- Statistics:
 - Number of standard deviations to be taken into account
- Summary of the results, which should not be filled in and provides:
 - The average pressure and power losses for all the tested flow conditions with the corresponding standard deviations
 - The equal pulmonary vascular resistance (EPVR) operating points for all the tested cardiac outputs
 - A graph with all the power losses and the EPVR data obtained for that model

B.2.2 No Flow Measurements

This spreadsheet contains the pressure measurements obtained with static fluid inside the loop, and will be used to retrieve the pressure head effect from other the pressure measurements. The import raw data macro may be called from that spreadsheet to import the acquired no flow measurements.

B.2.3 Raw Data

Template.xls is designed for a maximum of five cardiac outputs. There is one spreadsheet per flow rate. The raw data import macro can be called from each one of these spreadsheets. These raw measurements, which correspond to voltages, will

automatically be converted into pressure measurements using the conversion factor provided on the Summary page, and the No Flow measurements.

These raw pressure data are then automatically averaged and filtered using the tolerance set on the Summary page. The outliers will appear as zeros and should be manually erased for subsequent computations.

B.2.4 Processed Data

The data are then processed and can be visualized at different stages:

- Summary and comparison of the pressure measurements obtained with the different pressure transducers
- Power loss computation spreadsheet
- Summary and comparison of the power losses obtained with the different transducers
- Equal pulmonary resistance computation

To compute the equal pulmonary resistance points, the pressure and power loss data points are fitted with second order polynomial regressions. The equation of these regression curves should be manually entered into the corresponding fields, so as to be used in the computations.

All the results are summarized on the Summary sheet (Figure B.1).

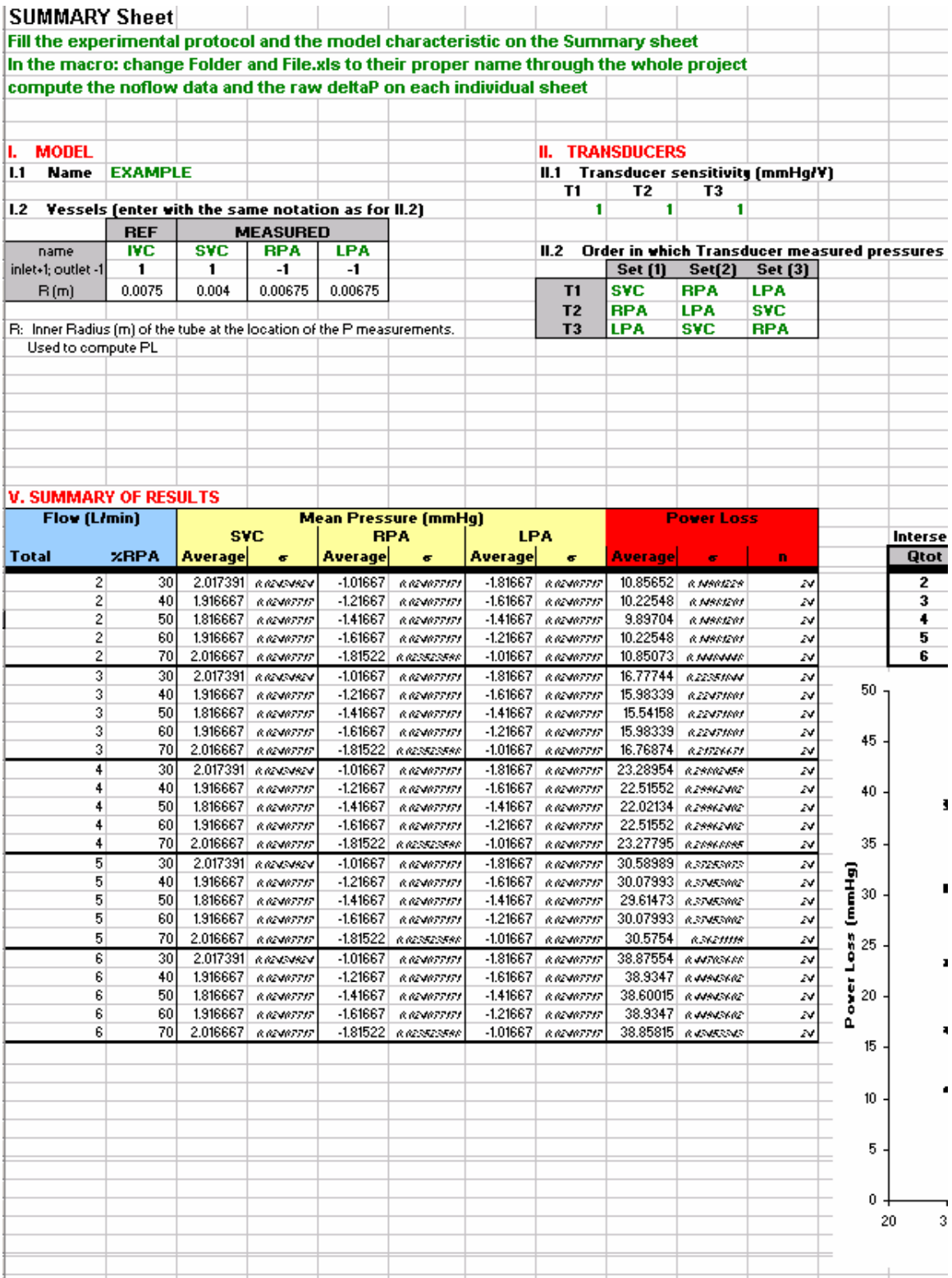


Figure B.1: Typical Summary page of the Microsoft® Excel files that were used in this study to compute the power losses

III. STATISTICS

III.1 Error on flow rate reading (L/min)

0.1

III.2 # of stdev taken into account in the average dP

- for dP 2

- for 0 offset 3

measured pressures

IV. FLOW

Designed for 5 total flow rates, 5 splits. Enter all 5, even if it's 5 times the same split

Q total L/min	Flow split (% total flow)				X axis, graphs	
	IVC	SVC	RPA	LPA	%RPA	
2	60	40	30	70	30	
3	60	40	40	60	40	
4	60	40	50	50	50	
5	60	40	60	40	60	
6	60	40	70	30	70	

Intersection: pulmonary flow split at equal lung resistance for the given Rlung

Qtot	%RPA	SVC	RPA	LPA	Power Loss	ϵ	n
2	49.98925	1.851881	-1.49683	48.56161	9.958527	R.14968301	2V
3	49.99186	1.851881	-1.49689	48.56689	15.63228	R.22471901	2V
4	49.99345	1.851881	-1.49692	48.5701	22.14403	R.29962902	2V
5	49.99452	1.851881	-1.49695	48.57227	29.76807	R.37453902	2V
6	49.99529	1.851881	-1.49696	48.57382	38.78365	R.44944902	2V

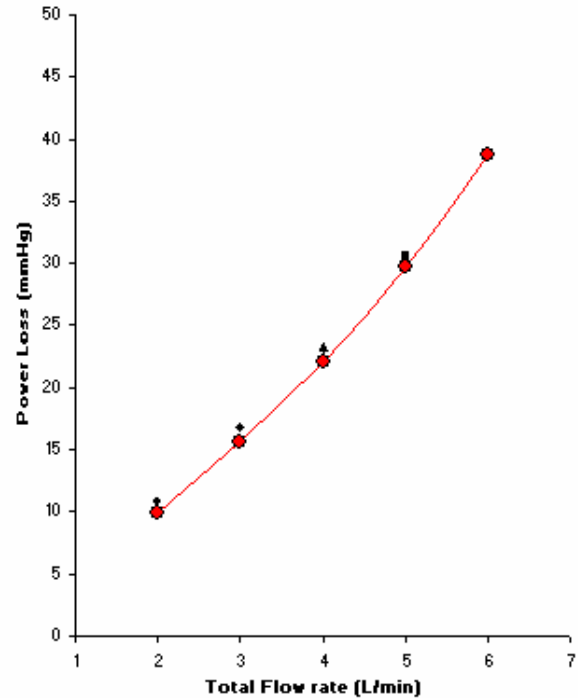
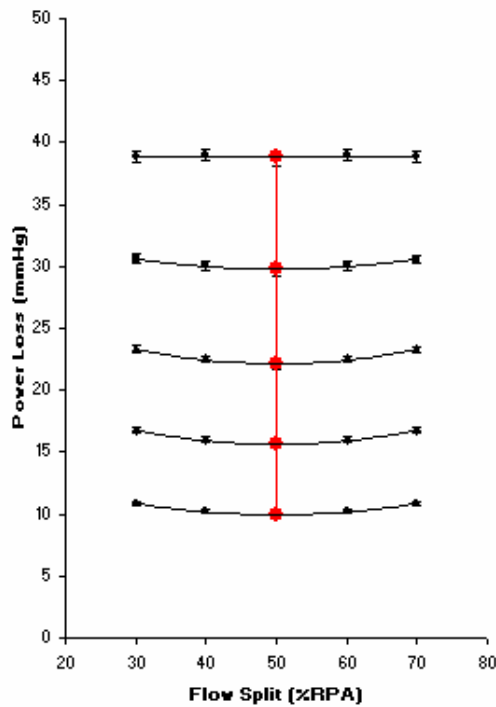


Figure B.1: continued

APPENDIX C

POWER LOSS AND PRESSURE DATA

C.1 Model 1

Table C.1: Summary of all power losses and pressure drop measurements for Model 1

Flow (L/min)		Mean Pressure (mmHg)						Power Loss (mW)	
Total	%RPA	SVC		RPA		LPA		Average	s
		Average	s	Average	s	Average	s		
2	30	0.011	0.027	-0.121	0.022	-0.302	0.053	1.038	0.185
2	40	-0.002	0.025	-0.160	0.026	-0.269	0.057	0.997	0.175
2	50	-0.022	0.026	-0.208	0.030	-0.222	0.041	0.943	0.137
2	60	-0.040	0.027	-0.257	0.037	-0.197	0.033	0.967	0.148
2	70	-0.061	0.027	-0.331	0.051	-0.163	0.031	1.056	0.179
4	30	0.114	0.097	-0.275	0.097	-0.862	0.103	5.850	0.892
4	40	0.060	0.076	-0.446	0.069	-0.626	0.098	5.137	0.681
4	50	0.015	0.060	-0.596	0.077	-0.492	0.077	5.104	0.673
4	60	-0.078	0.042	-0.783	0.102	-0.395	0.079	5.302	0.737
4	70	-0.159	0.057	-0.979	0.136	-0.367	0.069	5.852	0.924
6	30	0.313	0.252	-0.434	0.176	-1.572	0.260	15.884	2.170
6	40	0.255	0.256	-0.822	0.126	-1.117	0.234	14.679	1.737
6	50	0.162	0.246	-1.140	0.193	-0.823	0.224	14.686	2.137
6	60	-0.012	0.099	-1.416	0.190	-0.599	0.182	14.498	1.916
6	70	-0.333	0.099	-1.869	0.272	-0.638	0.156	15.877	2.762

Table C.2: Equal pulmonary vascular resistance points for Model 1

Flow (L/min)		Pressure (mmHg)			Power Loss (mW)
Total	%RPA	SVC	RPA	LPA	
2	50	-0.022	-0.205	-0.227	0.951
4	50	0.008	-0.597	-0.488	5.056
6	49	0.174	-1.099	-0.815	14.417

C.2 Model 2

Table C.3: Summary of all power losses and pressure drop measurements for Model 2

Flow (L/min)		Mean Pressure (mmHg)						Power Loss (mW)	
Total	%RPA	SVC		RPA		LPA		Average	s
		Average	s	Average	s	Average	s		
2	30	0.002	0.015	-0.165	0.015	-0.345	0.028	1.217	0.077
2	40	-0.020	0.017	-0.205	0.015	-0.286	0.028	1.064	0.132
2	50	-0.037	0.013	-0.260	0.017	-0.249	0.028	1.012	0.210
2	60	-0.049	0.013	-0.301	0.022	-0.222	0.024	1.083	0.120
2	70	-0.082	0.014	-0.375	0.024	-0.205	0.028	1.213	0.096
3	30	0.028	0.015	-0.250	0.034	-0.697	0.022	3.553	0.105
3	40	-0.031	0.018	-0.346	0.029	-0.514	0.023	2.894	0.109
3	50	-0.085	0.013	-0.461	0.046	-0.422	0.016	2.807	0.166
3	60	-0.104	0.016	-0.539	0.033	-0.380	0.024	2.891	0.123
3	70	-0.150	0.014	-0.625	0.044	-0.348	0.028	2.941	0.222
4	30	0.041	0.023	-0.484	0.033	-1.047	0.065	7.301	0.392
4	40	-0.066	0.028	-0.578	0.045	-0.853	0.046	6.371	0.327
4	50	-0.165	0.022	-0.730	0.030	-0.737	0.042	6.156	0.259
4	60	-0.249	0.028	-0.959	0.049	-0.601	0.039	6.368	0.255
4	70	-0.320	0.028	-1.118	0.042	-0.599	0.037	6.765	0.248
5	30	0.108	0.013	-0.634	0.050	-1.574	0.028	13.565	0.294
5	40	-0.179	0.007	-0.841	0.034	-1.227	0.036	11.125	0.381
5	50	-0.296	0.017	-1.065	0.036	-1.026	0.028	10.726	0.269
5	60	-0.351	0.023	-1.227	0.090	-0.929	0.036	10.747	0.660
5	70	-0.636	0.072	-1.752	0.102	-1.037	0.082	12.989	0.718
6	30	0.225	0.050	-0.743	0.086	-2.035	0.159	20.965	1.995
6	40	-0.104	0.095	-1.024	0.125	-1.653	0.122	18.127	1.216
6	50	-0.336	0.048	-1.304	0.091	-1.321	0.092	16.440	0.919
6	60	-0.504	0.035	-1.629	0.108	-1.147	0.077	16.461	1.087
6	70	-0.652	0.048	-1.997	0.095	-1.088	0.055	17.322	0.916

Table C.4: Equal pulmonary vascular resistance points for Model 2

Flow (L/min)		Pressure (mmHg)			Power Loss (mW)
Total	%RPA	SVC	RPA	LPA	
2	50	-0.035	-0.253	-0.249	1.020
3	50	-0.079	-0.455	-0.419	2.788
4	50	-0.164	-0.744	-0.718	6.153
5	50	-0.285	-1.028	-1.010	10.429
6	50	-0.343	-1.321	-1.323	16.525

C.3 Model 3

Table C.5: Summary of all power losses and pressure drop measurements for Model 3

Flow (L/min)		Mean Pressure (mmHg)						Power Loss (mW)	
Total	%RPA	SVC		RPA		LPA		Average	s
		Average	s	Average	s	Average	s		
2	30	0.707	0.085	-0.126	0.078	-0.282	0.073	2.564	0.255
2	40	0.672	0.078	-0.154	0.054	-0.241	0.049	2.454	0.274
2	50	0.641	0.074	-0.206	0.038	-0.229	0.036	2.478	0.281
2	60	0.627	0.072	-0.257	0.042	-0.222	0.049	2.538	0.298
2	70	0.579	0.073	-0.382	0.069	-0.248	0.039	2.812	0.325
3	30	1.031	0.124	-0.160	0.027	-0.546	0.071	6.506	0.693
3	40	0.975	0.122	-0.231	0.034	-0.372	0.051	5.866	0.598
3	50	0.884	0.109	-0.310	0.056	-0.319	0.051	5.707	0.622
3	60	0.849	0.100	-0.396	0.056	-0.262	0.038	5.708	0.580
3	70	0.746	0.087	-0.611	0.089	-0.328	0.047	6.384	0.720
4	30	1.630	0.204	-0.282	0.039	-0.839	0.140	13.868	1.591
4	40	1.583	0.199	-0.396	0.048	-0.607	0.082	13.029	1.301
4	50	1.425	0.172	-0.462	0.063	-0.560	0.067	12.577	1.171
4	60	1.306	0.163	-0.653	0.089	-0.419	0.055	12.369	1.186
4	70	1.163	0.153	-0.873	0.114	-0.453	0.069	12.874	1.375
5	30	2.187	0.297	-0.560	0.234	-1.677	0.447	28.737	3.805
5	40	2.023	0.299	-0.665	0.232	-1.073	0.273	24.472	2.717
5	50	1.905	0.234	-0.782	0.206	-0.938	0.189	23.822	2.188
5	60	1.774	0.255	-0.929	0.143	-0.814	0.215	23.072	2.262
5	70	1.515	0.266	-1.435	0.207	-0.911	0.230	25.032	2.807
6	30	2.869	0.775	-0.568	0.170	-2.274	0.276	45.889	2.498
6	40	2.648	0.775	-0.880	0.243	-1.349	0.273	38.899	5.855
6	50	2.229	0.722	-0.953	0.266	-1.092	0.411	36.148	5.297
6	60	2.223	0.384	-1.309	0.237	-0.991	0.211	36.908	3.659
6	70	2.047	0.300	-2.135	0.332	-0.968	0.203	41.804	3.028

Table C.6: Equal pulmonary vascular resistance points for Model 3

Flow (L/min)		Pressure (mmHg)			Power Loss (mW)
Total	%RPA	SVC	RPA	LPA	
2	50	0.645	-0.199	-0.223	2.457
3	50	0.901	-0.303	-0.296	5.636
4	50	1.439	-0.490	-0.510	12.519
5	51	1.893	-0.774	-0.865	23.187
6	51	2.320	-1.003	-1.038	35.979

C.4 Model 4

Table C.7: Summary of all power losses and pressure drop measurements for Model 4

Flow (L/min)		Mean Pressure (mmHg)						Power Loss (mW)	
Total	%RPA	SVC		RPA		LPA		Average	s
		Average	s	Average	s	Average	s		
2	30	0.904	0.151	-0.068	0.029	-0.317	0.049	2.947	0.404
2	40	0.858	0.145	-0.100	0.029	-0.228	0.041	2.513	0.529
2	50	0.831	0.144	-0.176	0.045	-0.198	0.045	2.679	0.392
2	60	0.800	0.138	-0.245	0.036	-0.160	0.043	2.704	0.368
2	70	0.766	0.134	-0.365	0.056	-0.143	0.047	2.659	1.025
3	30	1.312	0.236	-0.134	0.050	-0.620	0.105	7.546	0.974
3	40	1.254	0.221	-0.234	0.062	-0.415	0.103	6.789	0.917
3	50	1.200	0.217	-0.325	0.097	-0.329	0.073	6.632	0.888
3	60	1.182	0.219	-0.487	0.089	-0.302	0.075	7.069	0.890
3	70	1.129	0.213	-0.676	0.114	-0.267	0.068	7.586	1.042
4	30	2.597	0.469	-0.283	0.042	-1.041	0.126	18.568	2.016
4	40	2.363	0.347	-0.451	0.064	-0.753	0.096	16.773	1.810
4	50	2.189	0.301	-0.544	0.068	-0.550	0.099	15.617	1.634
4	60	2.076	0.306	-0.849	0.158	-0.448	0.129	16.252	2.199
4	70	1.978	0.301	-1.146	0.161	-0.486	0.075	17.564	2.208
5	30	3.150	0.551	-0.404	0.069	-1.443	0.195	30.678	3.800
5	40	3.067	0.552	-0.612	0.088	-1.043	0.160	28.680	3.613
5	50	3.002	0.485	-0.833	0.096	-0.782	0.093	28.112	2.812
5	60	2.815	0.447	-1.021	0.119	-0.540	0.064	27.096	2.673
5	70	2.566	0.411	-1.655	0.206	-0.620	0.076	30.451	3.421
6	30	3.868	0.676	-0.629	0.113	-2.046	0.202	49.337	4.714
6	40	3.797	0.663	-0.971	0.135	-1.471	0.198	46.484	5.180
6	50	3.660	0.619	-1.229	0.169	-1.125	0.189	45.233	5.049
6	60	3.453	0.552	-1.555	0.209	-0.732	0.092	44.048	4.454
6	70	3.194	0.533	-2.325	0.382	-0.880	0.150	49.344	6.550

Table C.8: Equal pulmonary vascular resistance points for Model 4

Flow (L/min)		Pressure (mmHg)			Power Loss (mW)
Total	%RPA	SVC	RPA	LPA	
2	50	0.829	-0.169	-0.188	2.608
3	50	1.208	-0.337	-0.329	6.675
4	50	2.194	-0.588	-0.548	15.812
5	50	2.986	-0.786	-0.746	27.540
6	50	3.663	-1.196	-1.061	44.562

C.5 Model 5

Table C.9: Summary of all power losses and pressure drop measurements for Model 5

Flow (L/min)		Mean Pressure (mmHg)						Power Loss	
Total	%RPA	SVC		RPA		LPA		(mW)	
		Average	s	Average	s	Average	s	Average	s
1	30	0.110	0.029	-0.078	0.013	-0.078	0.013	0.440	0.041
1	50	0.110	0.009	-0.114	0.027	-0.114	0.027	0.380	0.032
1	70	0.127	0.013	-0.199	0.019	-0.199	0.019	0.483	0.031
2	30	0.315	0.100	-0.240	0.034	-0.240	0.034	2.729	0.270
2	40	0.263	0.078	-0.389	0.068	-0.389	0.068	2.782	0.288
2	50	0.305	0.060	-0.407	0.066	-0.407	0.066	2.610	0.263
2	60	0.326	0.081	-0.447	0.092	-0.447	0.092	2.568	0.386
2	70	0.366	0.074	-0.514	0.076	-0.514	0.076	2.754	0.304
3	30	0.609	0.141	-0.375	0.064	-0.375	0.064	8.158	0.809
3	40	0.494	0.109	-0.555	0.129	-0.555	0.129	7.108	0.955
3	50	0.498	0.090	-0.619	0.068	-0.619	0.068	6.657	0.442
3	60	0.630	0.100	-0.695	0.099	-0.695	0.099	6.552	0.833
3	70	0.748	0.098	-1.024	0.157	-1.024	0.157	8.029	0.970
4	30	1.189	0.240	-0.568	0.130	-1.775	0.378	18.720	2.087
4	40	0.962	0.193	-1.054	0.338	-1.599	0.313	18.321	2.013
4	50	0.977	0.109	-1.343	0.173	-1.085	0.152	17.122	1.149
4	60	1.263	0.127	-1.370	0.198	-0.769	0.053	17.162	1.258
4	70	1.324	0.159	-1.669	0.158	-0.446	0.110	18.217	1.127
5	30	1.506	0.290	-0.893	0.249	-2.657	0.234	34.120	1.812
5	40	1.197	0.167	-1.595	0.243	-2.104	0.158	31.571	1.591
5	50	1.363	0.142	-1.743	0.118	-1.518	0.117	29.754	1.151
5	60	1.716	0.160	-1.838	0.243	-1.044	0.113	29.649	0.999
5	70	1.742	0.399	-2.557	0.342	-0.745	0.106	33.893	2.341
6	30	1.723	0.274	-2.439	0.387	-5.035	0.563	72.477	5.360
6	40	1.397	0.198	-2.225	0.272	-3.249	0.292	54.167	3.358
6	50	1.861	0.232	-2.224	0.191	-2.296	0.307	49.700	2.696
6	60	2.400	0.387	-3.050	0.514	-1.734	0.555	55.313	5.729
6	70	2.599	0.491	-3.917	0.467	-1.068	0.330	61.223	3.789

Table C.10: Equal pulmonary vascular resistance points for Model 5

Flow (L/min)		Pressure (mmHg)			Power Loss (mW)
Total	%RPA	SVC	RPA	LPA	
1	50	0.109	-0.114	-0.100	0.371
2	50	0.290	-0.418	-0.375	2.632
3	50	0.510	-0.604	-0.596	6.532
4	50	1.021	-1.284	-1.159	17.323
5	50	1.377	-1.712	-1.545	29.624
6	50	1.827	-2.334	-2.326	50.278

C.6 Model 6

Table C.11: Summary of all power losses and pressure drop measurements for Model 6

Flow (L/min)		Mean Pressure (mmHg)						Power Loss (mW)	
Total	%RPA	SVC		RPA		LPA		Average	s
		Average	s	Average	s	Average	s		
1	30	0.786	0.132	-0.551	0.101	-3.694	0.291	6.008	0.433
1	50	0.746	0.128	-0.748	0.096	-2.247	0.218	3.727	0.258
1	70	0.749	0.154	-0.955	0.081	-0.748	0.283	2.471	0.199
2	30	3.348	0.633	-1.040	0.582	-14.353	1.221	45.554	4.566
2	40	3.424	0.679	-1.505	0.483	-11.092	0.809	34.575	3.233
2	50	3.267	0.617	-2.337	0.891	-8.989	1.324	28.873	4.599
2	60	3.015	0.596	-2.629	1.147	-7.151	1.284	23.723	4.804
2	70	3.078	0.610	-3.347	1.346	-4.772	1.837	20.817	5.909
3	30	5.322	1.460	-1.168	0.291	-27.658	1.834	123.874	11.033
3	40	5.623	0.961	-1.798	0.358	-22.461	1.404	96.925	8.228
3	50	4.903	0.848	-3.849	0.858	-18.642	1.215	80.943	5.147
3	60	4.592	0.773	-5.295	0.532	-13.333	1.110	64.395	5.779
3	70	4.385	0.438	-6.547	0.603	-8.930	0.393	55.276	3.862

Table C.12: Equal pulmonary vascular resistance points for Model 6

Flow (L/min)		Pressure (mmHg)			Power Loss (mW)
Total	%RPA	SVC	RPA	LPA	
1	62	0.740	-0.542	-1.537	2.521
2	70	3.000	-3.024	-5.220	20.480
3	70	4.265	-6.429	-9.000	54.233

C.7 RP Model 1

Table C.13: Summary of all power losses and pressure drop measurements for the RP Model 1

Flow (L/min)		Mean Pressure (mmHg)						Power Loss (mW)	
Total	%RPA	SVC		RPA		LPA		Average	s
		Average	s	Average	s	Average	s		
2	30	0.027	0.007	-0.183	0.018	-0.320	0.017	1.201	0.061
2	40	-0.008	0.008	-0.224	0.015	-0.257	0.020	1.070	0.062
2	50	-0.029	0.009	-0.253	0.020	-0.229	0.012	1.048	0.055
2	60	-0.054	0.005	-0.293	0.010	-0.216	0.015	1.005	0.208
2	70	-0.077	0.005	-0.351	0.009	-0.201	0.016	1.135	0.041
4	30	0.148	0.016	-0.554	0.017	-1.009	0.047	7.590	0.279
4	40	0.038	0.013	-0.649	0.017	-0.800	0.024	6.711	0.155
4	50	-0.112	0.014	-0.807	0.026	-0.700	0.032	6.529	0.227
4	60	-0.191	0.015	-0.916	0.029	-0.620	0.027	6.411	0.218
4	70	-0.326	0.019	-1.125	0.048	-0.668	0.033	6.930	0.309
6	30	0.395	0.037	-1.013	0.051	-1.966	0.177	22.177	1.908
6	40	0.192	0.036	-1.205	0.038	-1.550	0.101	19.850	1.074
6	50	-0.076	0.044	-1.401	0.084	-1.308	0.054	18.431	0.893
6	60	-0.472	0.030	-1.736	0.133	-1.160	0.052	17.553	1.299
6	70	-0.736	0.059	-2.139	0.236	-1.285	0.067	18.846	2.336

Table C.14: Equal pulmonary vascular resistance points for the RP Model 1

Flow (L/min)		Pressure (mmHg)			Power Loss (mW)
Total	%RPA	SVC	RPA	LPA	
2	50	-0.031	-0.254	-0.229	1.020
4	50	-0.087	-0.781	-0.687	6.431
6	50	-0.099	-1.413	-1.289	18.276

C.8 Anatomic Intra-Atrial Model

Table C.15: Summary of all power losses and pressure drop measurements for the anatomic intra-atrial model

Flow (L/min)		Mean Pressure (mmHg)						Power Loss (mW)	
Total	%RPA	SVC		RPA		LPA		Average	s
		Average	s	Average	s	Average	s		
1	30	-0.856	0.996	-3.856	2.481	-10.654	2.691	17.577	4.563
1	50	-0.748	1.002	-5.224	2.686	-7.619	2.584	13.341	4.901
1	70	-0.704	0.971	-6.790	2.527	-4.569	2.477	12.802	4.668
2	30	4.122	2.332	-6.225	2.753	-29.418	2.194	100.706	10.004
2	40	5.462	2.012	-7.850	2.287	-22.251	6.691	79.233	7.858
2	50	4.514	2.108	-9.576	2.781	-18.147	3.045	67.522	11.328
2	60	4.570	1.778	-10.936	2.755	-13.729	2.968	60.333	11.988
2	70	5.013	1.840	-12.917	2.694	-10.775	3.458	62.030	10.311
3	30	5.590	2.524	-7.666	4.140	-42.196	7.973	205.422	40.312
3	40	6.244	3.588	-10.218	2.652	-37.476	4.263	181.088	23.271
3	50	7.392	2.987	-13.573	3.322	-32.891	2.767	167.481	18.265
3	60	7.608	3.291	-15.294	3.453	-24.180	2.356	141.354	17.239
3	70	4.904	7.008	-21.255	3.321	-14.483	2.665	136.397	20.525

Table C.16: Equal pulmonary vascular resistance points for the anatomic intra-atrial model

Flow (L/min)		Pressure (mmHg)			Power Loss (mW)
Total	%RPA	SVC	RPA	LPA	
1	59	-0.723	-5.955	-6.335	12.782
2	64	4.857	-11.823	-12.736	60.860
3	65	6.183	-18.673	-19.913	141.186

C.9 Anatomic Bilateral SVC Model

Table C.17: Summary of all power losses and pressure drop measurements for the anatomic bilateral SVC model

Flow (L/min)		Mean Pressure (mmHg)								Power Loss (mw)	
Total	%RPA	RSVC		LSVC		RPA		LPA		Average	s
		Average	s	Average	s	Average	s	Average	s		
2	70	-0.024	0.383	-0.103	0.528	-1.708	0.245	-1.683	0.910	5.111	1.206
2	60	-0.036	0.411	-0.043	0.364	-1.245	0.453	-2.401	0.867	5.849	1.778
2	50	0.011	0.412	0.014	0.241	-1.186	0.146	-2.876	0.881	7.613	1.630
2	40	-0.058	0.367	-0.075	0.248	-0.815	0.502	-3.292	1.012	8.433	2.028
2	30	0.077	0.208	-0.207	0.340	-0.409	0.151	-4.644	1.134	12.543	2.674
3	70	-0.025	0.469	0.246	0.421	-3.119	0.319	-2.343	0.928	10.110	5.307
3	60	0.142	0.349	0.170	0.293	-2.232	0.213	-3.899	0.766	12.537	5.627
3	50	0.163	0.255	-0.006	0.294	-1.658	0.161	-5.030	0.813	15.787	6.705
3	40	0.164	0.410	-0.085	0.318	-1.103	0.189	-6.363	1.099	20.532	8.843
3	30	0.116	0.403	-0.418	0.436	-0.660	0.418	-8.131	1.606	27.743	12.476
4	70	-0.129	0.736	0.291	0.491	-6.155	0.953	-5.187	1.769	33.888	8.255
4	60	-0.062	0.620	-0.049	0.573	-4.935	1.326	-7.063	1.933	37.924	11.582
4	50	-0.132	0.789	-0.324	0.634	-3.978	0.808	-9.262	1.947	46.408	9.620
4	40	-0.094	0.758	-0.620	0.672	-2.818	0.673	-11.266	2.271	55.392	11.826
4	30	0.028	0.495	-0.797	0.347	-2.178	0.731	-12.800	2.052	65.350	12.466

Table C.18: Equal pulmonary vascular resistance points for the anatomic bilateral SVC model

Flow (L/min)		Pressure (mmHg)				Power Loss (mW)
Total	%RPA	RSVC	LSVC	RPA	LPA	
2	61	-0.03	-0.04	-1.42	-2.29	5.63
3	61	0.10	0.18	-2.37	-3.40	11.95
4	62	-0.12	0.01	-5.14	-7.00	37.87

APPENDIX D

POWER LOSS VS. FLOW RATE

D.1 30/70 RPA/LPA

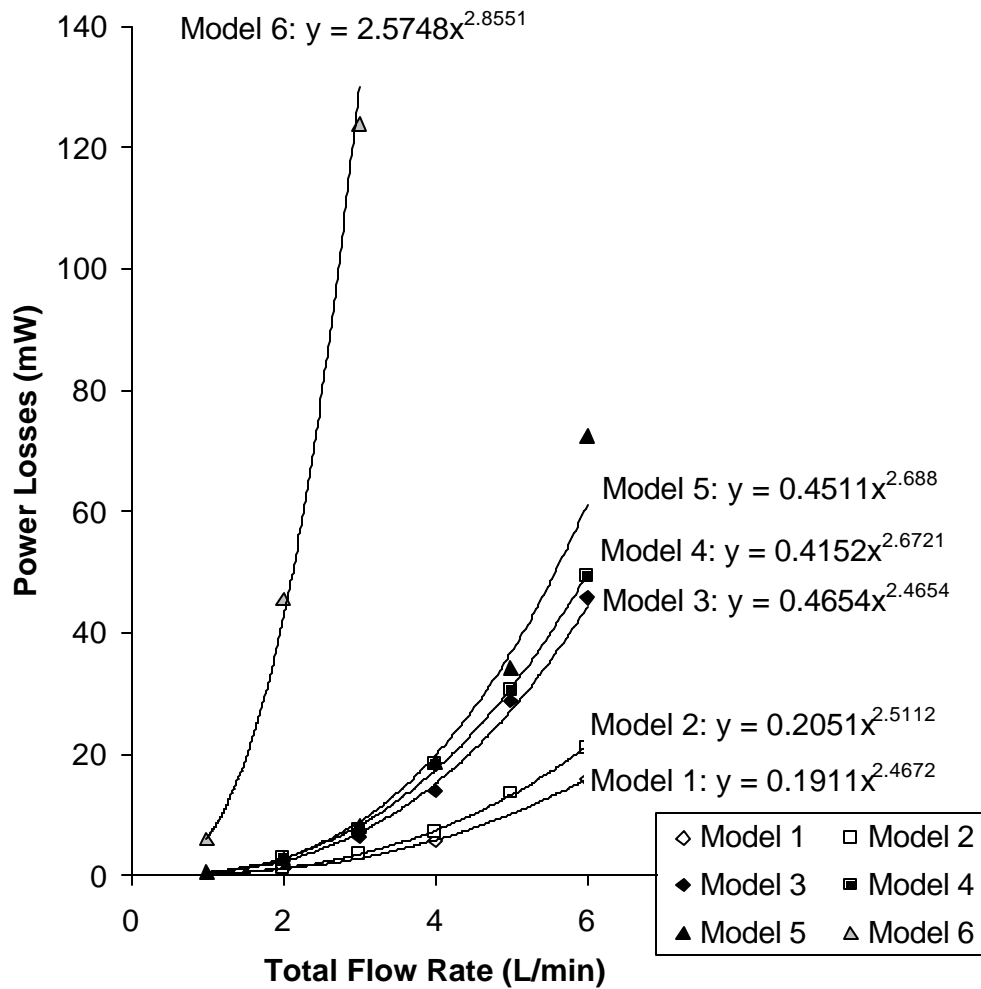


Figure D.1: Power losses in the six simplified glass models at 60/40 IVC/SVC and 30/70 RPA/LPA as a function of the total flow rate.

D.2 40/60 RPA/LPA

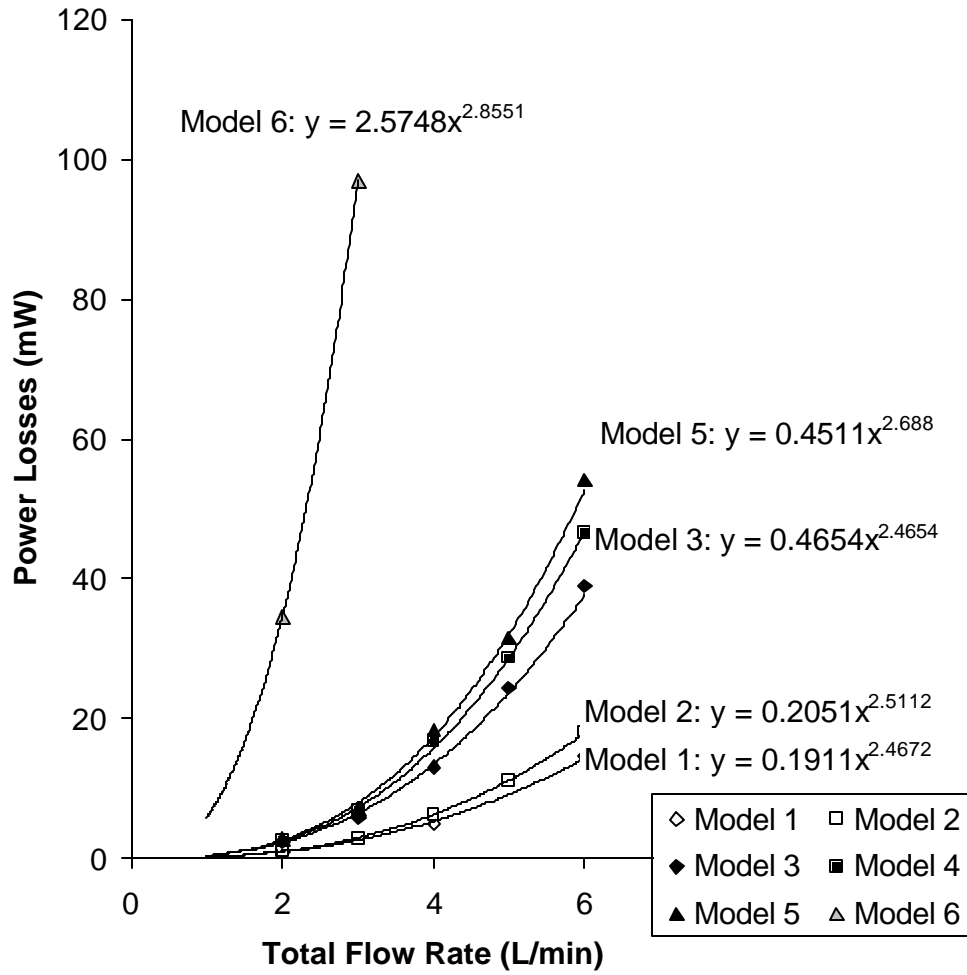


Figure D.2: Power losses in the six simplified glass models at 60/40 IVC/SVC and 40/60 RPA/LPA as a function of the total flow rate.

D.3 50/50 RPA/LPA

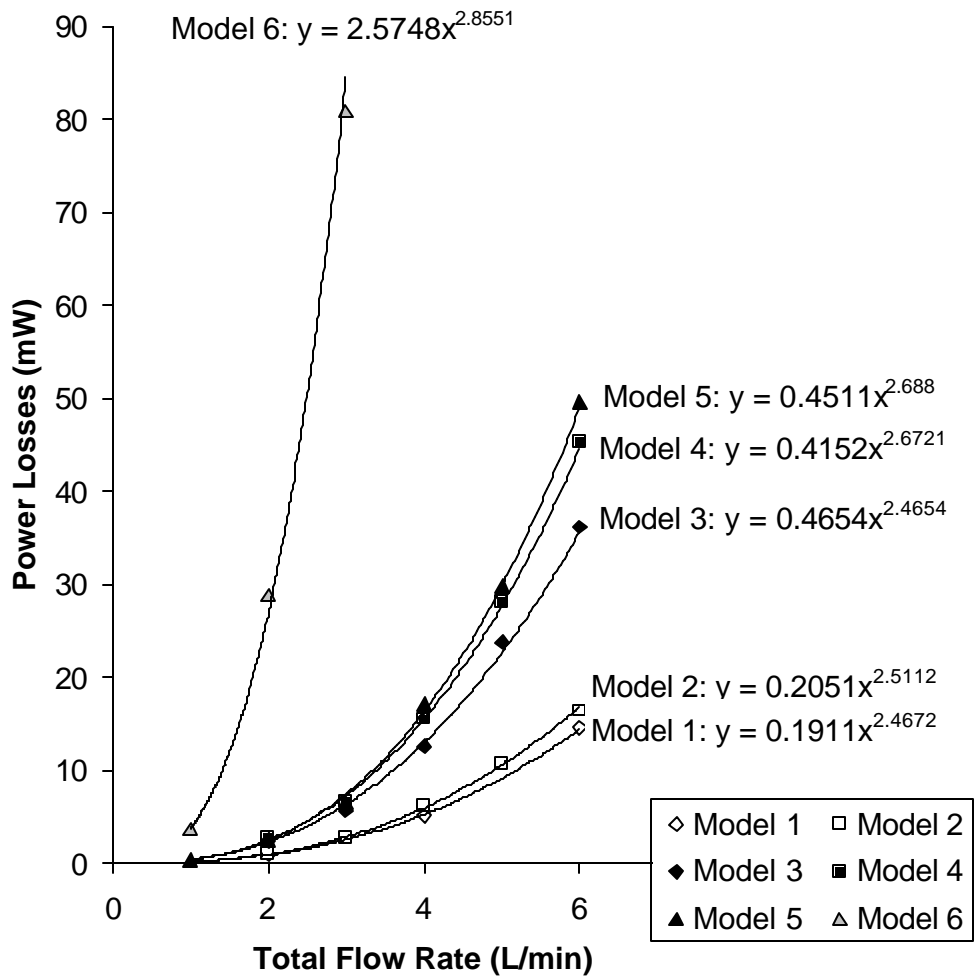


Figure D.3: Power losses in the six simplified glass models at 60/40 IVC/SVC and 50/50 RPA/LPA as a function of the total flow rate.

D.4 60/40 RPA/LPA

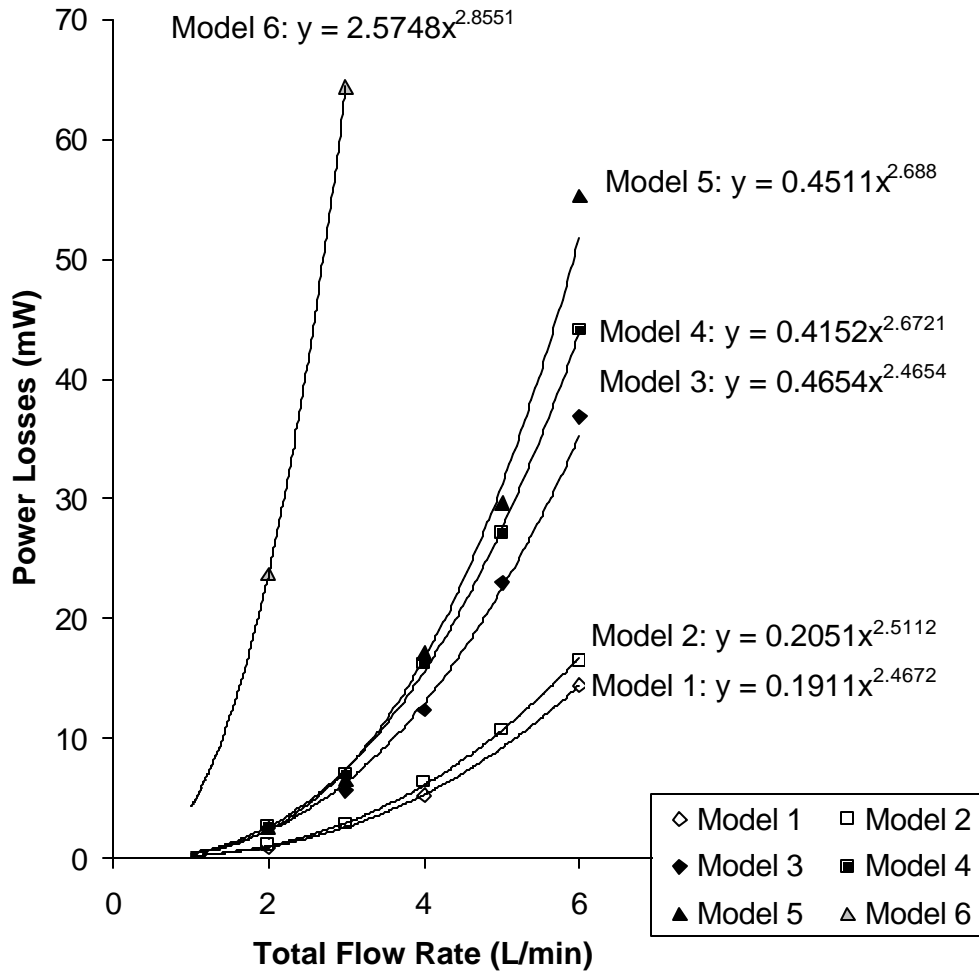


Figure D.4: Power losses in the six simplified glass models at 60/40 IVC/SVC and 60/40 RPA/LPA as a function of the total flow rate.

D.5 70/30 RPA/LPA

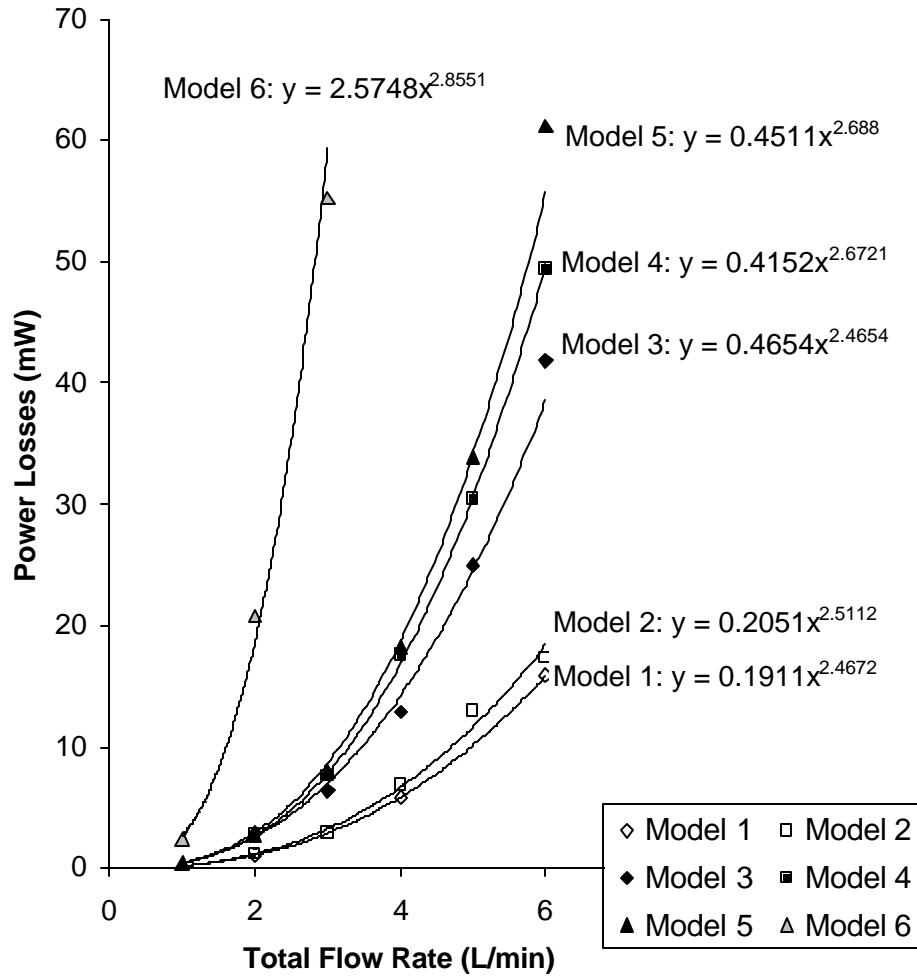


Figure D.5: Power losses in the six simplified glass models at 60/40 IVC/SVC and 70/30 RPA/LPA as a function of the total flow rate.

REFERENCES

- Amodeo, A., L. Galletti, S. Marianeschi, S. Picardo, S. Giannico, P. Di Renzi, and C. Marcelletti, Extracardiac Fontan operation for complex cardiac anomalies: seven years' experience: *J Thorac Cardiovasc Surg*, 1997; 114 (6): 1020-30; discussion 1030-1.
- Anderson, R. N., and B. L. Smith, Deaths: leading causes for 2001: *Natl Vital Stat Rep*, 2003; 52 (9): 1-85.
- Augst, A. D., D. C. Barratt, A. D. Hughes, F. P. Glor, G. T. S. A. Mc, and X. Y. Xu, Accuracy and reproducibility of CFD predicted wall shear stress using 3D ultrasound images: *J Biomech Eng*, 2003; 125 (2): 218-22.
- Bale-Glickman, J., K. Selby, D. Saloner, and O. Savas, Experimental flow studies in exact-replica phantoms of atherosclerotic carotid bifurcations under steady input conditions: *J Biomech Eng*, 2003; 125 (1): 38-48.
- Blalock, A., and H. B. Taussig, The surgical treatment of malformations of the heart in which there is pulmonary stenosis or pulmonary atresia: *J. Amer. Med. Assoc.*, 1945; 128): 189-202.
- Bolzon, G., G. Pedrizzetti, M. Grigioni, L. Zovatto, C. Daniele, and G. D'Avenio, Flow on the symmetry plane of a total cavo-pulmonary connection: *J Biomech*, 2002; 35 (5): 595-608.
- Bridges, N. D., R. A. Jonas, J. E. Mayer, M. F. Flanagan, J. F. Keane, and A. R. Castaneda, Bidirectional cavopulmonary anastomosis as interim palliation for high-risk Fontan candidates. Early results: *Circulation*, 1990; 82 (5 Suppl): IV170-6.
- Bull, K., The Fontan procedure: lessons from the past: *Heart*, 1998; 79 (3): 213-4.
- Cebral, J. R., P. J. Yim, R. Lohner, O. Soto, and P. L. Choyke, Blood flow modeling in carotid arteries with computational fluid dynamics and MR imaging: *Acad Radiol*, 2002; 9 (11): 1286-99.
- Chong, C. K., C. S. Rowe, S. Sivanesan, A. Rattray, R. A. Black, A. P. Shortland, and T. V. How, Computer aided design and fabrication of models for in vitro studies of vascular fluid dynamics: *Proc Inst Mech Eng [H]*, 1999; 213 (1): 1-4.

- Choussat, A., F. Fontan, F. Besse, F. Vallot, A. Chauve, and H. Bricaud, Selection criteria for Fontan's procedure, In Anderson R, Shinebourne E (eds.): Paediatric Cardiology. Churchill Livingstone, Edinburgh, 1978
- Chowdhury, U. K., S. S. Kothari, A. Saxena, A. Govil, G. Subramaniam, and B. Airan, Viable Extracardiac Total Right Heart Bypass: Technical Considerations and Mid-term Results: Heart, Lung and Circulation, 2004; 13 (1): 56-63.
- Chuk, R. N., and V. J. Thomson, A comparison of rapid prototyping techniques used for wind tunnel model fabrication: Rapid Prototyping Journal, 1998; 4 (1): 185-196.
- Coleman, H. W., Some observations on uncertainties and the verification and validation of a simulation: J. Fluids Eng., 2003; 125 (1): 733-35.
- Coon, P. D., J. Rychik, R. T. Novello, P. S. Ro, J. W. Gaynor, and T. L. Spray, Thrombus formation after the Fontan operation: Ann Thorac Surg, 2001; 71 (6): 1990-4.
- Cotran, R. S., S. L. Robbins, and V. Kumar, Robbins Pathologic Basis of Disease, W.B. Saunders Company, Philadelphia, PA, 1994
- de Leval, M. R., G. Dubini, F. Migliavacca, H. Jalali, G. Camporini, A. Redington, and R. Pietrabissa, Use of computational fluid dynamics in the design of surgical procedures: application to the study of competitive flows in cavo-pulmonary connections: J Thorac Cardiovasc Surg, 1996; 111 (3): 502-13.
- de Leval, M. R., P. Kilner, M. Gewillig, and C. Bull, Total cavopulmonary connection: a logical alternative to atriopulmonary connection for complex Fontan operations. Experimental studies and early clinical experience: J Thorac Cardiovasc Surg, 1988; 96 (5): 682-95.
- de Zélicourt, D.A., Pekkan, K., Wills, E., Kanter, K., Forbess, J., Sharma, S., Fogel, M., and A. P. Yoganathan, In Vitro Flow Analysis of a Patient Specific Intra-Atrial TCPC: Ann Thorac Surg (conditional acceptance) November 2004
- DeGroff, C. G., B. L. Thornburg, J. O. Pentecost, K. L. Thornburg M. Gharib, D. J. Sahn, and A. Baptista, Flow in the early embryonic human heart: a numerical study: Pediatr Cardiol, 2003; 24 (4): 375-80.
- DeGroff, C. G., J. D. Carlton, C. E. Weinberg, M. C. Ellison, R. Shandas, and L. Valdes-Cruz, Effect of vessel size on the flow efficiency of the total cavopulmonary connection: in vitro studies: Pediatr Cardiol, 2002; 23 (2): 171-7.
- Dobell, A. R., G. A. Trusler, J. F. Smallhorn, and W. G. Williams, Atrial thrombi after the Fontan operation: Ann Thorac Surg, 1986; 42 (6): 664-7.
- Driscoll, D. J., K. P. Offord, R. H. Feldt, H. V. Schaff, F. J. Puga, and G. K. Danielson, Five- to fifteen-year follow-up after Fontan operation: Circulation, 1992; 85 (2): 469-96.

- Ensley, A. E., A Fluid Mechanic assessment of the Total cavopulmonary Connection, Georgia Institute of Technology, Atlanta, 2000
- Ensley, A. E., P. Lynch, G. P. Chatzimavroudis, C. Lucas, S. Sharma, and A. P. Yoganathan, Toward designing the optimal total cavopulmonary connection: an in vitro study: *Ann Thorac Surg*, 1999; 68 (4): 1384-90.
- Farhat, C., S. Lanteri, and H. D. Simon, TOP/DOMECA software tool for mesh partitioning and parallel processing: *J. Comput. Sys. in Eng.*, 1995; 6 (1): 13-26.
- Fogel, M. A., P. M. Weinberg, A. J. Chin, K. E. Fellows, and E. A. Hoffman, Late ventricular geometry and performance changes of functional single ventricle throughout staged Fontan reconstruction assessed by magnetic resonance imaging: *J Am Coll Cardiol*, 1996; 28 (1): 212-21.
- Fogel, M. A., P. M. Weinberg, J. Rychik, A. Hubbard, M. Jacobs, T. L. Spray, and J. Haselgrove, Caval contribution to flow in the branch pulmonary arteries of Fontan patients with a novel application of magnetic resonance presaturation pulse: *Circulation*, 1999; 99 (9): 1215-21.
- Fontan, F., and E. Baudet, Surgical repair of tricuspid atresia: *Thorax*, 1971; 26): 240-248.
- Fontan, F., J. W. Kirklin, G. Fernandez, F. Costa, D. C. Naftel, F. Tritto, and E. H. Blackstone, Outcome after a "perfect" Fontan operation: *Circulation*, 1990; 81 (5): 1520-36.
- Frakes, D. H., C. P. Conrad, T. M. Healy, J. W. Monaco, M. Fogel, S. Sharma, M. J. Smith, and A. P. Yoganathan, Application of an adaptive control grid interpolation technique to morphological vascular reconstruction: *IEEE Trans Biomed Eng*, 2003; 50 (2): 197-206.
- Frakes, D. H., Pekkan, K., Smith, M.J.T., Yoganathan, A. Three-Dimensional Velocity Field Reconstruction. *J. of Biomechanical Eng.* (article in press)
- Francois, K., M. Tamim, T. Bove, K. D. Groote, D. De Wolf, D. Matthys, B. Suys, H. Verhaaren, and G. Van Nooten, Is Morbidity Influenced by Staging in the Fontan Palliation? A Single Center Review: *Pediatr Cardiol*, 2004.
- Fratz, S., R. Geiger, H. Kresse, G. Roemer, M. Hennig, W. Sebenig, and J. Hess, Pulmonary blood pressure, not flow, is associated with net endothelin-1 production in the lungs of patients with congenital heart disease and normal pulmonary vascular resistance: *J Thorac Cardiovasc Surg*, 2003; 126 (6): 1724-9.
- Freitas, C. J., Journal of fluids engineering editorial policy statement on the control of numerical accuracy: *J. Fluids Eng.*, 1993; 115 (1): 339-40.

- Freitas, C. J., Perspective: Selected benchmarks from commercial CFD codes: *J. Fluids Eng.*, 1995; 117.
- Freitas, C. J., The issue of numerical uncertainty: *Applied Mathematical Modeling*, 2002; 26 (1): 237-48.
- Friedman, M. H., Arteriosclerosis research using vascular flow models: from 2-D branches to compliant replicas: *ASME J. Biomech. Eng.*, 1993; 115 (1): 595–601.
- Ge, L., S. C. Jones, F. Sotiropoulos, T. M. Healy, and A. P. Yoganathan, Numerical simulation of flow in mechanical heart valves: grid resolution and the assumption of flow symmetry: *J Biomech Eng*, 2003; 125 (5): 709-18.
- Gerdes, A., J. Kunze, G. Pfister, and H. H. Sievers, Addition of a small curvature reduces power losses across total cavopulmonary connections: *Ann Thorac Surg*, 1999; 67 (6): 1760-4.
- Gersony, D. R., and W. M. Gersony, Management of the Postoperative Fontan patient: *Progress in Pediatric Cardiology*, 2003; 17 (1): 73-79.
- Geva, T., D. J. Sahn, and A. J. Powell, Magnetic Resonance Imaging of Congenital heart Disease in Adults: *Progress in Pediatric Cardiology*, 2003; 17 (1): 21-39.
- Gewillig, M. H., U. R. Lundstrom, C. Bull, R. K. Wyse, and J. E. Deanfield, Exercise responses in patients with congenital heart disease after Fontan repair: patterns and determinants of performance: *J Am Coll Cardiol*, 1990; 15 (6): 1424-32.
- Gilmanov, A., and F. Sotiropoulos, Numerical Simulation of Fish Swimming at Low Reynolds Numbers: American Physical Society, Division of Fluid Dynamics 55th Annual Meeting, 2002.
- Glenn, W. W. L., Circulatory bypass of the right side of the heart: *N. Engl. J. Med.*, 1958; 259): 117-120.
- Grigioni, M., A. Amodeo, C. Daniele, G. D'Avenio, R. Formigari, and R. M. Di Donato, Particle image velocimetry analysis of the flow field in the total cavopulmonary connection: *Artif Organs*, 2000; 24 (12): 946-52.
- Guadagni, G., E. L. Bove, F. Migliavacca, and G. Dubini, Effects of pulmonary afterload on the hemodynamics after the hemi-Fontan procedure: *Med Eng Phys*, 2001; 23 (5): 293-8.
- Guide for the verification and validation of computational fluid dynamics simulations: American Institute of Aeronautics and Astronautics (AIAA), 1998, G-077-1998.
- Guyton, A. C., J. E. Hall, and W. Schmitt, *Human Physiology and Mechanisms of Disease*, WB Saunders Company, Philadelphia, Pennsylvania, 1997

- Haas, G. S., H. Hess, M. Black, J. Onnasch, F. W. Mohr, and J. A. van Son, Extracardiac conduit fontan procedure: early and intermediate results: *Eur J Cardiothorac Surg*, 2000; 17 (6): 648-54.
- Haroutunian, V., M. S. Engelman, and I. Hasbani, Segregated finite element algorithms for the numerical solution of large-scale incompressible flow problems.: *Int. J. Numer. Methods Fluids.*, 1993; 17 (1): 323-348.
- Healy, T. M., C. Lucas, and A. P. Yoganathan, Noninvasive fluid dynamic power loss assessments for total cavopulmonary connections using the viscous dissipation function: a feasibility study: *J Biomech Eng*, 2001; 123 (4): 317-24.
- Healy, T. M., Multi-Block and overset-block domain decomposition techniques for cardiovascular flow simulation, Georgia Institute of Technology, Atlanta, 2001
- Hjortdal, V. E., K. Emmertsen, E. Stenbog, T. Frund, M. R. Schmidt, O. Kromann, K. Sorensen, and E. M. Pedersen, Effects of exercise and respiration on blood flow in total cavopulmonary connection: a real-time magnetic resonance flow study: *Circulation*, 2003; 108 (10): 1227-31.
- Hopkins, L. M., J. T. Kelly, A. S. Wexler, and A. K. Prasad, Particle image velocimetry measurements in complex geometries: *Experiments in Fluids*, 2000; 29 (1): 91-95.
- Hsia, T. Y., F. Migliavacca, S. Pittaccio, A. Radaelli, G. Dubini, G. Pennati, and M. de Leval, Computational fluid dynamic study of flow optimization in realistic models of the total cavopulmonary connections: *J Surg Res*, 2004; 116 (2): 305-13.
- Hughes, T. R. J., and A. N. Brooks, 1979, A multidimensional upwind scheme with no crosswind diffusion, in: *Finite Element Methods for Convection Dominated Flows*, edited by T.J.R. Hughes, New York, p. 19-35.
- Hughes, T. R. J., L. P. Franca, and M. Becestra, A new finite element formulation for computational fluid dynamics, V. Circumventing the Babuska-Brezzi conduction, A stable Petrov-Galerkin formulation of the Stokes problem accommodating equal-order interpolations: *Comp. Meth. Appl. Mech. Eng.*, 1986; 59 (1): 85-89.
- Ibrahim, M., R. G. Masters, P. J. Hendry, R. A. Davies, S. Smith, C. Struthers, V. M. Walley, and W. J. Keon, Determinants of hospital survival after cardiac transplantation: *Ann Thorac Surg*, 1995; 59 (3): 604-8.
- Iordanis, C., V. D. Butty, V. B. Makhijani, D. Poulidakos, and Y. Ventikos, Pulsatile blood flow in anatomically accurate vessels with multiple aneurysms: A medical intervention planning application of computational haemodynamics: *Flow, Turbulence and Combustion*, 2003; 71 (1): 333-46.

- Johnston, B. M., P. R. Johnston, S. Corney, and D. Kilpatrick, Non-Newtonian blood flow in human right coronary arteries: steady state simulations: *J Biomech*, 2004; 37 (5): 709-20.
- Justino, H., L. N. Benson, and R. M. Freedom, Development of unilateral pulmonary arteriovenous malformations due to unequal distribution of hepatic venous flow: *Circulation*, 2001; 103 (8): E39-40.
- Kanter, K. R., R. N. Vincent, and A. A. Raviele, Importance of acquired systemic-to-pulmonary collaterals in the Fontan operation: *Ann Thorac Surg*, 1999; 68 (3): 969-74; discussion 974-5.
- Karypis, G., and V. Kumar, MeTIS - A software package for partitioning unstructured graphs, partitioning meshes and computing fill-reducing orderings of sparse matrices (Version 3.0), University of Minnesota, Department of Computer Science/Army HPC research center, 1997
- Keane, R. D., and R. J. Adrian, Optimization of particle image velocimeters. Part I: double pulsed systems: *Meas. Sci. Technol.*, 1990; 1 (1): 1202-1215.
- Kerber, C. W., C. B. Heilman, and P. H. Zanetti, Transparent elastic arterial models. I: A brief technical note: *Biorheology*, 1989; 26 (6): 1041-9.
- Khunatorn, Y., R. Shandas, C. DeGroof, and S. Mahalingam, Comparison of in vitro velocity measurements in a scaled total cavopulmonary connection with computational predictions: *Ann Biomed Eng*, 2003; 31 (7): 810-22.
- Kiaffas, M. G., R. Van Praagh, C. Hanioti, and D. W. Green, The modified Fontan procedure: morphometry and surgical implications: *Ann Thorac Surg*, 1999; 67 (6): 1746-53.
- Kim, Y. H., P. G. Walker, A. A. Fontaine, S. Panchal, A. E. Ensley, J. Oshinski, S. Sharma, B. Ha, C. L. Lucas, and A. P. Yoganathan, Hemodynamics of the Fontan connection: an in-vitro study: *J Biomech Eng*, 1995; 117 (4): 423-8.
- Kreutzer, G., E. Galindez, H. Bono, C. De Palma, and J. P. Laura, An operation for the correction of tricuspid atresia: *J Thorac Cardiovasc Surg*, 1973; 66 (4): 613-21.
- Ku, D. N., and D. P. Giddens, Laser Doppler anemometer measurements of pulsatile flow in a model carotid bifurcation: *J Biomech*, 1987; 20 (4): 407-21.
- Ku, J. P., M. T. Draney, F. R. Arko, W. A. Lee, F. P. Chan, N. J. Pelc, C. K. Zarins, and C. A. Taylor, In vivo validation of numerical prediction of blood flow in arterial bypass grafts: *Ann Biomed Eng*, 2002; 30 (6): 743-52.
- Laccarino, G., Predictions of a turbulent separated flow using commercial CFD codes: *J. Fluids Eng.*, 2001; 123 (1): 819-28.

- Langhaar, H.: J. Appl. Mech., 1942; 9 (1): 55-58.
- Lardo, A. C., P. J. del Nido, S. A. Webber, I. Friehs, and E. G. Cape, Hemodynamic effect of progressive right atrial dilatation in atriopulmonary connections: J Thorac Cardiovasc Surg, 1997; 114 (1): 2-8.
- Lardo, A. C., S. A. Webber, I. Friehs, P. J. del Nido, and E. G. Cape, Fluid dynamic comparison of intra-atrial and extracardiac total cavopulmonary connections: J Thorac Cardiovasc Surg, 1999; 117 (4): 697-704.
- Lemler, M. S., W. A. Scott, S. R. Leonard, D. Stromberg, and C. Ramaciotti, Fenestration improves clinical outcome of the fontan procedure: a prospective, randomized study: Circulation, 2002; 105 (2): 207-12.
- Leo, H. L., Z. He, J. T. Ellis, and A. P. Yoganathan, Microflow fields in the hinge region of the CarboMedics bileaflet mechanical heart valve design: J Thorac Cardiovasc Surg, 2002; 124 (3): 561-74.
- Liu, Y., K. Pekkan, C. Jones, and A. P. Yoganathan, The effects of different mesh generation methods on fluid dynamic analysis and power loss in total cavopulmonary connection (TCPC). J. of Biomech. Eng., 2004; (in press)
- Low, H. T., Y. T. Chew, and C. N. Lee, Flow studies on atriopulmonary and cavopulmonary connections of the Fontan operations for congenital heart defects: J Biomed Eng, 1993; 15 (4): 303-7.
- Mair, D. D., F. J. Puga, and G. K. Danielson, Late functional status of survivors of the Fontan procedure performed during the 1970s: Circulation, 1992; 86 (5 Suppl): II106-9.
- Marcelletti, C. F., F. L. Hanley, C. Mavroudis, D. B. McElhinney, R. F. Abella, S. M. Marianeschi, F. Seddio, V. M. Reddy, E. Petrossian, T. de la Torre, L. Colagrande, C. L. Backer, A. Cipriani, F. S. Iorio, and F. Fontan, Revision of previous Fontan connections to total extracardiac cavopulmonary anastomosis: A multicenter experience: J Thorac Cardiovasc Surg, 2000; 119 (2): 340-6.
- Mavroudis, C., V. R. Zales, C. L. Backer, A. J. Muster, and L. A. Latson, Fenestrated Fontan with delayed catheter closure. Effects of volume loading and baffle fenestration on cardiac index and oxygen delivery: Circulation, 1992; 86 (5 Suppl): II85-92.
- McGuirk, S. P., D. S. Winlaw, S. M. Langley, O. F. Stumper, J. V. de Giovanni, J. G. Wright, W. J. Brawn, and D. J. Barron, The impact of ventricular morphology on midterm outcome following completion total cavopulmonary connection: Eur J Cardiothorac Surg, 2003; 24 (1): 37-46.

- Mertens, L., D. J. Hagler, U. Sauer, J. Somerville, and M. Gewillig, Protein-losing enteropathy after the Fontan operation: an international multicenter study. PLE study group: *J Thorac Cardiovasc Surg*, 1998; 115 (5): 1063-73.
- Metcalf, R. W., The promise of computational fluid dynamics as a tool for delineating therapeutic options in the treatment of aneurysms: *Am. J. Neuroradiol.*, 2003; 24 (1): 553-554.
- Migliavacca, F., G. Dubini, E. L. Bove, and M. R. de Leval, Computational fluid dynamics simulations in realistic 3-D geometries of the total cavopulmonary anastomosis: the influence of the inferior caval anastomosis: *J Biomech Eng*, 2003; 125 (6): 805-13.
- Migliavacca, F., M. R. de Leval, G. Dubini, and R. Pietrabissa, A computational pulsatile model of the bidirectional cavopulmonary anastomosis: the influence of pulmonary forward flow: *J Biomech Eng*, 1996; 118 (4): 520-8.
- Migliavacca, F., M. R. de Leval, G. Dubini, R. Pietrabissa, and R. Fumero, Computational fluid dynamic simulations of cavopulmonary connections with an extracardiac lateral conduit: *Med Eng Phys*, 1999; 21 (3): 187-93.
- Migliavacca, F., P. J. Kilner, G. Pennati, G. Dubini, R. Pietrabissa, R. Fumero, and M. R. de Leval, Computational fluid dynamic and magnetic resonance analyses of flow distribution between the lungs after total cavopulmonary connection: *IEEE Trans Biomed Eng*, 1999; 46 (4): 393-9.
- Moller, J. H., and R. C. Anderson, 1,000 consecutive children with a cardiac malformation with 26- to 37-year follow-up: *Am J Cardiol*, 1992; 70 (6): 661-7.
- Moore, J. A., D. A. Steinman, S. Prakash, K. W. Johnston, and C. R. Ethier, A numerical study of blood flow patterns in anatomically realistic and simplified end-to-side anastomoses: *J Biomech Eng*, 1999; 121 (3): 265-72.
- Mott, A. R., T. L. Spray, J. W. Gaynor, R. I. Godinez, S. C. Nicolson, J. M. Steven, W. M. DeCampli, G. J. Schears, and G. Wernovsky, Improved early results with cavopulmonary connections: *Cardiol Young*, 2001; 11 (1): 3-11.
- Norwood, W. I., and M. L. Jacobs, Fontan's procedure in two stages: *Am J Surg*, 1993; 166 (5): 548-51.
- Nowak, N., P. P. Kakade, and A. V. Annapragada, Computational fluid dynamics simulation of airflow and aerosol deposition in human lungs: *Ann Biomed Eng*, 2003; 31 (4): 374-90.
- Oddou, C., P. Flaud, and D. Geiger, 1978, Model of non-linear viscoelastic wall rheology applied to arterial dynamic, in: *The Arterial System*, R.D. Bauer and R. Busse, eds, Springer Berlin, p. 101-108.

- Orlando, W., J. Hertzberg, R. Shandas, and C. DeGroff, Reverse flow in compliant vessels and its implications for the Fontan procedure: numerical studies: *Biomed Sci Instrum*, 2002; 38): 321-6.
- Pearl, J. M., H. Laks, D. G. Stein, D. C. Drinkwater, B. L. George, and R. G. Williams, Total cavopulmonary anastomosis versus conventional modified Fontan procedure: *Ann Thorac Surg*, 1991; 52 (2): 189-96.
- Pekkan, K., D. de Zélicourt, L. Ge, F. Sotiropoulos, D. H. Frakes, M. A. Fogel, and A. P. Yoganathan, Physics-driven CFD modeling of complex anatomical cardiovascular flows-a TCPC case study: *Ann. Biomed. Eng.*, 2004; (in press).
- Petrossian, E., V. M. Reddy, D. B. McElhinney, G. P. Akkersdijk, P. Moore, A. J. Parry, L. D. Thompson, and F. L. Hanley, Early results of the extracardiac conduit Fontan operation: *J Thorac Cardiovasc Surg*, 1999; 117 (4): 688-96.
- Pike, N. A., L. A. Vricella, J. A. Feinstein, M. D. Black, and B. A. Reitz, Regression of severe pulmonary arteriovenous malformations after Fontan revision and "hepatic factor" rerouting: *Ann Thorac Surg*, 2004; 78 (2): 697-9.
- Podzolkov, V. P., S. B. Zaets, M. R. Chiaureli, B. G. Alekryan, L. M. Zotova, and I. G. Chernikh, Comparative assessment of Fontan operation in modifications of atriopulmonary and total cavopulmonary anastomoses: *Eur J Cardiothorac Surg*, 1997; 11 (3): 458-65.
- Potts, W. J., S. Smith, and S. Gibson, Anastomosis of the aorta to a pulmonary artery: *J. Amer. Med. Assoc.*, 1946; 132): 627-631.
- Quinones, J. A., S. Y. Deleon, T. J. Bell, F. Cetta, S. M. Moffa, J. E. Freeman, D. A. Vitullo, and E. A. Fisher, Fenestrated fontan procedure: evolution of technique and occurrence of paradoxical embolism: *Pediatr Cardiol*, 1997; 18 (3): 218-21.
- Roache, P. J., *Verification and Validation in Computational Science and Engineering*, Hermosa publishers, New Mexico, 1998:
- Rosano, A., L. D. Botto, B. Botting, and P. Mastroiacovo, Infant mortality and congenital anomalies from 1950 to 1994: an international perspective: *J Epidemiol Community Health*, 2000; 54 (9): 660-6.
- Rychik, J., and M. I. Cohen, Long-term outcome and complications of patients with single ventricle: *Progress in Pediatric Cardiology*, 2002; 16 (1): 89-103.
- Rydberg, A., D. E. Teien, and P. Krus, Computer simulation of circulation in patient with total cavo-pulmonary connection: inter-relationship of cardiac and vascular pressure, flow, resistance and capacitance: *Med Biol Eng Comput*, 1997; 35 (6): 722-8.

- Ryu, K., T. M. Healy, A. E. Ensley, S. Sharma, C. Lucas, and A. P. Yoganathan, Importance of accurate geometry in the study of the total cavopulmonary connection: computational simulations and in vitro experiments: *Ann Biomed Eng*, 2001; 29 (10): 844-53.
- Ryu, K., The importance of realistic geometry in the study of the total cavopulmonary connection, Georgia Institute of Technology, Atlanta, 2000
- Saber, N. R., A. D. Gosman, N. B. Wood, P. J. Kilner, C. L. Charrier, and D. N. Firmin, Computational flow modeling of the left ventricle based on in vivo MRI data: initial experience: *Ann Biomed Eng*, 2001; 29 (4): 275-83.
- Salim, M. A., T. G. DiSessa, K. L. Arheart, and B. S. Alpert, Contribution of superior vena caval flow to total cardiac output in children. A Doppler echocardiographic study: *Circulation*, 1995; 92 (7): 1860-5.
- Schneider Children's Hospital, New Hyde Park, NY:
http://www.schneiderchildrenshospital.org/peds_html_fixed/peds/cardiac.
 Accessed July 2004
- Seliem, M., A. J. Muster, M. H. Paul, and D. W. Benson, Jr., Relation between preoperative left ventricular muscle mass and outcome of the Fontan procedure in patients with tricuspid atresia: *J Am Coll Cardiol*, 1989; 14 (3): 750-5.
- Shachar, G. B., B. P. Fuhrman, Y. Wang, R. V. Lucas, Jr., and J. E. Lock, Rest and exercise hemodynamics after the Fontan procedure: *Circulation*, 1982; 65 (6): 1043-8.
- Shahcheraghi, N., H. A. Dwyer, A. Y. Cheer, A. I. Barakat, and T. Rutaganira, Unsteady and three-dimensional simulation of blood flow in the human aortic arch: *J Biomech Eng*, 2002; 124 (4): 378-87.
- Sharma, S., A. E. Ensley, K. Hopkins, G. P. Chatzimavroudis, T. M. Healy, V. K. Tam, K. R. Kanter, and A. P. Yoganathan, In vivo flow dynamics of the total cavopulmonary connection from three-dimensional multislice magnetic resonance imaging: *Ann Thorac Surg*, 2001; 71 (3): 889-98.
- Sharma, S., S. Goudy, P. Walker, S. Panchal, A. Ensley, K. Kanter, V. Tam, D. Fyfe, and A. Yoganathan, In vitro flow experiments for determination of optimal geometry of total cavopulmonary connection for surgical repair of children with functional single ventricle: *J Am Coll Cardiol*, 1996; 27 (5): 1264-9.
- Shemin, R. J., W. H. Merrill, J. S. Pfeifer, D. M. Conkle, and A. G. Morrow, Evaluation of right atrial-pulmonary artery conduits for tricuspid atresia. Experimental study: *J Thorac Cardiovasc Surg*, 1979; 77 (5): 685-90.
- Shiota, T., R. Lewandowski, J. E. Piel, L. S. Smith, C. Lancee, K. Djoa, N. Bom, A. Cobanoglu, M. J. Rice, and D. J. Sahn, Micromultiplane transesophageal

- echocardiographic probe for intraoperative study of congenital heart disease repair in neonates, infants, children, and adults: *Am J Cardiol*, 1999; 83 (2): 292-5, A7.
- Simon, H. A., Influence of the implant location on the bing and leakage flow fields through bileaflet mechanical heart valves, Georgia Institute of Technology, Atlanta, 2004,
- Sittiwangkul, R., A. Azakie, G. S. Van Arsdell, W. G. Williams, and B. W. McCrindle, Outcomes of tricuspid atresia in the Fontan era: *Ann Thorac Surg*, 2004; 77 (3): 889-94.
- Springer, A. M., Application of rapid prototyping methods to high-speed wind tunnel testing: Project 96-21, NASA Marshall Space Flight Center Technical Publication, 1998; 05-01.
- Srivastava, D., T. Preminger, J. E. Lock, V. Mandell, J. F. Keane, J. E. Mayer, Jr., H. Kozakewich, and P. J. Spevak, Hepatic venous blood and the development of pulmonary arteriovenous malformations in congenital heart disease: *Circulation*, 1995; 92 (5): 1217-22.
- Tam, V. K., B. E. Miller, and K. Murphy, Modified Fontan without use of cardiopulmonary bypass: *Ann Thorac Surg*, 1999; 68 (5): 1698-703; discussion 1703-4.
- Tang, H. S., C. Jones, and F. Sotiropoulos, An overset-grid method for 3D unsteady incompressible flows: *J. Comput. Phys.*, 2003; 191 (2): 567-600.
- Tanoue, Y., A. Sese, Y. Imoto, and K. Joh, Ventricular mechanics in the bidirectional glenn procedure and total cavopulmonary connection: *Ann Thorac Surg*, 2003; 76 (2): 562-6.
- Tanoue, Y., A. Sese, Y. Ueno, K. Joh, and T. Hijii, Bidirectional Glenn procedure improves the mechanical efficiency of a total cavopulmonary connection in high-risk fontan candidates: *Circulation*, 2001; 103 (17): 2176-80.
- Thomas, J. B., J. S. Milner, B. K. Rutt, and D. A. Steinman, Reproducibility of image-based computational fluid dynamics models of the human carotid bifurcation: *Ann Biomed Eng*, 2003; 31 (2): 132-41.
- Thompson, L. D., E. Petrossian, D. B. McElhinney, N. A. Abrikosova, P. Moore, V. M. Reddy, and F. L. Hanley, Is it necessary to routinely fenestrate an extracardiac fontan? *J Am Coll Cardiol*, 1999; 34 (2): 539-44.
- Van Haesdonck, J. M., L. Mertens, R. Sizaire, G. Montas, B. Purnode, W. Daenen, M. Crochet, and M. Gewillig, Comparison by computerized numeric modeling of energy losses in different Fontan connections: *Circulation*, 1995; 92 (9 Suppl): II322-6.

- Wilson, W. C., D. P. Kapelanski, J. L. Benumof, J. W. Newhart 2nd, F. W. Johnson, and R. N. Channick, Inhaled nitric oxide (40 ppm) during one-lung ventilation, in the lateral decubitus position, does not decrease pulmonary vascular resistance or improve oxygenation in normal patients: *J Cardiothorac Vasc Anesth*, 1997; 11 (2): 172-6.
- Yalcinbas, Y. K., E. Erek, E. Salihoglu, A. Sarioglu, and T. Sarioglu, Early results of extracardiac Fontan procedure with autologous pericardial tube conduit, 2004.
- Yedavalli, R. V., F. Loth, A. Yardimci, W. F. Pritchard, J. N. Oshinski, L. Sadler, F. Charbel, and N. Alperin, Construction of a physical model of the human carotid artery based upon in vivo magnetic resonance images: *Journal of Biomechanical Engineering*, 2001; 123 (4): 372-376.